University of Bath

PHD

Integrated marine biorefineries for the production of advanced liquid fuels and value-added materials

Jones, Ed

Award date:
2023

Awarding institution:
University of Bath

Link to publication

Alternative formats
If you require this document in an alternative format, please contact:
openaccess@bath.ac.uk

Copyright of this thesis rests with the author. Access is subject to the above licence, if given. If no licence is specified above, original content in this thesis is licensed under the terms of the Creative Commons Attribution-NonCommercial 4.0 International (CC BY-NC-ND 4.0) Licence (https://creativecommons.org/licenses/by-nc-nd/4.0/). Any third-party copyright material present remains the property of its respective owner(s) and is licensed under its existing terms.

Take down policy
If you consider content within Bath's Research Portal to be in breach of UK law, please contact: openaccess@bath.ac.uk with the details. Your claim will be investigated and, where appropriate, the item will be removed from public view as soon as possible.

Download date: 03. Mar. 2023

Integrated marine biorefineries for the production of advanced liquid fuels and value-added materials

submitted by

Edward Jones

in partial fulfillment of the requirements for the degree of Doctor of Philosophy

of the

University of Bath

Department of Chemical Engineering

October 2022

COPYRIGHT

Attention is drawn to the fact that copyright of this thesis rests with the author. A copy of this thesis has been supplied on condition that anyone who consults it is understood to recognise that its copyright rests with the author and that they must not copy it or use material from it except as permitted by law or with the consent of the author.

Signed on behalf of the Faculty of Engineering and Design .....

Acknowledgements

Thanks to my supervisor, Professor Chris Chuck. As a supervisor he has shown kindness and compassion towards my personal circumstances throughout my time in Bath and has been pragmatic and flexible in his approach to supporting my academic work.

Thanks to the friends I made from my PhD cohort (CSCT CDT 2018 intake). Peer support has been so very important through this experience, and I have made friends for life during this time.

Thanks to friends and colleagues in my research group too. To Luca and Stef, the post-graduate researchers that always had time to help. Thanks to Jackie, Julia, Monty, Vanessa, Lorraine, Andre, and Scott - research group members who have helped me with advice, who performed synthesis, repeats, and data-collection at times on my behalf, and who provided friendship and support in equal measure. Thanks to Jack, Aezaz, Ben, Ivor, and Jordan, the undergraduate chemical engineers who helped develop the foundation process models during their undergraduate masters project work.

Thanks to the staff at the University of Bath. To the Dept. of Chemical Engineering technical team, to the technicians of the MC2 analytical facility, and to the Estates team for helping me gain access to their composting site.

To friends and family. To those that started the journey with me, those that joined me on the path, and those that I lost along the way. The time you gave to me through this process will always be deeply appreciated.

This thesis was funded through an Engineering and Physical Sciences Research Council

grant (EP/L016354/1), by way of a Centre for Doctoral Training administered by the Centre for Sustainable and Circular Technologies (University of Bath, UK).

Abstract

Marine biorefineries process marine-sourced biomass, such as seaweed (macroalgae) into fuels, chemicals, and new materials. Macroalgae are large multi-cellular and visible plant-like marine algae, commonly referred to as seaweeds. As a source of biomass, macroalgae represents a highly attractive feedstock for the extraction and isolation of high value biomacromolecules, as well as the conversion via thermochemical processing into fuel products, and carbonaceous solids suitable for soil amelioration and carbon sequestration. The potential applications of the marine microalgal biorefinery are well established, however there are limited reports of the technoeconomic feasibility of macroalgal biorefinery processes for the production of fuels, carbonaceous solids, or downstream high-value materials such as composite biopolymers.

Initially a hydrothermal macroalgae-to-biocrude conversion route was investigated. A general purpose macroalgal hydrothermal liquefaction (HTL) process model was developed with a combination of experimental and published data, and this model was used to design and cost a simplified large-scale industrial process with the aim of investigating the economic feasibility of producing HTL-biocrude from a macroalgae feedstock.

While the lab-scale experimental demonstration of the macroalgae-to-biocrude process has been shown previously, this work demonstrated that the minimum selling price of the corresponding bio-barrel of crude (bioBBL) would be 5 to 10 times that of currently available fossil crudes, with reasonable prices only being achieved with significant additional valorisation of wastes and legislative incentives.

Attention was therefore turned towards the using the biorefinery for production of a composite biopolymer product based primarily on the extraction of algal polysaccharides and coupling with a thermochemical conversion process for the production of carbonaceous solids from the extracted macroalgae residues as an additional value-stream. Excitingly, process models, plant design, and technoeconomic analysis of this biorefinery concept demonstrated that a bulk alginate-based polymer could be produced at cost-parity to existing biopolymer products currently available on the market.

Experimental investigations into the coupled biomacromolecule extraction biorefinery and char-production revealed the technical feasibility of combining a number of different extraction steps for isolation of different algal fractions rich in different compounds. Slow pyrolysis was demonstrated as the preferable process for production of a carbon sequestration material and soil ameliorant. However, despite numerous previous reports into suitability of alginate composites for food packaging applications, this work found poor water contact and water barrier properties of these simple polysaccharide films.

In an attempt to improve the water contact properties, agar was functionalised with a C16 fatty-acid residue. This new functionalised material was found to be practically insoluble in all common lab solvents, thus melt-flow processing was successfully demonstrated by way of rheometry assessments and extrusion processing of the functionalised material.

Finally, the end-of-life disposal routes of the demonstrated algal biopolymers was considered in aerobic composting and anaerobic digestion. In both cases, simple alginate materials were found to degrade extremely rapidly. Functionalised agar was significantly slower, however began to show consistent degradation after day 40 in the anaerobic digestion process, and day 56 in the composting trials.

This work has presented two new process modelling methods for the processing of macroalgae in the biorefinery, demonstrated that economic feasibility is achievable when the right products are targeted, and that newly produced biopolymer products are highly degradable in two common end-of-life disposal routes for organic wastes. The

macroalgal marine biorefinery remains a highly attractive prospect for the production of new and alternative materials.

Dissemination

Arising primarily from work printed in this thesis.

Journal Arcticles

Amponsah L., Jones E.S., Parsons S., Chuck. C., LCA and TEA of the Macroalgal Film Biorefinery, manuscript in preparation for submission to *Journal of Cleaner Production* or *ACS Environmental Science & Technology.*

Conference Contributions

CSCT Summer Showcase 2022: Molecules to Materials for a Sustainable Future (Bath, UK), 27 - 28 June 2022. Poster presentation, *"Technoeconomic Analysis and Predictive Modelling for the Macroalgal Hydrothermal Liquefaction Marine Biorefinery".*

CSCT Summer Showcase 2021: Race to Zero (Bath UK and on-line), 7 – 9 July 2021. Ignite Talk, *"Macroalgae, and the Marine Biorefinery".*

CSCT Winter Showcase 2020: Changing the World Through Sustainable Technologies — A Vision for 2050 (Bath UK and on-line), 14 – 18 December 2020. Poster presentation, *"Towards the Marine Biorefinery: Seawater Fractionation and HTL of Marine Algaes".*

Outreach

Glastonbury Festival: Science Futures Field (Glastonbury Festival, UK), 22 - 26 June 2022. Public engagement at Univesity of Bath research stand, *"History of Polymers, and showcase of Univeristy of Bath Research and Spinouts"*.

List of Figures

1.1 The extent of the June 2018 great Atlantic sargassum belt, direction of the north Atlantic meridional overturning circulation, and the influence of West African upwelling and Amazon basin run off. 7

1.2 Artists impression of the combined ocean-farm and offshore windfarm proposed by North Sea Farmers consortium and planned for 2030. 10

1.3 The structures of **a)** alginate, consisting of G and M blocks, **b)** carrageenans and **c)** agar. 11

1.4 The presumed structure of fucoidan. 13

1.5 Flow chart showing methods to separate sodium alginate, fucoidan and laminarin from *Sargassum fusiforme*. 16

1.6 A novel ultrasound-assisted method for extracting alginate from *S. muticum*. The conventional procedure is represented by grey dashed words, symbols and boxes. 17

1.7 Phase diagram of water showing its states, and characteristic points, with the subcritical region for hydrothermal processing indicated. SCF = supercritical fluid. 20

1.8 Simplified reaction pathway of hydrothermal liquefaction. 22

2.1 Global annual fossil fuel consumption and cumulative consumption (Gtoe, 1965 to 2017), and cumulative history of proven fossil reserves (Gtoe, 1980 to 2017). 31

2.2 Energy ratio vs. biocrude yield for **a)** various experimental flow HTL set-ups, where Circles: algal biomass; Squares: waste biomass; Triangles: wood; Diamonds: lignin. **b)** Subset of data from plot a) but demonstrating the impact of increasing mass concentration in the feed. 36

2.3 Example of the Xylene chain, including bulk intermediates, commodity chemicals, and the types of products that xylene chemicals end up in. . . 41

2.4 Simple kinetic reaction network for HTL reaction of biochemical content of biomass. 54

2.5 Kinetic reaction network for HTL reaction of biochemical content of biomass including char production. 57

2.6 A-100: Biomass receiving and pre-processing process flow diagram . . . 60

2.7 A-200: HTL Reaction and Separation Process Flow Diagram 61

2.8 A-400: Utilities and Services Process Flow Diagram 62

2.9 Process flow diagram of process simulation of the implementation of Area-200 in Aspen Plus V10. 65

2.10 Mass repartition summary of the acid pre-treatment for Spirulina and Sargassum. 75

2.11 Mass repartition summary of HTL reactions for Spirulina and Sargassum species in air atmosphere. 77

2.12 Total mass repartition of acid pre-treatment and HTL reactions for Spirulina and Sargassum species in air atmosphere, relative to starting biomass. 78

2.13 Estimated boiling curves of algal biocrudes compared to fossil crude. . . 82

2.14 Estimated petroleum fractions as yield on crude for spirulina biocrude and BP Azeri Ceyhan fossil crude. 83

2.15 Experimental vs. predicted values with the linear multi-component additive models for **a)** carbon, hydrogen, nitrogen, and oxygen dry wt. %, **b)** carbohydrate, protein, and lipid using the inverse matrix approach of section 2.4.2.3, and **c)** same parameters as figure b) but re-plotting parameters as per equations 2.22 85

2.16 **a)** R^2 correlation coefficient between predicted and experimental biocrude yields, for various HTL biocrude yield models in the literature and determined in this work, and **b)** the sum-squared error (SSE) of residuals between experimental and predicted biocrude yields for each model. . . . 90

2.17 Scatter plot of predicted biocrude yield vs. the experimental biocrude yields for model 3 (described by Eq. 2.26) using parameters listed in table 2.14. 91

2.18 Estimated build cost and specific build cost of the HTL plant equipment at feed rates scaling from 0.5 ton/day to 1000 ton/day.Individual equipment contributions to total plant cost. 95

2.19 Net-present value of the Macroalgae HTL plant for the production of bio-crude, assuming a selling price of biocrude from $50 per bio-barrel ($/bio-BBL) to 1000 $/bio-BBL at different algal dry flows, with a fixed macroalgal price of $200 /ton (dry). 97

2.20 The effect on NPV of the 100 ton/day HTL plant with a fixed biocrude price of $100/bio-BBL and feedstock cost of $200/ton (dry), when **a)** selling the HTL aqueous phase from $ 100 to $1000 per ton, and **b)** accounting for a carbon tax rising from $30/ton in year to $56/ton from year 10 onwards. 98

3.1 A-100: Biomass receiving and pre-processing process flow sheet 108

3.2 A-200: Alginate extraction and separation flowsheet. 109

3.3 A-300: Polymerisation, formulation, and biopolymer film production flowsheet. 110

3.4 A-400: Nanocellulose production train by acid digest flowsheet. 111

3.5 A-500: Biomass residue drying and slow-pyrolysis flowsheet. 112

3.6 A-600: Services and utilities provision flowsheet. 113

3.7 Aspen Plus implementation of the process critical unit operations in Area-100 and Area-200, the seaweed washing and alginate extraction processes. 117

3.8 Aspen Plus implementation of the process critical unit operations in Area-300, polymer formulation and solvent drying. 118

3.9 Aspen Plus implementation of the process critical unit operations in Area-400, nanocellulose generation and washing. 118

3.10 Aspen Plus implementation of the process critical unit operations in Area-500, slow pyrolysis reactor, residue dryer, and char coolers. 119

3.11 Resulting polymer film outlet temperature at different heater set-point temperatures and exhaust purge ratios, for the 10,000 ton year^{-1} biorefinery. Dotted red operating line at 150 ^{circ}C represents maximum allowable polymer temperature before onset of thermal degradation. 132

3.12 Total required duty for air trim heater (H-302) as a function of air-heater temperature set-point, for the 10,000 ton year^{-1} biorefinery, and subject to the variable fresh-air flow rate design spec to respect the maximum film moisture. For Exhaust purge ratios of 0.05, 0.1, and 0.15 the trends are clipped for operating conditions where the maximum polymer temperature is not respected. 133

3.13 Indicative power requirement for dryer recirculation fan, F-301, as a function of H-302 outlet temperature and the exhaust purge ratio for the 10,000 ton year^{-1} biorefinery, and subject to the variable fresh-air flow rate design spec to respect the maximum film moisture. For Exhaust purge ratios of 0.05, 0.1, and 0.15 the trends are clipped for operating conditions where the maximum polymer temperature is not respected. . 135

3.14 Indicative hourly operating cost for D-301 major equipment, for the 10,000 ton year-1 biorefinery and using electrical unit price of \$0.10 kWh^{-1} and thermal unit price of \$0.05 kWh^{-1}. 136

3.15 Total installed equipment cost as a function of installed plant scale, and by pyrolysis treatment option. 138

3.16 Summary of total year-on-year operating expenses incurred for a 10,000 tonne year^{-1} plant, with macroalgae supplied at 2,000 $ tonnne^{-1}, operating with a pyrolysis plant, on-site nitrogen generation, and no additional valorisation of char. 139
3.17 Repartition of total annual operating expenses for years in full production (year-5 onwards) for different scale plants, with different pyrolysis options, and a seaweed supply price of 2000 $ tonne^{-1}. 139
3.18 Annual biopolymer production quantity vs. total capital investment for biorefineries modelled in this work, and various commercial scale biopolymer plants including PLA, PBAT, PHA, and FDCA production facilities. 143
3.19 Comparison of bulk polymer prices for a range of traditional virgin polymers, recycled resins of mixed sources (traditional and biopolymers), biopolymers, and the alginate/cellulose composite polymer presented in this work at seaweed supply prices of 500 $ tonne^{-1} and 2000 $ tonne^{-1}. 145
3.20 Scatter plot of various polymer bulk supply prices compared to the bulk supply capacity for various polymer, biopolymer, and recycled granules, from suppliers with available on-line pricing. 146

4.1 Typical lag-time plot of pressure (or Q_t) as a function of changing time (t) used to assess gas permeability of polymeric membranes. 155
4.2 Diagram of custom gas permeation rig used to test the gas permeability of various test films. 157
4.3 Exploded schematic view of test-cell used in gas permeation rig. 157
4.4 Cascading multi-step extraction procedure, modified from Wahlstrom et al. (2018). 160
4.5 **a)** Particle size distribution (PSD) of the crystalline nanocellulose solution (CNC) produecd by acid digest of micro-crystalline cellulose, and measured by dynamic light scattering, and **b)** FeSEM imagery of crystalline nanocellulose solution. 163
4.6 Mass yields of single-step extractions of macroalgae species, using different extraction techniques to target different components. 173

4.7 FT-IR spectra of single-fraction protein rich isolates from macroalgaes, with commercial soy protein isolate included as a reference. 174

4.8 FT-IR spectra of single-fraction Alginate rich isolates from macroalgaes, with commercial alginic acid included as a reference. 175

4.9 FT-IR spectra of single-fraction agar/carrageenan rich isolates from macroalgaes, with commercial agar and κ-carrageenan included as a reference. . 176

4.10 FT-IR spectra of single-fraction isolates produced with the hot-acid extraction from macroalgaes, with commercial laminarin and fucoidan included as a reference. 177

4.11 FT-IR spectra of single-fraction Lipid/Fatty-acid isolates produced with the hot-acid extraction from macroalgaes, with vegetable oil and soybean oil included as a reference. 178

4.12 Dry and ash-free mass yields of multi-step extractions of macroalgae species, relative to the original starting mass, using stepwise application of different extraction techniques to target different components. 179

4.13 Scatter plot comparing total mass yield (dry and ash-free basis, DAF) of different fractions recovered by single-fraction approach vs. cascading mutli-fractionation approach. 180

4.14 Bar plot of total mass repartition throughout the cascading multi-fractionation approach. 181

4.15 FT-IR spectra of different extract fractions of *Gracillaria sp.* (GR). . . . 182

4.16 Sketch of the appropriate position to take the radicle length measurement from. 186

4.17 **a)** Germinated radish seeds after 48 hours of incubation in various test conditions, and **b)** average radicle length for each test condition. n=3 replicates for each condition, each replicate contains 24 seeds. Error bars are at 95 % confidence interval in the mean. 187

4.18 Oxygen permeability coefficients for various alginate based films, traditional food-wrap films, and aluminium foil. 190

4.19 Water vapour transmission rate (WVTR) for various alginate based films, commercially available food wraps, and aluminium foil. 192
4.20 2-second Water Contact Angle silhouettes for **a)** standard sodium alginate, and **b)** polyvinylchloride. 193
4.21 Water contact angle (WCA) evolution over time for a) standard sodium alginate film, and b) sodium alginate film with 10 % wt. crystalline nano-cellulose included. 194
4.22 Example of the type of swelling observed with all alginate based films during extended water contact (60s). 194
4.23 Loss in mass vs time for different applied coatings when bagasse trays are used to contain **a)**, tap water; **b)** 0.1 M citric acid; and **c)** shop-bought pasta sauce. 195
4.24 FTIR transmittance spectra of **a)** commercial agar, **b)** agar extracted from Gracilaria seaweed, **c)** palmitic acid, and **d)** Gracilaria agar that has been functionalised with palmityl-chloride. 197
4.25 **a)** Flow consistency index (K), and **b)** Flow behaviour index (n), of C16 functionalised biological grade agar between melt flow temperatures of 140 °C to 180 °C, under heating and cooling conditions. 199
4.26 Specific motive power required to produce viscous flow of functionalised materials within the Haake Minilab II micro-compounding twin-screw extruder, for agar functionalised with 5 molar equivalents of C12-laurate and C16-palmitate, at screw speeds 150 rpm and 20 rpm. 200
4.27 Specific motive power required to convey: **a)** C16-palmitate functionalised agar at temperatures 110 °C to 150 °C and 20 rpm, 50 rpm, and 150 rpm; and **b)** C16-palmitate functionalised kappa-carrageenan at temperatures 40 °C to 130 °C and 20 rpm, 50 rpm, and 150 rpm. 201
4.28 Scatter plots of extruder screw torque as a function of screw speed for **a)** C16-palmitate functionalised agar at temperatures 110 °C to 150 °C, and **b**) C16-palmitate functionalised κ-carrageenan at temperatures 40 °C to 130 °C. 203

4.29 Scatter plots of extruder screw power as a function of screw speed for C16-palmitate functionalised agar at temperatures 110 °C to 150 °C, and C16-palmitate functionalised κ-carrageenan at temperatures 40 °C to 130 °C. 204
4.30 Bar plots of specific motive power (left-axis), and the internal pressure at the inlet (P_{D1}) and outlet (P_{D3}) of the extruder recirculation channel (right-axis). 205
4.31 Qualitative representation of the apparent viscosity behaviour for a shear-thinning fluid. 212
4.32 Fluid behaviour index (n) and fluid consistency index (K) for various polymers, blends of polymers, and resin formulations, tested at flow temperatures from 140 °C to 230 °C. 213

5.1 Arrangement of test-film enclosed in 13 mm mesh envelope for mechanical support during compostability testing. 220
5.2 Pictures of the final composting set up, showing **(a)** the arrangement of test articles placed into the test-bed prior to capping over with fresh nettles and part-finished compost, **(b)** wide-view of the testbed on the top of the pile, and **(c)** closer view of the capped over testbed marked with four corner posts. 221
5.3 Temperature trend log from the centre of the compost testbed, as well as the ambient air temperature recorded at midnight (00:00) by a local weather station. 223
5.4 State of Alginic Acid and Functionalised Agar films uncovered after 4 weeks of composting. 227
5.5 State of Alginic Acid and Functionalised Agar films uncovered after 6 weeks of composting. 228
5.6 State of Functionalised Agar film uncovered after 8 weeks of composting. 229
5.7 FT-IR spectra of functionalised agar (AgaF) films recovered from the compost pile at day 0 (control), day 28 (week 4), day 42 (week 6), and day 56 (wk8). 229

5.8 Excess biogas normal volume produced in each bioreactor in comparison to the negative control (AD sludge only). 231

6.1 Macroalgae biorefinery process flow where pre-treatment, multi-step fractionation, thermochemical treatment of residues, and secondary chemical conversion are integrated for the production of multiple product streams, and end-of-life disposal options are included. 245

SI1 QR code of URL directing to public git repository of on-line supplementary information ix

A1 FT-IR spectra of different extract fractions of *Ulva lactuca* (UL). xi

A2 FT-IR spectra of different extract fractions of *Spinosum sp.* (SP). xii

A3 FT-IR spectra of different extract fractions of *Saccharina latissima* (SL). xiii

A4 FT-IR spectra of different extract fractions of *Sargassum sp.* (SG). . . . xiv

A5 low-sweep rheogram of viscosity (η, Pa.s) and shear-stress (σ, MPa) plotted against shear rate (γ, s^{-1}) for the C16 functionalised biological grade agar 140 °C. xv

A6 Flow-sweep rheogram of viscosity (η, Pa.s) and shear-stress (σ, MPa) plotted against shear rate (γ, s^{-1}) for the C16 functionalised biological grade agar 150 °C. xv

A7 Flow-sweep rheogram of viscosity (η, Pa.s) and shear-stress (σ, MPa) plotted against shear rate (γ, s^{-1}) for the C16 functionalised biological grade agar 155 °C. xvi

A8 Flow-sweep rheogram of viscosity (η, Pa.s) and shear-stress (σ, MPa) plotted against shear rate (γ, s^{-1}) for the C16 functionalised biological grade agar 160 °C. xvi

A9 Flow-sweep rheogram of viscosity (η, Pa.s) and shear-stress (σ, MPa) plotted against shear rate (γ, s^{-1}) for the C16 functionalised biological grade agar 165 °C. xvii

A10 Flow-sweep rheogram of viscosity (η, Pa.s) and shear-stress (σ, MPa) plotted against shear rate (γ, s^{-1}) for the C16 functionalised biological grade agar 170 °C. xvii

A11 Flow-sweep rheogram of viscosity (η, Pa.s) and shear-stress (σ, MPa) plotted against shear rate (γ, s^{-1}) for the C16 functionalised biological grade agar 175 °C. xviii
A12 Flow-sweep rheogram of viscosity (η, Pa.s) and shear-stress (σ, MPa) plotted against shear rate (γ, s^{-1}) for the C16 functionalised biological grade agar 180 °C. xviii
A13 Flow-sweep rheogram of viscosity (η, Pa.s) and shear-stress (σ, MPa) plotted against shear rate (γ, s^{-1}) for the C16 functionalised biological grade agar 175 °C after descending in temperature from having been worked at 180 °C. xix
A14 Flow-sweep rheogram of viscosity (η, Pa.s) and shear-stress (σ, MPa) plotted against shear rate (γ, s^{-1}) for the C16 functionalised biological grade agar 170 °C after descending in temperature from having been worked at 180 °C. xix
A15 Flow-sweep rheogram of viscosity (η, Pa.s) and shear-stress (σ, MPa) plotted against shear rate (γ, s^{-1}) for the C16 functionalised biological grade agar 165 °C after descending in temperature from having been worked at 180 °C. xx
A16 Flow-sweep rheogram of viscosity (η, Pa.s) and shear-stress (σ, MPa) plotted against shear rate (γ, s^{-1}) for the C16 functionalised biological grade agar 160 °C after descending in temperature from having been worked at 180 °C. xx
A17 Flow-sweep rheogram of viscosity (η, Pa.s) and shear-stress (σ, MPa) plotted against shear rate (γ, s^{-1}) for the C16 functionalised biological grade agar 140 °C after descending in temperature from having been worked at 180 °C. xxi

List of Tables

1.1 Summary of Sheng et al. (2018)'s findings on biocrude composition when studying binary interaction of feedstock components in HTL reactions. . 23

2.1 Summary of investment changes required in major energy sectors to align with the International Energy Agency's (IEA) Sustainable Development Scenario (SDS). Data from the IEA Energy investments in fuels, power, and End-use (respectively), in the Sustainable Development scenario.[127] 29

2.2 Comparison of typical properties of both petroleum crude and HTL biocrude oils. 40

2.3 Fixed fraction coefficients ($k_{BC,j}$) of previously published HTL MCA product yield models. 53

2.4 $a_{i,j}$ and b_i model coefficients for prediction of bio-crude elemental composition from algal HTL. 59

2.5 Estimated fixed wt. % elemental composition of gas and char HTL products. 59

2.6 Proximate, biochemical, and ultimate analysis of macroalgae used in the Aspen model in this work. Values are taken as an average from multiple sources. 68

2.7 Financial and plant reliability assumptions for the NPV and discount cashflow analysis. 69

2.8 Basis of fixed costs of plant equipment in plant costing model. 70

2.9 Experimental CHNSO and TGA results for *Spirulina* and *Sargassum* algae for both raw and acid pre-treated biomass. Values expressed as the weight % of the whole biomass, the dry biomass (d), or the dry and ash-free fraction (df). 73

2.10 Summary of HTL product yields with varying reactor filling and headspace gas. 79

2.11 Experimental biocrude properties and typical fossil crude properties for comparison. Values expressed as the weight % of the dry fraction (d), or as the dry and ash-free fraction (df). 80

2.12 Fitted parameters for use in estimation of elemental ultimate analysis (C, H, O, N wt. %) from biochemical proximate, using equations 2.15 to 2.18. 86

2.13 Fitted parameters for use in estimation of biochemical proximate analysis (carbohydrate, lipid, protein) from elemental ultimate analysis (C, H, O, N wt. %), using equation 2.22. 87

2.14 Fixed fraction coefficients ($k_{BC,j}$) determined in this work by least-squares regression fitting to published experimental results. 89

2.15 Conventional compounds commonly identified in HTL bio-oils of algaes and macroalgaes, and their relative abundance when found. 92

2.16 Predicted HTL Biocrude mass yield and properties for plant scale HTL process of *Sargassum spp.* and *Saccharina spp.*, and experimental results from earlier for comparison. 93

3.1 Macroalgae-to-bioethanol biorefineries modelled using different simulation software for technoeconomic analysis. 104

3.2 Component mass balance modelled in the V-201 RYield block used for modelling seaweed extraction. 117

3.3 Target ultimate and proximate analysis of the blended biomass product. 123

3.4 Additional direct costs and indirect cost uplift applied to the installed equipment cost. 125

3.5 Overall equipment effectiveness (OEE) production metrics throughout start-up and commissioning period. 126
3.6 Labour and supervision plan for different scale plants. 127
3.7 Unit prices and financial constants for the base year, 2020 (Year 0). . . . 128
3.8 Comparison of bulk density and heat capacity, of predicted values from Aspen Plus and literature results. 130
3.9 Summary capital expenditure for 10,000 tonne year^{-1}, 1,000 tonne year^{-1}, and 250 tonne year^{-1} biopolymer biorefineries. For each scale the plant is presented including the slow-pyrolysis section and without, and with two different options for the provision of purging nitrogen to the pyrolysis reactor. 137
3.10 Minimum biopolymer selling price for different scale biorefineries with different macroalgae cost price, with cost of finance spread evenly over 20-year amortized loan period. No additional valorisation of the char is considered. 140
3.11 Impact of different char valorisation scenarios on MBPS for different scale biorefineries and a fixed price of 2000 $ tonne^{-1} for seaweed supply. . . . 141

4.1 Summary results of thermal and elemental characterisation of macroalgal species. 170
4.2 Summary results from the thermal and hydrothermal processing of macroalgae and macroalgal solids by hydrothermal carbonisation (HTC) and slow pyrolysis (SP). 184
4.3 Summary of char oxidative stability and biomass carbon sequestration potential for a selection of macroalgae chars produced under hydrothermal carbonisation (HTC) and slow pyrolysis (SP). 185
4.4 Summary results of the germination rates, relative radicle growth, and germination index for radish seeds germinated in different strength aqueous extractions of pyrolysis char and HTC hydrochar. 188
4.5 Summary of 2s water contact angle measurements for alginate based films, PE, PVC, and PLA/PBAT films. 192

4.6 Flow consistency index (K) and flow behaviour index (n) as a function of melt temperature (T) and direction of temperature change. 199

5.1 Visual observations and change in mass and thickness during composting trials. 224

5.2 Result of initial substrate characterisation for anaerobic digestion (AD) assay. 230

A1 P-values for significance of contriobution of calculated $a_{i,j}$ parameters to the models described by equations 2.15 to 2.18. xxii

A2 P-values for significance of contribution of calculated $a'_{i,j}$ parameters for use in estimation of biochemical proximate analysis (carbohydrate, lipid, protein) from elemental ultimate analysis (C, H, O, N wt. %), using equation 2.22. xxii

A3 Full instruement setting details for the DataPhysics OCA 20 contact angle measurement. xxiii

Table of Contents

Acknowledgements **i**

Abstract **iii**

Dissemination **vi**

List of Figures **xvii**

List of Tables **xxi**

Table of Contents **xxii**

1 Introduction & Literature Review **1**

1.1 Introduction 1

1.2 Marine Biorefineries: A review of existing approaches 3

1.2.1 Cultivation and harvesting of marine biomass 4

1.2.1.1 Industrial cultivation 5

1.2.1.2 Wild harvest 6

1.2.1.3 Future macroalgae production 8

1.2.1.4 Co-production and symbiotic projects 9

1.2.2 Primary products from macroalgae crops 9

1.2.2.1 Agar 10

1.2.2.2 Alginate 11

1.2.2.3 Carrageenan 12

1.2.2.4 Fucoidan . . . 13
1.2.2.5 Cellulose . . . 13
1.2.2.6 Other carbohydrates . . . 14
1.2.3 Primary extraction techniques . . . 14
1.2.3.1 Preliminary processing . . . 14
1.2.3.2 Extracting polysaccharides . . . 16
1.2.4 Uses of primary products . . . 18
1.2.5 Secondary products and downstream processing . . . 19
1.2.5.1 Thermochemical treatment . . . 19
1.2.5.2 Hydrothermal techniques . . . 20
1.2.5.3 HTL mechanism and products . . . 21
1.3 Process and systems modelling . . . 24
1.3.1 Process modelling tools . . . 24
1.3.2 Implementations of in-silico biorefineries . . . 25
1.4 Thesis scope and general objectives . . . 27

2 Hydrothermal liquefaction for production of macroalgal biocrude 28
2.1 Introduction . . . 28
2.2 Background . . . 31
2.2.1 HTL Reactors . . . 33
2.2.2 Batch HTL Reactors . . . 33
2.2.3 Flow Reactors Design Considerations . . . 34
2.2.4 Practical Considerations in Further Scale Up . . . 37
2.2.5 Downstream Process Integration . . . 39
2.2.5.1 Differences between Petro-crude and HTL biocrude . . . 39
2.2.5.2 Bio-crude upgrading . . . 42
2.2.5.3 Integration into existing petro-plants . . . 43
2.3 Materials and Methods . . . 45
2.3.1 Experimental Methods . . . 45
2.3.1.1 Pre-treatment of Algal Solids . . . 45
2.3.1.2 Batch Hydrothermal Liquefaction . . . 46

2.3.2 Analytical Methods 47
2.3.3 Computational Methods 49
2.3.3.1 Prediction of Biochemical Proximate prediction and Ultimate CHNO Analysis 49
2.3.3.2 HTL Yield Models 51
2.3.3.3 Qualitative HTL Product Quality Prediction 58
2.3.4 Plant Modelling and Configuration 59
2.3.4.1 Process Description 63
2.3.4.2 HTL Process Simulation in Aspen Plus 64
2.3.4.3 Pre-treatment, Utilities, and Services Sizing 66
2.3.4.4 Biomass Supply 67
2.3.5 Economic Model 67
2.3.5.1 Fixed costs 69
2.3.5.2 Variable costs 71
2.4 Results 72
2.4.1 Experimental Results 72
2.4.1.1 Biomass Properties 72
2.4.1.2 Pre-treatment mass balance 74
2.4.1.3 Batch Hydrothermal Liquefaction 75
2.4.1.4 Influence of head-space gas 77
2.4.1.5 Properties of biocrude 80
2.4.1.6 Boiling behaviour of biocrudes 81
2.4.2 Modelling Results 83
2.4.2.1 Biochemical and Ultimate analysis predictive model . . 83
2.4.2.2 Predicting Ultimate Analysis from Biochemical Proximate 84
2.4.2.3 Predicting Biochemical Proximate Analysis from Ultimate 86
2.4.2.4 Quantitative HTL Product Yield Models 88
2.4.2.5 Approximation of Bio-crude components 90
2.4.2.6 Predicted Plant Scale HTL Results 93
2.4.3 Financial Modelling Results - Net Present Value 94

2.5 Conclusions 98

3 Process Design and Technoeconomic Analysis of a Polysaccharide Film Biorefinery 101

3.1 Introduction 101

3.2 Methods 105

3.2.1 Plant Modelling and Configuration 105

3.2.2 Process Description 105

3.2.3 Aspen simulation and optimisation 115

3.2.4 Pre-treatment, Utilities, and Services Sizing 121

3.2.5 Biomass Supply and Quality 122

3.2.6 Equipment costing basis 122

3.2.7 Economic model 124

3.2.7.1 Total Capital Expenditure 124

3.2.7.2 Operating expenditure 124

3.2.7.3 Minimum Biopolymer Selling Price 128

3.2.7.4 Impact of Char 129

3.3 Results 130

3.3.1 Aspen Plus Simulation results 130

3.3.1.1 D-301 Film Belt Dryer Optimisation 130

3.3.2 Financial results and MBPSP 135

3.3.2.1 Total Capital Investment 135

3.3.2.2 Operating Expenses 137

3.3.2.3 Minimum Biopolymer Selling Price 138

3.3.2.4 Impact of Char Valorisation 141

3.4 Discussion 142

3.5 Conclusions 147

4 Experimental Biorefinery and Polysaccharide Film Development 149

4.1 Introduction 149

4.2 Materials and Methods 151

4.2.1 Materials . . . 151
4.2.2 Analytical Methods . . . 152
4.2.2.1 Thermal Characterisation . . . 152
4.2.2.2 Elemental Microanalysis (C,H, N, and S) . . . 153
4.2.2.3 FT-IR Spectroscopy . . . 153
4.2.2.4 Film permeability . . . 154
4.2.2.5 Water contact angle . . . 158
4.2.3 Experimental Methods . . . 159
4.2.3.1 Washing and pre-processing of macroalgae . . . 159
4.2.3.2 Polysaccharide extractions . . . 159
4.2.3.3 Nanocellulose production . . . 162
4.2.3.4 Thermochemical processing . . . 163
4.2.3.5 Char stability and germination trials . . . 164
4.2.3.6 Functionalisation of polysaccharides . . . 166
4.2.3.7 Films and coatings . . . 166
4.2.3.8 Rheometery . . . 167
4.2.3.9 Extrusion . . . 168
4.3 Results . . . 169
4.3.1 Macroalgae characterisation . . . 169
4.3.2 Polysaccharide extractions . . . 171
4.3.2.1 Single fractions . . . 171
4.3.2.2 Multi-fractionation . . . 178
4.3.3 Thermochemical processing of seaweeds and extracted residues . 183
4.3.4 Char stability and germination . . . 184
4.3.5 Films and coatings . . . 189
4.3.5.1 Thin films . . . 189
4.3.5.2 Coatings . . . 193
4.3.6 Functionalisation of extracted agar fractions . . . 196
4.3.7 Rheometry . . . 197
4.3.8 Extrusion processing . . . 198

4.4 Discussion . . . 205
4.5 Conclusions . . . 213

5 End-of-life Processing **216**
5.1 Introduction . . . 216
5.2 Materials and Methods . . . 218
5.2.1 Materials . . . 218
5.2.2 Methods . . . 219
5.2.2.1 Film preparation . . . 219
5.2.2.2 Compostability . . . 219
5.2.2.3 AD substrate characterisation . . . 221
5.2.2.4 Anaerobic digestion . . . 222
5.3 Results . . . 223
5.3.1 Compostability . . . 223
5.3.2 Anaerobic digestion . . . 226
5.4 Discussion . . . 232
5.5 Conclusions . . . 235

6 Conclusions and Further Work **238**
6.1 Conclusions . . . 238
6.2 Future Work . . . 242

References **246**

Supporting Information **ix**

Appendix **xi**
A0.1 Supplementary Figures . . . xi
A0.1.1 IR Spectra . . . xi
A0.1.2 Rheograms . . . xv
A0.2 Supplementary Tables . . . xxii

Chapter 1

Introduction & Literature Review

1.1 Introduction

The 26th UN Climate Change Conference of the Parties (COP26), held 31 October to 13 November 2021 in Glasgow (UK), aimed to deliver a legally binding agreement that obligated countries to deliver progress towards four key goals:

1. Secure global net-zero nationally declared contribution (NDC) emissions by mid-century in order to limit global atmospheric heating to 1.5 °C above pre-industrial average temperatures.

2. Rapidly adapt to protect communities and natural habitats already suffering the negative impacts of climate change.

3. Mobilise finance by ensuring that developed countries deliver their promise of investing $100 billion every year in climate finance to support developing countries, by incentivising the release of private finance by making climate a part of every financial decision that is made, and by Central Banks verifying that national financial systems are robust to the impacts of climate change and support the transition to net zero.

4. Work together to finalise the Paris Rulebook (the detailed rules that make the

2015 Paris Agreement operational), and accelerate action to tackle the climate crisis through collaboration between government, business, and individuals.

National governments and international unions alike are introducing policy and legislation to begin delivering on these goals, with the UK government signing multiple declarations of intent to cut emissions and support developing nations, and the European Union (EU) energy policy targeting 27 % of total energy consumption to be derived from renewable sources by 2030.[1] Large scale electrification of industry allows leveraging of the booming market for traditional renewable energy technologies such as solar PV and wind generation, however despite the progress towards renewable electricity, an enduring need for biomass derived energy vectors is clearly identified in scenario modelling.[2] Similarly, the demand for fossil-derived materials does not simply cease when we transition our primary energy supplies away from fossil resources, and in fact development of new materials is required to help facilitate the transition to more robust renewable energy generation and storage.[3]

Many common materials were developed directly as a result of the integration of the refining and petrochemical industries, and hence huge sections of the global economy are based on the use and provision of materials downstream of the traditional petrochemical refinery.[4] However, this is not to demonize the materials and products developed from petrochemicals. For example the use of sterile single-use medical equipment has become common practice worldwide, with corresponding positive impact to patient outcomes as well as lower costs to healthcare providers.[5, 6] Use of polymers in food packaging has greatly reduced the global burden of food waste, resulting in net reductions in resource consumption due to greater farm-to-fork yields delivered by less spoilage en-route.[7] And, development of advanced polymer composites in automotive and engineering applications delivers lightweight and strong materials, increasing the energy efficiency of vehicles and machinery, and increasing pedestrian safety as vehicles become lighter.[8] Replacement of the upstream material source with equivalent renewable materials allows us to keep the technological benefits of materials developed in the post-industrialisation era.

Biomass is therefore central to both the future provision of non-electrical energy vectors, as well as production of industrially relevant materials. Sustainable exploitation of biomass may be achieved in biorefineries, a concept similar to the traditional petrochemical refinery, the key difference being that renewable biomass is used as the feedstock instead of fossil resources.

1.2 Marine Biorefineries: A review of existing approaches

The biomass of an ecosystem is the total mass of living organisms in the given ecosystem at a certain time, and includes animals, plants, fungi, and microorganisms. Primary producers or autotrophs (photosythesisers and chemosynthesisers) make up the base of the biomass pyramid, since they are able to make their own food rather than consuming other organisms. Autotrophs are therefore the starting point of all food-chains, with all higher order heterotrophic organisms requiring the metabolic production of the autotrophs for their own sustenance.

Specifically in the marine ecosystem, primary producers can be classified into the following categories:

1. Cyanobacteria – specialist photosynthetic prokaryotic bacteria
2. Algae – despite common misconception, alga are not plants. They lack roots, stem, or leaves. They can be subcategorized by size:
   (a) Microalgae – microscopic plant-like photosynthetic protists and phytoplankton. Typically single cellular, but sometimes multi-cellular organisms.
   (b) Macroalgae – larger multi-cellular and visible plant-like marine algae, commonly called seaweeds.
3. Marine plants – The result of terrestrial plant evolution returning to the oceans, includes species like mangroves and sea-grasses.

Humans have successfully utilized biomass from the marine environment for millennia, from early coastal hunter-gatherers, to more recent marine aqua-culture (marine

farming) for the production of fish, shellfish, or macroalgae crops.[9] More modern applications of macroalgae include uses as varied as biotechnology (e.g. bacteriological agar), human food additives (various hydrocolloid thickeners, e.g. agar, alginates, carrageenans), pharmaceuticals (hydrocolloids, and active sulphated compounds), foodstuff without further processing (e.g. Nori: *Pyropia/Porphyra*, Kelp: *Laminaria, Saccharina, Undaria*, Dulse: *Palmaria palmata*), and various industrial uses of extracted compounds.[10] In fact, the global commercial seaweed market was valued at 15 billion U.S. dollars in 2021, and forecast to rise to almost 25 billion U.S. dollars by 2028.[11]

Composition of macroalgae biomass is typically high in carbohydrates (e.g. hydrocolloid polysaccharides, oligosaccharides, storage glucans, sugar alcohols, etc.) making up 23 to 48.9 % of dry mass, a low to medium protein content (e.g. 6 to 15 % of dry mass), and a typically low lipid content (<0.7 to 6.9 % dry mass).[12–16] The drive towards utilisation of marine biomass as a feedstock material for a biorefinery process comes with a number of distinct advantages compared to terrestrial biomass. The lack of lignin in the biomass makes for a simpler processing and extraction process with less residual material, the avoidance of using any terrestrial land in means there's no competition with food production as is common with first generation biomass crops, and macroalgae typically have a higher photosynthetic efficiency resulting in higher per-hectare production yields compared to terrestrial crops.[17–19] Disadvantages however include the typically high ash content (e.g. greater than 40 % dry weight is not uncommon), and the necessity to either pre-dry the biomass for processing or storage, or that the biorefinery is designed to work with significant quantities of water in the feedstock.[13]

1.2.1 Cultivation and harvesting of marine biomass

The cultivation cost of biomass is the key parameter that makes or breaks a biofuel process, and both 1G and 2G processes require dedicating significant arable land to producing the required fuel-crops. Alternatively, mariculture (marine farming, a specialist branch of aquaculture) may be considered instead of agriculture or microalgal aquaculture (farming of aquatic species, including fresh and marine species).

Macroalgae (seaweed) share many of the advantages of microalgae, however with a number of key differences. Firstly, as a higher order plant than the single celled micro-scale organisms that make up microalgae, the harvesting of macroalgae is far simpler. Instead of expensive filtration or centrifugation to concentrate the dry mass, harvesting of macroalgae can be as simple as walking along a beach at low tide and dragging the biomass above the high-water mark to air-dry on the beach. Secondly, as a marine biomass it requires zero land usage. Open raceway ponds (ORP) and photobioreactors (PBR) both achieve much higher specific productivity compared to all terrestrial fuel crops, however, still require the use of land to do so. Marine macroalgae on the other hand grows in parts of the ocean where there is no competition for food or industry.

A consequence of turning to a wild-growing biomass as a potential feedstock for a biofuel process is a relatively poor understanding of the true productivity and potential costs. Microalgae cultivation has been a research focus for decades, with various programs from the U.S. Dept. of Energy for example aiming to optimise their production process for domesticated strains. As such, industrial microalgae processes exist at scale already.

1.2.1.1 Industrial cultivation

Industrially, around 20 Kt to 35 kT of dry microalgal biomass was produced annually as of 2016.[20, 21]

In contrast, global production of macroalgae topped 32 Mt (wet weight) in 2018, three orders of magnitude higher than the total dry weight of microalgae, and more than double the 15.7 Mt of macroalgae produced in 2006.[22] This rapid growth is driven by aquaculture rather than wild harvesting, with wild-harvest quantities remaining relatively stable at 1.09 Mt, 1.29 Mt, and 1.09 Mt throughout 2006, 2013, and 2015 respectively.[23, 24] Of this approximate 30 Mt annual aquaculture production, Asian countries produce the bulk with China, Indonesia, Phillippines, and the Republic of Korea responsible for 29 Mt.[23]

European aquaculture of seaweed was approximately 1500 tons in 2016, with France as the largest producer reporting 500 tons.[25] However, the wild-harvest quantities in

Europe is much larger, with estimates of the total quantity harvest by EU, Iceland, and Norway ranging from 250 Kt to 293 Kt in 2016. [23, 25] Assuming a 10 wt. % solids content in the wet macroalgal biomass, this puts the total dry-mass of wild-harvest macroalgae in EU, Iceland, and Norway in the same order of magnitude for the estimated global quantity of cultivated microalgae.

Cost of aquaculture cultivation is an open question, with past estimates ranging as low as US$155 per tonne (dry) and as high as US$16,630 per tonne (dry).[25] More recent economic models fall between the two extremes, with a 2016 study concluding that cultivation of macroalgae in the North Sea would cost $1,747 per tonne (dry). [26] Additionally, a 2018 experimental study found that the actual cultivation cost of the macroalgae *Saccharina latissima* on fixed lines in deep-ocean sites dropped by almost a factor of 4 from €36.73 per kg (dry) to €9.27 per kg (dry), when the harvesting routine was modified toward multiple-partial harvests to avoid costly re-seeding activities. [27]

1.2.1.2 Wild harvest

A potential alternative source of marine macroalgal biomass would be to utilise wild invasive nuisance algal blooms. Beginning in 2014, the Mexican Caribbean coast began receiving massive quantities of the pelagic *Sargassum* spp. (*S. fluitans*, and *S. natans*, commonly referred to as sargasso), with 2,360 m^3 of algae arriving per km of coast line. In subsequent years, the quantity of sargasso arriving on beaches and coastal communities in Mexico increased to a peak in May 2018 of 8,793 m^3 km^{-1}.[28]

This annual accumulation of sargasso in the Atlantic has been observed in satellite imagery since 2011, tracked by mixed layer satellite imagery by various institutions such as the Optical Oceanography Laboratory at the University of South Florida, whom have developed and established a Satellite-based Sargassum Watch System (SaWS).[29, 30] Seed populations of sargasso are abundant in the Sargasso Sea, with rapid blooming growth each year appears to be driven by West African upwelling during the boreal winter and Amazon River discharge during spring and summer. The recurrent annual phenomenon has since been named the great Atlantic *Sargassum* Belt (GASB), and the

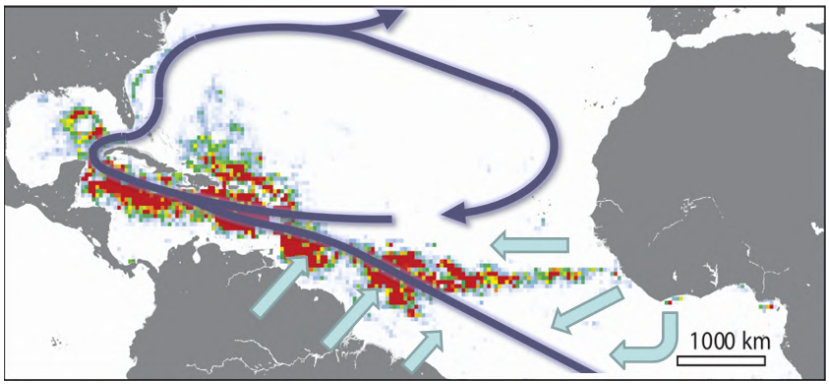

Figure 1.1: The extent of the June 2018 great Atlantic sargassum belt, direction of the north Atlantic meridional overturning circulation (indigo arrow), and the influence of West African upwelling and Amazon basin run off (blue arrows). Figures adapted from Wang et al., and Praetorius.[32, 33]

increasing severity and impact of sargasso blooms has been suggested to be driven by rising seawater surface temperatures.[31]

This blooming growth is collected by North Atlantic surface ocean currents (Atlantic meridional overturning circulation - AMOC), which delivers large quantities of sargasso into the Caribbean (figure 1.1).[32, 33]

The impact of this annual biomass deposition on local communities is not trivial, causing both environmental and economic problems. Mass mortality of marine biota in the Mexican Caribbean has been associated with large beaching events, with crustaceans and coastal sea floor dwelling fish being the most severely impacted. The apparent cause being hypoxia and water quality deterioration, as tonnes of sargasso washes up on beaches and rots causing high concentrations of ammonium and hydrogen sulfide in the water column.[34] The choking blanket of sargassum also has direct economic impacts, with popular tourist destinations forced to close, and the local fishing industry struggling to maintain their catch.[35, 36] Finally, there are human health concerns. The ammonia and hydrogen sulfide gases produced by the rotting mass results in chronic and sub-chronic exposure of coastal communities, with doctors reporting over 11,000 cases of acute H_2S exposure in Guadeloupe and Martinique between January and August 2018.[37]

The countries of the Caribbean have adopted various strategies to deal with the annual inundation of sargasso. From low-tech solutions such as composting or applying directly to crop land or feeding to livestock, to seeking more applied valorisation routes that convert the biomass to high value products e.g. nutraceuticals.[38–41] However, Sargassum (and other macroalgae)'s tendency to accumulate heavy metals such as arsenic introduces problems for several applications, including its use as a soil ameliorant. Rodríguez-Martínez (2020) recently reported median arsenic concentrations of 80 ppm, and a maximum of 172 ppm in sargasso samples collected along the Mexican Caribbean coast.[28] For reference, the maximum allowable arsenic concentration in animal fodder within the EU is 40 ppm, and the maximum allowable concentration in agricultural soil in Mexico is 22 ppm.[42, 43] It is clear therefore that at least some basic processing is required on this material to prevent the toxic accumulation of heavy metals in food chains and farm land, and this in itself present an opportunity to build a new industry around using this biomass.

1.2.1.3 Future macroalgae production

A number of recent commercial ventures have launched in and around European seas, attempting to significantly increase the size of the domestic European macroalgae industry. Groups such as the Dutch North Sea Farmers (NSF) consortium or Seaweed for Europe (SfE) trade group are pioneering scalable technologies such as mechanised offshore harvesting from submerged lines, or are combining their influence to lobby regional government to set production targets and provide financial support to the blossoming industry.[44, 45]

One particular project is that of Ocean Rainforest, based in the Faroe Islands. Ocean Rainforest began in 2010, and are working towards developing large volumes of farmed seaweed species such as *Saccharina latissima*, *Alaria esculenta*, *Laminaria digitata*, and *Palmaria palmata*, for applications such as animal feed, food, cosmetics, and to collaborate on research projects. They have recently attracted a significant investment, closing a $1.5 million round in mid 2020 led by the World Wildlife Fund (WWF), and more recently they led a consortium of cross-disciplinary partners to landing a successful €9

million grant for the upscaling of seaweed production and market applications.[46, 47]

Whilst it appears that there has been healthy market appetite to invest in seaweed technologies, there are government sponsored research programs in motion too. The United States Advanced Research Projects Agency–Energy's (ARPA-E) Macroalgae Research Inspiring Novel Energy Resources (MARINER) program seeks to develop tools to assist with the production of marine biomass. Of the 20 projects that fall under the MARINER banner, a number seek to set out the pathway to drastically reduced costs of producing macroalgal biomass.[48] Estimates of achievable production costs range from $125 to $145 per dry tonne for anchored systems, or from $75 to $180 for free-floating systems.[49, 50] The programme has also predicted that the US could produce as much as 500 Mt per year of macroalgae to feed energy and material markets.

1.2.1.4 Co-production and symbiotic projects

Macroalgae cultivation can naturally sit within existing marine economic activities. North Sea Farmers consortium are planning to build a commercial scale ocean farm in an existing off-shore windfarm. Using the space between wind turbines for the production of seaweed, shellfish, and to host floating solar arrays allows for far greater productivity from that area of ocean surface (e.g. figure 1.2). In addition, cultivation of macroalgae will likely have a positive impact on many ecosystem services, with cultivation plots providing habitats for fish and other marine species (provisioning), by helping to regulate the local ecosystem through uptake of nutrients and toxins, and by providing food for the local ecosystem.[19]

1.2.2 Primary products from macroalgae crops

The primary products of macroalgae are the three major phyco-colloidal polysaccharides extracted from seaweed: agar, alginate, and carrageenan. These polysaccharides are found in dramatically different proportions in different kinds of seaweed, especially between the three classes (red, brown, green), and each has distinct properties.[52] Additionally, smaller quantities of other molecules can be isolated from macroalgae such as fucans and fucoidan, cellulose, laminarin, sargassan, ulvans, and various other

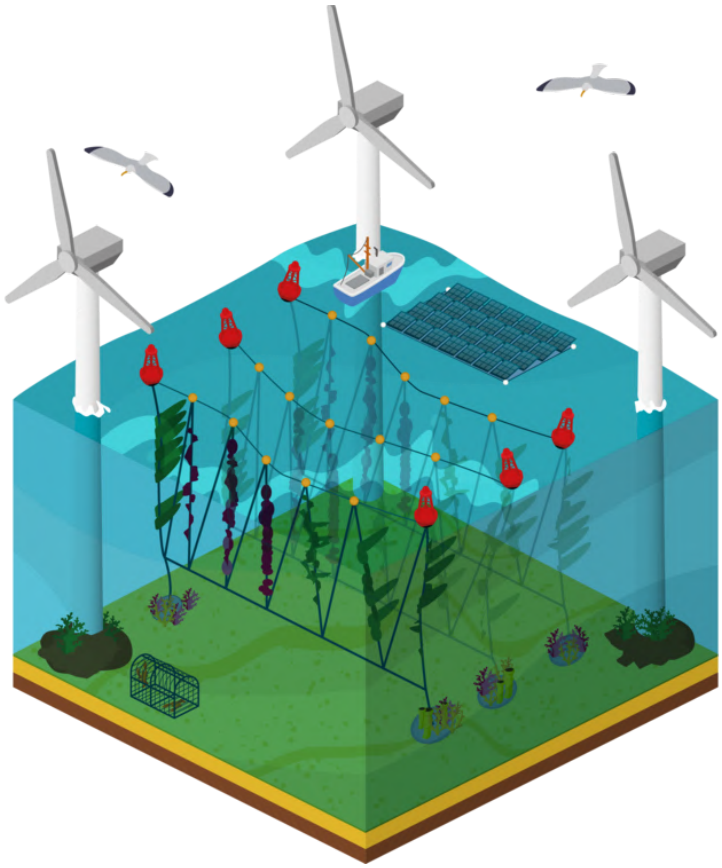

Figure 1.2: Artists impression of the combined ocean-farm and offshore windfarm proposed by North Sea Farmers consortium and planned for 2030. Submerged lines are used to grow seaweed and shellfish, pots are placed to catch crustaceans, and floating solar arrays supplement the electricity generation from the existing wind turbines. Image from North Sea Farmers.[51]

sulfated galactans and xylans.[53, 54] Here, the chemical structure of each of the major polysaccharides (agar, alginate, and carrageenan) as well as some of the other interesting biomolecules are described, along with information regarding which algal taxa they are present in, what their characteristics are, and how they currently are used industrially.

1.2.2.1 Agar

Agar consists of approximately 70 % agarose and 30 % agaropectin and is commonly found in red seaweeds, especially in the genera Gracilaria, Gelidium, Pterocladia and Gelidiella.[55] It contains hydrophilic galactans made up of alternate α-1,3 and β-1,4 linkages, in which the α-linked galactopyranose is made up of L-galactopyranose 6-

sulfate (see figure 1.3c).[56] Agar is commonly used as a gelling and thickening agent, but is susceptible to photo-degradation and temperature/humidity fluctuations, which can affect the gel's crystallinity and cause the formation of micro-fractures and polymer embrittlement.[57] Chemical additives are therefore required to transform it into a useful biopolymer material. Agar-based composites have been developed for a variety of applications including (food) packaging, antimicrobial films, antifoaming films and polymer electrolytes.[58] Most studies on agar polymers have involved the manufacture and testing of thin and flexible films made using a solution casting method. Characteristics that lend agar to applications as food packaging material include good tensile strength, biodegradability and antimicrobial properties.[59]

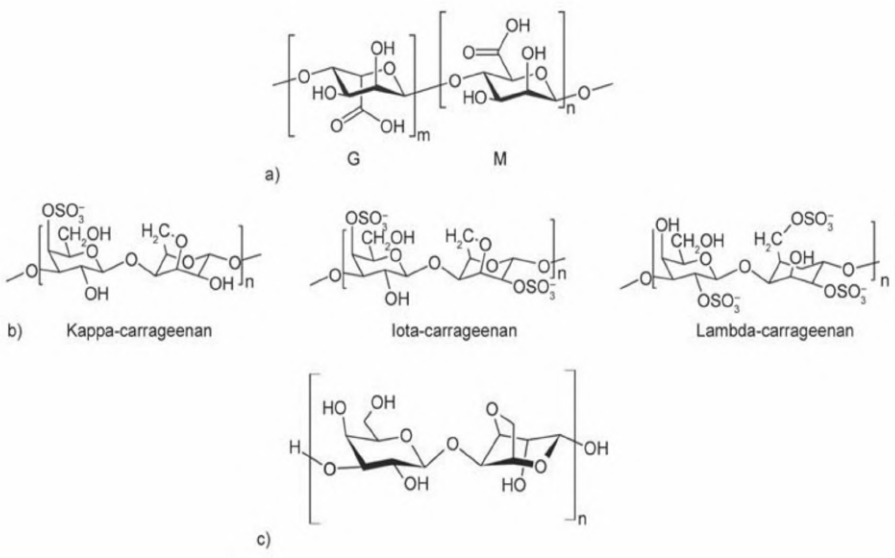

Figure 1.3: The structures of **a)** alginate, consisting of G and M blocks, **b)** carrageenans and **c)** agar. Reproduced from Abdul Khalil et al., 2017.[53]

1.2.2.2 Alginate

Alginates are found in brown seaweeds, in which they account for 22-44 % dw, and are typically extracted for commercial purposes from *Laminaria hyperborean, Macrocystis pyrifera, Laminaria digitata* and *Ascophyllum nodosum.*[52] Alginates readily dissolve in water and form thermally stable hydrogels in the presence of di- or tri-cations, particularly Na^{+}, K^{+} and Ca^{2+}, forming an arrangement commonly referred to as an egg-

box conformation.[59] Consequently, alginates are used in various industries as gelling, thickening, stabilising or emulsifying agents.[60] Alginates are linear polysaccharides consisting of (1→4)-linked units of β-D -mannuronate (M) and α-L-guluronate (G) arranged as homo- and hetero-polymeric (MM, MG and GG) blocks (see figure 1.3a).[61] The proportions and distribution of these blocks affect the physicochemical properties of alginates, in that alginates with higher proportions of G blocks form rigid gels with higher Ca^{2+} concentration whereas alginates with higher proportions of M blocks form gels that are soft and elastic.[62] It is estimated that global annual production of alginate is at least 30,000 metric tonnes, with major producers concentrated in six countries: China, USA, UK, Japan, Chile and Germany.[63] Normally, alginate abundance reaches a maximum in brown seaweeds during summer months when water temperature and irradiance are relatively high, so this is the optimal time to harvest algae for alginate production.[64]

1.2.2.3 Carrageenan

Red seaweeds (Rhodophyta) contain an additional family of polysaccharides called carrageenans, which are highly anionic, water-soluble polysaccharides consisting of linear chains of sulphated galactans (D-galactose and D-anhydrogalactose) (see figure 1.3b).[65] Carageenans are typically extracted from genera including *Kappaphycus, Gigartina, Eucheuma, Chondrus*, and *Hypnea* and can be categorised into three types depending on the number and position of sulphate ester groups: kappa, iota and lambda carrageenan.[66] The properties of carrageenans are determined by the conformation of monosaccharide units and the associated cations. κ-Carrageenan forms rigid, brittle gels, whereas ι-carrageenan forms softer, elastic gels and λ-carrageenan does not form gels.[53] Carrageenans are the most economically important hydrocolloids on the global market, have very low toxicity, are commonly used in the food industry as thickening agents and have been the target of considerable research into the development of drug delivery systems and edible packaging materials such as food coatings.[62, 67]

1.2.2.4 Fucoidan

Fucoidans are sulphated polysaccharides (fucans) that are commonly present in the interstitial tissue or mucus matrix of brown, but not red or green, seaweeds and are known for their broad range of bioactive effects resulting from sulphation, including anticoagulation properties.[54] Fucoidans were first isolated from brown seaweed over 100 years ago and can constitute >40 % wt of isolated cell walls.[68, 69] Liu et al. (2020) extracted fucoidan from *S. pallidum* and found that the monosaccharide composition comprised mostly L-fucose, mannose and galactose with minor amounts of glucose, xylose and rhamnose randomly connected within the polymer network.[70] The structure, molecular weight and sulphate content of fucans vary with algal species, life-stage and environment, affecting properties such as antioxidant capacity.[71] The proposed structure is shown in figure 1.4.

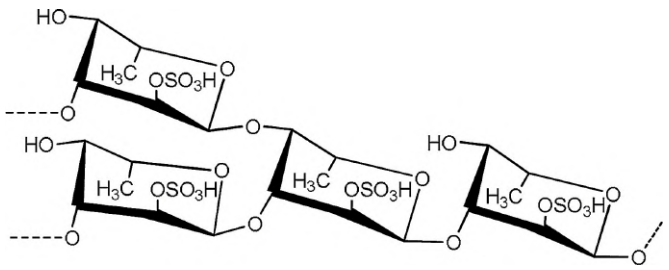

Figure 1.4: The presumed structure of fucoidan. Reproduced from Zhang et al., 2020.[72]

1.2.2.5 Cellulose

Cellulose is a linear glucan polymer comprising β-1,4 linked D-glucose units and has four types of crystalline structure of which type II has best thermodynamic stability.[73] It is extremely abundant and inexpensive but is valued in a variety of industries for its biodegradable and renewable properties.[53] It has gained attention as a renewable, environmentally benign and economical reinforcement material for biocomposite materials, particularly in the form of crystalline nanocellulose (CNC), also referred to as nanocrystalline cellulose (NCC) or nanowhiskers.[74] CNC consists of rod-shaped nanoparticles and can be prepared by a number of methods, including acid hydrolysis and high-pressure homogenization.[75–77] It has interesting properties including low den-

sity, high specific strength and tensile modulus and a large, reactive surface area that can bind to polysaccharide functional groups.[78]

1.2.2.6 Other carbohydrates

Laminarin is a low molecular weight (3600 kDa), neutrally-charged polysaccharide found in brown seaweeds, including Sargassum, where its function is as a storage glucan (energy reserve).[53] It exists in both soluble and insoluble forms and consists of a mixture of different glucopyranose (glucose) monomers.

Sargassan is a sulphated heteropolysaccharide, first extracted from *S. linifolium* using hydrochloric acid followed by aqueous sodium carbonate and ethanol.[79] It consists of a chain of glucuronic acid, mannose and galactose residues with side-chains of galactose, xylose and fucose.[80] It has known anticoagulant activity but its exact structure is yet to determined.[81]

Green seaweeds (Chlorophyta) additionally contain sulphated galactans and xylans, such as the family of ulvans.[54, 82]

1.2.3 Primary extraction techniques

1.2.3.1 Preliminary processing

Cleaning and sorting are often required prior to further processing of collected seaweed. For example, mounds of beached Sargassum contain the two primary holopelagic species, *S. natans* and *S. fluitans*, plus a variety of associated epiphytes, bacteria, microalgae, invertebrates, and marine pollution such as nylon fishing equipment. There will also be sand and various salts.[40, 71]

Due to seasonal variation in both macroalgae supply, and the biochemical composition of macroalgae, it is likely that a certain quantity of incoming material will need to be stockpiled to allow year-round operation. Alternatively, designing the biorefinery with a certain amount of agnosticism towards the feedstock composition (within limits) would allow supplementing of additional in-season biomass or waste-materials when the

primary macroalgal harvesting season has ended.

Macroalgal biomass will rot if stored damp or in humid conditions, thus it must be dried or ensiled to ensure a consistent feedstock quality is maintained through the period of storage. Milledge and Harvey reported that ensiling *Sargassum muticum* prior to anaerobic digestion for the production of biomethane produced minimal impact on the total quantity of biomethane produced.[71] However, Adams et al. noted that the month of harvest had a significant impact on the mean pH of ensiled macroalgae.[83] Additionally, it has been reported that the diversity of morphology both between multiple, and within a single macroalgal species, makes for a difficult mixed material to consistently ensile. Thin flimsy thalli through to relatively thick blades with consequent differences in the physical nature and robustness of the material, and difference in the biochemical composition (carbohydrate, protein, lipids) means that no single approach may be applicable.[84, 85]

Drying and dewatering techniques on the other hand largely rely on physical removal of water by either pressing or forced air convection. Gallagher et al. report on the impact of using a screw-press on fresh/damp macroalgae samples to remove excess water, and to produce extract juice from the macroalgae in order to raise its dry-matter fraction (DM%).[84] They report that the use of a screw press following various pre-treatment options (e.g. HCl acid treatment) was successful in increasing the DM%, however they also note that both seasonal and species variation has an impact on this process too, with samples higher in alginate for example typically holding more water throughout the pressing and subsequent air-drying step.

The impact of both oven- and air-drying of macroalgae biomass have been demonstrated too. Silva et al. report on the impact of using heat to assist drying of macroalgae, varying oven temperature from 25 °C to 60 °C.[86] They report that oven drying promoted the extraction of chlorophylls and carotenoids, whereas both the yield of phenolics and the anti-oxidant activity of resulting extracts were diminished compared to low temperature drying techniques like freeze drying. The recovery of major polysaccharide components like agar however were not impacted by the drying process in the studied

range.

1.2.3.2 Extracting polysaccharides

There are well-established industrial methods for extracting the main hydrocolloid carbohydrates from seaweeds, typically involving multiple stages, but these methods have limitations with respect to process efficiency and product consistency, hence ongoing research into the development of novel methods.[55] Proposed methods that reduce the demand for energy, chemicals or water involve the utilisation of microwaves, ultrasound or enzymes to assist extraction. Alternatively there are supercritical fluid extraction, pressurised solvent extraction, reactive extrusion and photobleaching processes.[55]

Brown seaweeds are frequently treated with formaldehyde/formalin and hydrochloric acid to polymerise phenolic compounds so that their solubility is lessened and they attach less strongly to polysaccharides and to ensure that salts become readily water soluble.[87, 88] Various chemical treatments can be used to extract algal polysaccharides without undesired components.

Hot water is the most popular solvent for hydrocolloid extraction, except for alginate, which must be extracted using hot alkali to solubilise salts.[55] Algae can be washed with a non-polar or less polar organic solvent such as hexane, diethyl ether, chloroform or ethanol to remove lipids, pigments and other non-polar molecules.[54] Fucoidan or alginic acid can then be extracted using a suitable medium with optimised pH and other conditions, before lowering the dielectric constant or changing the pH using complexing agents.[89] Figure 1.5 outlines the methods of extracting alginic acid, fucoidan and laminarin from *Sargassum fusiforme*.

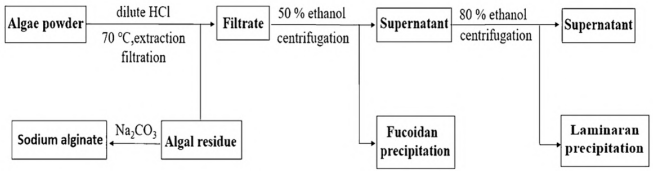

Figure 1.5: Flow chart showing methods to separate sodium alginate, fucoidan and laminarin from *Sargassum fusiforme*. Figure reproduced from Zhang et al.[72]

Alginates can then be extracted using an alkaline solution (Na_2CO_3 or NaOH), using a flocculant and aeration to remove alkaline insoluble matter, leaving an alginate-rich viscous liquid underneath.[54] Florez-Fernandez et al. (2019), in a novel approach to extracting alginate from *S. muticum*, found that ultrasound reduced the lowest molecular weights and increased the ratio of mannuronate/guluronate monomers, producing gels with stable and thermo-reversible characteristics (see figure 1.6).[90]

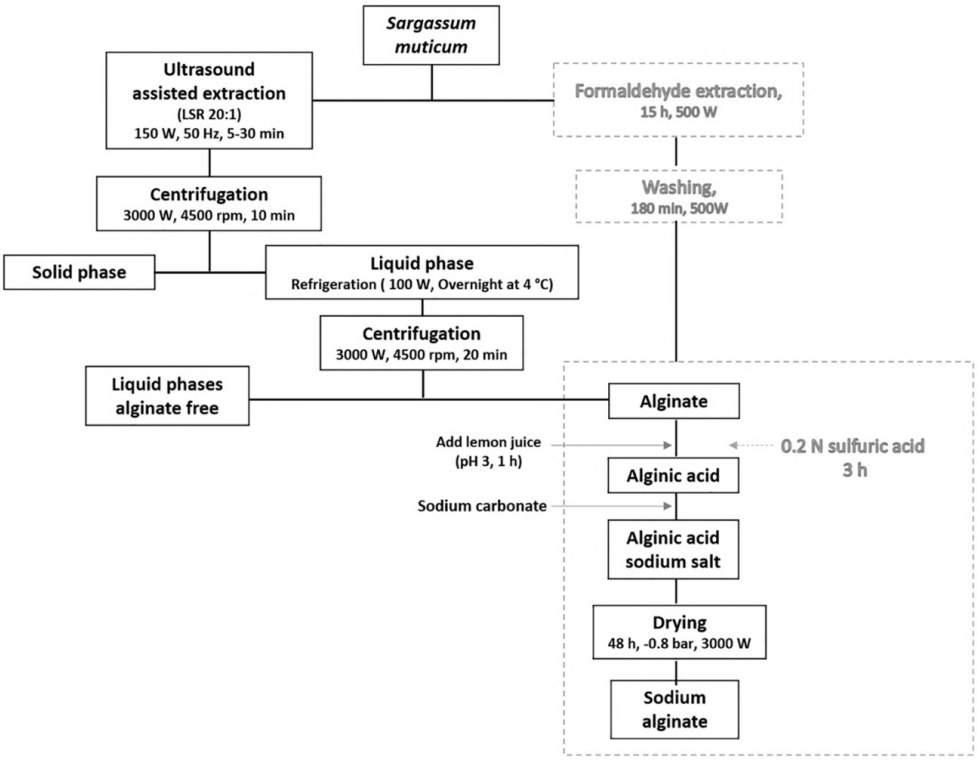

Figure 1.6: A novel ultrasound-assisted method for extracting alginate from *S. muticum*. The conventional procedure is represented by grey dashed words, symbols and boxes. Figure reproduced from Flórez-Fernández et al.[90]

Liu et al. (2020) used hot water extraction and gradient precipitation followed by purification to isolate fucoidan from *S. palladium*.[70] Similarly, Allahgholi et al. used hot water pre-treatment (121 , 20 or 60 min) followed by a two-step extraction with mild acid (0.1 M HCl) then alkali (0.15 M Na_2CO_3, 80 °C) to extract carbohydrates from *L. digitata*.[91]

1.2.4 Uses of primary products

There are already well-established industrial processes producing primary polysaccharide products for the global market. Agar production and industrial use has grown from 6,800 tonnes worth US$ 82.2 million in 2002, to 9,600 tons worth US$ 173 million in 2009,and 14,500 tons worth US$ 247 million in 2015.[92, 93] The main use of agar is as a gelling agent in industry, food, and pharmaceutical domains.[92] Alginate production in 2009 was 26,000 tons with a market value of US$ 318 million, but declined to 24,644 in 2015 worth US$ 345 million. Carrageenan was 50,000 tons in 2009 at a value of US$ 527 million, and 57,500 tons in 2015 at a value of US$ 517 million.[93] For both alginate and carrageenan the major uses are similar to agar, gelling agents in food and pharmaceutical applications. The use of carrageenan in pharmaceuticals is however somewhat limited, due to the variability in structure and properties.[92] Growth of the total hydrocolloid market (including non-algal hydrocolloids) is expected to result in a market value of US$ 10.2 billion by 2027 (4.4 % compound annual growth) at a volume of 3,879 million tonnes, up from US$ 5.4 billion and 2.2 million tonnes in 2018.[94]

Alternatively, the carbohydrate content of seaweeds may be used as a feedstock for a microbial fermentation process. One recent study explored the application of single-step microwave hydrolysis for the production of a feedstock of fermentable mono-, di-, and oligo-saccharides, and the impact on the yield of microbial lipids under fermentation with the oleaginous yeast *Metschnikowia pulcherrima*.[95] Similarly, numerous studies have reported on the production of traditional fermentation products (acetone, butanol, ethanol) using seaweed as a base feedstock. [96–100]

There is also a blossoming industry focusing on the development of petro-polymer replacement products using macroalgal polysaccharides. For example, free standing sodium alginate films have been proposed for food packaging applications. [60, 101, 102] However, sodium alginate films where the native alginate is present in its sodium salt form are freely water soluble. A barrier film may still have utility in food packaging even *if* it is a rapidly soluble film, however there are also options for the producing insoluble algal films.[60, 103] Conversion of the sodium alginate based film into its calcium

salt form renders the film insoluble. Whilst this sodium-/calcium-alginate switching process is far from novel, there are a number of reasonably new companies attempting to commercialise products based on this simple core technology. Similarly, free-standing agar films have been demonstrated for the application of food or product packaging. Whilst the agar films are *insoluble* in water at room temperatures so will provide a better native water barrier compared to sodium-alginate, the agar films are still soluble at high temperatures, and the water resistance (vapour transmission rate) is less that desired.[104, 105]

1.2.5 Secondary products and downstream processing

Extraction of the major macroalgal polysaccharides is commonly done to produce foods, feedstock for fermentations and further materials processing.[10, 95] However, it is also possible to process the whole biomass without prior extraction, and produce a bio-crude product which can be converted into a range of fuel or chemical products.

1.2.5.1 Thermochemical treatment

Thermochemical treatments of biomass have gained attention recently as a method to directly convert biomass into useful products. Direct thermochemical conversion has the advantages of avoiding typically expensive and more complex biotech solutions such as fermentation, however does so by indiscriminate breakdown of biomass structures, resulting in the complete loss of potentially high-value polysaccharides. Thermochemical techniques such as pyrolysis and gasification have been studied for decades. They are broadly similar techniques that involve controlled heating of the biomass to a target temperature zone (typically 350 °C to 500 °C for pyrolysis, $>$ 500 °C for gasification), by applying a controlled rate of heating, all under a controlled atmosphere to prevent combustion. Much research has been done on pyrolysis of wood, forestry residues, and lignocellulosic feedstocks, with the yields of target products such as syngas, pyrolysis oils, and solid fuel briquettes being tuned by careful process optimisation with the heating rates, target temperature, and residence times.[106]

One key disadvantage of pyrolysis techniques is the requirement for the biomass to be

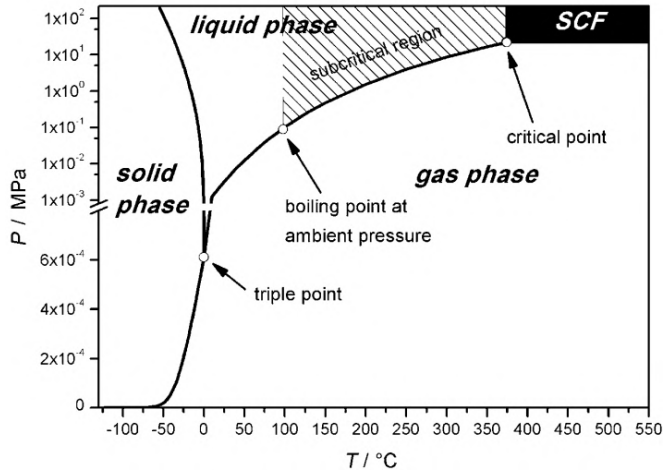

Figure 1.7: Phase diagram of water showing its states, and characteristic points, with the subcritical region for hydrothermal processing indicated. SCF = supercritical fluid. Figure adapted from Möller et al. (2011).[107]

dry. This is not a large penalty when processing dry biomass (e.g. miscanthus straw or air-dried wood), but the cost for aquatic or marine biomass is severe. Alternatively, hydrothermal conversion techniques apply similar conditions to pyrolysis, however, do so in sub-critical water in a high-pressure reactor.

1.2.5.2 Hydrothermal techniques

Processing biomass directly in water has the obvious advantage of never requiring the biomass to be dried out before processing. However, at atmospheric pressure the reaction temperature would be limited to < 100 °C to prevent constant boiling. By containing the autogenous pressure that is generated at temperatures above 100 °C, you avoid boiling and hence avoid the energy loss associated with the latent heat of vaporisation. Additionally, as pressurised water approaches its critical temperature its properties change dramatically. Hydrothermal biomass processing is achieved by dispersing biomass in water, and then raising the temperature of the mixture to sub-critical temperatures and pressures (figure 1.7).

Viscosity, surface tension, and dielectric constant all drop, resulting in a fluid that behaves more closely to a non-polar organic solvent than water under standard conditions. The decreased viscosity and surface tension leads to enhanced mass transfer, with cor-

responding increase in mass-transfer limited chemical reactions. Decreasing dielectric constant results in a lower solubility of ionic products, but a corresponding increased solubility of hydrophobic molecules. Simultaneously, the ion product of water (K_W) increases by three orders of magnitude between 25 °C and 300 °C, resulting in a 1000x increase in the concentration of both H_3O^+ and HO^- ions in solution, whilst still maintaining a neutral pH. These phenomena combined make for a powerful effect on biomass extraction reactions, where species that were insoluble at room temperature will now readily dissolve, and reactions that pass through a polar transition state or those that involve water as a reactant are favoured.[107]

The nature of the conversion process is a function of reaction temperature, with hydrothermal carbonization (HTC) typically at lower temperatures (100 °C to 250 °C), hydrothermal liquefaction (HTL) up to approximately the critical temperature of water (250 °C to 350 °C), and hydrothermal gasification (HTG) at higher temperatures (350 °C to 750 °C).[107] Typically, solid, liquid, and gaseous products are formed at all temperatures, however the mass partition into the dominant product shifts from solids (low temp), via liquids (medium temp), to gas (high temp).[107] Increasing process temperature has the typical effect of increasing thermal energy, and allows reactions to take place at increasing rates. Reaction time decreases from the range of hours/days for HTC, via minutes for HTL, to the order of seconds for HTG. Accordingly, as the temperature increases the reaction mechanism changes. Whilst ionic reactions dominate at lower temperatures, high temperatures favour homolytic bond breakage and formation of radicals.[107]

1.2.5.3 HTL mechanism and products

Fully resolving the exact reaction mechanisms for whole biomass HTL has thus far eluded researchers. Since biomass is a complex mixture of carbohydrates, lignin, lipids, proteins, and inorganic salts, the exact chemistry and mechanism of biomass liquefaction reactions is also highly complex.[108] Despite the precise mechanism of hydrothermal liquefaction reactions of biomass remaining uncharacterised, the overall process is understood to follow three major steps: depolymerisation, degradation, re-polymerisation

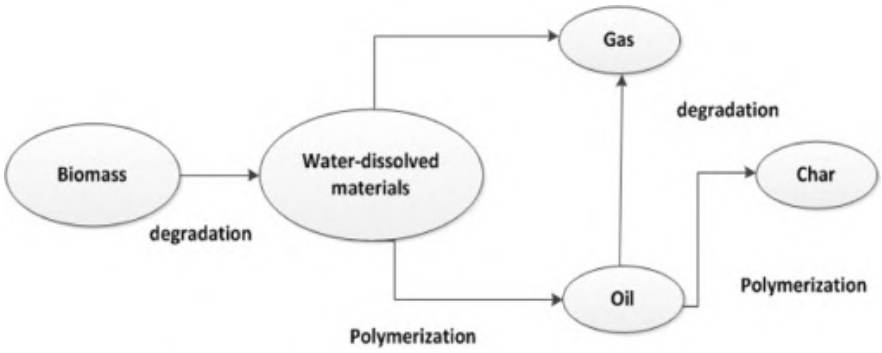

Figure 1.8: Simplified reaction pathway of hydrothermal liquefaction. Adapted from Gollakota et al. (2018).[108]

(figure 1.8). Briefly, biomass will decompose and depolymerise into reactive intermediates which dissolve in the aqueous phase. These reactive intermediates then undergo further reaction, either further degradation and forming volatile or gaseous products, or undergoing re-polymerisation to form an organic biocrude or solid char phase. The end products of the HTL reaction once cooled down from reaction temperature is a gaseous phase containing mostly CO_2 and some volatiles, an aqueous organic phase of water soluble decomposition products (e.g. organic acids, alcohols), an organic bio-crude phase that naturally separates from the aqueous phase, and the residual solids that contain the starting ash and any coke/polymerisation products.[108–110]

Various model compounds have been studied under HTL conditions in an attempt to elucidate specific pathways for each of the major biochemical fractions. Single components are selected to represent carbohydrates (e.g. glucose, or cellulose), proteins (e.g. soy protein, or various amino acid residues), and lipids (e.g. castor oil, or triglycerides such as tripalmitin) under reaction conditions. HTL reactions of single components, as well as binary and ternary mixtures, reveal that the impact on biocrude yield of the concentration of components in the starting material is of the order lipid $>$ protein $>$ carbohydrate.[110–113]

From the binary mixtures, certain interactions can be deduced also. Biocrude yields from HTL of mixtures of castor oil (lipid) and soya protein (protein) were 2.3 wt. % higher than individual biocrude yields. Under HTL, fatty acids derived from lipids can

react with amino acids and amines derived from proteins to produce esters, amides, N-heterocyclic compounds and N,O-heterocyclic long chain compounds.[111] Similar positive yield interactions are observed for HTL reactions on the binary mixture of tripalmitin (lipid) and phenylalanine (amino acid, protein residue), where after hydrolysis of tripalmitin to palmitic acid residues and decarboxylation of phenylalanine to phenylethylamine, the long-chain cyclic amide phenylethylpalmitamide is produced in the biocrude.[110]

Similarly complex interaction for carbohydrate and lipid, and protein and carbohydrate binary mixtures have been made. Total biocrude yield increases in most cases, however effect on the composition of biocrude is not always clear (e.g. table 1.1).[111]

Table 1.1: Summary of Sheng et al. (2018)'s findings on biocrude composition when studying binary interaction of feedstock components in HTL reactions. Feedstocks comprised of 1:1 wt/wt mixtures model compounds for lipids (L), protein (P), and carbohydrate(C). Arrows indicate the relative change in the wt. % composition of the various compound classes found in biocrude of the mixture, compared to a the mixture of individual HTL biocrudes. A single arrow indicating a shift in direction within the same order of magnitude, double arrows indicating a shift by one order of magnitude, and three arrows indicating a shift of 2 orders of magnitude.[111]

Feedstock	N-[a]	FA[b]	Esters	Amides	OC[c]	N,O-[d]	AC[e]	Others
L&P	↑	↓	↑↑↑	↑↑	↓	↑↑	↑	↓
L&C	-	↓	↑	-	↑	-	↓	↑
P&C	↑	-	↑↑	↓	↓	↑	↓↓	↑

a) N-hetrocyclic compounds.

b) Fatty acids.

c) Oxygenated compounds.

d) N,O- hetrocyclic long chain compounds (C no. of branched chain > 10).

e) Aromatic compounds.

The key benefit of hydrothermal processing is that you can quickly process wet biomass without drying. However, since maximum char generation is achieved with relatively long reaction times, the energy investment up-front to pre-dry the biomass may well be worthwhile when compared to the comparatively long reaction duration at high temperature, and by offering the opportunity to use established and well understood techniques such as slow pyrolysis.

1.3 Process and systems modelling

Currently no industrial scale plants hydrothermally process seaweed, and it's not clear on the cost or impact of such a system. Hence, several attempts have been made to develop process and economic models of seaweed biorefineries, and specifically of those featuring hydrothermal processes.

The advantage of developing models in conjunction with lab- and pilot-scale processes is that the early-stage development of technoeconomic analysis (TEA) tools helps to inform on economic pinch points in the process whilst it is still relatively inexpensive to make changes to the process, thus allowing alternative options and risk mitigation strategies to be considered well before attempting to launch a business venture.

The combined analysis techniques of TEA and pilot-scale studies form a powerful set of tools to inform researchers, investors, and national governments about research and investment decisions. The result of which is an R&D program that is more likely to end in a successful product at lower cost, as many project risks will have been managed earlier in the process.

1.3.1 Process modelling tools

Developing the process model is a key element in producing both a TEA and an LCA, as the process model will inform assumptions and decisions that you will need to make for both TEA and LCA. There are a number of approaches to developing process models, which vary in complexity considerably. Simple process models may be constructed in basic spreadsheet programs, with experimentally and previously published relationships applied to model mass and energy flow rates, and simplified equipment sizing calculations (e.g. Coulson and Richardson's Chemical Engineering vol. 6). A disadvantage of the spreadsheet approach is the typically limited availability of iterative solving methods, meaning that any convergent solutions would typically be found "in hand" by the user selecting to solve the overall process model one variable at a time.

More complicated models may be built with programming languages such as MATLAB

or Python. These allow iterative solving methods to be employed natively, and the use of $n \times m$ dimension matrices when computing solutions. However, they typically have a higher barrier of user accessibility, and require the programming of all physical, chemical, and economic relationships. They are however almost infinitely customisable, as at their core models built in programming languages are simply computer programs themselves.

Chemical and process simulation software packages are a common tool, with industrially established programs such as Aspen Plus, Aspen HYSYS, and CHEMCAD being common tools. Simulation packages have the advantage of having large, verified databanks of component properties, and in-built thermodynamic property methods, unit operations, and equipment sizing functions. They are typically well suited to modelling conventional chemical processes, for steady state dynamic simulations, process design, performance modelling, and optimization. However, whilst access to commercial chemical simulation software is common in academia, for private companies and start-up ventures the cost of software licenses can be prohibitive. There are open-source offerings (e.g. BioSTEAM, DWSIM) which are built and maintained to be free and accessible to anyone with a computer, however adoption in industry is generally lower, and they come without the huge databases of components and chemical properties that the offerings from Aspentech come with for example.

When considered in the context of the biorefinery, adapting traditional chemical process simulation software to deal with complex biological molecules and reaction schemes requires some careful treatment. Complex biomass does not exist as a define species in the pre-prepared databanks, requiring the user to carefully define the non-conventional components by whichever criteria they require, and allow the software package to make estimates of bulk properties using inbuilt methods.

1.3.2 Implementations of in-silico biorefineries

Individual elements of the bulk simulation can be adjusted, for example the property estimation methods used to determine calorific value, bulk density, bulk reaction progress

may all be defined. For example, Lozano et al. made a comparison between experimental data and empirical correlations for both HHV and Standard Heat of Formation (h_f) for 30 types of woody biomass, and then used a MATLAB program to refit new direct correlation model parameters.[114] Whilst they *were* able to improve the fit between predicted and experimental values (both HHV and h_f), their work showed that both the Boie, and the Mott & Spooner correlations for HHV predicted average results within the margin of uncertainty of the average experimental result.

Similarly Li et al. and Jiang et al. have used custom computational methods to estimate reaction yields within Aspen Plus.[115, 116] These methods build on the simple linear multi-component additive models first proposed in the context of HTL by Biller and Ross, but with refitting of empirical fixed fraction coefficients with their own experimental data.[117]

Full scale biorefinery process simulations are complex, but a number do exist. The US Dept. of Energy (DOE)'s National Renewal Energy Lab (NREL) have published a number of models and made them available to the public. These include Dutta et al.'s Catalytic Fast Pyrolysis and upgrading model, Spath et al.'s wood gasification and upgrading process, Humbird et al.'s lignocellulosic biomass to ethanol biorefinery, and Davis et al.'s process design and economic model for production of algal biomass.[118–121] Hydrothermal liquefaction processes have also been modelled in Aspen Plus, with Jiang et al., Pedersen et al., Jones et al., and Hoffmann et al. all publishing articles with results gained from rigorous process modelling in Aspen Plus.[116, 122–124] Whilst none of these models were made publicly available, the modelling methods that are described typically follow the same underlying logic, thus replication can be attempted based on their process descriptions alone.

The leap forward that these models allows is the rapid identification of both technical and economic pinch-points, as well as quantifying the sensitivity of the process to both external factors (e.g. biomass composition or utilities price), and internal variables (e.g. heat exchanger heat transfer coefficient, reactor LHSV).[116] Identifying these variables *in-silico* before scale-up allows a much more robust process design, and further

informs experimental studies where there is still uncertainty. The effect of this iterative loop of experimental studies informing simulations, and simulations results informing experimental design is that any projects taken to pilot scale and beyond are much more likely to succeed, as wherever practicably possible many of the potential effects of remaining uncertainty has already been considered and mitigated against.

1.4 Thesis scope and general objectives

The aim of this thesis is to investigate valorisation strategies for the use and application of macroalgal biomass in the context of the marine biorefinery, using green technologies and sustainable process design to identify sustainable products. This aim will be approached via the following objectives:

- Develop an experimental understanding of hydrothermal processing for the production of an intermediate bio-crude platform material, and use this experimental work to guide the development of an in-silico process model for a base financial evaluation of a simple hydrothermal process.
- Develop a combined process and economic model for a biorefinery coupled with a thermochemical remediation step for the combined production of high-value biorefinery products *and* the production of a stable carbon rich char.
- Demonstration of the practical implementation of the biorefinery steps, and assessment of the impact of the char production process.
- Evaluation of the technical performance of the biorefinery products in their intended application, and the fate of the biorefinery products at the end of their useful life.

Chapter 2

Hydrothermal liquefaction for production of macroalgal biocrude

2.1 Introduction

The International Energy Agency's (IEA) Sustainable Development Scenario (SDS) sets out the major transformations that they state are required in the global energy system. The SDS aims to deliver the three main energy related goals of the United Nations Sustainable Development Goals (SDGs), and to help deliver the requirements of the 2015 Paris Agreement.[125, 126] These transformations include strong drives towards widespread electrification and access to clean cooking facilities (in line with SDG 7), reducing the severe health impacts of exposure to smoke from indoor cook fires (related to SDG 3), and helping to tackle climate change (SGD 13). Significant change in investment is anticipated, with sectors of power generation and transmission, End-use, and Fuels all seeing a general trend of increased investment in renewables and efficiency, and decreasing investment in fossil resources (Table 2.1).[127]

Existing power generation technology from fossil fuel sources will see a large drop in investment (-73 % compared to the 2015-20 baseline), but with a modest emergence of a carbon capture and usage (CCUS) industry attached to fossil power generation.

Table 2.1: Summary of investment changes required in major energy sectors to align with the International Energy Agency's (IEA) Sustainable Development Scenario (SDS). Data from the IEA Energy investments in fuels, power, and End-use (respectively), in the Sustainable Development scenario.[127]

Sector	Technology	Average annual investment over time period, trillion US$ (2018)		
		2015-20	2015-30	% change
Fuels	Oil	0.453	0.331	-27 %
	Natural Gas	0.282	0.259	-8 %
	Coal	0.088	0.016	-82 %
	Biofuels	0.009	0.052	+510 %
	Total, all fuel technologies	0.831	0.658	-21 %
Power	Fossil Fuels (w/o CCUS[a])	0.134	0.036	-73 %
	Fossil Fuels (w/ CCUS[a])	-	0.025	-
	Nuclear	0.034	0.061	+79 %
	Renewables	0.308	0.635	+106 %
	Networks	0.287	0.500	+74 %
	Batteries	0.003	0.028	+755 %
	Total, all power technologies	0.767	1.285	+68 %
End-use	Renewables	0.026	0.143	+457 %
	Efficiency	0.247	0.631	+155 %
	Other	0.003	0.272	+8896 %
	Total, all End-use technologies	0.276	1.045	349 %
Total, all sectors		1.874	2.988	+59 %

a) Carbon capture, usage, and storage

Fossil resources for fuels will see a massive decline, with natural gas, oil, and coal seeing -8 %, -27 %, and -82 % investment respectively. Biofuels are expected to see a +510 % increase over the same period, however the Fuels sector as a whole is expected to see -39 % investment in total.[127]

Reduction in sector-wide investments will result in corresponding drop in the size of industry, with overall less 'fuel' being consumed. This will be driven by the shift toward electrification of traditional fuel uses, such as cooking and personal transport. However, despite the drive towards widespread electrification and recent advances in battery electric vehicle (BEV) technology, liquid fuels for transportation will always be required. Aviation and maritime sectors have no feasible alternative to high-density calorific liquid

chemical fuels, and despite recent announcements from the UK Government about moving towards the cessation of sale of new petrol and diesel vehicles by 2030, internal combustion engine (ICE) vehicles are still expected to be in the majority globally well into the 2040's.[128, 129] Simply, whilst there is still a market pull for liquid fuels, the demand will be met by the most economically viable option.

At present, biofuel investment makes up a relatively small proportion of the global fuel sector investment (1 % of all fuels investment, Table 2.1), with a similarly small contribution towards global energy consumption at 0.6 % to 0.8 % for 2017.[129, 130] However, quantities of biofuel production have increased dramatically with worldwide production almost doubling between 2008 and 2018 from 49 Mtoe in 2008 to 95 Mtoe in 2018.[130] Despite this apparent doubling in 10 years, adoption of transport biofuels is still far behind the IEA's SDS targets of 298 Mtoe by 2030.[131]

To date, the continued use of fossil resources remains the cheapest process to produce liquid fuels, and in many countries the adoption of biofuels is due to a legislative drive. The use of national policy to drive biofuel into the local market is done either in an earnest effort towards climate change mitigation (EU), or as an attempt to increase domestic energy security (US). Thus, biofuel products are often heavily subsidised (US/Brazil bioethanol), or if produced at lower cost come with dubious sustainable credentials at best (Palm-oil biodiesel). The policies that drive these actions are well meaning, but ultimately fail to address the issue at its root. Production of fossil fuels is too cheap for any bio-fuel product to compete on a purely cost-of-production basis.

Resource scarcity will not likely push the market to adopt biofuels in the short- to medium-term either. Current known hydrocarbon reserves are greater than we have used in total over the last 52 years, hence it seems unlikely that there will be a "Peak Oil" crisis where scarcity of fossil resources drives industry towards an alternative. Figure 2.1 shows the estimated annual global oil consumption, as well as the cumulative consumption since 1965, and the cumulative proven oil reserves since 1980.[130] As of the end of 2017 humans have used an estimated 175 giga-tonnes of oil equivalent (Gtoe), with annual consumption since 2010 in excess of 4 Gtoe year^{-1}. Global proven reserves

of oil (reserves that the oil producers have high confidence they can produce, using only currently known technology, and today's economic models) totalled approximately 225 Gtoe in 2017. Simply, even if the oil industry stopped looking for new oil prospects in 2017, there was still 50 years supply left in the ground at present day consumption rates. Using this fossil resource in full would generate a sufficient quantity of emissions that would take us well beyond even the highest over-shoot scenario of the 1.5 °C of global heating as set out by the IPCC in its 2018 special report.[132]

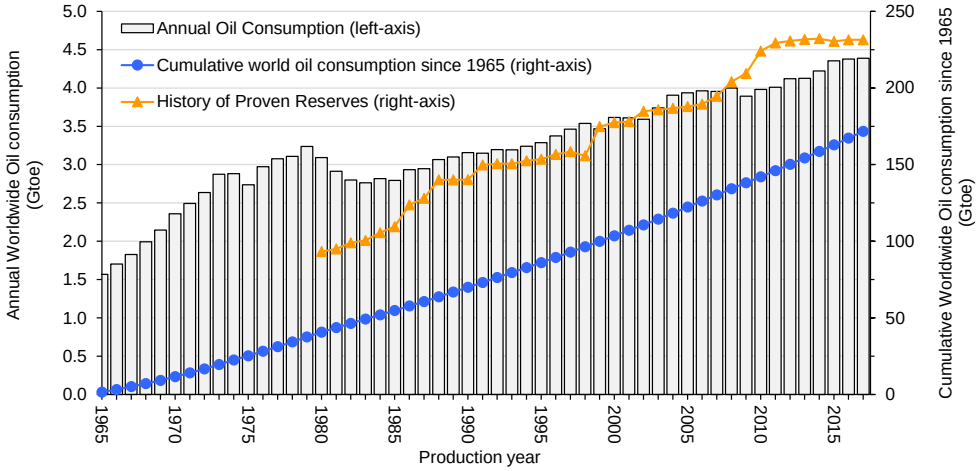

Figure 2.1: Global annual fossil fuel consumption and cumulative consumption (Gtoe, 1965 to 2017), and cumulative history of proven fossil reserves (Gtoe, 1980 to 2017)[130].

Adoption of biofuels will therefore continue to be driven by legislation. Either by directly mandating minimum bio-origin components in fuels sold, incentivising use of bio-origin fuels over (e.g. with bio-fuel subsidies), or by disincentivising the consumption of fossil resources (e.g. with a carbon tax, climate levy, or similar).

2.2 Background

Production of sustainable biofuels as drop-in replacements for petro-fuels is a goal for many research scientists, engineers, and technologists. Coordinated national and international research initiatives such as the U.S. Dept. of Energy's (DOE) Bioenergy Technologies Office (BETO), or the European Union's (EU) ReFuelEU proposals aim to boost both supply and demand for biofuel by pushing both legislation and R&D to-

gether. One example from Europe is the incremental changes to the EN 590 automotive diesel fuel requirements European Standard, where the maximum allowable content of fatty acid methyl esters (FAME) has been gradually increased from 0 % in 2000, to 5 % in 2004, up to 7 % since BS EN 590:2009+A1:2010.

To meet the demand created by changes in legislation, a number of different biofuel technologies have been developed to date, which can be categorised into broad generations. First-generation (1G) biofuels such as FAME biodiesels, hydro-treated vegetable oils (HVO), or hydro-processed esters and fatty-acid (HEFA) aviation fuels, make use oil-crops grown exclusively for the production of fuels, such as rapeseed or oil-palm. There is however criticism of the first-generation concept of using arable land for growing biofuel feedstock, since it displaces food crops for human consumption.[133] To avoid local conflict over land usage, most of the biodiesel consumed in the EU is imported. In 2018 over 3,300 MT was imported from outside of the EU block, compared to 13.4 MT of production within.[134] Of the imported material 49.5 % was produced in Argentina, which a 2008 comparative LCA found to have a worse performance than fossil diesel produced and used in Switzerland in impact categories such as global warming potential, eutrophication potential, acidification potential, terrestrial and aquatic ecotoxicity, human ecotoxicity, and overall land use.[135]

Second generation (2G) biofuels such as the Iogen Corporation's bioethanol use lower value biomass by-products such as lignocellulosic or waste agricultural residues. [136] Utilizing of the whole plant as well as low-value residues requires different applied technologies (e.g. enzymatic hydrolysis of cellulose), however avoids the food vs. fuel conflict by utilising the by-products of food production or dedicated non-edible fuel crops such as miscanthus or SRC poplar/willow. However, there is still a large land requirement to produce biomass, and the conversion technology to utilise lignocellulosic material in 2G biofuel processed is more complicated and hence expensive than the processes required to treat vegetable lipids and simple saccharides consumed in 1G biofuel processes.

Third generation (3G) biofuels take the concept of 2G and advance it further. Targeting

higher specific yields by using microalgal organisms, utilization of industrial waste as a fertilizer, cultivation on non-arable land, and often the co-generation of a secondary product or value stream alongside the biofuel product.[137] However, to date microalgal 3G fuels have yet to reach a commercial reality. Numerous demonstration plants have clearly shown technologically viable routes from microalgal biomass to drop-in fuel products, yet the jump from a successful technology demonstration to a successful business venture has so far eluded all companies in this space. Almost 80 % of the cost of microalgal biofuel is the cost of producing the biomass, with projected minimum ash-free dry weight (AFDW) selling prices in the range $392 to $649 per ton.[138, 139] This high AFDW of the raw biomass translates to an microalgal biofuel of about $1.24 per litre of gasoline equivalent fuel (DOE 2022 projection for HTL pathway), compared to $0.62 to $1.00 per litre for a 2G bioethanol process, or $0.94 per litre for a 1G soybean-oil biodiesel process.[138, 139] So while the HTL pathway is extremely promising from a sustainability point of view, it is clear that a lower price of feedstock is necessary. This could potentially be achieved using macroalgae rather than microalgae.

2.2.1 HTL Reactors

Much has been published about batch reactor tests of biomass HTL, due to their relative simplicity in operation and low barriers of accessibility to researchers.[140, 141] However, when comparing batch reaction results, even when the headline reaction conditions may be identical (mass loading, reaction temperature, reaction time etc.), often there is variation between publications. Whilst most experimental studies use batch reactors for the reasons already stated, a few publications have successfully demonstrated HTL under continuous flow.

2.2.2 Batch HTL Reactors

To achieve the high reaction temperature target, batch reactors are often either submerged in a pre-heated isothermal heat bath at reaction temperature (e.g. fluidized sand or high-temp silicone oil), make use of an external heating jacket or mantle to directly control internal reactor temperature, or use a pre-heated furnace set at a constant

high-temperature and control the reaction temperature transiently by insertion/removal of the reactor.[117, 142–146] This variation in approaches to heat application and time at reaction temperature potentially have impacts on the reaction mechanism and hence product profile. Additionally, investigations under batch conditions come with a number of distinct disadvantages compared to flow conditions such as the inability to separate linked transient effects (e.g. time and temperature).

Likely the biggest reason to avoid batch reactors however, is the significant distance from industrial implementation they represent. Batch reactors are normally justified for producing high value products, or where significant plant flexibility is required. In the case of crude oil and petroleum processes, typical flow rates to industrial plants regularly exceed tens of thousands of barrels per day. Any reactor system aiming producing products on a similar scale will be required to do so at high throughput, with minimum energy expenditure, and minimal overall cost - an optimization problem readily tackled under flow conditions.[140]

2.2.3 Flow Reactors Design Considerations

Flow reactors developed for HTL processes vary in design. The most common reactor design is tubular (plug flow reactor, PFR), which lends itself to simple scalability and has the advantage of having no moving parts. The main disadvantages appear to be the risk of plugging in tubular reactors, and the rate of heating. CSTR reactors have also been used in HTL processes, which have the design advantage of eliminating the risk of blocking, but also enhanced heat transfer allowing faster heating rates to the fresh feed as it's introduced. However, as known from general theory, CSTR reactors often have lower theoretical conversions compared to plug flow reactors. To overcome this, some groups have paired an initial CSTR reactor to give good mixing and slurry homogeneity whilst heating to reactor temperature, with a section of PFR following the CSTR to give residence time to allow for high total conversion.[140, 141]

When comparing flow-HTL systems, the first point of comparison is typically the overall biocrude yield. However, the quality of biocrude is also extremely important. Oxygen

content in the biocrude has the potential to disrupt downstream processing, and generally dilutes the useful energy content (HHV). It follows therefore, that a lower total mass yield of biocrude may be favourable, if the loss in mass yield is achieved by preferential deoxygenation of the species in the bio-crude phase. Castello et al. (2018) proposed energy yield, Y_E, as a more sensible tool for comparison, defined as the ratio of energy in the biocrude to the energy in the feed material (equations 2.1 to 2.3).[140]

$$Y_E = \frac{HHV_{bc} \cdot Y_{bc}}{HHV_0} = r \cdot Y_{bc} \tag{2.1}$$

$$r = \frac{Y_E}{Y_{bc}} \tag{2.2}$$

$$r_{max} = \frac{1}{Y_{bc}} \tag{2.3}$$

where HHV_{bc} and HHV_0 is the higher-heating value of the biocrude and starting biomass respectively, Y_{bc} is the mass yield of biocrude, and r is the effective energy ratio. By plotting the energy ratio (r) against the biocrude mass-yield (Y_{bc}) for individual experiments, you can make quick comparisons of effective performance of each system (figure 2.2a). Operating lines of constant energy yield (Y_E) appear as asymptotes on the plot, tending to infinity as Y_{bc} approaches 0. On this plot, points representing reactions that appear closer to the $Y_E = 1$ operating line represent a better energy recovery.

Figure 2.2b shows the same plot, but with data limited to that which multiple comparable mass concentrations are available for each reactor set up. It shows a clear trend that increasing mass concentration of biomass in the HTL feed has a positive effect on the overall energy yield, in all cases moving the reaction closer to the $Y_E = 1$ operating line. High solids loading therefore has a positive impact on the reaction yield, however high solids loadings result in a slurry that is significantly more difficult to pump.

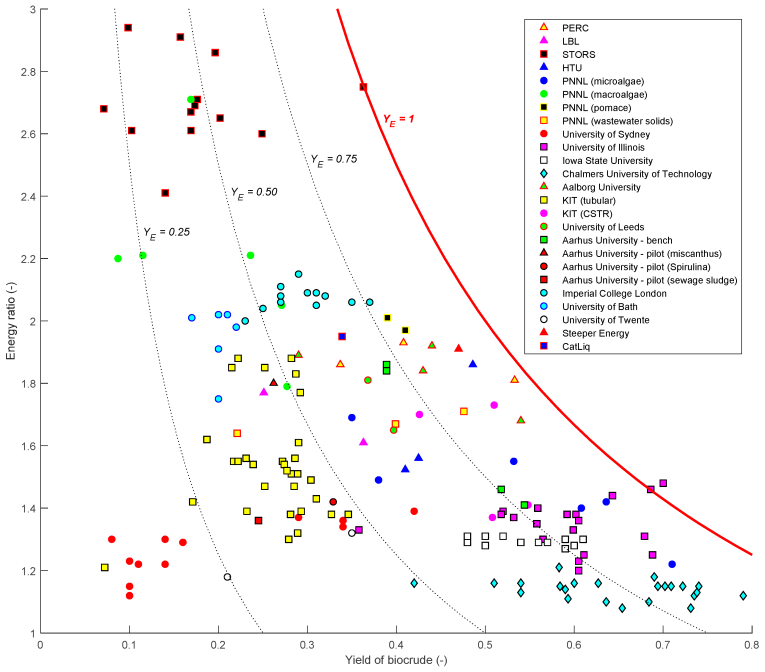

(a)

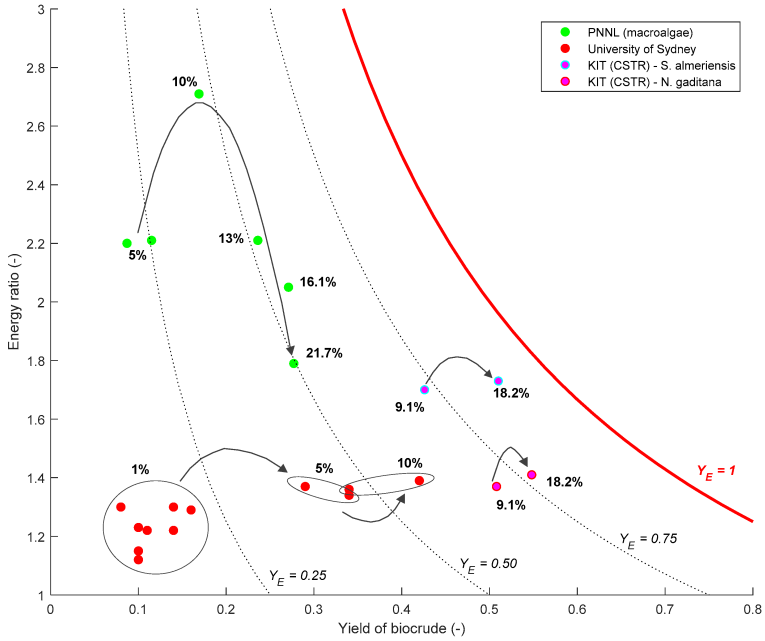

(b)

Figure 2.2: Energy ratio vs. biocrude yield for **a)** various experimental flow HTL set-ups, where Circles: algal biomass; Squares: waste biomass; Triangles: wood; Diamonds: lignin. **b)** Subset of data from plot a) but demonstrating the impact of increasing mass concentration in the feed.

2.2.4 Practical Considerations in Further Scale Up

Selection of appropriate plant equipment and construction materials is critical to the success of a large scale process. From earlier discussions, it is clear that any engineer performing a detailed plant design will have a number of key concerns that must be addressed:

- Pumping a high-solids slurry at high pressure (200 + bar is to be expected).
- Managing the fouling risk of heat exchange surfaces.
- Selecting appropriate materials of construction to mitigate corrosion risks of superheated water and acidic biocrude.
- Separation of the residual solids from the reactor effluent, and further separation of the gas, aqueous, and organic biocrude phases.
- Maintaining flowability of a viscous biocrude and avoiding formation of chars, coke, waxes, or other similar materials that risk causing restrictions and blockages.

Imparting the required mechanical work on the slurry of biomass and water is clearly not a trivial specification. At the lab scale, the selection of pumping equipment is often guided more by equipment availability and the available budget, rather than matching requirements of a full-scale plant. Hence, to-date the published lab scale continuous flow rigs have adopted many approaches, e.g. adapting HPLC pumps to drive pistons loaded with slurry, using high-pressure gases to pressurise a feed reservoir of slurry, dual in-line high-pressure syringe driver pumps, or triplex homogenizer piston pumps.[141, 145, 147, 148] The non-conventional nature of the various approaches found in literature reflects the non-conventional nature of the job being done by the pump. Conveying of high solid content slurries itself is not a particularly challenging problem, with common pump designs with well established performance, e.g. double diaphragm, peristaltic pumps, rotary lobe, or progressive cavity pumps.[149] However, the combined requirement of high pressure complicates the equipment selection. High pressure pumps usually achieve their performance by maintaining tight internal clearances and minimising the leakage

path for the working fluid. Solids can be accounted for in the design and specification, however there is often a particle size requirement to be respected. In addition the presence of any particularly hard or abrasive particles (e.g. sand), may cause excessive wear and degradation in performance.

Fouling and plugging of plant equipment is a risk when operating at subcritical conditions. Dissolved inorganics that are readily soluble and commonly found in ordinary tap water and industrial grey-water, will precipitate easily when approaching the critical domain where HTL processes necessarily operate.[150] Whilst this phenomena of concentrating dissolved inorganics into the solids matrix has been identified as a potentially useful phenomena for remediation of heavy-metal contaminated wastes, it also presents an operational risk.[151] Additionally, the formation of hydro-char solids from the depolymerised biomass itself poses a potential blockage risk.[145] Thus, careful process supervision will be required to ensure that reactor temperature and pressure profiles are maintained to minimise generation of solids, whilst simultaneously maintaining sufficient flow-conditions to prevent settling of the inorganic precipitates that are formed.

Novel flow regimes such as force flow oscillation have been proposed as potential solutions to mitigate some of the process problems associated with pumping the biomass slurry at high pressure. Johannsen et al. (2021) found that introducing a periodic flow oscillation from 0.4 m/s to 1 m/s at a frequency of 0.1 Hz resulted in a dramatic reduction in heating costs for their HTL process, due mainly to improvements in heat-transfer gained by increasing local shear rates and hence the mixing of the highly viscous non-Newtonian (shear thinning) biomass slurry.[152] This improvement in heat transfer rate allowed a modest increase in the overall quantity of heat recovery in the reactor feed/effluent heat exchanger, resulting in a reduction of heating costs in line with previous studies of around 30 %.[153]

Materials selection for reactor and heat-exchanger construction becomes more important as the scale of process plant increases. To date, the majority of lab- and pilot-scale HTL processes use reactors and heat exchangers made from common alloys such as stainless steel.[107] However, common stainless steel alloys (e.g. 316) have been demonstrated

to have limited inertness and resistivity to subcritical water. Holliday et al. (1998) reported that their 316 stainless steel reactors showed signs of deterioration after a large number of reactions with water at sub-critical conditions (300 °C to 355 °C), resulting in metal contamination of their reaction products.[154] Whilst this modest degradation rate is typically acceptable for lab-scale operations, it would not be for an industrial scale plant where continuous reliable up-time will be required.

Nickel superalloys (e.g. Hastelloy-C, Monel, Inconel) show overall better resistance to degradation under hydrothermal process conditions, and in the case of Monel have an established history of use in the petroleum refinery already.[155] However, due to the combination of additional material expense (e.g. Inconel-600 costs on the order of 4x the cost of 316L stainless), more complex machining processes, and higher skilled fabrication techniques, the use of highly corrosion resistant nickel-based superalloys for the construction of the reactor and main heat-exchanger is an expensive prospect.[156, 157]

2.2.5 Downstream Process Integration

2.2.5.1 Differences between Petro-crude and HTL biocrude

Whilst similar to petroleum crudes in some ways, HTL biocrudes are not hydrocarbons. A true hydrocarbon is a compound consisting entirely of carbon and hydrogen, whereas HTL biocrudes contain significant quantities of other elements. Additionally, they have different physical and chemical properties, and require some special treatment before you could consider using them as a feedstock for a traditional petrochemical refinery process.

Some of the main physical and chemical properties of biocrudes produced by HTL reactions are summarised in table 2.2. Compared to petro-crude, HTL biocrudes have increased density, higher viscosity, lower calorific value (HHV), significantly higher heteroatom content (O, N, S), much lower aromatic content (depending on biomass source), much higher asphaltene content, and a significantly higher acidity (TAN).

Table 2.2: Comparison of typical proeprties of both petroleum crude and HTL biocrude oils.

Properties		Petroleum crude[a]	HTL biocrude
Density	g cm^{-3}	0.81 to 0.94	0.97 to 1.04[b]
Viscosity	cSt (@ 40 °C)	4.24[g]	11.97[f]
HHV	MJ kg^{-1}	42.15 to 47.05	30 to 43[b]
Oxygen	wt. %	0.47 to 1.62	≈10[c]
Nitrogen	wt. %	< 0.001 to 0.53	0.4 to 6[c]
Sulfur	wt. %	< 0.001 to 6.06	0.6 to 2[b]
C/H	(atomic ratio)	0.44 to 0.58	0.61 to 0.67[c]
Aromatic	wt. %	18 to 49.6	Undetected to < 10[c,d]
Asphaltenes	wt. %	0.1 to 13.9	43 to 60[e]
TAN	mg/g	0.3 to 2.7	11.6 to 256.5[b]

a) Data from Gawel et al. (2014) unless otherwise cited.[158]
b) Xu et al. (2018)[159]
c) Biller and Roth (2018)[109]
d) Zhou et al. (2010)[160]
e) Bjelić et al. (2018)[161]
f) Hoffmann et al. (2016)[162]
g) BP, Azeri (Ceyhan) assay (2017)[163]

Among these differences, the significance of them depends on the downstream products and processes. Oxygen content significantly impacts the total calorific value of the HTL biocrude, thus any process producing energy dense liquid fuels will likely need to reduce the oxygen content. High nitrogen content in the feed material is potentially disastrous on the downstream catalytic processes. Levels of nitrogen as low as 0.4 % can cause a decreased in FCC catalyst activity by as much as 10 % in a petroleum gasoil cracker, and presence of nitrogen in vacuum gasoil (VGO) has been shown to significantly increase the rate of coke formation on sulfided CoMo hydrotreating catalyst.[164, 165]

Aromatics are an important component of petroleum hydrocarbons. Bulk aromatic products like benzene, toluene, and xylene isomers, are critically important platform chemicals for the downstream production of high performance polymers and resins, pesticides, dyes, adhesives, polyester fibres for apparel, insulation foams, etc. (see figure 2.3).[166]

Asphaltene content in crude oil is an important parameter to track also, as it can

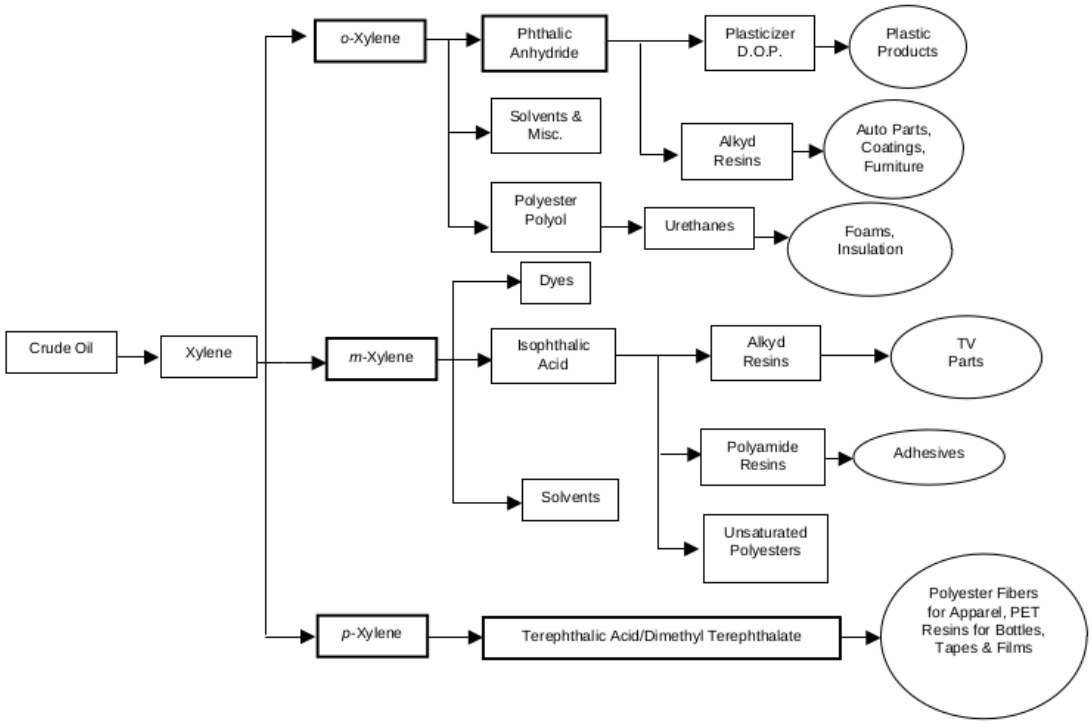

Figure 2.3: Example of the Xylene chain, including bulk intermediates, commodity chemicals, and the types of products that xylene chemicals end up in. Figure reproduced from Stolz et al. (2003).[166]

affect the yield and treatment prior to the main fractionation process. Asphaltenes are the remnants of complex organic molecules originally found in plants and animals, that have been only partially broken down by the action of temperature and pressure over geologic time.[167] In the refinery, asphaltenes may cause a number of problems including blockages and fouling of pipes and equipment if they flocculate or precipitate from solution.

Asphaltenes may also act as surfactants, having both polar and non-polar regions with affinity for water and oil respectively.[168] The result of a successful desalting operation is an aqueous brine phase, a relatively dry and de-salted hydrocarbon phase, and an intermediate *rag layer* that contains a high concentration of complexed asphaltenes. Further processing of this rag layer is difficult, and if not treated properly it presents toxic and hazardous effects on the environment and living organisms.[168, 169]

2.2.5.2 Bio-crude upgrading

Upgrading of biocrude serves a number of purposes. Reducing the content of undesirable heteroatoms, boosting the calorific value of the biocrude product, producing a higher fraction of aromatics, and stabilising the viscosity of biocrudes to prevent ageing and self-polymerisation. Various upgrading routes are investigated in the literature for high oxygen content bio-oils, including catalytic deoxygenation, in-situ catalytic treatments within the HTL reactor itself, and numerous hydrotreatments such as hydrodeoxygenation (HDO) or hydrogenation.[170–172]

ZSM-5 type zeolite catalysts have been used in both catalytic fast pyrolysis (CFP) and catalytic-HTL processes to generate bio-oils with lower oxygen content, and higher aromatic and hydrocarbon content compared to non-catalytic processes. However, catalysts can quickly be deactivated due to coking, and bio-oil yields may be lower due to formation of gasses, water, and coke.[170, 171]

Hydrotreatments typically involve heating the bio-oil in the presence of both hydrogen and Pt group metal catalysts. HDO is typically achieved in a two-step process, with a mild hydrogenation first stage treatment to stabilize the bio-oil and reduce the coke formation in the more severe downstream treatments.[170] Following the initial stabilising treatment, sulfided CoMo and Ni catalyst are often used due to their high specificity toward deoxygenation rather than bulk hydrogenation.[173] Elliot et al. (2013) found that hydrotreating of various HTL biocrudes over a two stage CoMo catalyst bed resulted in reduction of nitrogen and sulfur to near immeasurable levels, and almost total deoxygenation depending on the space-velocity of catalyst bed that was used. Additionally, the hydrotreatment increased the bio-oil density, drastically reduced the TAN, and reduced the viscosity.[172]

The oxygen removed from the biocrude partitions out as water in a new aqueous phase, and carbon dioxide/monoxide in a new gaseous phase. Nitrogen removed in this process forms ammonia, which is present both dissolved in the new aqueous phase, and in significant quantities in the new gaseous phase. In addition to losing oxygen and nitrogen,

the hydrotreatment results in loss of carbon from the biocrude. The H_2-free composition of off-gas from the hydrotreatment step is majority hydrocarbon (methane, ethane) in nature, clearly demonstrating a loss of bio-crude yield.[172] However the treatment of sour-water (containing ammonia) and acid gas (containing CO_2 and/or H_2S) streams is well understood in the context of the petroleum refinery, and there are already mature processes capable of extracting value from these new waste streams.

2.2.5.3 Integration into existing petro-plants

Blending of biocrude or biocrude derivatives into an existing refinery feedstock allows the continued operation of existing capital infrastructure, thus de-risking the transition to bio-based feedstocks by allowing existing petroleum producers to manage a phased approach whilst getting maximum value from already invested equipment. The precise point of introducing the biocrude (raw, partially- or fully-hydrotreated) into the petro-refinery is another variable. Blending a raw or partially treated bio-crude in with the raw petroleum crude would have the benefit of allowing existing petro-crude washing equipment (desalter units) to co-process the petro- and bio-crudes together. The resulting petro-/bio-crude blend would then be directed to the main crude furnace for pre-heating prior to fractionation in the main column, and the bio- content in the mixed feed would be distributed across the various cuts extracted from the fractionating column. Ramirez et al. (2017) found that simple room-temperature mixing of petro-crudes and untreated liquefaction biocrudes was insufficient to generate homogeneous solutions with significant differences in functionality detected by FTIR depending on the height of sampling in the mixture, but that the boiling behaviour of the mixture was at least predictable.[174]

Alternatively, it may be preferred to introduce the hydrotreated biocrude (HT-biocrude) into one or more of the fractions after the initial fractionation. This allows the bio-content to be directed towards specific products rather than spread across the whole refinery product range, and potentially represents an opportunity to save a modest amount of energy by reducing the boil-up and condenser duty of the fractionating column. Elliot et al. (2013) found that the majority of their hydrotreated biocrude (80

% to 85 %) would be suitable for directly blending in the diesel pool with no further processing.[172]

Whilst direct blending into a fuel product seems initially an attractive option, it is unlikely that specific fuel characteristics such as those defined in EN 590 will be met with 100 % HT-biocrude diesel. Additionally, with clear signals from national governments that they wish to legislate away ICE vehicles, it may be more prudent to adapt the HT-biocrude as a feedstock suitable for the whole range of refinery products.

The overall aim of this package of work is to evaluate the technoeconomic viability of a macroalgal HTL process, for the production of a biocrude product from *Sargassum* as a suitable drop-in replacement for petroleum crude in the existing petroleum refinery. The overall economic viability of a process must be considered when assessing its overall sustainability. Not only must this macroalgae-to-biocrude process be environmentally, and socially sustainable, it must also be able to operate with a minimum level of profit to meet the overall requirements of the three common pillars of sustainability (People, planet, and profit). To achieve this aim, the following objectives are defined:

1. Experimental studies into typical biocrude yields, product elemental distribution, and predicted boil-up behaviour of biocrude, when using macroalgae as an HTL feedstock - these experimental studies will provide useful information that will assist in the development of a generalised HTL model.

2. Development of general purpose and transferable predictive models, that allow determination of HTL product yields from simple biomass analysis (C, H, N, O, S analysis).

3. Development of an HTL process model in Aspen Plus that incorporates the previously developed yield prediction model to allow key equipment (e.g. heat exchangers, pumps) to be sized and costed easily at different macroalgal feed flow rates.

4. Net-present value (NPV) assessment by discounted cash-flow (DCF) analysis on the main process plant equipment, to investigate the economic feasibility of a

macroalgae-HTL plant for the production of biocrude, and the combination of economic constraints that bound the limits of operation.

2.3 Materials and Methods

Experimental Materials Food grade Naturya brand Organic Spirulina Powder was sourced from a local supermarket and used throughout this work as a model microalgae for comparison. Macroalgae Sargassum sp. was wild-harvested from Broadsands Beach, Paignton (50° 24' 24.9" N, 3° 33' 16.2" W) between November 2017 and January 2018. Samples were frozen at -80 °C and then freeze dried at -55 °C (Coolsafe, Scanvac) and then triturated to a fine powder, sieved to $<$ 1.4mm, and stored in sealed containers at -80 °C to prevent degradation. The impact of the freeze-drying process is not considered in this work, however previous studies indicate the impact of this pre-processing lead to a modest reduction of overall biocrude yield.[175]

2.3.1 Experimental Methods

2.3.1.1 Pre-treatment of Algal Solids

Acid and base pre-treatment conditions were selected based on previous work.[176] 180 g of 2 vol. % H_2SO_4 (0.36M) was pre-heated to 30 °C on a hotplate controlled by IKA ETS-D5 electronic contact thermometer immersed into the solution. Constant stirring was achieved by use of an overhead stirrer set to 750 rpm, with a 35 mm diameter propeller stirrer. To this solution, 20 g (10 wt. %) of biomass (microalgae, or macroalgae) was quickly added and a stop-watch started. This solution was continuously stirred at constant temperature for 20 minutes.

After the reaction time had elapsed, the solids were separated by vacuum filtration of the whole reaction mixture through a QL100 qualitative filter paper set in a Buchner funnel. Solids retained on the filter paper were thoroughly washed with DI water to remove any acid/base residue, and the filter paper/solids were dried in a laboratory oven (Plus II Oven, Gallenkamp) at 60 °C until constant weight was achieved.

2.3.1.2 Batch Hydrothermal Liquefaction

Hydrothermal liquefaction (HTL) was performed on solids from the pre-treatment, or untreated-biomass, as described by Raikova et al.[13] Batch reactors previously fabricated in the group using stainless steel tubing with Swagelok® fittings were used. The tubular reactor was loaded with 3 g of oven-dried primary solids and 15 g of DI water, and sealed shut. Total product yields are calculated on the basis of the dry and ash-free (DAF) content of the initial load of biomass solids. For experiments where headspace atmosphere was exchanged for N_2, a high-pressure N_2 supply was connected to the reactor vent needle valve and the reactor was alternately pressurised to 5 bar and vented for a minimum of 5 pressure swing cycles. The reactor was then heated within a vertical tubular furnace until the reaction temperature of 350 °C was reached, then removed from the furnace and allowed to cool to room temperature.

After cooling, gaseous products were released via the needle valve into an inverted, water-filled measuring cylinder to measure gaseous fraction volume. Gas phase yields are calculated using the ideal gas law, and approximating the gas phase as 100 % CO_2, with a molecular weight 44 g mol^{-1}, and ideal volume 24.6 dm^3 mol^{-1}, as previously demonstrated by Raikova et al.[13, 151, 177] The yield of gaseous product was determined as described by equation 2.4:

$$Yield_{Gas} = \frac{(V_{Gas} \times 1.789 \times 10^{-3})}{m_{drybiomass}} \times 100\% \tag{2.4}$$

Where V_{Gas} is the collected gaseous fraction volume in mL, and m is the mass of the subscripted species in grams.

Following this, the aqueous phase was decanted from the reactor contents and filtered through a Fisher Scientific brand QL100 grade qualitative filter paper pre-dried overnight at 60 °C. The product yield in the water phase was determined by leaving a 2.5 g aliquot of the aqueous phase to dry in a 60 °C oven overnight and scaling the residue yield to the total aqueous phase mass. Aqueous phase residue yield was

determined by equation 2.5:

$$Yield_{AQ} = \frac{m_{AqResidue}}{m_{drybiomass}} \times 100\% \tag{2.5}$$

The remaining biocrude and char phase was washed from the reactor using chloroform until the solvent ran clear, and filtered through the same filter paper used to separate the aqueous phase (after drying with an air stream to ensure evaporation of residual water). The filter paper and collected char were washed thoroughly with chloroform to remove all remaining biocrude. The filtrate was collected, and solvent removed under vacuum (40 °C, 72 mBar) until no further solvent evaporation was observed visually. Biocrude samples were transferred to 20 mL vials using a small volume of chloroform; solvent was removed in vacuo, and vials were left to vent to atmosphere via a needle for a further 12 h to remove residual solvent. Biocrude yield was determined by equation 2.6:

$$Yield_{BC} = \frac{m_{Biocrude}}{m_{drybiomass}} \times 100\% \tag{2.6}$$

The solids char yield was calculated from the mass of the retentate collected on the filter paper after drying overnight in an oven at 60 °C. Solid yield was determined by equation 2.7:

$$Yield_{Char} = \frac{m_{Char}}{m_{drybiomass}} \times 100\% \tag{2.7}$$

2.3.2 Analytical Methods

Elemental analysis (C, H, N, and S) was performed by OEA Laboratories Ltd (Exeter, UK). Where appropriate, Oxygen content was approximated by subtracting C, H, N, and S content from 100 %. In percentage elemental analysis (EA) of CHNSO, milligram amounts of samples are combusted or pyrolyzed at high temperature in a helium carrier gas. After suitable preparation the measurable gases (CO_2, H_2O, N_2, SO_2, or CO)

are separated on a chromatography column. The gases are passed in turn through a thermal conductivity detector (TCD) where the gases are quantified against know reference standards.

Thermogravimetric analysis (TGA) was performed on a Setaram Setsys Evolution TGA 16/18. The Calisto programme was used to collect and process data. Samples were loaded individually into a 170 μL alumina crucible. Under an argon atmosphere, samples were held at room temperature for 20 min, with temperature ramped to 800 °C over 20 min, and held at 800 °C under argon for 30 min. The atmosphere was then swapped to air whilst maintaining a temperature of 800 °C for 40 min, followed by cooling to ambient temperature over 20 min. Moisture was determined by the mass loss at 100 °C relative to the starting mass, volatile matter determined as mass lost between 100 °C and 800 °C under argon, fixed carbon the mass lost at 800 °C upon introduction of air, and ash content was determined by taking the final mass of residue at the end of the 40 min under air.

$$Moisture\% = \frac{m_{100^\circ C}}{m_{starting}} \times 100\% \tag{2.8}$$

$$VM\% = \frac{m_{100^\circ C} - m_{800^\circ C}}{m_{100^\circ C}} \times 100\% \tag{2.9}$$

$$FC\% = \frac{m_{800^\circ C_{Ar}} - m_{800^\circ C(air)}}{m_{100^\circ C}} \times 100\% \tag{2.10}$$

$$Ash\% = \frac{m_{800^\circ C(air)}}{m_{100^\circ C}} \times 100\% \tag{2.11}$$

Biochemical composition (carbohydrate, lipid, and protein wt. %) is determined by estimating the biochemical content according to mass loss differences at various temperatures during TGA, as described by Biswas et al. (2017), and Ross et al. (2008).[178, 179] These estimates are then expressed as a percentage of the dry-weight of material

($m_{100°C}$) (equations 2.12 to 2.14).

$$Carbohydrate\% = \frac{m_{180°C} - m_{270°C}}{m_{100°C}} \times 100\% \tag{2.12}$$

$$Protein\% = \frac{m_{320°C} - m_{450°C}}{m_{100°C}} \times 100\% \tag{2.13}$$

$$Lipid\% = \frac{m_{600°C} - m_{800°C(Ar)}}{m_{100°C}} \times 100\% \tag{2.14}$$

2.3.3 Computational Methods

Various modelling software was used in this work, including scripts written in Python 3.8.0, and process models developed in Aspen Plus V10. Specific model details and methodology are discussed later in this work.

2.3.3.1 Prediction of Biochemical Proximate prediction and Ultimate CHNO Analysis

Equation 2.15 describes the general form of the linear MCA model that has been used throughout literature to predict ultimate analysis (C, H, N, and O) from biochemical proximate analysis (carbohydrates, protein, or lipids). M_i represents the weight percentage (wt. %) of component i, x_j represents the feedstock descriptor (carbohydrate, protein, or lipid), $a_{i,j}$ is the gradient coefficient for the i and j components, and b_i is the intercept constant. Expanding equation 2.15 for i elements C, H, N, and O, and j variables of carbohydrate, protein, and lipid allow a set of equations to be cast into the matrix form represented by equation 2.16. This can be simply represented by equation 2.17, where $\mathbb{M}$, $\mathbb{A}$, $\mathbb{J}$, and $\mathbb{B}$ represent the individual matrices in equation 2.16.

$$M_i = \sum(a_{i,j}x_j) + b_i \tag{2.15}$$

$$\begin{bmatrix} M_C \\ M_H \\ M_N \\ M_O \end{bmatrix} = \begin{bmatrix} a_{C,Carb} & a_{C,Prot} & a_{C,Lipd} \\ a_{H,Carb} & a_{H,Prot} & a_{H,Lipd} \\ a_{N,Carb} & a_{N,Prot} & a_{N,Lipd} \\ a_{O,Carb} & a_{O,Prot} & a_{O,Lipd} \end{bmatrix} \times \begin{bmatrix} x_{Carb} \\ x_{Prot} \\ x_{Lipd} \end{bmatrix} + \begin{bmatrix} b_C \\ b_H \\ b_N \\ b_O \end{bmatrix} \tag{2.16}$$

$$\mathbb{M} = \mathbb{A} \times \mathbb{X} + \mathbb{B} \tag{2.17}$$

Determination of coefficients $a_{i,j}$ and b_i is made by using a non-linear least squares regression tool, comparing experimental values of the weight percentage (wt. %) to the predicted values of M_i. A dataset of 94 mixed micro- and macro-algal biomass records were collated as comma separated values, and a short script written in Python (version 3.8.0) utilising the optimize.least_squares method provided by the SciPy package (version 1.5.2).[180] Example code and input files are available in the digital supporting information.

The $a_{i,j}$ and b_i coefficients determined by Jiang were selected as initial values, and the least-square regression was used to minimise the error between experimental and predicted values of M_i with bounds set to limit $0 \leq a_{i,j} \leq 1$ where i was C, N, and O, and $0 \leq b_i \leq 100$ where i was C, N, O, and H.[116] Determination of $a_{H,j}$ was made by subtractive mass balance for each biochemical component j such that the relationship described by equation 2.18 was true.

$$a_{H,j} \leq 1 - (a_{C,j} + a_{N,j} + a_{O,j}) \tag{2.18}$$

Contribution of each of the determined $a_{i,j}$ coefficients to the overall model was then assessed by T-test of the determined value compared against zero, at an alpha level 0.05. Values of $a_{i,j}$ with a p-value of greater than 0.05 were discarded, as their inclusion in the model was not determined to be statistically significant.

For prediction of the biochemical proximate analysis from the ultimate analysis, two methods were compared. Firstly, parameters of $a_{i,j}$ and b_i that were determined were used to populate the $\mathbb{A}$ and $\mathbb{B}$ matrices for the elements C, N, and O. The resulting

$\mathbb{A}_{C,N,O}$ matrix is a 3x3 square matrix, thus a simple linear-algebra solver was used to determine the corresponding exact values of the $\mathbb{J}$ matrix for a given value of the $\mathbb{M}$ and $\mathbb{B}$ matrices (equations 2.19 and 2.20). Python was again used to implement the linalg.solve method provided by the NumPy package (version 1.19.1).[181]

$$\begin{bmatrix} M_C - b_C \\ M_N - b_N \\ M_O - b_O \end{bmatrix} = \begin{bmatrix} a_{C,Carb} & a_{C,Prot} & a_{C,Lipd} \\ a_{N,Carb} & a_{N,Prot} & a_{N,Lipd} \\ a_{O,Carb} & a_{O,Prot} & a_{O,Lipd} \end{bmatrix} \times \begin{bmatrix} x_{Carb} \\ x_{Prot} \\ x_{Lipd} \end{bmatrix} \tag{2.19}$$

$$(\mathbb{M}_{C,N,O} - \mathbb{B}_{C,N,O}) = \mathbb{A}_{C,N,O} \times \mathbb{X} \tag{2.20}$$

$$(\mathbb{M}_{C,N,O} - \mathbb{B}_{C,N,O}) \times \mathbb{A}^{-1}_{C,N,O} = \mathbb{X} \tag{2.21}$$

The second method compared was to compute a new set of $a'_{i,j}$ and b_j parameters for a new set of linear MCAs, following the same method as previously when computing the $a_{i,j}$ and b_i parameters. The $a'_{i,j}$ and b_j parameters are then used in the system of equations described by equation 2.22, and the SciPy non-linear least squares method was used in much the same fashion.

$$x_j = \sum (a'_{i,j} M_i) + b_j \tag{2.22}$$

2.3.3.2 HTL Yield Models

Accurate prediction of HTL reaction yields is critical to development of relevant process models. Proximate analysis (carbohydrate, protein, and lipid), and HTL product yields from 119 published macroalgae HTL experiments were collated, and were used to re-fit empirical coefficients for numerous reaction models. The re-fitting was accomplished by use of a Python script applying the SciPy least squares non-linear regression tool to minimise the sum of squared residuals (SSE) between predicted and experimental product yields.

Multi-Component Additive Models: Following the work of Biller & Ross, the

multi-component additive (MCA) model methodology for making accurate quantitative predictions of the product mass-yields from HTL processes has become adopted throughout the literature.[115–117, 182–185] The original MCA model is a simple set of linear equations that results in a weight percentage (wt. %) yield of all four HTL products (equation 2.23). Where Y_i is the wt. % yield of HTL product i, $k_{i,j}$ is the fixed fraction of biomass component j (L, P, and C, referring to lipid, protein, and carbohydrate respectively) that is partitioned into HTL product i (BC, AQ, GS, and CHR, referring to bio-crude, aqueous organic, gas, and char respectively), and x_j is the wt. % of the biomass component j in the starting biomass.

$$Y_i = \sum Y_{i,j} = \sum (k_j \times x_j) \tag{2.23}$$

$$Y_{BC} = k_{BC,L} x_L + k_{BC,P} x_P + k_{BC,C} x_C \tag{2.24}$$

The fixed fraction coefficients ($k_{i,j}$) are fitted using a wide selection of experimental HTL results, with varying biomass composition to ensure a spread of x_j values are covered. Many authors have attempted to fit parameters for the linear model, with the aim of accurately predicting the bio-crude yield (Y_{BC}) (equation 2.24). In most cases the MCA model fitted parameters do a reasonable job of predicting the mass yield of the various HTL products, however the simple linear model described by equation 2.24 makes no allowance for interactions between products and/or intermediates in the HTL reaction. [115–117, 182–185]

The simple linear model has been refined with additional interaction terms, in models used by Teri et al. and Lu et al. (equation 2.25), and Sheng et al. (equation 2.26). [186–188]

$$Y_{BC} = \sum (k_{BC,j} x_j) + k_{BC,LC} x_L x_C + k_{BC,LP} x_L x_P + k_{BC,PC} x_P x_C \tag{2.25}$$

$$Y_{BC} = \sum(k_{BC,j}x_j) + k_{BC,LC}\frac{x_L x_C}{|x_L - x_C|} + k_{BC,LP}\frac{x_L x_P}{|x_L - x_P|} + k_{BC,PC}\frac{x_P x_C}{|x_P - x_C|} \quad (2.26)$$

However, in each case the fitted parameters are specific to the experiment. Variations between reactor set-up, residence time, reaction temperature, temperature ramping rate, and downstream separation and work-up are not accounted for in these simple models. Attempts have been made to apply both the simple and more complex MCA model parameters developed on microalgae to macroalgae, however these have shown poor correlation when directly applying previously published parameters.[13]

In this work, the set of fixed fraction coefficients ($k_{i,j}$) for each bio-crude yield prediction model (equations 2.24 to 2.26) are re-fit using the same SciPy least-squares method adopted previously. Initial parameters were taken from the previously published values of $k_{i,j}$ listed in table 2.3.

Table 2.3: Fixed fraction coefficients ($k_{BC,j}$) of previously published HTL MCA product yield models.

Author(s)	Model Eq.	Parameters						Ref.
		$k_{BC,L}$	$k_{BC,P}$	$k_{BC,C}$	$k_{BC,LC}$	$k_{BC,LP}$	$k_{BC,PC}$	
Biller & Ross	Eq. 2.24	0.80	0.18	0.06	-	-	-	[117]
Leow et al.	Eq. 2.24	0.97	0.42	0.17	-	-	-	[182]
Wagner et al.	Eq. 2.24	0.96	0.161	0.024	-	-	-	[183]
Wagner et al.	Eq. 2.24	1.013	0.286	0.036	-	-	-	[183]
Shakya et al.	Eq. 2.24	0.90	0.32	0.22	-	-	-	[185]
Shakya et al.	Eq. 2.24	0.96	0.43	0.30	-	-	-	[185]
Li et al.	Eq. 2.24	0.85	0.45	0.22	-	-	-	[184]
Teri et al.	Eq. 2.25	0.951	0.334	0.058	-0.00016	0.271	-0.00019	[186]
Teri et al.	Eq. 2.25	0.949	0.316	0.061	-0.212	0.359	0.00038	[186]
Lu et al.	Eq. 2.25	0.82	0.211	0.0457	0.000	0.000	0.00479	[187]
Sheng et al.	Eq. 2.26	0.90	0.385	0.025	0.052	0.093	0.003	[188]

Kinetic Models for Macroalgal HTL: Use of experimental results from multiple literature sources however comes with a distinct downside. Previously mentioned important influences of residence time, reaction temperature, and other specific experimental factors are in no way accounted for in any of the MCA models. Accuracy of

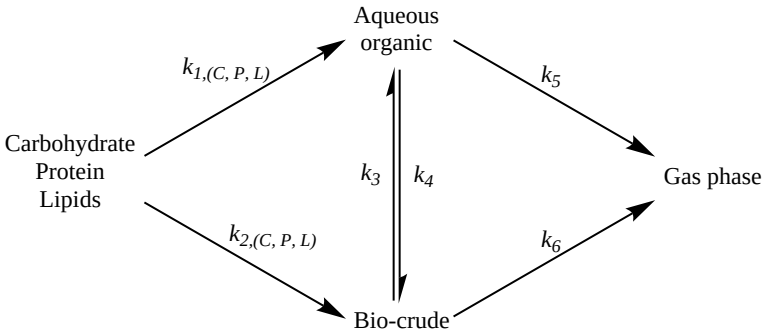

Figure 2.4: Simple kinetic reaction network for HTL reaction of biochemical content of biomass. Adapted from Valdez et al. (2014). [189]

any such MCA model relies on exploring an experimental space (varying carbohydrate, lipid, and protein concentration) whilst controlling variables not included in the models (residence time, temperature, etc.). Whilst there is a relative glut of experimental data for microalgal HTL processes, there is in comparison relatively little information for macroalgae. In order to try and address this, inclusion of more factors into the reaction model can be considered.

Valdez et al. proposed a simple kinetic model for HTL of microalgae (see figure 2.4), which allows the inclusion of both steady state reaction temperature and reaction time as experimental variables.[189] Use of a kinetic model allows a more broad selection of macroalgal experimental results to be included whilst fitting the model, since you are no longer constrained to a narrow window of process conditions.

Treating each pathway of the network described in figure 2.4 as a first-order reaction, the network resolves to the set of ordinary differential equations (ODE) described by eq. 2.27 to 2.32.

$$\frac{dx_{_C}}{dt} = -(k_{_{1,C}} + k_{_{2,C}})x_{_C} \tag{2.27}$$

$$\frac{dx_{_L}}{dt} = -(k_{_{1,L}} + k_{_{2,C}})x_{_L} \tag{2.28}$$

$$\frac{dx_{_P}}{dt} = -(k_{_{1,P}} + k_{_{2,C}})x_{_P} \tag{2.29}$$

$$\frac{dx_{BC}}{dt} = -(k_3 + k_6)x_{BC} + k_{1,C}x_C + k_{1,L}x_L + k_{1,P}x_P + +k_4 x_{AQ} \tag{2.30}$$

$$\frac{dx_{AQ}}{dt} = -(k_4 + k_5)x_{AQ} + k_{2,C}x_C + k_{2,L}x_L + k_{2,P}x_P + +k_3 x_{BC} \tag{2.31}$$

$$\frac{dx_{GAS}}{dt} = k_5 x_{AQ} + k_6 x_{BC} \tag{2.32}$$

Where x_i refers to the dry and ash-free (DAF) weight % of each component i, subscripts C, L, and P, refer to carbohydrate, lipid, and protein fraction in the starting biomass respectively, and subscripts BC, AQ, and GAS refer to the bio-crude, aqueous-organic, and gas phase products produced by the HTL reaction. $k_{n,i}$ is the kinetic rate constant for the degradation of component i (where defined), and following the numeric pathway n (1 to 6) as detailed in figure 2.4. Each kinetic rate constant is further described by the Arrhenius equation (eq. 2.33).

$$k_{n,i} = A_i e^{\frac{-(E_a)_i}{RT}} \tag{2.33}$$

Where subscript i defines the reacting component, A_i is the pre-exponential factor, $(E_a)_i$ is the activation energy for the reaction, R is the molar gas constant, and T is the reaction temperature (K).

119 individual experimental records of macroalgal HTL were collated from the published literature. For each record, the biochemical proximate analysis DAF weight %, HTL product mass yield on a DAF basis (wt. %), reaction time (t_f, seconds), and reaction temperature (T, Kelvin) were recorded. Where not present in the original literature, the biochemical proximate composition (carbohydrate, lipid, protein wt. %) were estimated using the previously described technique.

The Euler method for estimating the numerical solution to a set of ODEs was applied in a Python script, and Arrhenius parameters of A_i and $(E_a)_i$ were adjusted with the SciPy least-squares non-linear method to minimise the error between the predicted bio-crude yield (x_{BC} at time $t = t_f$) and experimental bio-crude yield for each experimental record. The general form of the implemented Euler method is shows by equations 2.34

to 2.36.

$$x_{i_{t+1}} = x_{i_t} + dt\lambda x_{i_t} \tag{2.34}$$

$$x_{i_{t+1}} = (1 + dt\lambda)^{t+1} x_{i_0} \tag{2.35}$$

$$|1 + dt\lambda_i| \leq 1 \tag{2.36}$$

Where x_{i_t} represents the wt. % of component i evaluated at time t, x_{i_0} is the initial concentration of x_i at time $t = 0$, dt is the Euler time-step, and λ_i is the derivative function of x_i (detailed in equations 2.27 to 2.32). Equation 2.36 defines the stability criteria for the Euler method, and sets a maximum limit on the size of dt. The size of the time-step in this case was determined by calculating the minimum number of Euler time-steps to satisfy equation 2.36 for all λ_i, and then doubling it to give the total number of computation steps for each solution.

Initial values of A_i and $(E_a)_i$ for each of the individual biomass components were taken from the microalgal work of Sheehan and Savage (2017), and each individual Arrhenius parameter was bounded to a maximum of ±30% deviation from its initial value.[190]

Compared to microalgal HTL, macroalgal HTL results in significantly higher yield of residual solids and char. The average residual solids or char yield in the experimental data set collated in this work is 28.2 wt. % (DAF), with inter-quartile range of 18.5 to 34.5 wt. % (DAF) (See table ESI 1 in online supporting info). HTL of microalgae typically results in solids well below 10 wt. %, with detailed technical reports produced by the US Department of Energy considering 2 wt. % a reasonable level of residual solids in their techno-economic analysis.[116, 123]

Mechanisms for formation of the solids are explored in more detail in studies considering hydrothermal carbonisation (HTC) and the formation of primary and secondary hydrochar as solids from that precipitate following reaction of dissolved intermediates.[191, 192] The Valdez microalgal model was adapted and with a further modification to the model to resolve the solid char phase produced by HTL of macroalgae (figure 2.5).

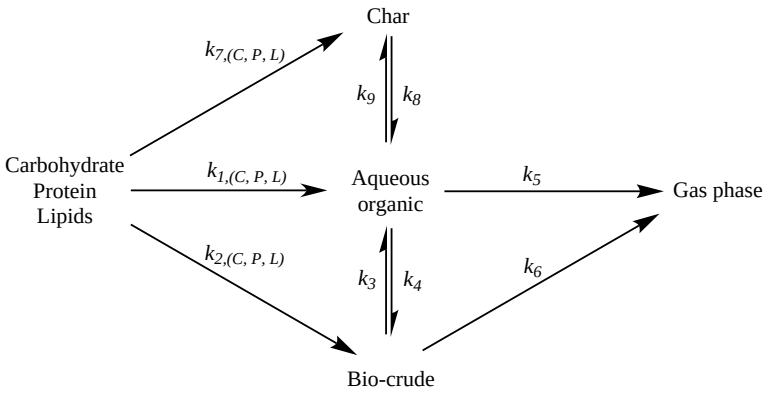

Figure 2.5: Kinetic reaction network for HTL reaction of biochemical content of biomass including char production. Char is assumed to form directly from starting solids, and precipitate from dissolved aqueous intermediates, in this model lumped together with all aqueous species.

This modification allows for the formation of solids by dissolved aqueous species, as well as the direct conversion of initial biomass solids to the char phase.

$$\frac{dx_{CHR}}{dt} = -k_8 x_{CHR} + \sum_{i=(C,P,L)} k_{7,i} x_i + k_9 x_{AQ}^n \tag{2.37}$$

Jatzwauck and Schumpe found that the reaction step of forming solid hydrochar from dissolved intermediates was not well modelled as first order, and that when modelled an order of $n = 1.53$ was found to best model their experimental data. The modified reaction network (figure 2.5) results in an additional differential term (equation 2.37), as well as 5 additional kinetic constants ($k_{7,(C,P,L)}$, k_8, and k_9). Where subscript CHR refers to the char phase, and n is the reaction order for the aqueous-to-char conversion step. The existing set of ODEs (equations 2.27 to 2.32) are updated to include these additional pathways, and parameters fit in the same method as previous utilising the Euler method and non-linear least-squares regression to adjust A_i and $(E_a)_i$ for the kinetic constants. Initial values for Arrhenius parameters for $k_{7,i}$ through to k_9 are taken from Jatzwauck and Schumpe's (2015) work studying kinetics of HTC of soft rush. [191]

2.3.3.3 Qualitative HTL Product Quality Prediction

In addition to predicting the mass yield of products of the HTL reaction, it is important to consider the distribution of elements (CHONS) into the different HTL products. Prediction of the elemental distribution not only allows satisfaction of the elemental balance when performing reactor modelling, but also allows estimation of some of the crucial quality parameters of the HTL products. Higher-heating value (HHV) of the bio-crude for example is strongly impacted by the oxygen, nitrogen, and sulfur content. Similarly, bio-crudes with lower H/C ratios usually have higher boiling points. [116] Both Li et al., and Jiang et al. used the following simple linear model (equation 2.38) to predict the elemental composition of the HTL products, with Jiang et al. making some improvements to the model parameters proposed by Li. [115, 116]

$$M_i = \sum a_{i,j} \times x_j + b_i \tag{2.38}$$

$$AOS_C = \frac{(3 \times Nmol\% + 2 \times Omol\% + 2 \times Smol\% - Hmol\%)}{Cmol\%} \tag{2.39}$$

$$M_{AQ} = M_{Biomass} - \sum M_i \times Y_i \tag{2.40}$$

Where M_i is the wt. % of element M in product i, x_j is the wt. % of feedstock descriptor j, and $a_{i.j}$ and b_i are the model coefficients. AOS_C refers to the average oxidation state of the feedstock carbon, and is calculated by equation 2.39. Parameters used in this work to estimate bio-crude elemental content are listed in table 2.4, and were directly taken from Jiang et al. with the exception of prediction of C and H in the bio-crude for which Li's method was used instead.[115, 116] Given that the gas product is dominated by carbon dioxide ($>$ 90 %), and the combined ash and char product is comprised of non-volatile fixed carbon, the weight fraction of elements in both phases are assumed to be constant wt. % fractions listed in table 2.5. Finally, estimation of the elemental composition of the aqueous fraction is made by mass-balance as detailed in equation 2.40.

Table 2.4: $a_{i,j}$ and b_i model coefficients for prediction of bio-crude elemental composition from algal HTL.

M_i	x_j	$a_{i,j}$	b_i	Ref.
$C_{Bio-crude}$	AOS_C	-8.37	68.55	[115]
$H_{Bio-crude}$	AOS_C	-2.61	8.20	[115]
$O_{Bio-crude}$	Y_{BC}	0.238	-0.049	[116]
$N_{Bio-crude}$	x_{Prot}	0.093	-	[116]
$S_{Bio-crude}$	x_{Prot}	0.012	-	[116]

Table 2.5: Estimated fixed wt. % elemental composition of gas and char HTL products.

wt. %	M_C	M_H	M_O	M_N	M_S
Gas	0.2881	0.0119	0.7000		
Biochar & Ash	0.5008	0.0290	0.3961	0.0457	0.0284

Fixed fractions taken from Jiang et al. [116]

2.3.4 Plant Modelling and Configuration

The plant configuration was designed to allow various sources of biomass to be received and managed, with primary stock control managed by use of front-end loaders or similar mechanical handling equipment. The plant design selected in this work was reached by following the work of Knorr et al. in their detail design study of an advanced biofuels plant utilising hydrothermal liquefaction of woody biomass.[193]

Similar to previous works by PNNL, the availability of fresh biomass varies seasonally. In this conceptual plant, provisions are made to receive varying quantities of biomass throughout the year, dry the biomass to reduce the moisture content below a critical level of 15 wt. % required to prevent spoilage, and storage of large quantities of milled and dried biomass for re-feeding to the HTL process when the fresh supply of material drops below requirements. [194] Process flow diagrams for the main process areas are shown in figures 2.6 to 2.8.

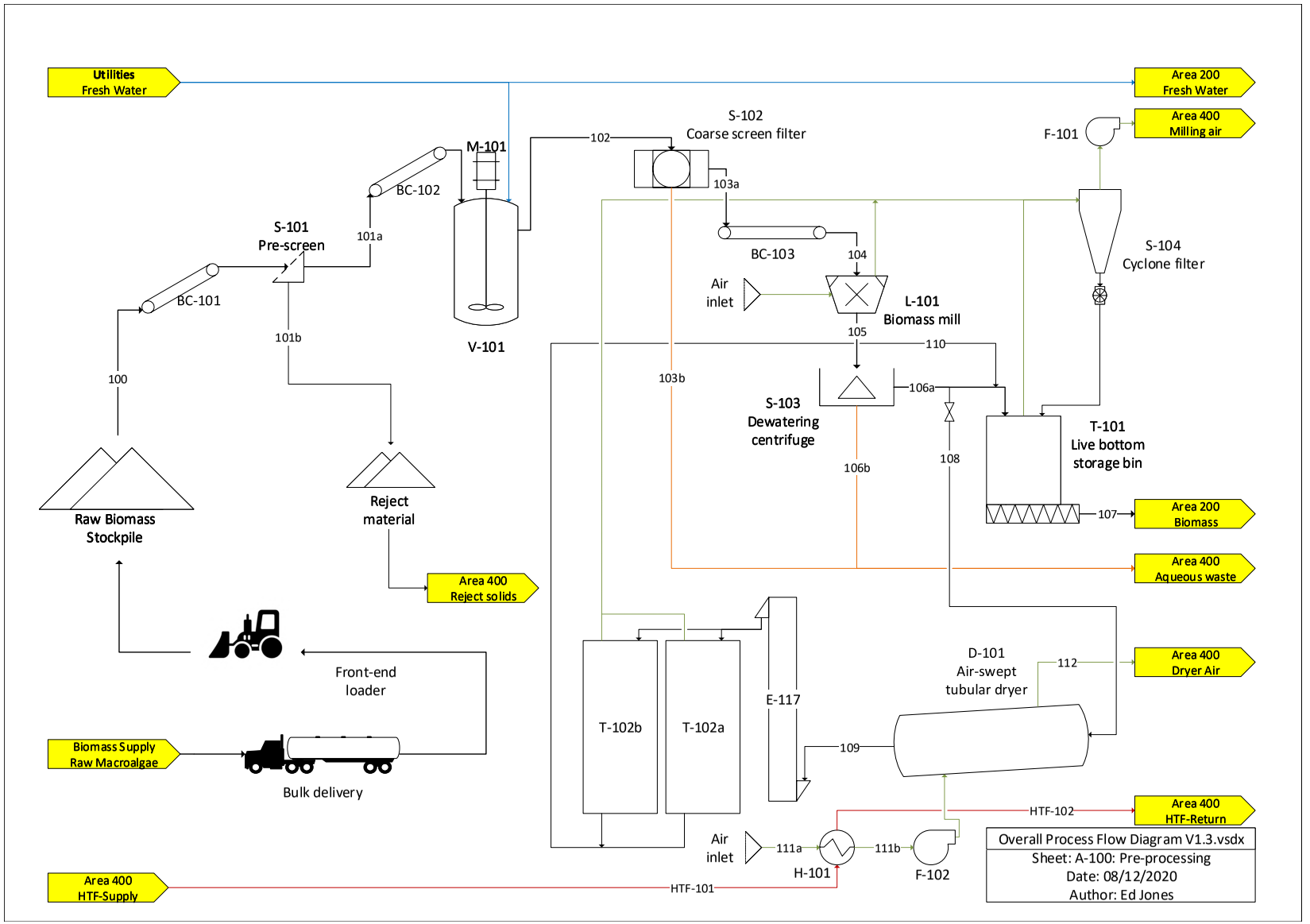

Figure 2.6: A-100: Biomass receiving and pre-processing process flow diagram

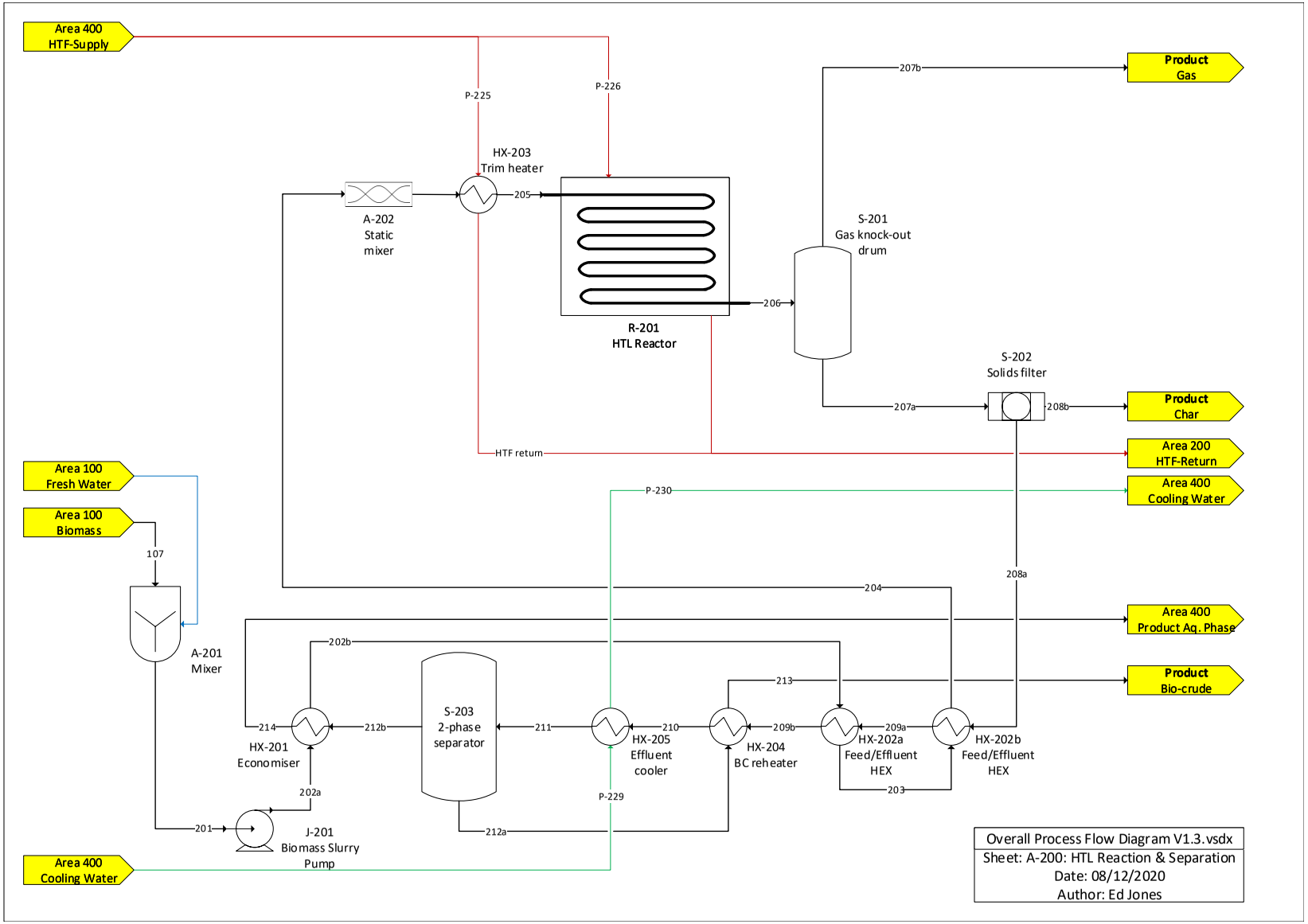

Figure 2.7: A-200: HTL Reaction and Separation Process Flow Diagram

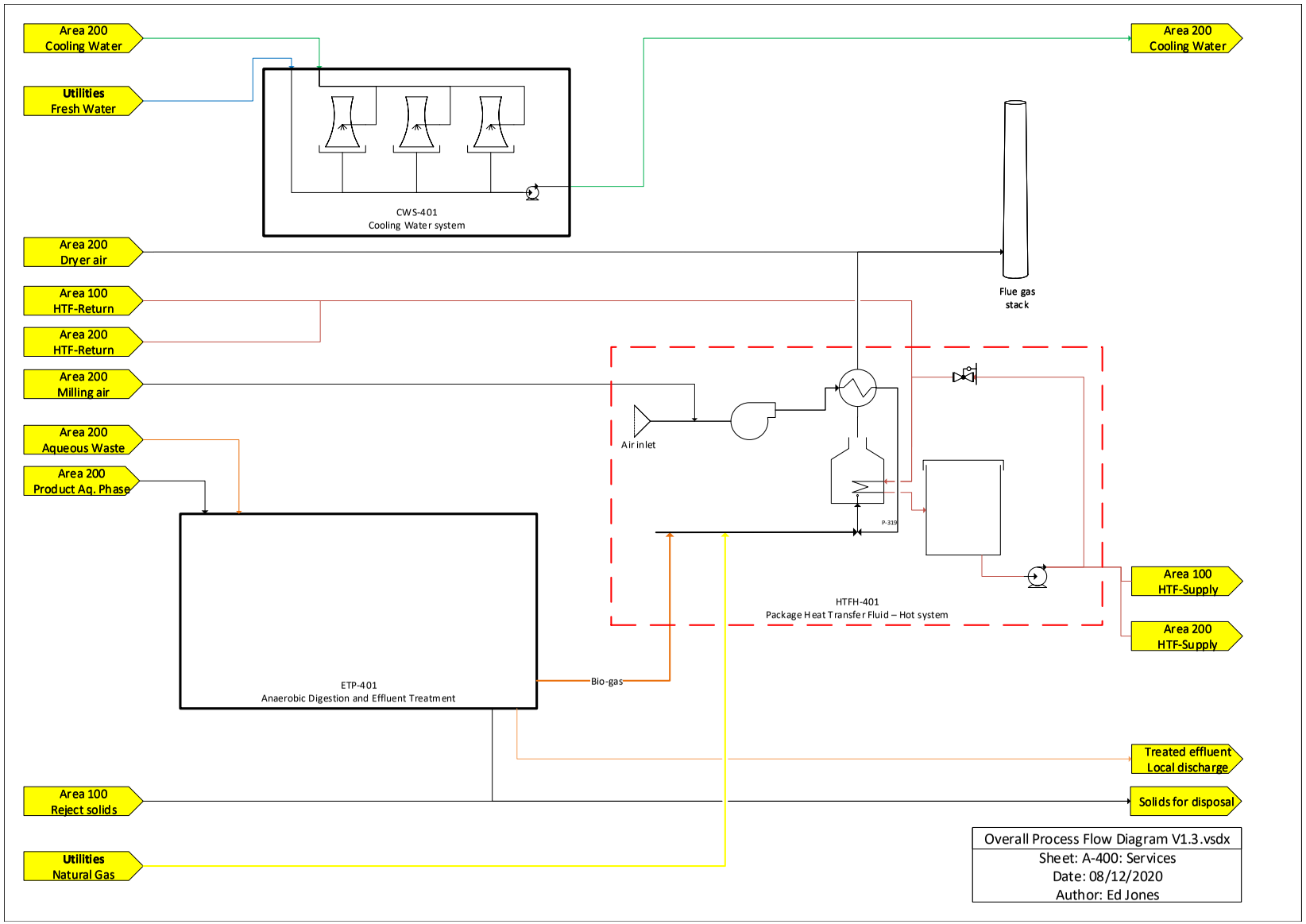

Figure 2.8: A-400: Utilities and Services Process Flow Diagram

2.3.4.1 Process Description

In the biomass receiving and pre-processing (Area-100, figure 2.6), raw macroalgal biomass is delivered to site by bulk transport. It is assumed that this biomass will still be water-wet with seawater from harvesting, and be contaminated with marine debris. A coarse pre-screening step (S-101) is included to remove the large contaminants and any hard materials that might damage downstream equipment. The screened biomass is them washed with fresh-water (vessel V-101) at a 2:1 water:biomass mass ratio, in a batch process on a 15-minute cycle. The washed biomass solids are once again separated by filtration, allowing salt, sand, silt, and fine contaminants to be washed away with the aqueous effluent. Washed and filtered biomass solids are then passed to a cutter/mill (L-101) to reduce the mean particle size to d50 $<$ 2.75mm to ensure good pumpability and homogeneity of the algal slurry. Following the biomass mill, the resulting wet-solids are partially dewatered in a continuous centrifuge (S-103) to reduce the moisture content of the biomass from approx. 90 wt. % when harvested down to 20 wt. %. Following partial dewatering, the biomass is diverted either to a live-bottom storage bin that doses the material into the HTL process feed (T-101), or the material is diverted for drying and long-term storage. Material that is sent to T-101 is fed to the HTL process immediately, whereas material sent to the rotary dryer (D-101) is dried to $<$ 15 wt. % and ensiled in storage silos (T-102a/b) for use over winter.

In the HTL Reaction and Separation section of the plant (Area-200, figure 2.7), algal solids are combined with fresh water and then pumped to approximately 200 bar by pump J-201. The high-pressure algal slurry is pumped through a series of heat exchangers (Hx-201, HX-202a and HX-202b) to recover heat from the reactor effluent stream and pre-heat the reactor feed, before passing through a final static mixer and trim-heater to bring the algal slurry to the reaction temperature. The HTL reactor is a continuous tubular plug-flow reactor, operating at 350 °C and 200 bar, as demonstrated with microalgae HTL at the Pacific Northwest National Lab (PNNL).[123, 172] The reactor is modelled as a shell and tube construction, with the reaction tube being fully surrounded by hot heating oil in the shell-side to maintain isothermal conditions

inside the reactor. Reaction products are first diverted to a gas knock-out drum (S-201) which separates the hot gaseous products, followed by a filter (S-202) to separate solid hydrochar. The remaining two fluid phases (aqueous and bio-crude) are then used to pre-heat the algal slurry, and cooled to 75 °C and separated in a two-phase separator (S-203). The bio-crude phase is then re-heated to 120 °C by cross-exchanging with the hot reactor products, in preparation for a downstream upgrading process.

Utilities and services are managed in Area-400 (figure 2.8). The carbonaceous aqueous fraction from the HTL reaction, is combined with aqueous waste from the various washing steps and is treated in a package effluent treatment plant (ETP-401). Anaerobic digestion is employed to recover carbon from the aqueous waste streams as bio-gas, which is used to partially fuel the HTF heater package. The hot heat-transfer fluid (HTF) is supplied by a package system (HTF-401), which uses natural gas to supplement the supply of bio-gas generated in the ETP-401 digesters. Treated effluent from the ETP is then discharged locally, and accumulated bio-solids are combined with solids waste generated in Area-100 for off-site disposal. Finally, the cooling water utility is maintained by a package cooling tower system (CWS-401), which both cools the return water, tops-up evaporative losses with fresh water, and pumps the water back up to supply pressure.

Details of the generation and supply of biomass is defined as out-of-scope of this work, and similarly the upgrading or conversion of the bio-crude in in a petrochemical process are also not considered. For purpose of comparison to existing processes, the functional unit of a barrel of bio-crude (bio-BBL) is defined as a volume of bio-crude equal to the standard imperial barrel (1 bbl = 42 U.S. gal $\approx 1.59\times10^{-1}$ m^3).

2.3.4.2 HTL Process Simulation in Aspen Plus

Figure 2.9 shows the process model built in Aspen Plus V10, following the design of the conceptual plant depicted in figure 2.7. The NRTL property method was used to predict properties of conventional components, and the inbuilt property methods of HCJ1BOIE, and DCOALIGT were used to estimate enthalpy and density respec-

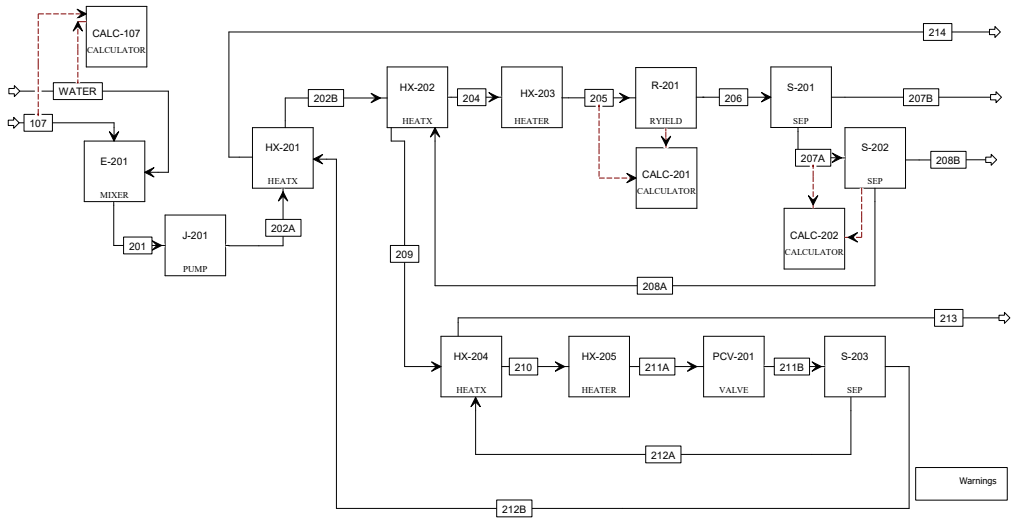

Figure 2.9: Process flow diagram of process simulation of the implementation of Area-200 in Aspen Plus V10

tively for the non-conventional components. The mass flowrate of biomass is the key independent variable, with all other flowrates and equipment sizes scaling from this. Algal biomass defined as a non-conventional solid, and the dry mass flowrate is set in stream 107 along with the biochemical proximate analysis. The carbohydrate, lipid, protein, and ash composition of the feed macroalgae is defined as a user specified property set, of the non-conventional material. Calculation block CALC-107 is then used to estimate the elemental ultimate analysis using the method described in section 2.4.2.2, and to populate the non-convention component attributes (ULTANAL, SULFANAL, PROXANAL) for the MACROALG material.

The HEATX model was used to model all heat exchangers where the process stream is used for cross exchange (HX-201, HX-202, and HX-204), whilst the HEATER model was used for heat exchangers that use either HTF or cooling-water to achieve a required temperature (HX-203 and HX-205). The SEP model of separator was used to

simulate both the gas knock-out drum (S-201) and solids filter (S-202), to ensure that product phases are cleanly separated for the purpose of heat-exchanger sizing in the heat exchanger train.

An RYield reactor block was used to model the HTL reaction, with the reaction yield being calculated in the CALC-201 calculation block. The selected reaction model identified from those discussed in section 2.4.2.4 was implemented in the Fortran77 language, and lumped product mass-yields are defined for non-conventional reaction products: HTL-OIL, HTL-AQ, HTL-CHAR, and HTL-GAS. Predicted elemental distribution of C, H, N, O, and S in each product phase was made by implementing methods described in section 2.3.3.3 into the CALC-201 calculation block, such that the lumped mass yields of the HTL-OIL, -AQ, -CHAR, and -GAS products were also assigned predicted ULTANAL, PROXANAL, and SULFANAL attributes. Enthalpy and density of the non-conventional products were again predicted with the HCJ1BOIE and DCOALIGT methods. In the case of the HTL-OIL product the predicted C, H, N, O, and S content were further used to convert to a mass distribution of conventional components as described in section 2.4.2.5. This further refinement of prediction of the HTL-OIL product to conventional components allows the powerful Aspen Simulation engine to better estimate the thermophysical and chemical interactions, and thus generate better estimates of the sizes and power requirements of key pieces of equipment.

2.3.4.3 Pre-treatment, Utilities, and Services Sizing

Sections of plant and equipment not featured in the Aspen Process simulation model (figures 2.9 and 2.7) are sized according to the total mass flow rate of macroalgae, and/or total predicted heating duty where the Aspen model provides sufficient information. Knorr et al. (2013) produced a comprehensive set of HTL plant designs for processing wood waste which includes sufficient sizing, scaling, and costing details to adapt the large supporting equipment packages as singular unit operations.[193]

2.3.4.4 Biomass Supply

The predictable supply of material to the biorefinery is critical to the operation. Previous work in microalgae HTL biorefinery modelling attempts to quantify the impact of uncertainty in certain key parameters of the biomass, such as the residual moisture in the biomass when received or the quantity of protein and lipids.[116] In most previous cases the supply of biomass is assumed to come from an industrial algal farm, where quantity and quality of the algal solids can be well predicted.[116, 121, 123]

In this work, two sources of macroalgae are considered in the process and economic model. *Sargassum spp.* is selected to represent a free-floating pelagic seaweed, the type that may be collected by the MARINER program SeaweedPaddock system.[50] *Saccharina spp.* (e.g. sugar kelp) is selected to represent a more traditionally aquacultured marine biomass, the type grown on fixed lines in fixed locations. Summarised data for each of these macroalgae species is displayed in table 2.6. Seasonal variation in the macroalgae analysis is not considered within this work, and the properties listed in table 2.6 are assumed to be constant throughout the growing season.

Cost to supply the biomass is assumed constant, however, seasonal variation in biomass availability is considered. It is assumed that farmed *Saccharina spp.* is available relatively early in the year due to the peak growth season starting in January, but *Sargassum spp.* as only available later in the year once the pelagic blooms have formed and drifted close to land.[32, 195]

2.3.5 Economic Model

The process model developed in Aspen Plus is used to specify and size the main pieces of capital expenditure equipment that make up the process flow shown in figure 2.7. The process plant simulation and associated costing is completed at a range of nominal name-plate algae capacities, ranging from 0.5 tonne/day up to 1000 tonne/day. Plant equipment installed cost (C_I) is estimated by scaling equipment prices from the literature, or by using the in-built equipment cost estimation tool in Aspen Plus. When required, the equipment cost is adjusted for scale using equation 2.41, where F_I, C_0, S,

Table 2.6: Proximate, biochemical, and ultimate analysis of macroalgae used in the Aspen model in this work. Values are taken as an average from multiple sources.

		Sargassum spp.		*Saccharina spp.*	
		Value	Refs.	Value	Refs.
Proximate					
Moisture	wt. %	90.0	Design Spec.	90.0	Design Spec.
Ash	dry wt. %	28.2	[13–15]	24.1	[16, 196]
Biochemical					
Carbohydrate	daf wt. %	80.5	[13–15]	42.5	[12]
Protein	daf wt. %	15.3	[13–15]	14.4	[12, 16]
Lipid	daf wt. %	4.6	[13–15]	2.0	[12, 16]
Ultimate					
C	daf wt. %	34.6	This work	40.1	[16, 196]
H	daf wt. %	4.9	This work	6.4	[16, 196]
O	daf wt. %	39.7	This work	48.2	[16, 196]
N	daf wt. %	1.8	This work	2.8	[16, 196]
S	daf wt. %	0.1	This work	1.1	[16, 196]
Supply					
Landed cost	US $/dry-ton	200[a]	[49, 50]	300[b]	[26, 27, 49]
Availability		Jul to Oct[c]	[32]	Mar to Jun[d]	[195]

a) Upper estimate + 10 % contingency on figures from MARINER program.

b) Average of upper estimate from MARINER program and a 4-fold improvement on price from van den Burg et al. (2016).

c) Peak bloom period observed by Wang et al. (2019) for the Great Atlantic Sargassum Belt.

d) Peak growth period for sugar kelp identified by Broch and Slagstad (2012), excluding the first 2 months of growth to allow stocks to replenish.

S_0, and sf denote installation factor, equipment cost at the base scale, new scale, base scale, and scale factor respectively.[116] Additionally all equipment costs are scaled to 2019 as the basis year using the Chemical Engineering Plant Cost Index (CEPCI) and equation 2.42 where $C_{I_{2019}}$ denotes the installed cost in 2019, C_{I_n} is the installed cost in year n, and $CePCI$ denotes the plant cost index for the equipment category being costed.[**ChemicalEngineeringPlant2020**]

$$C_I = F_I C_0 \left(\frac{S}{S_0}\right)^{sf} \tag{2.41}$$

$$C_{I_{2019}} = C_{I_n} \times \frac{CEPCI_{2019}}{CEPCI_n} \tag{2.42}$$

Net present value (NPV) analysis is carried out by way of discounted cashflow analysis, with key economic assumptions as listed in table 2.7. It is further assumed that the plant reliability will ramp up over a 6 year period that covers construction, build, commissioning, and ramp-up of the new plant. This production ramp up is captured by a budgeted overall equipment effectiveness (OEE) value, against an open run-time (T_0) of 8000 hours per year.

Table 2.7: Financial and plant reliability assumptions for the NPV and discount cashflow analysis.

Economic Assumptions			**Plant OEE**		
IRR	%	5	T_0	hrs	8000
Inflation	%	2	OEE Yr_0	%	0.00
Income Tax	%	35	OEE Yr_1	%	0.00
Project life	Yrs	30	OEE Yr_2	%	0.20
Utilities			OEE Yr_3	%	0.50
Gas Price	\$/kWh	0.05	OEE Yr_4	%	0.70
Elec Price	\$/kWh	0.10	OEE Yr_5	%	0.85
Water Price	$\$/m^3$	0.10	OEE Yr_{6+}	%	0.90

2.3.5.1 Fixed costs

Fixed costs of plant equipment purchase, installation, and construction are estimated and scaled as described above. Table 2.8 lists the costed equipment, the scaling variable used to adjust pricing, and the source of costing information.

Table 2.8: Basis of fixed costs of plant equipment in plant costing model.

Equipment No.	Equipment Description	Scale Variable	Installation Factor	Scale Factor	Costing Basis
J-201	Biomass slurry pump	Pump Feed	2.2	0.8	Knorr et al. (2013)[193]
HX-201/-202/-203/-204/-205	Heat exchangers, various	Area	2.2	0.7	Knorr et al. (2013)[193]
A-202	Static mixer	Flow	1	0.5	Knorr et al. (2013)[193]
R-201	Tubular HTL reactor	Flow / Volume	2	-	Knorr et al. (2013) and BSI 1600:1991[193, 197]
S-201	Gas knock-out drum	Volume	2	0.7	Knorr et al. (2013)[193]
S-202	Solids filter	Filter Feed	2	0.7	Knorr et al. (2013)[193]
S-203	2-phase Aq:Org separator	Separator Feed	2	0.7	Knorr et al. (2013)[193]
HTFH-401	Hot Oil Package	Duty	1.8	0.6	Knorr et al. (2013)[193]
ETP-401	Effluent Treatment Plant	Waste water flow	-	-	Ulrich and Vasudevan (2006)[198]
CWS-401	Cooling water system	Duty	-	-	Ulrich and Vasudevan (2006)[198]
V-101	Algal pre-wash tank	Volume	1	0.7	Knorr et al. (2013)[193]
M-101	Wash-tank agitator	V-101 volume	1	0.5	Knorr et al. (2013)[193]
L-101	Biomass mill	Feed Rate	1	0.8	Knorr et al. (2013)[193]
S-103	Dewatering centrifuge	Feed Rate	1	0.7	Davis et al. (2016)[121]
S-101 (and handling equipment)	Pre-treatment handling	Algal Feed	1	0.8	Knorr et al. (2013)[193]

For most equipment, the costing is scaled directly from previous HTL designs, or estimated using standard tools. The costing of the reactor (R-201) is made by scaling the unit cost of the tubular reactor in Knorr et al. (2013) as a function of the annular cross section of metal, and mapped to standard dimensional schedule XXH pipe listed in BSI 1600:1991. An ideal internal reactor diameter is computed which would maintain equal Reynolds number (Re) to that used in Knorr et al. (2013)'s work, and the next nominal pipe size above the ideal diameter is selected for the costing, and finally pipe length is determined to give a specified LHSV of 8 h^{-1}.[193, 197]

The pre-treatment section of the HTL plant (sheet A-100, figure 2.6) is sized and costed to provided 150 % of the nominal flow rate of the HTL plant (sheet A-200, figure 2.7). Providing the pre-treatment section sized at a $\frac{12}{8}$ ratio to the HTL plant allows 12-months' worth of biomass to be processed through the pre-treatment section during the 8-months where fresh biomass is available. The only exception is the rotary dryer (D-101, sheet A100, fig. 2.7) which is sized to dry 50 % of the nominal flow rate of the HTL plant, thus allowing 4-months' worth of over-winter stocks to be dried and placed into storage over the 8-months when biomass is available.

The feed handling and pre-treatment equipment (truck scales, stacker, coarse screen etc.) is lumped together as "pre-treatment" capex. In this category the mechanical equipment is only scaled for algal flow volumes above a minimum threshold. This minimum threshold represents the purchase of a single piece of equipment (e.g. 1 truck tipper) sufficient to handle the required throughput. For very low flow rates this represents a large over-specification (e.g. a 28-ton truck tipper would not be specified for a 0.5 ton/day process), however it is included as a cost since a low flow rate process would likely be managed with more manual and mechanically assisted handling compared to the automated handling equipment.

2.3.5.2 Variable costs

Variable costs considered were utilities provision (electricity, gas, water) and biomass supply. It is assumed that all heat demands are met by natural gas fired heating

operating at 100% efficiency, pumping is achieved with 90% electrical efficiency, and utilities prices are scaled yearly with an average 2 % inflation rate (table 2.7). Labour, interest and loan repayments, and marketing/transport expenses are not costed.

Drying in D-101 is achieved by counter-current convection of hot-air through a rotating drum which constantly tumbles the biomass. An air inlet temperature of 135 °C and outlet temperature of 60 °C is selected to avoid local overheating of the wet biomass. To achieve the required drying, a 5:1 mass ratio (hot-air:wet-biomass) is required to be maintained through the dryer. Assuming the hot-air is provided by direct fire heating with a natural gas process burner, the cost of provision of 5x the mass flow of partially dewatered algae to be dried is determined as simply the adiabatic sensible heat for the required mass of air, assuming an outside air temperature of 15 °C. This short-cut method negates some obvious factors such as the effect of humidity in the combustion flue gasses, however as an initial point of reference it will provide sufficient accuracy.

2.4 Results

2.4.1 Experimental Results

2.4.1.1 Biomass Properties

Experimental proximate, estimated biochemical, and elemental ultimate analysis for Spirulina and Sargassum samples are listed in table 2.9.

Moisture level of the raw algal material varied from 0.95 wt. % to 3.54, with the acid treated solids having much lower moisture levels at 0 wt. % to 0.45 wt. % for Spirulina and Sargassum respectively. For both raw and pre-treated biomass, Spirulina has a higher volatile fraction compared to Sargassum, and a lower fixed carbon fraction. This is to be expected, with a greater proportion of the macroalgal mass being dedicated to maintaining structure when compared to the single celled microalgal Spirulina. This observation is supported by the trend of the estimated carbohydrate fraction, with Sargassum having a higher fraction of carbohydrate under all conditions compared to Spirulina.

Table 2.9: Experimental CHNSO and TGA results for *Spirulina* and *Sargassum* algae for both raw and acid pre-treated biomass. Values expressed as the weight % of the whole biomass, the dry biomass (d), or the dry and ash-free fraction (df).

		Spirulina		**Sargassum sp**	
		Raw	Acid PT	Raw	Acid PT
Proximate[a]					
Moisture	wt.%	0.95	0.00	3.54	0.45
Volatile matter	wt.% (d)	92.61	92.32	86.18	81.86
Fixed carbon	wt.% (d)	0.19	4.88	3.58	15.59
Ash	wt.% (d)	7.20	2.80	10.25	2.55
Estimated Biochemical[a]					
Carbohydrate	wt.% (df)	8.02	11.64	14.11	22.10
Protein	wt.% (df)	23.34	27.55	16.22	15.35
Lipids	wt.% (df)	28.44	28.95	29.54	19.40
Elemental[b]					
C	wt.% (df)	50.67 (0.06)	50.06 (0.01)	34.64 (0.18)	46.88 (0.26)
H	wt.% (df)	7.19 (0.02)	7.25 (0.04)	4.86 (0.02)	5.83 (0.01)
N	wt.% (df)	11.69 (0.01)	11.75 (0.02)	1.83 (0.03)	3.08 (0.79)
S	wt.% (df)	2.00 (0.18)	2.38 (0.01)	< 0.1[c]	< 0.1[c]
O	wt.% (df)	27.96 (0.03)	27.04 (0.05)	39.66 (0.53)	42.35 (0.12)

a) Determined by TGA.

b) ± quoted as 95 % confidence interval about mean, n=2.

c) Below limit of detection.

However, the values of carbohydrate, protein, and lipid predicted by the equations 2.12 to 2.14 fall significantly short of typically published values (e.g. some typical values for Sargassum spp. are listed in table 2.6). The protein fraction appears a reasonable estimate (16.22 wt. % compared to a literature value of 15.33 wt. %), the carbohydrate prediction falls well short of expected values (14.11 wt. % vs. 80.5 wt. %), and the lipid fraction prediction is far greater than expected (29.54 wt. % vs. 4.6 wt. %).

Comparing the predicted values for carbohydrate, lipid, and protein in table 2.9 to the nutritional information on the packaging shows that protein is under predicted (23.34 wt. % predicted compared to 67 wt. % actual), carbohydrate falls short also (8.02 wt. % predicted compared to 18.5 wt. % actual), but lipid is over predicted (28.44 wt. % predicted compared to 1.3 wt. % actual fats). Use of the published relationships to predict the biochemical fractions from TGA data is therefore not a suitable substitute

to making specific analysis when applied to algal biomass.

The elemental analysis shows the CHNSO wt. % content of both the raw and pre-treated algal biomass. For Spirulina the acid pre-treatment appears to have had minimal impact on the partition of elements in the solid biomass. For Sargassum the acid pre-treatment has had the effect of concentrating the CHNSO elements, with all increasing when comparing acid pre-treatment to raw material. Of the individual elements, nitrogen content showed the largest relative increase of 68.4 % (1.83 wt. % to 3.08 wt. %). Oxygen showed the lowest relative increase of 6.8 % (39.66 wt. % to 42.35 wt. %), with relative increases in carbon and hydrogen concentration coming between the two.

The concentration of CHNSO elements can be partially attributed to the large reduction in ash seen for both types of biomass, with acid soluble inorganic being removed by the dilute H_2SO_4 wash. For Sargassum in particular however, the relative increase in nitrogen, along with the large increase in fixed carbon fraction, indicates that the acid treatment was removing more than just inorganics.

2.4.1.2 Pre-treatment mass balance

Acid pre-treatment of biomass is presented in figure 2.10. Total conversion of biomass from solids into hydrolysate varied from 24.7 % to 29.1 % for spirulina and sargassum species respectively, with residual solids yields of 65.2 % and 48.5 % for same. These conversions are similar to those previously observed for low-temperature acid pre-treatment of macroalgae, where acid pre-treatment of macroalgae (*Fucus serratus*) under similar conditions (2 vol. % H_2SO_4, 25 °C, 20 mins) resulted in approximately 45.5 % loss-in mass of the starting solids (54.5 % residual solids).[176] Total mass closure of the acid pre-treatment step ranged from 89.9 % to 77.5 %, resulting in between 10.1 % to 22.5 % mass lost during the acid pre-treatment process. This loss in mass is due in part to oxygen removal as water into the aqueous phase, for example the acid-catalysed dehydration of glucose to 5-HMF produces 3 molar equivalents of H_2O, or 30 % of the starting glucose mass.

The difference between total mass conversion of spirulina and sargassum through the

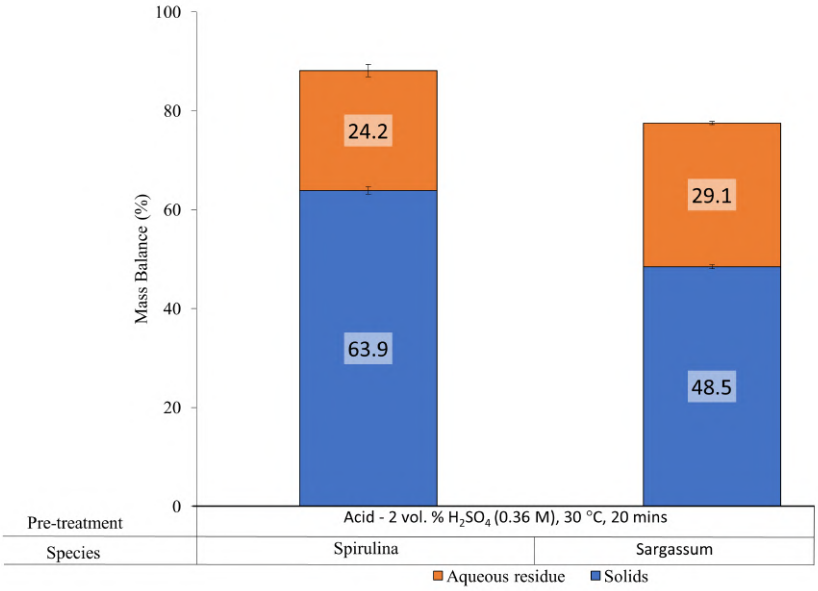

Figure 2.10: Average mass repartition summary of the acid pre-treatment for Spirulina (n=3) and Sargassum (n=2). Error bars displaying the standard error about the mean.

acid pre-treatment can be partially explained by the form of the algal mass being treated. Spirulina (and in fact, all microalgal species) exists as a micro-scale single celled organism, hence, requires no grinding to reduce its size to allow pumping or processing. Thus, when exposed to the acid pre-treatment, the majority of cell walls will be intact, and the acid pre-treatment will act mainly on the outside of the biomass. In comparison, macroalgae such as sargassum require mechanical size reduction to allow handling in process equipment, thus exposing the interior of the plant to the acid and enhancing the effect of the partial acid digest when compared to a single-celled microalgae.

2.4.1.3 Batch Hydrothermal Liquefaction

Mass yields of the four HTL product fractions for raw and pre-treated biomass are displayed in figure 2.11, for both Spirulina and Sargassum. The results of HTL on the raw Spirulina biomass fall broadly in line with previous published works, with bio-crude yield of 38.8 wt. %, aqueous residue of 12.1 wt. %, gas yield of 13.5 wt. %, and residual solids of 9.2 wt. %.[117, 146, 199] The raw sargassum HTL mass balance follows the broad trend of macroalgal HTL, with bio-crude yields typically in the tens of percent

(10.9 wt. % in this work), and solids making up the largest single fraction of mass (24.7 wt. %).[13]

For both algae, the total mass closure falls significantly short of 100 %, with 73.16 % and 59.47 % of the starting mass accounted for, for spirulina and sargassum respectively. This gap in the mass closure is typical for this HTL methodology, with the gap 20 to 40 % gap previously attributed to loss of volatiles light organics during the work-up or conversion of biomass to water.[13, 144, 176]

The effect of the acid pre-treatment is significant. With both algae, both the biocrude and the gas mass yields increased for acid treated biomass compared to the raw biomass. The spirulina biocrude yield increased by 12 % (from 38.3 wt. % to 43.0 wt. %), and sargassum biocrude a more modest increase in yield of 2.8 % (10.9 wt. % to 11.2 wt. %). Similarly, the gaseous phase yield increases were 25.9 % and 19.1 % for spirulina and sargassum respectively. However, the effect on both the aqueous phase and the solids residue was opposite for the two algae. There was a 93.4 % increase in aqueous products for the spirulina biomass, compared to an 82.8 % decrease for the sargassum. Conversely, for the solids there was a 62.0 % decrease in yield for the spirulina, but a 48.2 % increase for sargassum. The overall mass closure in both cases increased, with a higher proportion of the starting mass (relative to solids loaded into HTL reactor) being accounted for after the reaction. This suggests that acid pre-treatment results in lower production of volatiles and thus, loss of volatiles during work-up.

For the production of a biocrude product, the acid pre-treatment may initially seem like an attractive option. However, once the mass yield in the pre-treatment step is accounted for, the overall process yield of biocrude drops to 27.8 wt. % and 5.1 wt. % with respect to the starting biomass (prior to pre-treatment) for spirulina and sargassum respectively. Figure 2.12 shows the total mass balance relative to the starting mass prior to pre-treatment, and highlights the big impact on total process yield the pre-treatment has had. By including pre-treatment prior to HTL, the total mass loss through loss of volatiles or transfer losses rises to 16.6 % and 39.3 % of the total starting mass for spirulina and sargassum respectively. Again, this highlights the large difference

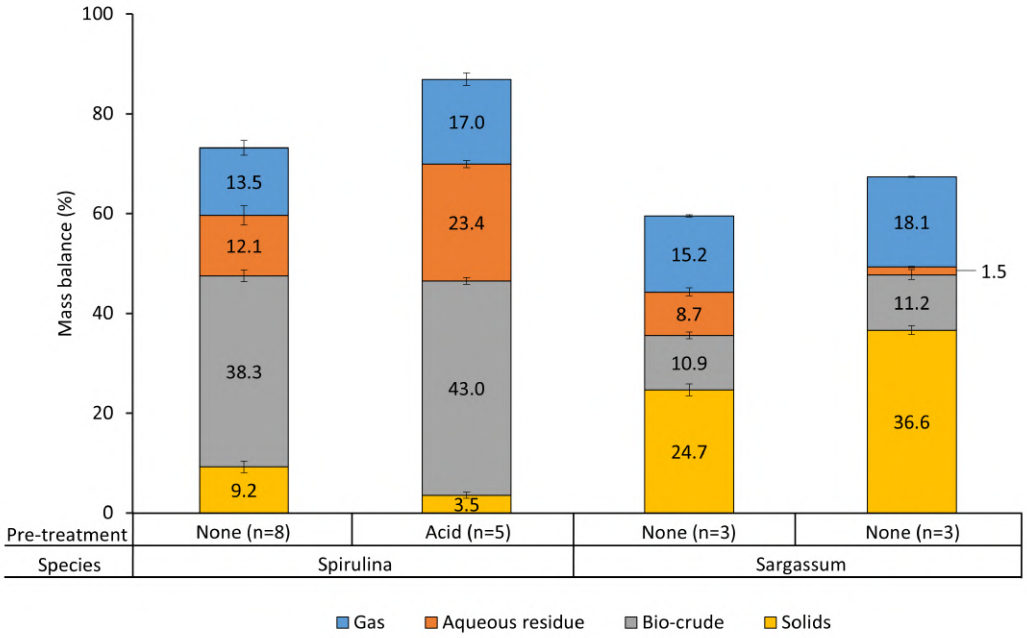

Figure 2.11: Mass repartition summary of HTL reactions for Spirulina and Sargassum species in air atmosphere. wt. % is expressed relative to the mass of algae loaded to the HTL reactor, not to the starting mass prior to pre-treatment. Error bars displaying the standard error about the mean, number of replicates quoted in the figure.

in behaviour between a single celled microalgae and a mechanically milled macroalgae when exposed to chemical and thermochemical treatments.

2.4.1.4 Influence of head-space gas

Reactor filling, ullage gas, and biomass loading were also briefly investigated using the spirulina biomass. Average mass yields of different reaction conditions are listed in table 2.10.

Exchanging the head-space gas for nitrogen has a minor effect on the bio-crude yield (approx. 1 % increase), however a marked decrease in the total generation of solids (9.19 wt. % to 4.62 wt. %), increase in aqueous phase (12.13 wt. % to 30.33 wt. %), and a minor decrease in gas yield (13.53 wt. % to 12.87 wt. %). Additionally, removal of a reactor oxygen atmosphere has had the effect of closing the overall mass balance, with the total mass closure increasing from 73.15 wt. % to 87.06 wt. % for air and nitrogen

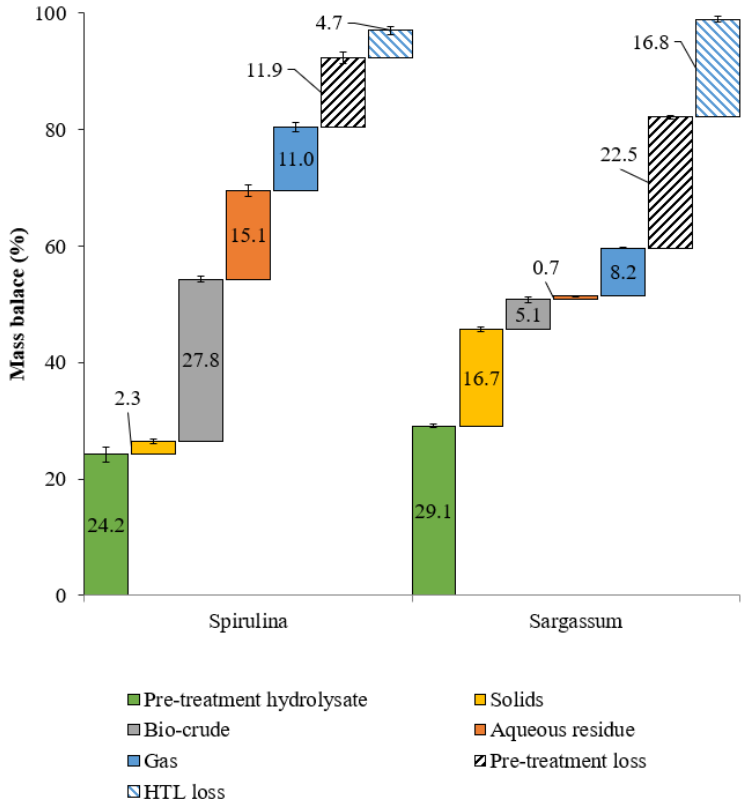

Figure 2.12: Total mass repartition of acid pre-treatment and HTL reactions for Spirulina and Sargassum species in air atmosphere, relative to starting biomass. wt. % is expressed relative to the mass of algae loaded to the HTL reactor, not to the starting mass prior to pre-treatment. Error bars displaying the standard error about the mean.

headspaces respectively.

A similar trend can be seen when increasing the filling of the reactor but maintaining the original air headspace gas. The change in biocrude yield remains less than 1 wt. %, but there is a significant decrease in solids (9.18 wt. % to 7.324 wt. %), an increase in aqueous fraction (12.13 wt. % to 23.52 wt. %), and a closure of the mass loss also. The scale of the difference is smaller than the effected noted when fully exchanging the head-space gas for nitrogen, but overall observed trend is identical. Controlling the availability of reactive oxygen is therefore a critical when considering running a plant scale HTL process.

Mass loading of solids is also significant, with biocrude yield increasing by 10 wt. % when

Table 2.10: Summary of HTL product yields with varying reactor filling and headspace gas.

Reactor set-up					
Headspace gas		Air	N_2	Air	Air
Total Reactor Charge	g	18	18	36	21
Estimated reactor filling	% vol.	36	36	72	42
Biomass loading	% wt.	17	17	17	29
HTL yields					
Bio-crude	% wt.	38.3	39.2	37.5	48.7
Solids	% wt.	9.2	4.6	7.3	6.4
Aqueous	% wt.	12.1	30.3	23.5	18.8
Aq. phase solids conc. [a]	% solids	4.7	5.7	5.6	8.8
Gas	% wt.	13.5	12.9	10.6	12.5
Mass loss	% wt.	26.9	12.9	21.0	13.6

a) Mass concentration of solids in total mass of recovered aq. phase

doubling the mass charge of biomass from 3 g to 6 g, but maintaining the same total quantity of water. This additional biomass has a minor volume filling effect, thus there is the effect of a slightly smaller quantity of reactive head-space gasses as previously discussed. However, the increase in biocrude yield is significantly different compared to previous experiments.

The generally understood mechanism for product formation in the HTL reaction starts with depolymerisation of starting biomass into the aqueous phase. From here the intermediates either undergo further breakdown into CO_2 and other light products found in the gas phase, are stabilized as relatively short polar species (e.g. carboxylic acids and alcohols) and remain in the aqueous phase, polymerize into heavier oxygenated hydrocarbons that phase separate from the aqueous fraction, or polymerize further into a solid char or coke like product.

Increasing the mass-loading of biomass in this case appears to have selectively driven a higher proportion of mass into the organic biocrude phase, whilst decreasing the production of solids, and having a minor effect on the yield of gasses. The increase in starting biomass inevitably increases the concentration of depolymerised fragments of

biomass in the aqueous reaction mixture during reaction, thus this selective increase in driving towards biocrude hints that the biocrude product is favoured over the gaseous and solids for the overall reaction equilibrium.

2.4.1.5 Properties of biocrude

Key properties of the biocrudes are listed in table 2.11, along with some typical values of the same properties for fossil crudes. Higher heating value (HHV) of the oils is estimated by the commonly employed Boie correlation, using the CHNSO values as parameters.[114]

Table 2.11: Experimental biocrude properties and typical fossil crude properties for comparison. Values expressed as the weight % of the dry fraction (d), or as the dry and ash-free fraction (df).

		Spirulina		**Sargassum sp**	**Fossil crude**
		Raw	Acid PT		
Proximate[a]					
Moisture	wt. %	4.3	5.5	0.6	-
Volatile matter	wt. % (d)	82.4	79.6	71.6	89.3[b]
Residue above 550 °C	wt. % (d)	19.0	21.0	29.2	10.7[b]
Ash	wt. % (d)	1.2	5.9	10.4	-
Elemental					
C	wt. % (df)	67.48	63.87	72.72	84.45[c]
H	wt. % (df)	8.33	8.02	8.38	13.59[c]
N	wt. % (df)	7.51	6.19	3.33	0.099[b]
S	wt. % (df)	2.26	1.75	1.58	0.151[b]
O	wt. % (df)	8.28	7.48	12.07	0.92[c]
C/H (atomic ratio)		0.68	0.67	0.73	0.52[c]
HHV[d]	MJ/kg	34.68	35.01	38.13	45.06[c]

a) Determined by TGA. Moisture determined at 100 °C, volatiles determined as residual mass under argon at 800 °C.

b) From BP Azeri Ceyhan 2017 sample assay.[163]

c) Taken as average of values reported by Gawel et al. (2014).[158]

d) Determined by Boie correlation.[114]

Key differences between the spirulina and sargassum biocrudes is the total volatility, with the sargassum having lower total volatile matter and a corresponding higher residue at 550 °C. Of the elemental composition the sargassum bio-oil has a higher carbon fraction than both raw and acid treated spirulina, similar hydrogen, but lower nitrogen

and sulfur. The lower nitrogen content is likely a result of the lower protein level of sargassum (approx. 15 %, table 2.6) compared to spirulina (approx. 67 %).

Sargassum biocrude is however much more highly oxygenated compared to spirulina. Presence of this additional oxygen is likely due to the higher proportion of carbohydrate in the starting sargassum compared to spirulina, and its presence in larger quantities acting as a potential cross-linking site for polymerisation between species in the biocrude could partly explain the lower total volatile fraction of sargassum biocrude compared to spirulina.

Comparing the algal biocrudes to the fossil crude gives the first clues about how the biocrude may be processed within a traditional petro refinery. The algal biocrudes all have a lower volatile fraction and corresponding higher heavy residue compared to the fossil crude. The lower carbon and hydrogen content of algal crudes is mostly a result of the high quantity of heteroatoms (N,S, and O) which, although present in fossil crude, are found at orders of magnitude lower concentrations.

The C/H atomic ratio is lower in the fossil crude, meaning comparatively the carbon atoms are more likely to be saturated. Conversely, the higher C/H atomic ratio in the algal biocrudes means there are effectively fewer hydrogen atoms per carbon atom on average, meaning there must be a lower degree of bond saturation, in addition to the inclusion of high heteroatom content.

2.4.1.6 Boiling behaviour of biocrudes

The estimated boiling curve for the biocrudes is determined by TGA, and plotting the % mass lost as a function of furnace temperature (see figure 2.13). At temperatures below about 250 °C the boiling behaviour of spirulina biocrude follows that of the fossil crude exactly, with divergence in the 300 °C to 500 °C boiling range. The sargassum biocrude boiling curve however shows a much lower light-volatile fraction, with the boiling curve not really starting to gain gradient until well above 100 °C. Thereafter however, the gradient of the boiling curve broadly follows the spirulina biocrudes and fossil crude, indicating that other than a lack of light-end components the remaining

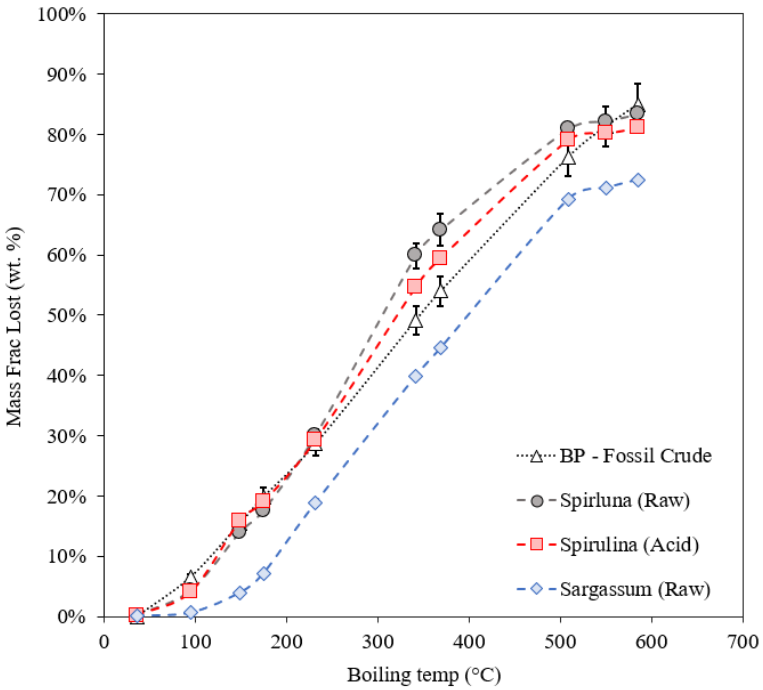

Figure 2.13: Estimated boiling curves of algal biocrudes compared to an average fossil crude. The "BP-Fossil Crude" is determined as a blended average of published assays for various BP crudes, excluding light and condensate petroleum sources. A blended mean average product was chosen to represent a mid-point, and allow the upper and lower bounds to be considered. Error bars plotted at 95 % CI. [163]

components are present in the expected ratios.

Expected total mass yield of each common petroleum fraction is determined as the total mass evaporated within that boiling range, and plotted on figure 2.14 for the raw spirulina biocrude and the BP Azeri Ceyhan crude assay.[163] This plot shows just how closely the spirulina biocrude boiling behaviour appears to match the Azeri Ceyhan crude, with the biggest deviations being the fraction of light gas-oil (spirulina produces more), and the light vacuum gas-oil (spirulina produces less).

It is likely therefore that a small quantity of algal biocrude could be successfully blended with a petroleum crude, and treated in existing the refinery with minor modifications. However, key concerns with applications of biocrude would be the presence of catalyst poisons and heteroatoms. Light hydrogenation or hydrodeoxygenation make be employed on the biocrudes prior to blending, which would have the effect of reducing

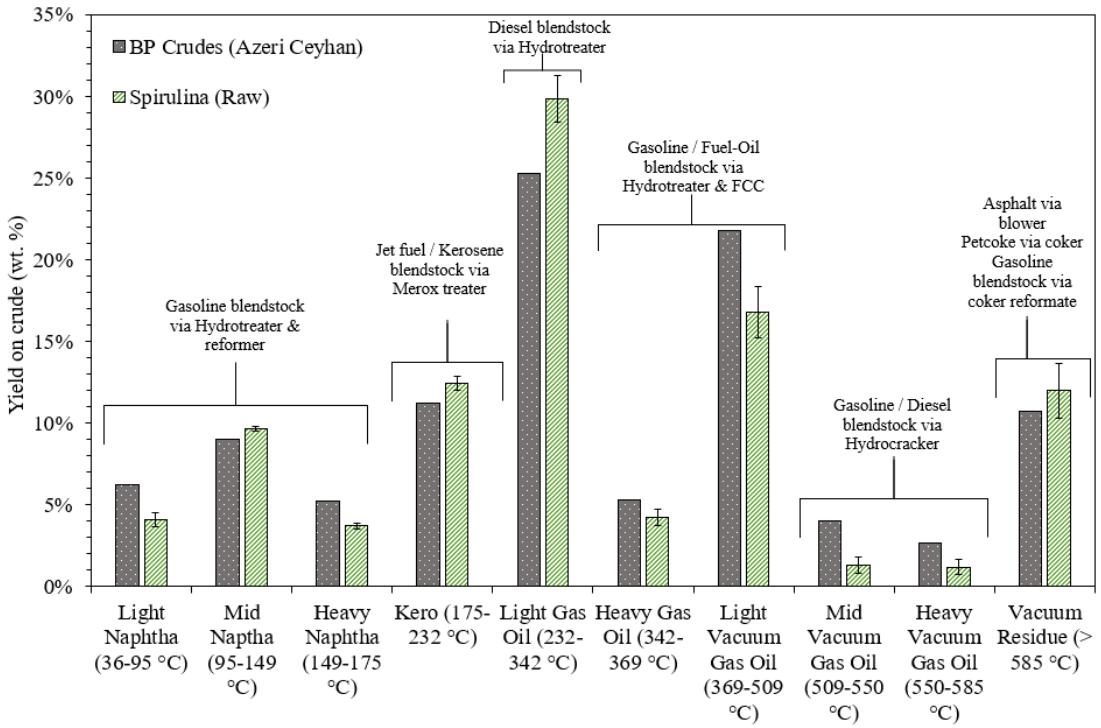

Figure 2.14: Estimated yields for petroleum fractions for spirulina biocrude and BP Azeri Ceyhan fossil crude. Quoted temperature range for each fraction is the approximate boiling range. Typical products and downstream processes employed for each petro fraction are labelled. [163]

the heteroatom content, and lowering the C/H atomic ratio - changes that reduce the chance of catalyst damage, and shift the atomic composition of the algal oil closer to petroleum crude.

2.4.2 Modelling Results

2.4.2.1 Biochemical and Ultimate analysis predictive model

Achieving an overall elemental balance of the HTL products is reliant on accurate prediction of the C, H, N, and O wt. % of the various product fractions. Jiang et al. used a multi-regression model to fit parameters to predict the distribution of C, H, N, and O elements from the microalgae biomass to the HTL products, thus allowing both an assessment of the HTL product quality, as well as achieving closure of the elemental balance. [116]

Li et al. developed a similar model for the prediction of the elemental composition of HTL products, as well as total product mass yield based on the mass distribution of biochemical proximate analysis (carbohydrate, protein, lipid), which itself was built on the original multi-component additive (MCA) HTL product yield prediction work of Biller & Ross.[115, 117] Combining Jiang and Li's models requires knowledge of both the biochemical proximate (carbohydrate, protein, lipid, ash), and the ultimate elemental (C, H, N, and O) analysis of the biomass, as well as experimental HTL results for the given biomass.

In many cases, authors have managed to fit model parameters for their own experimental set up, having designed their experiment to give them their required dataset. Or, authors have managed to pool experimental results from multiple independent studies to produce reasonable correlations.[114, 200–202] In the case of macroalgal HTL however, there is a dearth of published experimental data in comparison to using microalgal biomass. Previous attempts to use simple MCA models to predict macroalgal HTL product yields have shown poor fit, with relatively small datasets being a key contributory factor when trying to re-fit empirical factors. [13]

Limiting the source of data to just those experimental publications that include all required experimental data leaves a relatively small sample size, thus in this work Jiang's elemental content prediction model is adapted to both predict the C, H, N, and O content of a biomass from a given biochemical proximate analysis (carbohydrate, protein, and lipid content), but also the inverse operation, prediction of the proximate analysis from a given C, H, N, and O.

2.4.2.2 Predicting Ultimate Analysis from Biochemical Proximate

Figure 2.15a shows the correlation between the experimentally reported data for C, H, N, and O dry wt. % against the predicted values determined using methods described by equations 2.15 to 2.17, and $a_{i,j}$ parameters in table 2.12. The correlation of the data is good, with an R^2 of 0.956, and a least-squares line of regression slope of 0.918 ($\pm$ 0.032). The sum-squared error (SSE) gives a mean residual error of 4.9 wt. % compared

to the experimental result, however from observing the chart it is apparent that the bulk of the residuals are resultant from the prediction of carbon and oxygen.

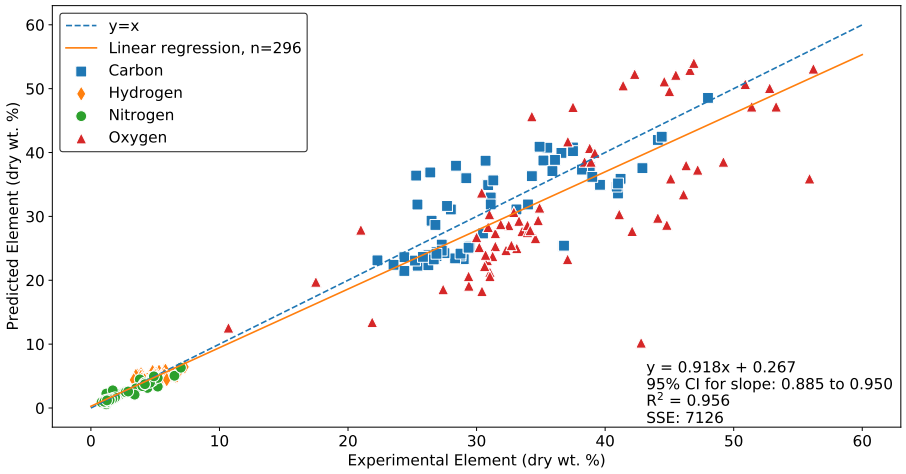

(a)

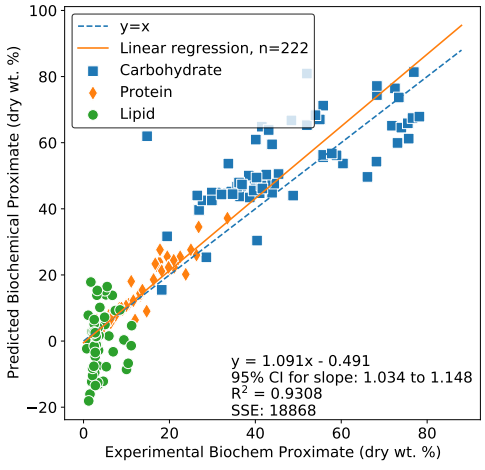

(b)

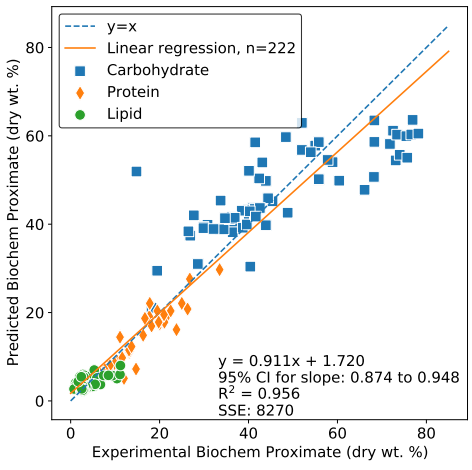

(c)

Figure 2.15: Experimental vs. predicted values with the linear multi-component additive models for **a)** carbon, hydrogen, nitrogen, and oxygen dry wt. %, **b)** carbohydrate, protein, and lipid using the inverse matrix approach of section 2.4.2.3, and **c)** same parameters as figure b) but re-plotting parameters as per equations 2.22

Table 2.12: Fitted parameters for use in estimation of elemental ultimate analysis (C, H, O, N wt. %) from biochemical proximate, using equations 2.15 to 2.18.

$a_{i,j}$	M_C	M_H	M_N	M_O
x_{Carb}	0.2890	0.0175	(-)[a]	0.6907
x_{Lipd}	0.7040	0.1175	(-)[a]	(-)[a]
x_{Prot}	0.6273	0.0316	0.1906	(-)[a]
b_i	7.3532	3.3140	(-)[a]	(-)[a]

a) Fitted parameters with p-values > 0.05 were discarded from the model. Details of significance values can be found in table A1.

2.4.2.3 Predicting Biochemical Proximate Analysis from Ultimate

Figure 2.15b shows the correlation between experimental and predicted values of carbohydrate, protein, and lipid using the inverse matrix method (equations 2.19 to 2.21) and $a_{i,j}$ parameters from table 2.12. Figure 2.15c shows the same correlation but using the newly computed set of $a'_{i,j}$ parameters listed in table 2.13. In both cases, the bulk prediction (sum of all biochemical components) results in a good correlation (R^2 of 0.931 and 0.956 for inverse matrix and $a'_{i,j}$ methods respectively), with slopes of linear regression close to 1 (1.091 $\pm$ 0.057, and 0.911 $\pm$ 0.037). Comparing figure 2.15b to 2.15c, in both cases the correlation of protein (orange diamonds) is very good, carbohydrate (blue squares) is moderate, but lipid (green circles) differs greatly. The inverse matrix method (fig. 2.15b) results in a large error in predicted lipid dry wt. % compared to the experimental value, with predicted values of lipids ranging from -20 % to +20 %. The plot of values determined with the newly computed $a'_{i,j}$ parameters shows a much lower error in the predicted lipid content, a visual observation that is supported by the reduced SSE for the $a'_{i,j}$ method compared to the inverse matrix method.

The large errors observed in the lipid prediction by the inverse matrix method are likely due to the relative size of the wt. % fractions of the biochemical components in the biomass, and the resulting influence the wt. % of each fraction has when generating the initial $a_{i,j}$ parameters listed in table 2.12. From table 2.12, it is seen that the estimated nitrogen and oxygen content is predicted by the wt. % content of a single

biochemical species (protein and carbohydrate respectively), whereas carbon and hydrogen content is predicted by all biochemical components. Therefore, when inverting the matrix described by $a_{i,j}$ parameters in table 2.12 to predict the biochemical content from a known C, H, N, and O content, the predicted protein and carbohydrate content will be *strongly* influenced by the N and O content respectively, and the effect of N and O is *unique* to protein and carbohydrate prediction. The predicted value of lipid has *no* unique relationship with any of the C, H, N, and O predictors, and in fact shares its predictors completely with carbohydrate and protein. Thus, it stands to reason that when generating the initial $a_{i,j}$ matrix, the influence of the larger biochemical wt. % fractions (carbohydrate and protein) were more dominant, and the total contribution of lipid in predicted C, H, N, O is relatively small given that actual lipid content is often an order of magnitude lower than either carbohydrate or protein. Further evidence of this can be found in figure 2.15b, where visually it can be seen that the absolute magnitude of the lipid prediction error appears larger for lower values of experimental lipid content.

With the prior knowledge that lipid content is highly correlated to overall biocrude yields, the newly generated $a'_{i,j}$ is selected as the more appropriate predictor tool since it results in a lower SSE overall, as well as much lower error in the lipid prediction specifically.

Table 2.13: Fitted parameters for use in estimation of biochemical proximate analysis (carbohydrate, lipid, protein) from elemental ultimate analysis (C, H, O, N wt. %), using equation 2.22.

$a'_{i,j}$	x_{Carb}	x_{Prot}	x_{Lipd}
M_C	0.3915	(-)[a]	0.0627
M_H	(-)[a]	(-)[a]	(-)[a]
M_N	(-)[a]	4.2444	0.7146
M_O	0.9479	(-)[a]	(-)[a]
b_j	(-)[a]	(-)[a]	(-)[a]

a) Fitted parameters with p-values > 0.05 were discarded from the model. Details of significance values can be found in table A2.

2.4.2.4 Quantitative HTL Product Yield Models

119 experimental records of hydrothermal liquefaction of macroalgae were gathered from the literature, and where missing the biochemical proximate data was estimated from the C, H, N, and O data provided, using methods previously described. k_{BC} parameters for methods described by equations 2.24, 2.25, and 2.26 (hereafter referred to as method 1, 2, and 3 respectively), and kinetic methods both without and with char (hereafter methods 4 and 5) are determined by case resampling with replacement. 10 experimental cases (approximately $\sqrt{119}$) are randomly sampled for a total of 100 resamples, computing the optimal k_{BC} parameters for each sub-sample of 10, and summarising individual k values for each sample as an average k_{BC} for all samples. This resampling strategy helps to mitigate the effect of any experimental outliers by only computing each sample k_{BC} from a subset of the total dataset, and results in each individual experimental record of the original 119 being sampled an average of 8.4 times.

Methods for predicting HTL biocrude yield described in section 2.3.3.2 are compared in figure 2.16. R^2 and SSE are calculated as a mean value for each author method for each resampling, with error bars at 95 % confidence intervals. Comparing the different methods for predicting biocrude yield, methods 3, 4, and 5 (described by equation 2.26) appear to give a better overall correlation, with R_2 values exceeding the highest out of the published model parameters (table 2.3). Between methods 3, 4, and 5 there is very little difference when comparing the correlation coefficient, however when checking the total error (SSE) for each model method 3 stands out as the best performer. This is somewhat surprising, as models 4 and 5 were included in the comparison in an attempt to give more mathematical dimensions to the solver (time and temperature) and hence allow a better overall fit to the experimental data. The Jones_3 method however is a simpler linear-additive model, and hence much simpler to implement into later process modelling sheets.

Fixed fraction coefficients determined by in this work are listed in table 2.14. The values of k_{BC} determined in this work fit in with the broad trends of literature val-

ues such as those listed in table 2.3. The fractional contribution of lipids ($k_{BC,L}$) to the overall biocrude yield was found to be the highest, followed by the protein ($k_{BC,P}$), with the carbohydrate fraction ($k_{BC,C}$) contributing the least. There is however some deviation with the interaction parameter. Teri et al. (2014) found that the lipid and protein interaction term had a net positive effect on the biocrude yield, with the lipid/carbohydrate and protein/carbohydrate terms having minor negative effects on the overall yield.[186] Lu et al. (2018) found no contribution to the overall model for the lipid/carbohydrate and lipid/protein interactions, with only a very minor contribution from the protein/carbohydrate interaction.[187] Finally, Sheng et al. (2018) found a small contribution from both lipid/carbohydrate and lipid/protein towards the yield, and a minor effect from protein/carbohydrate interactions.[188] In this work the lipid/carbohydrate interaction appears to be the most dominant, with an overall larger effect on the yield than the protein or carbohydrate fractions individually. Additionally, both the lipid/protein and the protein/carbohydrate interactions appear to have slight negative impacts on the total biocrude yield.

Figure 2.17 shows the scatter plot of predicted biocrude yield verses the experimental biocrude yields. Although method 3 has the best overall correlation and lowest overall root mean squared error (RMSE) of residuals for the methods tested in this work, visually the strength of correlation is not particularly strong, with significant residuals still present and not explained by this model.

Table 2.14: Fixed fraction coefficients ($k_{BC,j}$) determined in this work by least-squares regression fitting to published experimental results.

Method	Model Eq.	Parameters						R^2	RMSE[a]
		$k_{BC,L}$	$k_{BC,P}$	$k_{BC,C}$	$k_{BC,LC}$	$k_{BC,LP}$	$k_{BC,PC}$		
Jones_1	2.24	1.165	0.133	0.200	-	-	-	0.29	41.3
Jones_2	2.25	0.950	0.325	0.124	0.019	-0.022	-0.001	0.35	40.2
Jones_3	2.26	1.309	0.469	0.131	0.528	-0.011	-0.159	0.40	35.1

a) Root-mean square error for difference between predicted and experimental values.

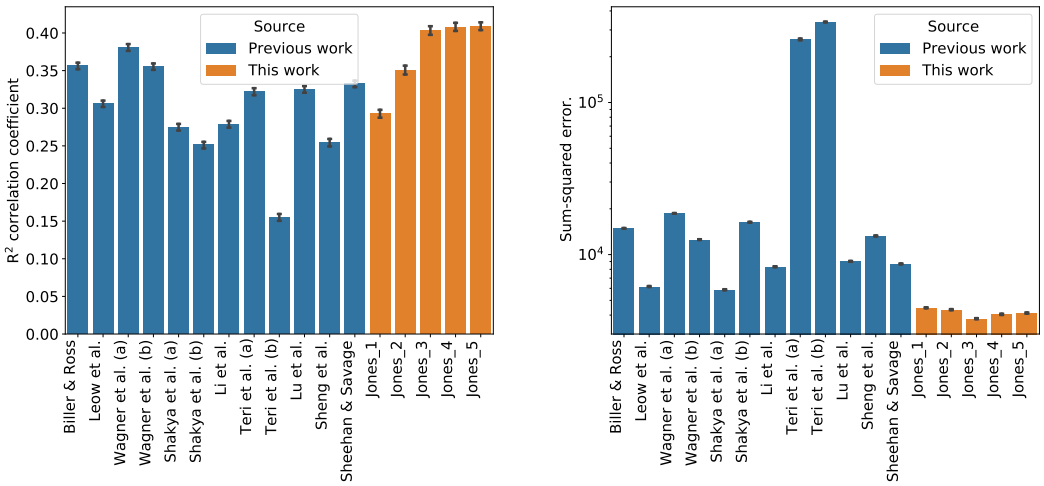

(a) **(b)**

Figure 2.16: a) R^2 correlation coefficient between predicted and experimental biocrude yields, for various HTL biocrude yield models in the literature and determined in this work, and **b)** the sum-squared error (SSE) of residuals between experimental and predicted biocrude yields for each model.

2.4.2.5 Approximation of Bio-crude components

Determination of a predicted CHONS content of the bio-crude product allows reasonable estimation of HHV and boiling-point. However, accurate modelling of the thermophysical properties of the mixed product is key to obtaining robust equipment sizing estimates when performing cost analysis on a plant-scale.

Relative abundance and simple chemical properties (molecular weight, formula) of 15 of the most common conventional products commonly identified in bio-crude produce by HTL of micro- and macro-algae were tabulated (see table 2.15). A synthetic bio-crude blend is defined by adjusting the wt. % of conventional components required to give a CHONS distribution identical to that predicted by the method described in section 2.3.3.3. This was achieved in the open source spreadsheet program LibrOffice Calc (version 6.0.7.3), using the built in Swarm Non-Linear Solver tool.

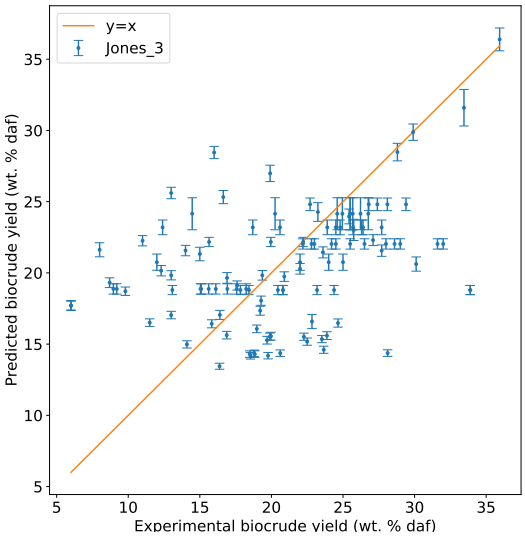

Figure 2.17: Scatter plot of predicted biocrude yield vs. the experimental biocrude yields for model 3 (described by Eq. 2.26) using parameters listed in table 2.14. Error bars show the effect of the 95 % confidence interval in each individual k_{BC} determined by the resampling strategy.

Table 2.15: Conventional compounds commonly identified in HTL bio-oils of algaes and macroalgaes, and their relative abundance when found.

Aspen ID	Compound Name	CAS Number	Formula	Molecular Weight	Relative abundance by reference (%) [a]				
					Jones et al. [123]	Xu et al. [203]	Li et al. [204]	Anastasakis and Ross [144]	Zhou et al. [160]
BC01	Palmitic acid (Hexadecanoic acid)	57-10-3	C16H32O2	256.42	10.18676	10.1443		23.9234	25.7263
BC02	Oleic acid	112-80-1	C18H34O2	282.5	1.69779			14.3541	17.1684
BC03	p-Cresol	106-44-5	C7H8O	108.14	5.09338	4.0276		4.7847	
BC04	Phenol	108-95-2	C6H6O	94.11		6.2460		9.5694	1.5512
BC05[b]	2,3-Dimethyl-2-cyclopenten-1-one	1121-05-7	C7H10O	110.15		6.2460		4.7847	5.1006
BC06	2-Methyl-2-cyclopenten-1-one	1120-73-6	C6H8O	96.13		4.8460		3.3493	6.8884
BC07	3-Methyl-2-cyclopenten-1-one	2758-18-1	C6H8O	96.13		4.5445		3.8278	5.4161
BC08	Ethyl alcohol	64-17-5	C2H6O	46.07			22.4595		
BC09	1-ethyl-2-pyrrolidinone	2687-91-4	C6H11NO	113.16	6.79117				
BC10	Myristamide (C14 amide)	638-58-4	C14H29NO	227.39	3.39559				
BC11	Tetradecanoic acid, Myristic acid	544-63-8	C14H28O2	228.37				14.3541	
BC12	Indole	120-72-9	C8H7N	117.15	5.09338				1.7484
BC13[c]	2,5-Octadiene	13643-08-8	C8H14	110.2			23.0270		
BC14	Phenol, 4-ethyl-	123-07-9	C8H10O	122.16	5.09338			4.7847	
BC15	N-methylthiopyrrolidone	10441-57-3	C5H9NS	115.2	1.02567				

a) Relative abundance calculated as a relative % of each compound in each publicartions base units. b) Compound substituted in Aspen with 2,4-dimethyl-2-cyclopenten-1-one (CAS: 999924-95-7). c) Compound substituted in Aspen with 2,4-Octadiene (CAS: 13643-08-8).

2.4.2.6 Predicted Plant Scale HTL Results

Given the input data listed in table 2.6, HTL reaction yield model parameters in table 2.14, and various predictive models for estimating bio-crude properties described in section 2.3.3.3, the summary of predicted outputs from the plant-scale HTL process is summarised in table 2.16.

Table 2.16: Predicted HTL Biocrude mass yield and properties for plant scale HTL process of *Sargassum spp.* and *Saccharina spp.*, and experimental results from earlier for comparison.

		Model results		**Exp. results**
		Sargassum spp	*Saccharina spp*	*Sargassum*
Yield Biocrude	wt. % (df)	23.2	12.6	10.9
AOS_C[a]		0.19	0.10	-
Elemental				
C	wt. % (df)	67.0	67.7	72.7
H	wt. % (df)	7.7	7.9	8.4
O	wt. % (df)	5.5	3.0	12.1
N	wt. % (df)	1.4	1.3	3.3
S	wt. % (df)	0.2	0.2	1.6
C/H (atomic ratio)		0.73	0.72	0.73
HHV[b]	MJ/kg	31.59	32.35	38.13

a) AOS_C = Average oxidation state of carbon in the feedstock, determined by equation 2.39

b) Determined by Boie correlation.[114]

For both modelled seaweeds, the predicted biocrude yield is higher than the experimental yield of Sargassum biocrude, however in the case of Saccharina it is very close (12.6 wt. % compared to 10.9 wt. %). Predicted elemental analysis shows broadly close alignment with the experimental values determined for Sargassum, albeit predicted values are lower than experimental for all elements. Whilst the absolute difference between predicted and experimental seems small, the relative error for predicted heteroatom content stands out however. Each individual predicted value of O, N, and S is less than half of the experimental value, which as discussed earlier is potentially highly significant for downstream upgrading operations.

Given how close the predicted elemental composition of both seaweed biocrudes is, the

methods described in section 2.4.2.5 to convert an elemental C, H, N, O, and S content into a wt. % distribution of conventional components is performed only once and used for both seaweeds.

2.4.3 Financial Modelling Results - Net Present Value

Total estimated build cost of the plant equipment is shown for a range of dry feed tonnages in figure 2.18a. Estimated equipment build cost increases from $ 1.3M for a 0.5 ton/day process to $ 37.3M for the 1000 ton/day process. The four order of magnitude jump in feed tonnage from 0.5 ton/day to 1000 ton/day is achieved with only a single order of magnitude increase in the total equipment installation cost. This is further highlighted in figure 2.18b, where the plant specific build cost (k$ per ton/day) is plotted against dry macroalgal feed rate. Figure 2.18b shows a rapid decrease in specific build costs as plant scale increases, dropping from $ 2,522k per ton/day for a small scale plant, to $ 37k per ton/day for the large scale.

Individual equipment contributions to the plant cost are plotted in figure 2.18c. On the whole the scaling relationship for major plant items shows the same general trend, with a straight line increase in gradient on a log-log plot of equipment cost and plant feed rate. However, some notable exceptions have been re-drawn on figure 2.18d. The process main slurry pump (J-201) has the steepest gradient of all plant equipment, starting as the third cheapest piece of equipment (of 11 costed) at the small scale (circa $10k at 0.5 ton/day) to joint fourth most expensive at the large scale (circa $3M at 1000 ton/day). The tubular reactor (R-201) initially scales in the same linear fashion until a significant price-break when jumping from 50 ton/day to 100 ton/day. This price break is due to the different reactor diameter required to maintain the required flow conditions (constant Re for all scales). When jumping from 50 ton/day to 100 ton/day the diameter of the ideal reactor increases enough to jump up from 0.75" nominal to 1.5" nominal, with a corresponding 3x reduction in total reactor length to maintain the 8 h^{-1} LHSV specified. Whilst the pricing of a unit length of 1.5" XXH steel pipe is greater, the large reduction in total required length more than offsets this. Pre-treatment and handling equipment costs have been briefly discussed already, with the total spend at

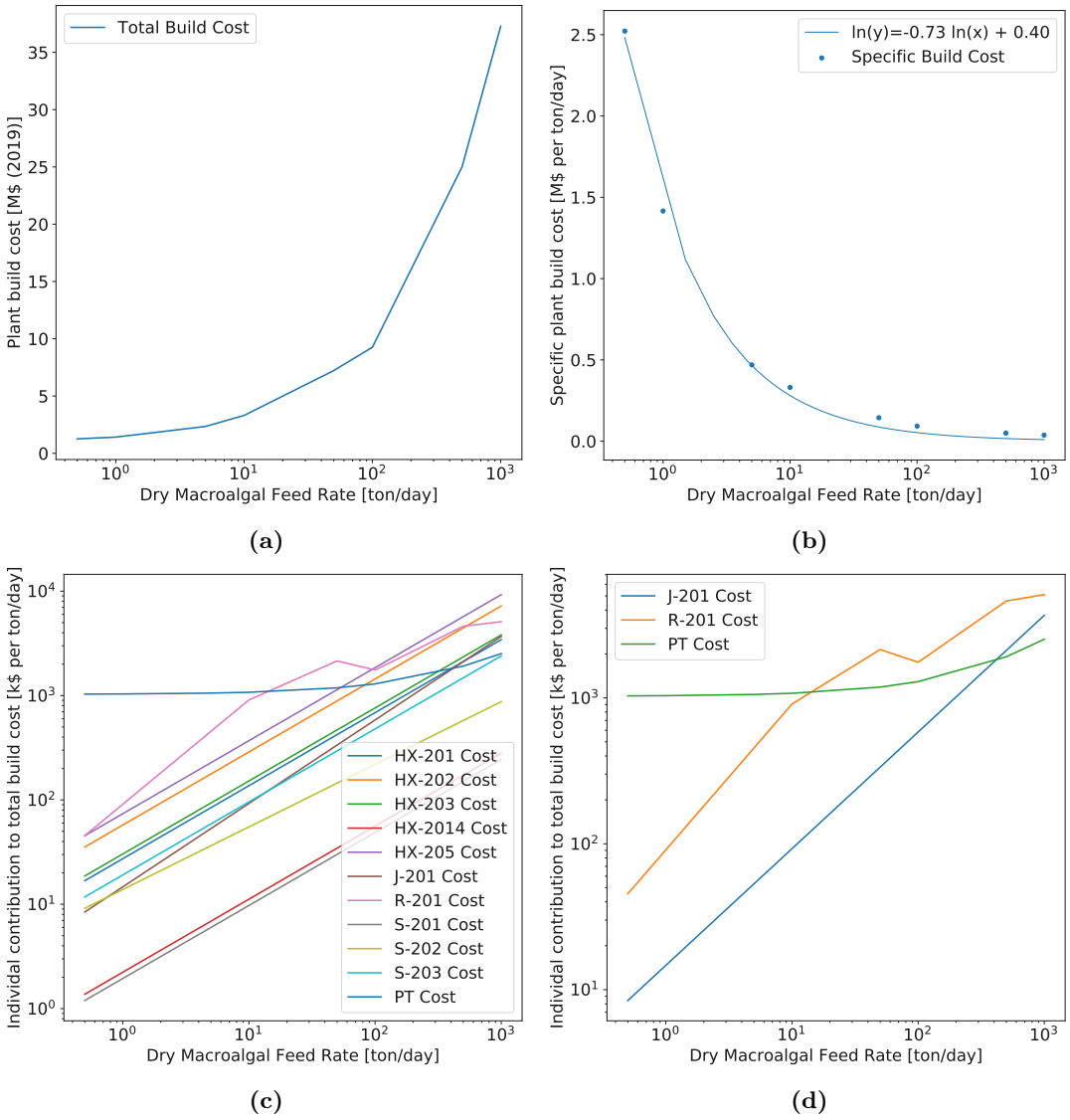

Figure 2.18: **a)** Estimated build cost and, **b)** specific build cost, of the HTL plant equipment at feed rates scaling from 0.5 ton/day to 1000 ton/day. **c)** Individual equipment contributions to total plant cost and, **d)** contribution of J-201 (slurry pump), R-201 (tubular HTL reactor), and PT (combined handling and pre-treatment equipment) only towards total plant cost.

low flow rates being approximately flat as the minimum sized equipment is significantly over-sized at the small scale. However, the pre-treatment and handling cost start to increase gradient also around 100 ton/day, indicating that at around this scale the equipment is fully utilised and minimum sized units are no longer over-specified for the required duty.

The 100 ton/day and 1000 ton/day cases are carried forward for net present value (NPV) assessment by the discounted cash-flow (DCF) method. The *Sargasssum spp.* species is considered as the only feedstock initially, as this species has already been shown to give the highest predicted biocrude yield whilst available at the lowest cost (tables 2.6 and 2.16).

Figure 2.19 shows the NPV for the macroalgal HTL process at 100 ton/day and 1000 ton/day scales, and a range of bio-crude selling prices. For both of these economic cases, it is assumed that *only* the bio-crude product is sold, and the gas, char, and aqueous phases are disposed at zero cost. As a point of reference, the UK Dept. for Business, Energy and Industrial Strategy (BEIS) has projected the wholesale price of crude oil rising from 57 $/BBL in 2020, to 90 $/BBL in 2035.[205, 206] For both the 100 ton/day scale plant (figure 2.19a) and the 1000 ton/day scale plant (figure 2.19b), the investment returns a positive NPV under 5 years for high oil prices ($\geq$500 $/bio-BBL, circa 5-10x current prices). Comparing the 100 ton/day to the 1000 ton/day cases, the 1000 ton/day scenario appears more profitable with an NPV payback earlier than the 100 ton/day plant. However, in both cases at more realistic bio-crude prices (50 to 100 $/bio-BBL) the investment continues to lose value over the entire 30 year term, shown by the descending gradient on all three trends.

Better profitability must be sought by valorising the remaining 3 product phases where possible (aqueous, gas, and char). The aqueous phase has been cited as potentially useful as an aqueous fertilizer, or potential feedstock to an anaerobic digester, and the bio-char potentially valuable as a soil amendment or simply being buried as a permanent carbon sequestration.[13, 49, 176] Figure 2.20a plots out the various projections for the NPV of a 100 ton/day HTL plant, with a fixed bio-crude price of 100 $/bio-BBL, and selling the aqueous phase at prices from $100 / ton to $1000 per ton. For reference, the average retail price for compound fertilizer in Scotland in the period 2010 to 2017 was 624 £/ton (approx. $750-850).[207] However, effectiveness of the aqueous phase as a compound fertilizer has yet to be demonstrated, thus it is prudent to assume a value of the HTL product to be significantly below the retail value of existing compound

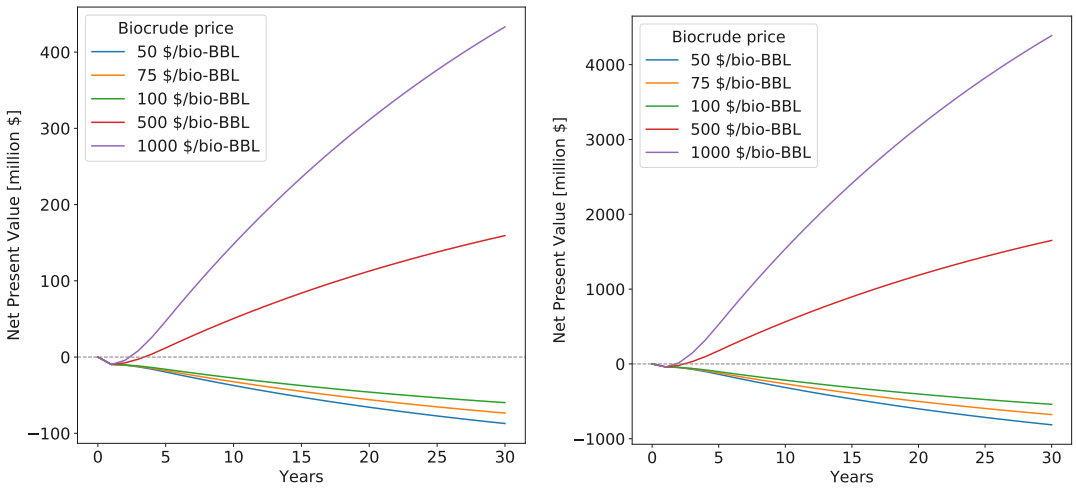

Figure 2.19: Net-present value of the Macroalgae HTL plant for the production of biocrude, with a fixed macroalgal price of $200 /ton (dry), assuming a selling price of biocrude from $50 per bio-barrel ($/bio-BBL) to 1000 $/bio-BBL for algal dry flows of **a)** 100 ton/day, and **b)** 1000 ton/day over a 30-year lifetime.

fertilizers.

The value of the combine char, and gaseous phases however may be directly linked to their carbon content. If we assign a value on removal of carbon from the atmosphere, then we must encounter a corresponding equal but opposite cost of releasing carbon with this process. The projected £/tonne price of CO_2 is taken from the UK Government BEIS price growth assumption publication, and a flat USD:GBP exchange rate of 0.77 is applied throughout.[206] The cost of CO_2 per tonne is then converted to a corresponding price of elemental carbon, and the relative value/cost of burying the char and releasing the gas phase, is determined by the estimated wt. % carbon in the product phase multiplied by the total mass flow. Figure 2.20b shows the impact of accounting for a carbon tax priced at $30 /ton in year 0 and stabilising at $56 /ton by year 10, with biocrude price fixed at $100/bio-BBL, and aqueous product sold between $400 and $600 per ton.

Figure 2.20b clearly shows that despite the process incurring significant additional costs associated with releasing the CO_2 rich gaseous phase, the effect of burying the char as a

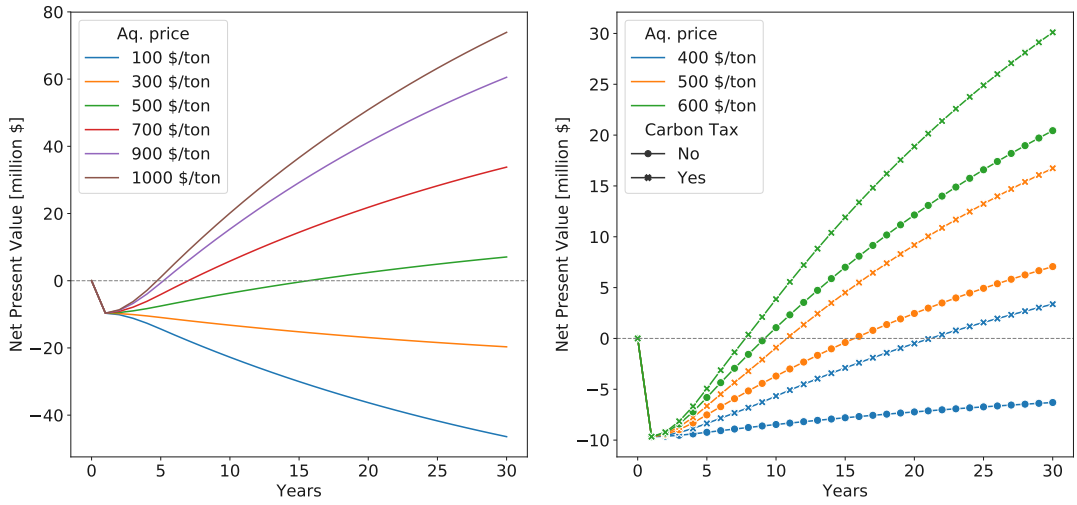

(a) **(b)**

Figure 2.20: The effect on NPV of the 100 ton/day HTL plant with a fixed biocrude price of \$100/bio-BBL and feedstock cost of \$200/ton (dry), when **a)** selling the HTL aqueous phase from \$ 100 to \$1000 per ton, and **b)** accounting for a carbon tax rising from \$30/ton in year to \$56/ton from year 10 onwards.

carbon sequestration and charging at the CO_2 equivalent price has a significant positive effect on the total NPV. In the case of low selling price of the aqueous phase (\$400 /ton), accounting for the carbon tax adjusts the NPV from a plant that is still significantly below the IRR of the investment at year 30, to one that returns a positive NPV in year 21. Similar observations can be made for mid-value aqueous phase price (\$500 /ton) and high-value (\$600 /ton), where the time to payback is reduced by approximately 5 years (from 15 to 10 years) and 1.3 years (from 9.5 to just over 8 years) respectively.

2.5 Conclusions

This work set out to explore both the technical and economic barriers to establishing an algal HTL to Bio-fuel process, based on the consumption of common farmed and pelagic wild-harvest seaweed species. Blending of algal HTL crude with a petro-refinery feedstock would allow production of bulk chemicals using existing industrial plants, and require minimal downstream changes to accommodate a bio-sourced refinery product, potentially having benefits in bio-fuel production, but also the dozens of bulk refin-

ery intermediate chemicals consumed in the manufacture of polymers, lubricants, and industrial chemicals.

Experimental work has shown that macroalgal HTL produces a biocrude product that is not dissimilar to petro-crude in terms of HHV, atomic ratios, and estimated boiling range, *however* also that the biocrude is significantly higher in oxygen content compared to petroleum crude. This work has also demonstrated a number of important variables around the HTL reactor *and* the overall process. Namely, elimination of gaseous O_2 from the HTL reactor is critical to avoid carbon yield loss out of the biocrude phase, and that acid pre-treatment on the biomass results in significant yield losses in the overall process. The route from a raw biocrude product to value-added refinery products, as well as the integration into existing petro-plants was out of the experimental scope for this work, however numerous studies have demonstrated successful hydrogenation and hydrodeoxygenation on HTL oils in pursuit of a high-quality upgraded bio-oil suitable for consumption in a petro-refinery process.

This work has explored a number of biomass property estimation models, including estimating the biochemical proximate (carbohydrate, lipid, and protein) from the elemental ultimate analysis (C, H, N, O, and S) and vice versa, and also tested a number of reaction models for suitability in predicting the bio-crude yields from a macroalgae HTL process. These models are incremental improvements on literature models, adapted and re-fit for application on macroalgae processes rather than microalgae or lignocellulosic processes. With these improved models, a chemical process model was built in Aspen Plus, and the process model used to help size a number of key pieces of process equipment required by industrial scale processes.

The process design showed a significant benefit to scaling up, with specific process costs falling significantly at scales of 100 ton/day and above. Specifically, this work finds an effective price-break at 100 ton/day, where the design of the reactor allows for a larger bore of piping whilst maintaining the required internal flow conditions to prevent blockage and fouling. However even at the largest scale modelled (1000 ton/day algal feed), the Net Present Value of the plant over 30 years only returned on the initial

investment when achieving a biocrude selling price in the order of 5x greater than the current and historical price for petroleum crude.

However, there are still potential routes to commercialisation, by realising the value in the non-biocrude products, and through effective legislative incentives. Of critical importance is the efficient valorisation of as much of the various product streams as possible. Selling the aqueous phase for at least $400 /ton enabled a project payback within the 30-year lifetime with a biocrude price of $100 /bio-BBL, but only when combined with an effective market for carbon credits that valued the char phase for application in carbon sequestration.

Chapter 3

Process Design and Technoeconomic Analysis of a Polysaccharide Film Biorefinery

3.1 Introduction

The previous chapter demonstrated a thermochemical approach to converting a low-value seaweed source into an array of low-value high-volume products (biocrude, low-grade aqueous fertilizer, carbon-rich char). This modelled biorefinery was not feedstock agnostic however and was only ever economically viable at extremely large scales ($>$ 1000 tonnes day^{-1}), when generating significant added value from the secondary and tertiary products, and with legislative support. Similarly, recent US Dept. of Energy models confirm technical feasibility of HTL process, however they draw the same major conclusion that the production of a bio-crude product only makes sense at huge scale and/or with significantly cheaper feedstock than is currently feasible.[208, 209] Given the limitations of biomass supply and land availability for large industrial refining processes, it seems unlikely that giga-scale biorefineries for producing petroleum products will ever be economical in UK or Europe.

Furthermore, hydrothermal processing methods are indiscriminate in their depolymerisation of biomass constituent molecules, with molecules of potentially higher value being lost in the process as mass is distributed between char, organic, aqueous, and gaseous phases. A better approach might be a cascading biorefinery, where higher-value products are extracted from the biomass in comparatively mild conditions to preserve the valuable structures, and low-value residues sent to an upgrading process where comparatively severe conditions are employed to reduce all left-over materials to a more basic and uniform low-value product. Additionally, the previous economic model showed that much of the value of the harsh thermochemical processing of biomass was attributed to the carbon sequestration service – hence we should aim to maximise the yield of stable carbon rich char compared to mass partitioned into the aqueous, gaseous, or biocrude phases.

One possible higher value product could be a biopolymer produced from some of the fractionated seaweed. Various biodegradable polymers have been developed, at least in part, from macroalgae-derived polysaccharides. These biopolymers have characteristics suitable for the replacement of some applications where petro-plastics are currently used. To meet sustainability goals these novel polymers must be renewable, biodegradable, biocompatible and environmentally friendly.[210]

Global production of plastic packaging is predicted to exceed 250 Mt yr^{-1} by 2050, much of which is for single-use applications.[211] Already, total plastic production exceeds 320 Mt yr^{-1} and continues to grow.[210] Currently, almost 95 % of plastic packaging is discarded after first use. The most common plastics used in packaging include polyethylene terephthalate (PET), polypropylene (PP), polyethylene (PE) and polystyrene (PS). As the energy industry begins to wean itself off fossil fuels, the manufacture of petroleum based plastics places a proportionately increasing demand on crude oil extraction and non-degradable plastic waste commonly finds its way into the terrestrial and marine environment, causing a range of negative environmental consequences.[212]

Almost all of the biopolymers developed using seaweed based hydrocolloids have been films produced by a solution casting-evaporation method.[58] However, biopolymer films

produced solely from seaweed generally have poor water vapour barrier and mechanical properties.[53] Though combining multiple polymer components can improve these characteristics, with the use of cellulose, clays, vegetable oils and other biopolymers the most commonly reported.[104, 105, 213–219]

While there has been extensive experimental reports on producing biopolymers from seaweeds, there are only a handful of examples of process modelling in the literature.

A relatively early example from Konda et al. (2015) is a process model built in SuperPro Designer to facilitate a technoeconomic analysis (TEA) of the macroalgae-to-ethanol biorefinery, based on a study undertaken by the National Renewable Energy Laboratory (NREL) for the production of ethanol from corn stover.[120, 220] Summary results highlight that the process is extremely cost-sensitive to the feedstock price of macroalgae, with indicative minimum ethanol sales price of $3.6 to $8.5 per gallon achieved at a seaweed price of $100 per metric tonne.

Bioethanol is a popular key product when building a macroalgal biorefiniery process model, as it represents both a fuel and a chemical feedstock, but can also represent any generic fermentation product. The bioethanol production process is well established at this point, with numerous biorefinery processes being designed to reduce a feedstock to a hydrosylate of fermentable sugars. Thereafter, the production and purification of ethanol from a fermentation broth is a well understood industrial process. Thus, numerous researchers have developed macroalgae-to-bioethanol process models using various different software, techniques, and levels of riguour, in order to produce TEA to answer various research questions (3.1).

Macroalgal biorefinery models that produce products other than ethanol have also been demonstrated. Brigljevic et al(̇2017) reported on a macroalgae-to-biodiesel process design and simulation in Aspen Plus software, using a simulated pyrolysis of pre-treated seaweed biomass and coupled hydrogenation of the resulting pyrolysis oil. They showed a minimum biodiesel selling price of $2.51 to $4.12 per litre, albeit achieved at rather low seaweed costs of $25 to $92 per dry-ton.[224]

Table 3.1: Macroalgae-to-bioethanol biorefineries modelled using different simulation software for technoeconomic analysis.

Seaweed	Software	Process condition	Feedstock price	Bioethanol price	Reference
Saccharina latissima	SuperPro Designer	Enzymatic hydrolysis, fermentation, distillation	\$100 / MT	\$ 3.8 to \$8.5 per gallon	Konda et al. (2015)[220]
Brown seaweed	Excel	Fermentation	\$ 98 / tonne (dry)	\$1.55 to \$1.93 per litre	Soleymani and Rosentrater (2017)[221]
Saccharina japonica	Aspen Plus	AD, fermentation, distillation, and hydrogentaion	\$70 / tonne (dry)	\$0.589 per litre	Brigljević et al(2018) [222]
Eucheuma cottonii	Aspen Plus V10	Enzymatic hydrolysis of macroalgal cellulosic residue, fermentation, distillation	\$ 72.6 per tonne	\$0.54 per kg	Chong et al. (2020)[223]

Similarly, Wong et al(2022) used Aspen Plus to simulate a combined bioethanol and L-lactic acid production process based on the saccharification of macroalgae cellulosic residues, such as those remaining after agar is extracted from red seaweed species. They demonstrated a plant able to produce combined bioethanol and L-Lactic acid products at 0.80 \$ kg^{-1} and \$ 2.49 \$ kg^{-1} respectively. At this product unit price, a plant payback was predicted to fall within 4.93 and 13.12 years, depending on various economic assumptions. However, again this was achieved with a perhaps unreasonably low predicted price for the feedstock of \$ 56 per tonne.[225]

In all previous works however, the target product is often a high-volume and low-value product (e.g. ethanol or biodiesel), or a specific chemical precursor to feed an existing industry (e.g. L-Lactic acid to produce polylactic acid polymer). Additionally, many of the example biorefineries are financially dependent on valorising waste materials, or producing secondary products to maximise the value gained from the feedstock. Given the extensive experimental reports of producing biopolymers from the native seaweed polysaccharides, there is a gap in the literature to consider a direct macroalgae-to-biopolymer process. As such in this chapter, an ASPEN model was built to examine the economic suitability of combining a polysaccharide biopolymer synthesis with thermochemical processing of the rest of the seaweed biomass.

3.2 Methods

3.2.1 Plant Modelling and Configuration

To model a biopolymer biorefinery, the previously modelled hydrothermal liquefaction plant has been redesigned to facilitate the extraction of sodium alginate from bulk seaweed delivery, the production of nano-cellulose from micro-crystalline cellulose, the production of bulk-reels of an alginate based biopolymer film, and the slow pyrolysis of seaweed residue to produce a stable carbon-rich char.

The first flowsheet is essentially identical to the HTL plant previously presented, since the activities of receipt and pre-processing of macroalgal biomass shares the same fundamental requirements independent of differentiation in the downstream treatments. To that end, pre-washing, milling, and provision for bulk storage of partially processed feed material is allowed for again, to help smooth out seasonal variations in supply (figure 3.1).

3.2.2 Process Description

The biomass receiving and pre-processing (Area-100, figure 3.1) is similar to the previously presented HTL biorefinery, however differs in the treatment and storage of the

algal biomass. Previous work considered the use of a single species of seaweed, thus supply would be limited to a single annual harvesting season and yearly operation would be maintained by storage of shredded and dried seaweed biomass. In this biorefinery it is assumed that a more distributed supply chain model is adopted, too allow more regular delivery from a much wider range of biomass suppliers. This requires biomass to be delivered minimally pre-processed (coarse milled and dried to < 15 wt. %), which then allows stockpiling of the biomass in covered storage. Managing multiple types and qualities of biomass is done to ensure a stable product is produced by the plant, and is achieved by maintaining multiple separate stockpiles, and having individual dosing hoppers (DH-101, DH-102, and DH-103) to allow a seaweed recipe to be managed by the plant operators. As previously, the coarse seaweed is screened to remove large debris and reject material. Screened biomass is then washed in V-101 to reduce the ash content and remove residual salt, after which the biomass is sieved and then milled to a uniform particle size (Mill L-101). Milled seaweed is then held in an interim storage bin and accumulated between batch extractions.

In the alginate extraction and separation section of the plant (Area-200, figure 3.2), macroalgal solids are combined with heated fresh water and sodium carbonate solution in the stirred reaction vessel V-201. Concentrated sodium carbonate solution is prepared in the V-202 batch preparation tank by combining dry Na_2CO_3 with fresh water and stirring until dissolved. The solution is then transferred to the T-201 storage tank by pump J-202, which holds pre-prepared solution for dosing into the extraction vessel. Pump J-202 is used both for transferring fresh batches to storage tank T-201, and for dosing the concentrate to the extraction vessel V-201. For each batch, the required volume of sodium carbonate concentrate is dosed into the extraction vessel (V-201), this is then diluted with pre-heated water, and ground macroaglae added under continuous stirring. After the required extraction time has elapsed, the contents of the vessel are transferred by the J-201 slurry pump to a continuous rotary filter (S-201) which separates the residual macroalgal solids from the extracted alginate rich fraction. Residual solids are sent to the drying and pyrolysis section of the plant (Area-500, figure 3.5), and the alginate rich aqueous stream is sent to the polymerisation section (Area-300,

figure 3.3).

Extraction conditions selected for the extraction are those of the alkaline extraction as described by MacHugh, that is a 1 % Na_2CO_3 solution strength, 2 hour extraction time, stirred at 50 °C, and with a macroalgal solids dosing rate of 20 wt. % with respect to the total weight of solution.[226]

Polymerisation, formulation, and film casting is achieved in Area-300 (figure 3.3), where the sodium alginate rich aqueous solution prepared in Area-200 is first pre-mixed with glycerol plasticizer, and nanocellulose solution prepared in Area-400 in vessel V-301. After pre-mixing to ensure homogeneity, a slow addition of dilute calcium chloride is made to partially reticulate the alginate polysaccharide. The calcium chloride addition is made slowly and at elevated temperature as described by Silva et al. to prevent local gelation of the alginate polysaccharide. [227]

Film-forming solution (FS) is then transferred to a buffer tank (T-301) where it is held and slowly discharged to the continuous film-belt dryer (D-301). Use of the buffer tank allows multiple batches to be poured as a continuous and uninterrupted film product. The film-belt dryer is based on the developments of the KODAK continuous film casting process, where the FS (also known as the dope solution) is continuously cast against a flat steel belt and heat applied both directly through the belt and in the form of heated air to facilitate the rapid evaporation of the carrier solvent, water in this case. [228]

Continuously produced film is collected from D-301 and is wound onto bulk reels via a commercial film winding system (C-301), where the bulk-reels are then sold to converters and manufacturers for use in numerous downstream applications. Energy integration is critical to the sustainable operation of the drying process, hence the hot exhaust gas from the dryer is firstly recycled back to the dryer air inlet by the drying process fan (F-301) after re-heating to the required process temperature (H-302). To prevent the accumulation of moisture within the dryer, an exhaust purge is maintained by adjusting the recycle damper valve (DV-301), where the purged exhaust flow is passed via a heat-exchanger (H-301) where fresh make-up air is pre-warmed before introduction to the

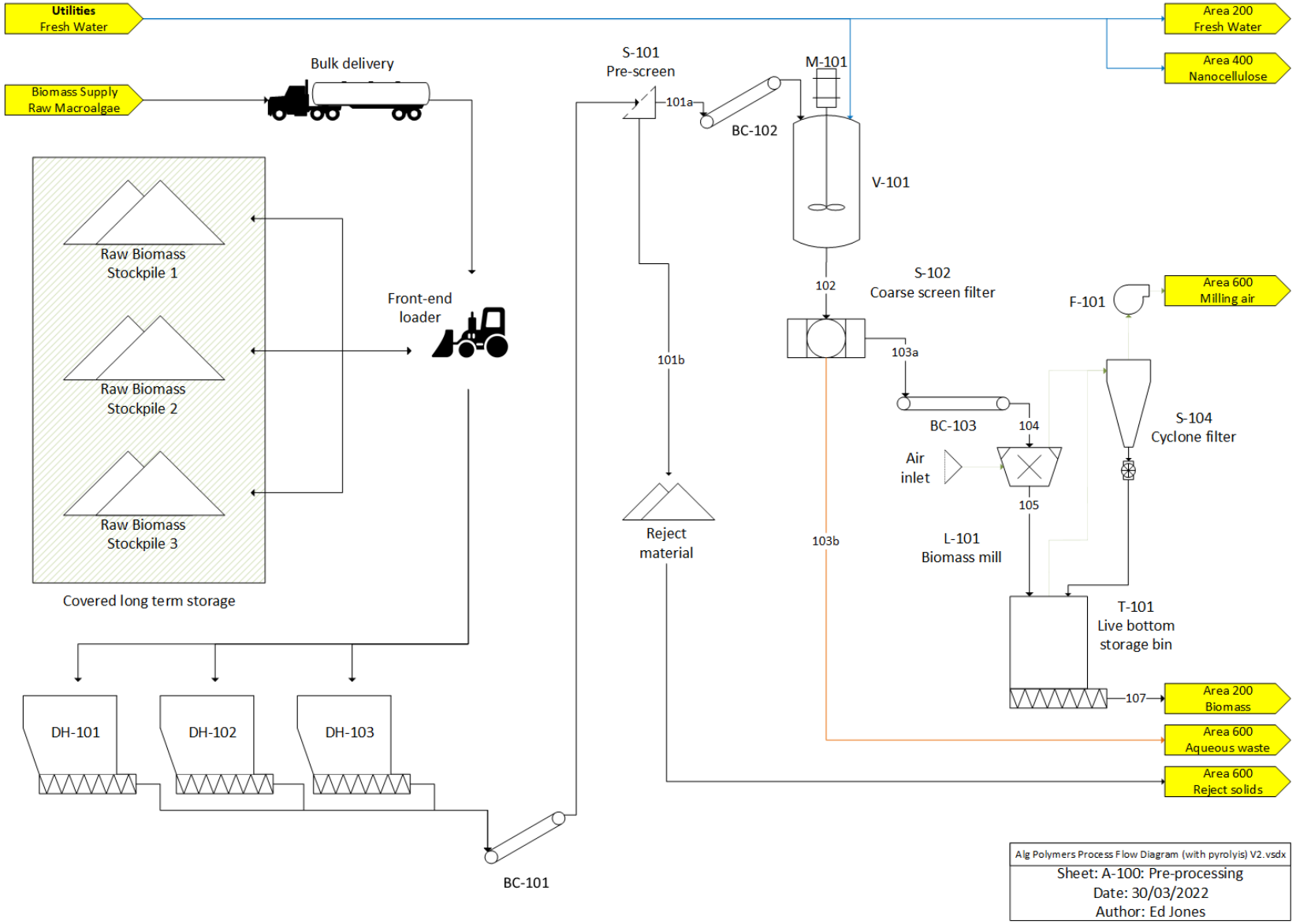

Figure 3.1: A-100: Biomass receiving and pre-processing process flow sheet

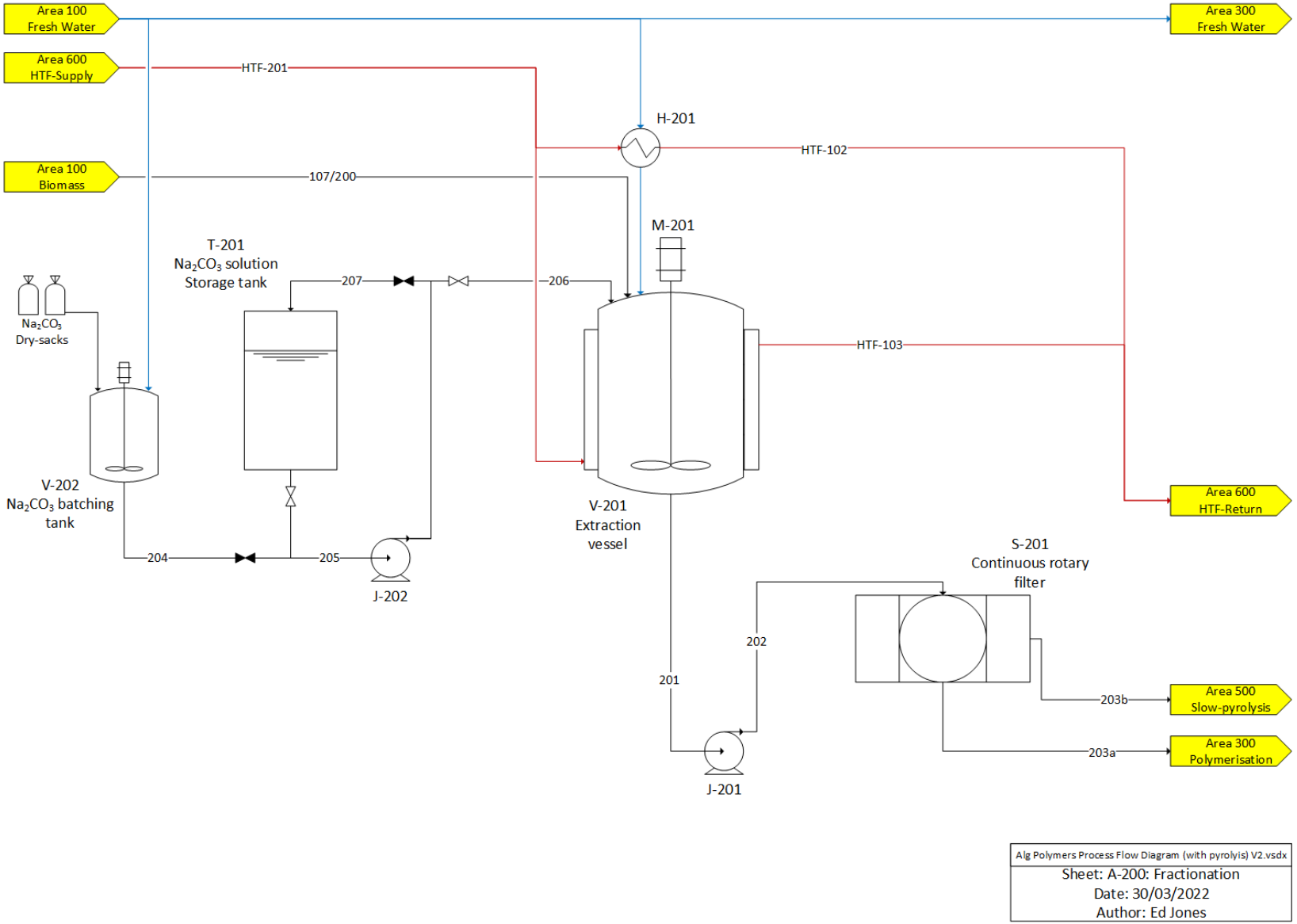

Figure 3.2: A-200: Alginate extraction and separation flowsheet.

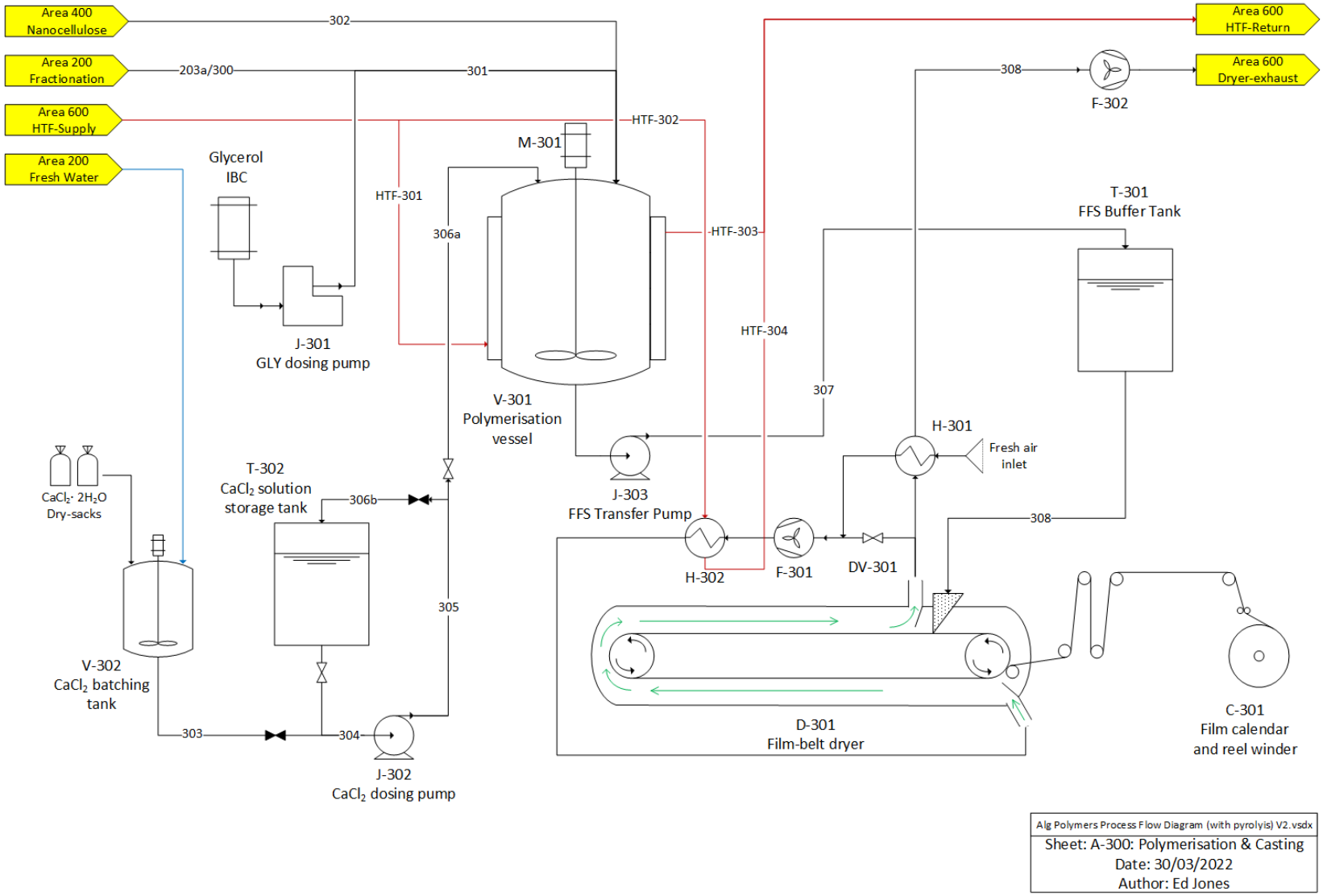

Figure 3.3: A-300: Polymerisation, formulation, and biopolymer film production flowsheet.

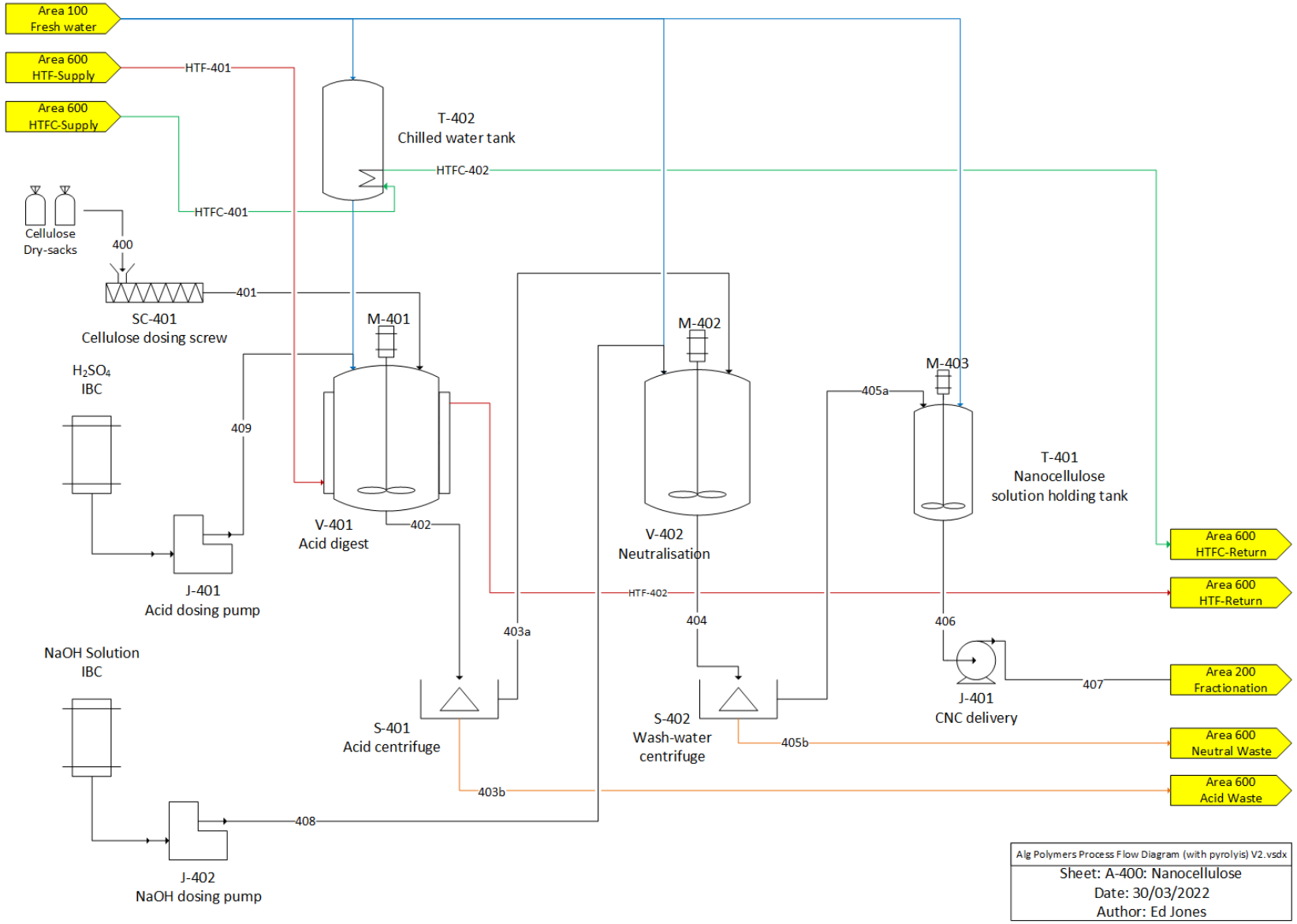

Figure 3.4: A-400: Nanocellulose production train by acid digest flowsheet.

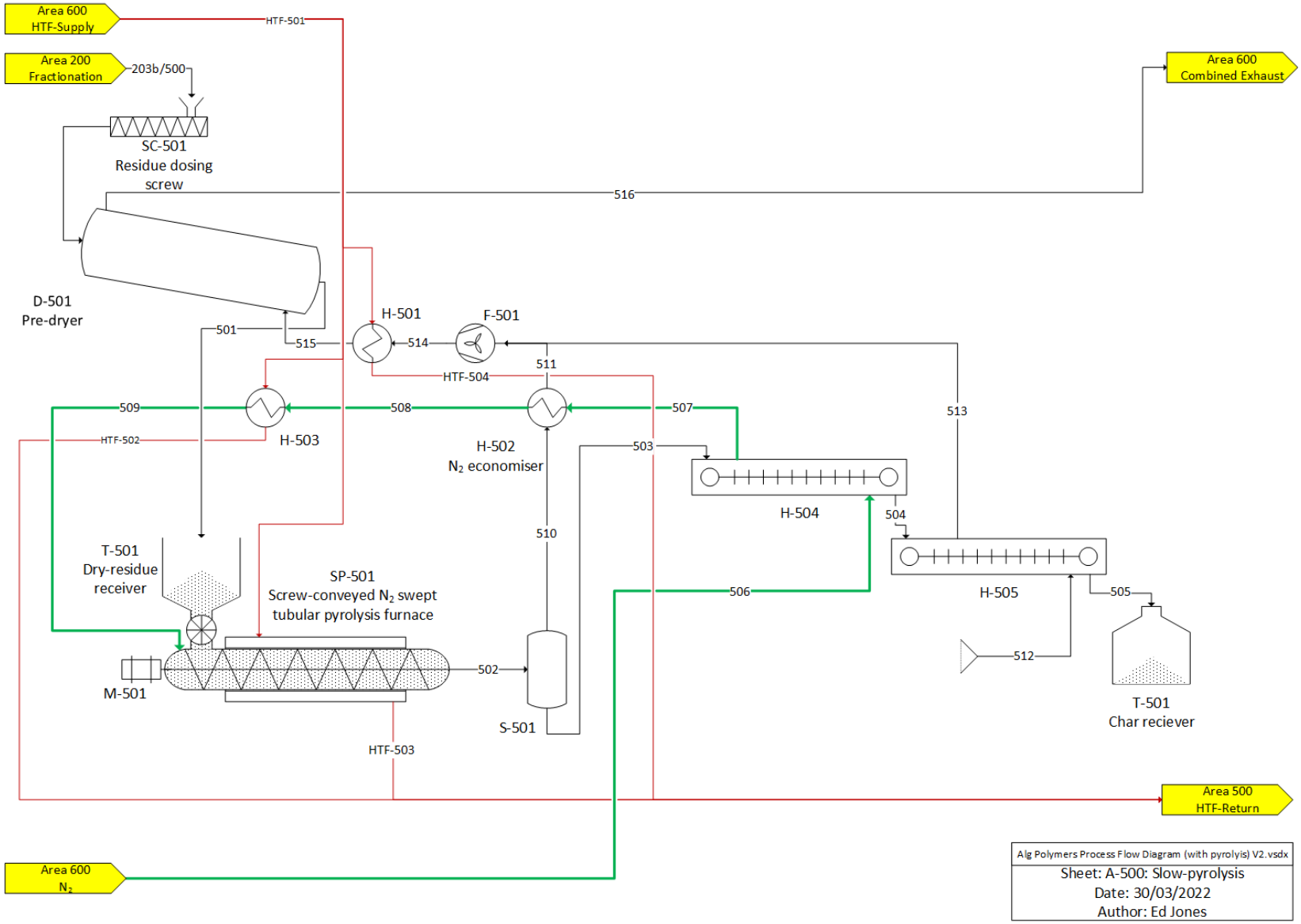

Figure 3.5: A-500: Biomass residue drying and slow-pyrolysis flowsheet.

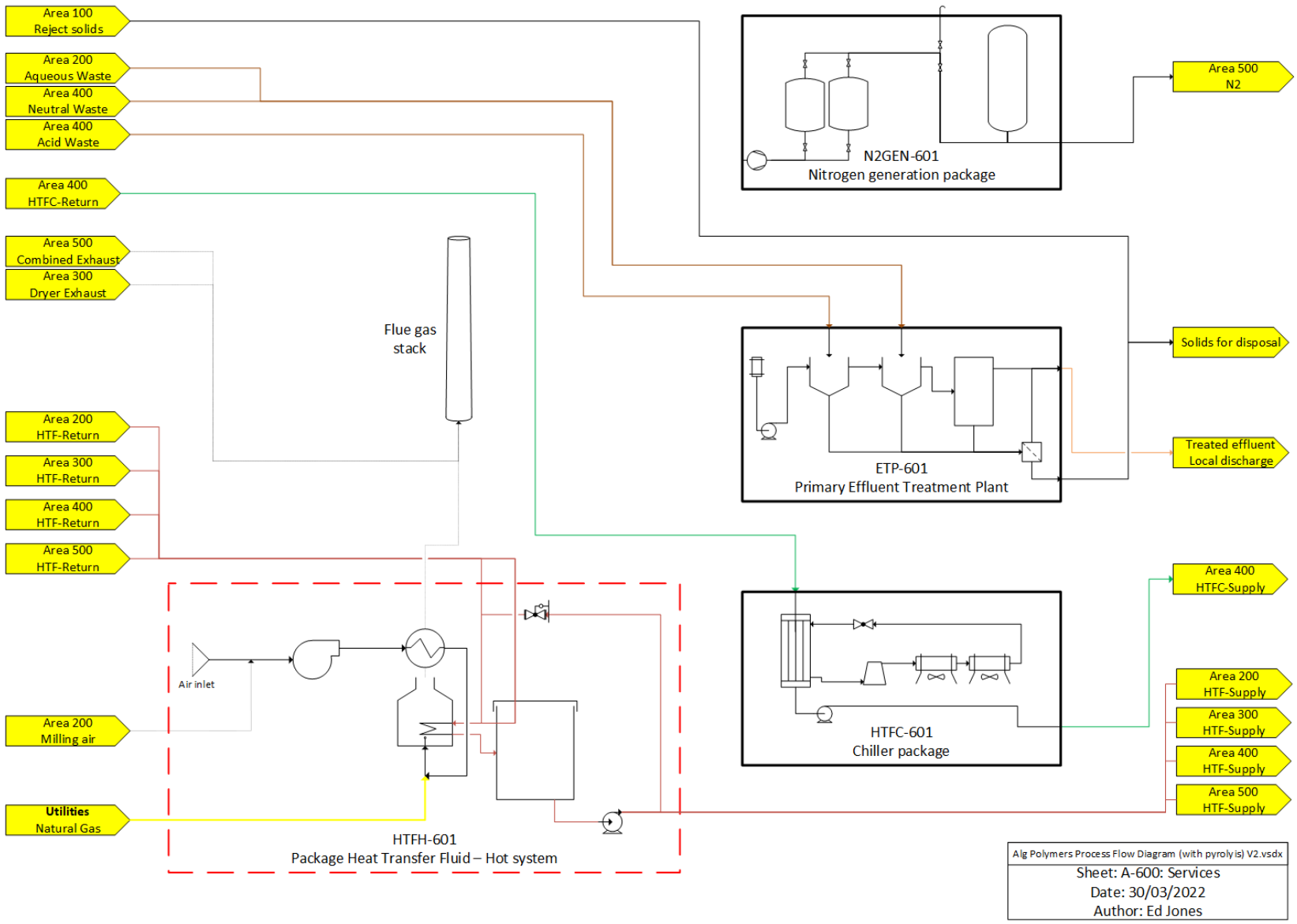

Figure 3.6: A-600: Services and utilities provision flowsheet.

recirculation duct upstream of the recirculation fan, and the heat-recovered exhaust is discharged via the exhaust fan (F-302).

Nano-cellulose is prepared in Area-400 (figure 3.4), following the well published acid-digest methodology.[75, 76, 229, 230] The acid digest solution (65 wt. % H_2SO_4) is prepared in the extract vessel (V-401) by slow addition of concentrated acid to pre-dosed plant water. Dry cellulose material is loaded into the dry material dosing screw (SC-401), where it is slowly added to the acid solution under constant stirring, and the acid digest proceeds at 45 °C for 2 hours. During reaction, water is pre-chilled in the chiller tank (T-402). After the required reaction time has elapsed, the acid digest reaction is quenched by rapid addition of 5 volumes of chilled water, and the resulting acidic suspension of crystalline nano-cellulose (CNC) is passed through the primary separation centrifuge (S-401). Acid supernatant waste is sent for effluent treatment, and the acid-wet solid CNC sludge material is dispersed in the neutralisation vessel (V-402) where slow addition of 4 wt. % NaOH solution is maintained until a neutral pH is achieved. Following neutralisation, additional water is added to V-402 to dilute neutralisation reaction products (Na_2SO_4). The resulting neutralised CNC suspension and dissolved neutralisation products are then passed to the secondary centrifuge (S-402), where the neutral pH effluent is again sent for effluent treatment, and the neutral and washed CNC solids are sent to the CNC solution holding tank (T-401), where additional water is added to bring the concentration of CNCs below the critical concentration where they become neutrally buoyant in water when in neutral pH conditions ($\leq$ 50 g L^{-1}).[231] From the holding tank (T-401), the solution is dosed at the required volume via the CNC dosing pump (J-401) to the polymerisation vessel (V-301, figure 3.3).

Insoluble residues isolated from the extraction process (S-201, figure 3.2) are passed to the slow pyrolysis section of the plant (A-500, figure 3.5). Residues are received in the hopper of the dryer dosing screw (SC-501), where they are dosed into a continuous rotary dyer (D-501) which pre-dries the wet residue from approx. 40 wt. % down to $<$ 4 wt. %. Dry solids still warm from the drying are then deposited into a feed hopper (T-501), where it is continuously dosed into the screw-conveyed tubular pyrolysis furnace

(SP-501). The pyrolysis takes place at 350 °C, and with a mean residence time of 1 hour. The pyrolysis reactor is continuously purged with hot nitrogen in order to maintain an inert atmosphere and prevent combustion of the biomass residue, in addition the flowing nitrogen serves to convey gaseous reaction products through the reactor.

Hot char, gaseous reaction products, and the nitrogen purge gas exits the tubular screw furnace into a disengagement volume (S-501) which allows entrained gasses to disengage from the hot char solids. Hot solids are passed to a cooler conveyor (H-504), through which the fresh nitrogen supply is passed. Nitrogen is used here to cool the char below 200 °C to reduce the risk of combustion in air, additionally the hot-char is used to pre-heat the nitrogen. Warm char is then further cooled (H-505) under flowing air, which brings the temperature down to 50 °C for safe handling.

Gaseous products from S-501 are sent primarily to an economiser heat-exchanger which recovers additional heat from the hot exhaust products into the warm nitrogen stream coming from the primary char cooler (H-504), the warm reaction gasses are then combined with the warm air produced by the secondary char cooler (H-505), passed through a fan (F-501) and re-heated to be used as the primary drying gas for the pre-dryer (D-501). The combined exhaust stream from D-501 contains the water vapour from the dryer, the gaseous products of the pyrolysis reaction, the nitrogen used to purge the pyrolysis reactor, and the air used to make the final cooling of the char. This combined exhaust stream is sent to a common discharge vent (Area-600, figure 3.6), along with other gaseous exhaust streams from other sheets.

Area-600 (figure 3.6) is the collected services area, where services such as plant-wide supply of hot heat-transfer fluid (HTFH-601), the chiller package (HTFC-601), on-site primary effluent treatment (ETP-601), and air separation to produce nitrogen for purging the pyrolysis reactor (N2GEN-601) are depicted.

3.2.3 Aspen simulation and optimisation

The simulation was based on a continuous process rather than a batch process. Modelling a continuous flow process allows simpler scaling of a single simulation to probe the

cost sensitivity of plant-size. The bounds of the Aspen simulation are set starting from sheet A200 (figure 3.2) onwards, however will also include the washing vessel V-101 in A-100 (figure 3.1) in order to capture the water consumption of this process step.

The NRTL-HOC (NRTL (Renon) / Hayden O'connell equation of state with Henry's Law) property method was used to predict the pure and interaction properties of conventional components, and the inbuilt property methods of HCJ1BOIE, and DCOALIGT were used to estimate enthalpy and density respectively for the non-conventional components. The mass flow rate of dry unwashed seaweed (stream 101A, figure 3.7) is the key independent variable, with all other flow-rates and equipment sizes scaling from this. Similar to the previous HTL plant model, macroalgal biomass defined as a non-conventional solid, and the dry mass flow-rate is set in stream 101A along with the compositional analysis (ULTANAL, SULFANAL, PROXANAL).

Wash water is introduced at a 2:1 mass ratio (water:macroalgae) and the algal slurry is stirred in V-101. This wash-step reduces the ash-content of the feed material by 53 wt. % (relative ash content reduction), as experimentally reported by Tabassum et al. [232] Ash reduction is achieved by modification of the relevant component attributes by the WASHCALC calculator block, where the first element of ULTANAL (Ash content, 1st element of the vector) is reduced, and the remaining elements of ULTANAL (C, H, N, Cl, S, and O content) are re-scaled such that the sum of all mass fractions is equal to 1.

Separation of the solids and wash-water is modelled in a simple SEP block, where 95 % of the water used in washing is recovered into the aqueous waste stream (103B), and the remaining water-wet seaweed is passed through stream 107 to a pre-heater. Alginate extraction is performed in block V-201 (figure 3.7), which utilises an RYield block to cast a given mass of "seaweed" into an equivalent mass yield of seaweed components (Table 3.2).

Extraction is modelled to occur in a 1 % sodium carbonate solution (stream FRAC-SOL, figure 3.7), at a 1:4 biomass:solution mass ratio. The required mass of extrac-

tion solution is pre-heated to extraction temperature (50 °C) by the HEATER block (SOLHEAT). Enthalpy of reaction for the extraction process is not considered to be significant compared to the energy cost of heating the significantly larger mass of water in the V-201 block. Assuming the extraction vessel is well insulated, the energy rquired to maintain an extraction temperature of 50 °C is negligable, hence not considered in this work.

Table 3.2: Component mass balance modelled in the V-201 RYield block used for modelling seaweed extraction.

V-201 Inlet		V-201 Outlet	
Component	Mass Fraction	Component	Mass Fraction
Seaweed	1.0	Fucoxanthin	0.029
		Alginate	0.210
		Fucoidan	0.060
		Cellulose	0.151
		Laminarin	0.050
		Protein	0.100
		Ash	0.240
		Lipid	0.010
		Mannitol	0.100
		Petro-polymer waste	0.050

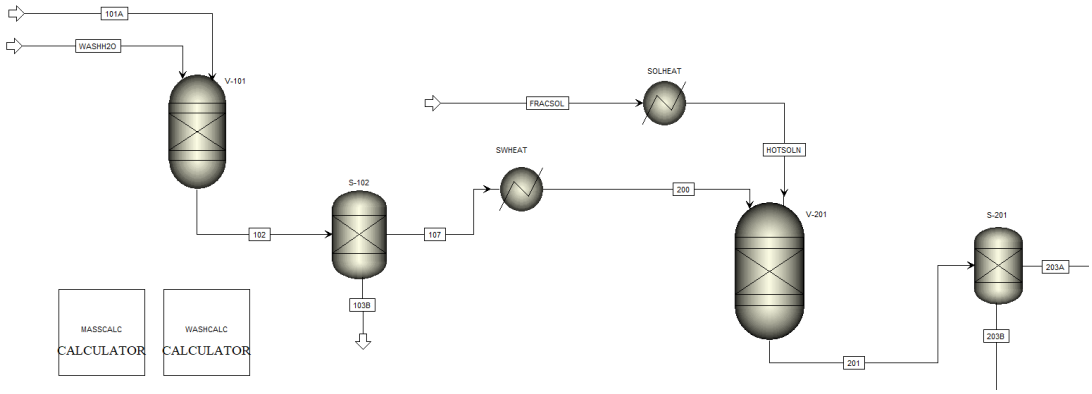

Figure 3.7: Aspen Plus implementation of the process critical unit operations in Area-100 and Area-200, the seaweed washing and alginate extraction processes.

Separation of extraction products is modelled in S-102 (SEP block) where the majority of water and water soluble products are cleanly separated into the aqueous products stream (203A), and the insoluble residues into the non-aqueous stream (203B).

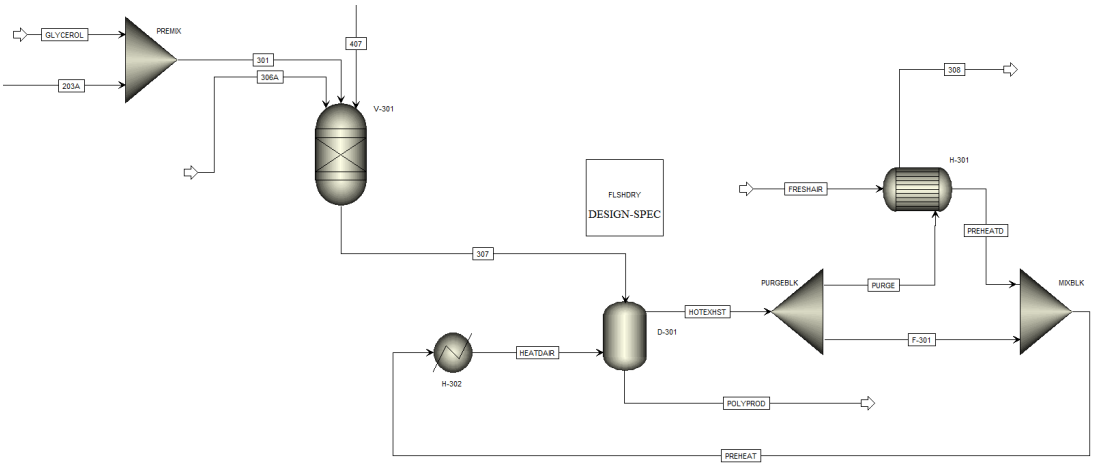

Figure 3.8: Aspen Plus implementation of the process critical unit operations in Area-300, polymer formulation and solvent drying.

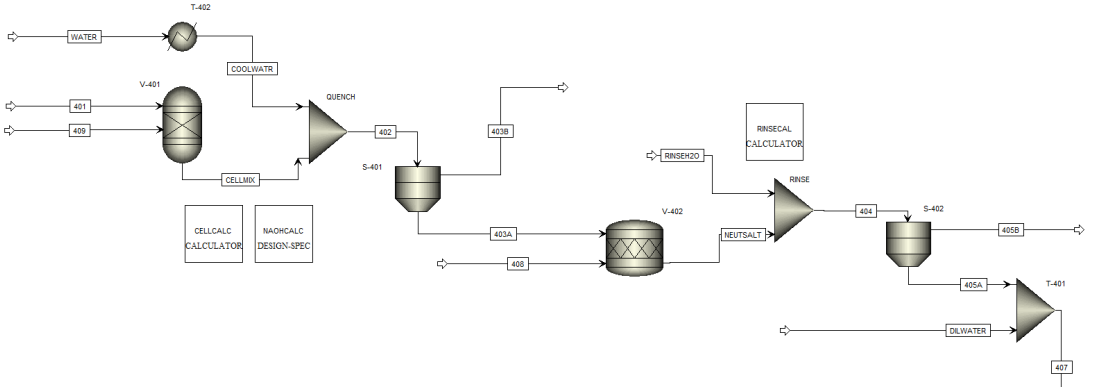

Figure 3.9: Aspen Plus implementation of the process critical unit operations in Area-400, nanocellulose generation and washing.

Formulation and polymer drying (figure 3.8) is simulated by using an RYield block to cast all the non-water and non-Na_2CO_3 components to a single "biopolymer" product. Drying (D-301) is modelled by introducing this warm film-forming solution (FS) into a Flash2 block and determining the vapour-liquid equilibrium between the FFS and the drying air (stream HEATDAIR). Fresh air is drawn in (stream FRESHAIR) and pre-warmed in the feed/exhaust heat exchanger (H-301), warm fresh air is then mixed in with the hot-recycled air being circulated by F-301, this mixture of fresh and recycled air is then re-heated with a trim-heater to the desired drying temperature (heater H-302), and diverted back into the dryer. The exhaust gas from the dryer first passes via

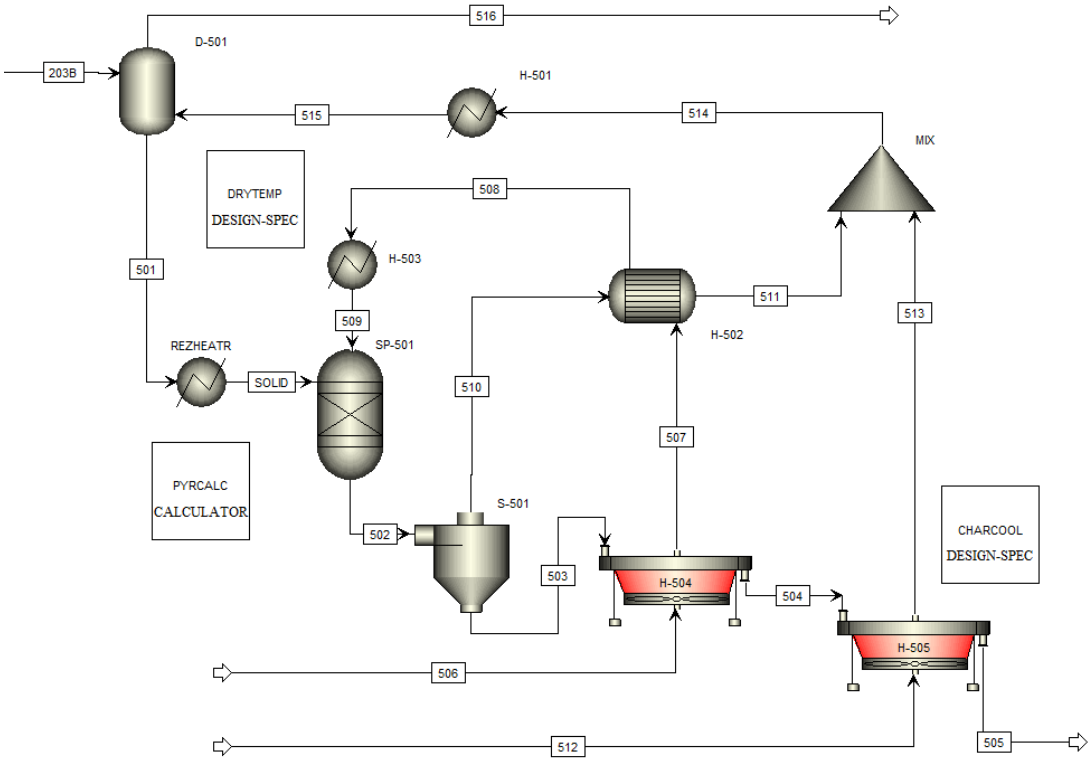

Figure 3.10: Aspen Plus implementation of the process critical unit operations in Area-500, slow pyrolysis reactor, residue dryer, and char coolers.

a splitter block, where a purge quantity is vented via the feed/exhaust heat exchanger (H-301), and the retained recycle flow meets the fresh air in the mixer block.

Process settings are determined dynamically. A design-spec is used to vary the mass-flow rate of fresh make-up air (stream FRESHAIR) introduced into the feed/exhaust heat exchanger (H-301), for a fixed purge/recycle ratio and a fixed drying temperature, in order to achieve a residual moisture of less than 5 wt. % in the finished polymer film. Sensitivity analysis is then used to vary the purge ratio (from 0.1 to 1, representing 90 % recycle down to 0 % recycle), and to vary the fixed drying temperature from 100 °C to 400 °C. The thermal power requirement of the trim heater (H-302), total mass-flow of recycled air, and fresh make-up air flow rate are then used to produce overall operating cost estimates for the whole drying system, which allow selection of the desired operating conditions.

Fan power estimates are made using the following relationships:

$$P_i = dPq \tag{3.1}$$

$$P = \frac{P_i}{\mu_f \mu_B \mu_m} \tag{3.2}$$

Where P_i and P are the ideal and actual fan operating power (W) respectively, dP is the differential pressure across the fan (Pa), q is the volumetric flow rate through the fan (m3 s^{-1}), and $\mu_{(f,B,m)}$ are the fan, belt, and motor efficiencies respectively.

Crystalline nano-cellulose (CNC) generation is handled by an RYield reactor. The reaction conditions are identical to those previously described, and the RYield reaction is modelled as a component map where cellulose remains chemically unchanged by the particle-size distribution (PSD) is shifted significantly. Cellulose is handled as a conventional solid in Aspen Plus, with the starting PSD map is specified to match the average micro-crystalline cellulose (MCC) for a d50 = 100 μm product as described O'Neil et al. (1999).[233] The CNC PSD is taken from Morán et al. (2008) in their experimental work where they produced CNC from both cellulose extracted from sisal fibres and from MCC, and produced using a 0.5 hr 60 % H_2SO_4 acid digest at 45 °C.[229]

Finally, pyrolysis is modelled in the flow-sheet displayed in figure 3.10. Damp insoluble seaweed residues resulting from separation of the fractionation process (3.7, S-201) are first pre-dried to less than 6 %. The drying process (D-501) is modelled using a Flash block, where the required enthalpy to meet the latent heat is provided by a stream of hot-air (stream 508) being heated by H-503. A design-spec is used to minimise the required temperature such that drying is achieved. The hot-air and vapour stream resulting from the dryer is exhausted (stream 516) as at this point the residual heat in this stream is relatively low. Dried residual seaweed solids (stream 501) are converted to char in an RYield reactor block (SP-501), where the total mass of all non-ash components is converted to char and CO_2 on a 57 % and 43 % mass yield basis respectively, whilst in the present of flowing nitrogen.[234, 235] For the sake of simplifying the simulation,

heating of the insoluble residue is achieved with a heater block (REZHEATR), and the total reaction enthalpy is calculated for the flowing mass of reacting components and a specific heat of reaction of 0.78 MJ kg^{-1}.[236]

Products of the slow-pyrolysis reaction (char, ash, and CO_2) are then passed to a cyclonic separator which separates the gas/vapour products from the solid ash and char. Hot char is initially used to pre-heat the nitrogen sweep gas in the char-cooler H-504. The required mass flow rate of nitrogen is determined such that any gaseous products of the pyrolysis reaction (43 % mass yield of non-ash components in the feed) is diluted by a factor of 3 (mass basis) in order to maintain inert condition and sweep out volatile pyrolysis products. The pre-heated nitrogen is then further heated by cross-exchanging with the hot gasses produced by the cyclone separator, this hot nitrogen is finally heated up to the reactor temperature (H-503) and sent to the reactor. A second advantage of using the hot-char to pre-heat the nitrogen is that this reduces the temperature of the char to below 200 °C, and thus a significantly lower risk of combustion. Partially cooled char is then cooled to below 50 °C with flowing air (H-505. The required mass flow of air is determined with another design spec, with the desired char temp of 50 °C selected as a safe handling temperature. The heated-air emitted by H-505 is then mixed with the combined nitrogen and reaction gas (streams 511 and 513), this mixed stream of warm waste gasses is then the gas stream used for the pre-drying, with the required drying temperature being trimmed with the H-501 heater.

3.2.4 Pre-treatment, Utilities, and Services Sizing

Similar to the previous HTL biorefinery simulation, the sections of plant and equipment not featured in the Aspen Process simulation model (figures 3.7 to 3.10) are sized according to the total mass flow rate of macroalgae, and/or total predicted heating duty where the Aspen model provides sufficient information. Again, the comprehensive desktop design study by Knorr et al(2013) is utilised to adapt the supporting equipment packages as singular unit operations.[193]

3.2.5 Biomass Supply and Quality

For the model presented in this chapter, it is assumed that all macroalgal biomass is suppled pre-dried and processed to a uniform coarse crushed material. Sun drying of seaweed is a cheap and low-technology solution to reducing the shipping weight of biomass, and has been shown not to affect bulk proximate composition compared to more energy intensive drying technologies (e.g. oven drying or freeze drying).[237] Furthermore it is assumed that up to three different sources of biomass will be used at any one time and blended on site. Having the option to manage a recipe of different biomass qualities allows for a more stable product to be produced with seasonal products by blending of different species or harvests to smooth out quality variations.

Therefore, the quality of seaweed feed used in the Aspen simulation represents an idealised "blend" quality. The target biochemical analysis of the blended seaweed product is described in table 3.3. This blended seaweed feedstock has properties broadly between those presented in the previous chapter on HTL (chapter 2, table 2.6) , and represents a medium quality that could be reasonably achieved by blending of mixed seaweed sources from a diverse (potentially global) supply chain.

Modelling of operations further up the supply chain, and the pre-processing undertaken by biomass suppliers is not considered in the scope of this work. As such, biomass of the quality described in table 3.3 is assumed to be delivered to the plant gate at a landed cost of between £500 /dry-ton and £2000 /dry-ton.

3.2.6 Equipment costing basis

Equipment is costed as previously described (chapter 2, section 2.3.5). Briefly, capital expenses are determined by itemising the required equipment. Where sufficient data is available from Aspen (eg $\dot{}$for material or heat flows) these are used to size equipment, where unavailable equipment is sized according to the plant throughput and the generic 6/10ths scaling laws after having found a suitable alternative sized and costed item in the literature.

Table 3.3: Target ultimate and proximate analysis of the blended biomass product.

Component	Composition	Unit
Ultimate analysis		
Ash	27.0	% wt(dry)
Carbon	31.8	% wt(dry)
Hydrogen	6.1	% wt(dry)
Nitrogen	1.9	% wt(dry)
Chlorine	0.0	% wt(dry)
Sulfur	0.8	% wt(dry)
Oxygen	32.4	% wt(dry)
Proximate analysis		
Moisture	11	% wt(wet)
Fixed Carbon	40	% wt(dry)
Volatile Matter	33	% wt(dry)
Ash	27	% wt(dry)
Biochemical analysis		
Carbohydrate	63	% wt(dry)
Lipid	1	% wt(dry)
Protein	14	% wt(dry)
Fibre	21	% wt(dry)

$$C_I = F_I C_0 \left(\frac{S}{S_0}\right)^{sf} \tag{3.3}$$

$$C_{I_{2020}} = C_{I_n} \times \frac{CEPCI_{2020}}{CEPCI_n} \tag{3.4}$$

Where C_I is the installed cost, F_I is the installation factor, C_0 is the equipment cost at the base scale, S and S_0 are the scales at the model and base scale respectively, and sf is the scaling factor for the equipment. Where values of sf are not readily available for specific items of equipment, a value of 0.6 is used as is the standard applications of the 6/10ths rule. All prices are adjusted to 2020 as a static base case by use of the Chemical Engineering Plant Cost Index ($CEPCI$) for both the base case year (n) and 2020 for each specific type of equipment.

3.2.7 Economic model

Capital expenses for major itemised equipment are determined as described in section 3.2.6, for plants running at a nominal feed rate of 250 tonnes/year, 1,000 tonnes/year, and 10,000 tonnes/year, and both with and without the pyrolysis section of the biorefinery. For the 'without pyrolysis' option the flow sheets are identical, with the exception that the plant shown in A-500 (figure 3.5) is entirely excluded.

3.2.7.1 Total Capital Expenditure

Total capital investment (TCI) is determined by summation of capital expenditure for installation of major equipment, additional direct costs, and costed indirect costs. Additional direct costs (e.g warehousing, site development, ancillary piping) are estimated as a percentage of the installed cost of the major equipment, and indirect costs (contractor insurance, field costs, project management etc.) estimated as a percentage uplift on top of the total direct cost (TDC). These uplifts are detailed in table 3.4.[121]

3.2.7.2 Operating expenditure

Annual operating expenses for the biorefinery are determined by evaluation of both variable and fixed costs. Variable costs are defined as those with are affected by the production volumes such as raw materials and utilities consumption. Fixed costs are those that are incurred independent of the production volumes, and in this case are defined as labour costs and the servicing of debt required to finance the construction of the biorefinery.

Start-up of a new manufacturing process inevitably produces off-spec product, with variable reliability, and at inconsistent production speeds. The production ramp-up of a newly starting manufacturing operation is modelled by utilisation of an Overall Equipment Effectiveness ratio (OEE), which combines production metrics that track Quality, Performance, and Availability together. The anticipated production metrics are detailed in table 3.5.

Table 3.4: Additional direct costs and indirect cost uplift applied to the installed equipment cost. Values from Davis et al. (2016).[121]

Item	Description	Cost uplift
	Additional direct costs	
Warehousing	On-site storage of equipment and supplies.	4.0 % of installed equipment costs for A-100 through to A-600
Site development	Includes fencing, curbing, parking lot, roads, well drainage, rail system, soil borings, and general paving. This factor allows for minimum site development assuming a clear site with no unusual problems such as right-of-way, difficult land clearing, or unusual environmental problems.	9.0 % of installed equipment costs for A-100 through to A-600
Ancillary piping	Connection of equipment both within plant boundaries and connection to utilities supplies outside of plant.	4.5 % of installed equipment costs for A-100 through to A-600
	Indirect costs	
Prorateable expenses	Includes fringe benefits, burdens, and insurance of the construction contractor.	4.0 % of TDC
Field expenses	Consumables, small tool and equipment rental, field services, temporary construction facilities, and field construction supervision.	4.5 % of TDC
Home office and construction	Engineering plus incidentals, purchasing, and construction.	10.3 % of TDC
Project contingency	Extra cash on hand for unforeseen issues during construction.	10.0 % of TDC
Other costs	Start-up and commissioning costs; land, rights-of way, permits, surveys, and fees; piling, soil compaction/dewatering, and unusual foundations; sales, use, and other taxes; freight, insurance in transit and import duties on equipment, piping, steel, and instrumentation; overtime pay during construction; field insurance; project team; and transportation equipment, bulk shipping containers and plant vehicles.	2.6 % of TDC

$$\text{OEE} = \text{Quality} \times \text{Performance} \times \text{Availability} \tag{3.5}$$

$$\text{Quality} = \frac{\text{Quanntity of product achieving First Pass quality}}{\text{Total quantity of material produced}} \tag{3.6}$$

$$\text{Performance} = \frac{\text{Actually achieved production velocity}}{\text{Budgeted nominal production velocity}} \tag{3.7}$$

$$\text{Availability} = \frac{\text{Actually achieved production hours}}{\text{Budgeted nomical production hours}} \tag{3.8}$$

Table 3.5: Overall equipment effectiveness (OEE) production metrics throughout start-up and commissioning period.

Production year, n	Quality metric	Performance	Availability	OEE
0	0 %	0 %	0 %	0 %
1	50 %	50 %	40 %	10 %
2	78 %	80 %	80 %	50 %
3	94 %	95 %	95 %	85 %
4 +	96.5 %	96.5 %	97 %	90 %

Variable costs are determined on a yearly basis by down-rating the steady-state consumption of utilities and materials according to the OEE, determining the inflationary uplift on the unit price for the year of operation:

$$VC_{i,n} = (Q_i \times t_{annual}) \times OEE_n \times P_i \times I_n \tag{3.9}$$

$$I_n = (1 + r)^n \tag{3.10}$$

Where $VC_{i,n}$ is the annual variable cost of component i (eġraw material, utilities) for year n, Q_i is the steady-state hourly consumption of component i, t_{annual} is the annual operating hours of the process, OEE_n is the OEE for year n (detailed in table 3.5), P_i is the unit price of component i (determined for year 0), I_n is the inflationary uplift applied to costs for subsequent years following year 0, and r is the average inflation rate expressed as a decimal fraction. Fixed costs are determined similarly.

Labour costs are determined according to the staffing deployment plan detailed in table

3.6. 2011 Salary is adjusted to 2020 using the Engineering and Supervision element of the Chemical Engineering Cost Price Index (CECPI), thereafter similarly to as the labour costs are uplifted on an annual basis according to average interest rate for the project lifetime.

Table 3.6: Labour and supervision plan for different scale plants. Values from Davis et al. (2016).[121]

		Number of staff employed in a plant of capacity:		
Job role	2011 Salary, $ USD	250 t/year	1,000 t/year	10,000 t/year
Plant Manager	155,400	1	1	1
Maintenance Supervisor	60,257	0	1	1
Maintenance Technician	42,286	1	2	3
Shift Supervisor	50,743	1	2	3
Production Operator	26,872	5	10	15
Clerks, Secretaries, and Aministration	38,057	1	2	3

Servicing of debt on an annual basis is determined by assuming that the Total Capital Investment (TCI) is financed through a debenture loan and paid back as an amortized bond. The annual repayment on the principal loan is therefore determined as follows:

$$A = TCI \times \frac{r_l(1+r_l)^n}{(1+r_l)^n - 1} \tag{3.11}$$

Where A is the fixed annual repayment amount, TCI is the principal loan, r_l is the annual interest rate offered on the loan, and n is the total number of years that the loan is offered over. Base costs (Year 0) for raw materials and utilities, as well as the

financial constants (interest, and loan terms) are detailed in table 3.7.

Table 3.7: Unit prices and financial constants for the base year, 2020 (Year 0).

Component	Unit price	Cost unit	Component	Unit price	Cost unit
Seaweed[a]	500 to 5,000	$ / tonne	Electricity[e]	0.10	$ / kWh
Sodium carbonate[b]	250	$ / tonne	Gas (heat)[e]	0.05	$ / kWh
Sulfuric acid[b]	888	$ / tonne	Towns water[f]	0.08	$ / m^3
Sodium hydroxide[b]	390	$ / tonne	Effluent treatment[g,h]	$0.6785 \times q^{0.9739}$	$ / year
Cellulose[b,c]	2,500	$ / tonne	Financial constants		
Glycerol[b]	500	$ / tonne	Inflation rate	3.00	% Annually
Calcium chlroide[b]	140	$ / tonne	Loan interest	5.00	% APR
Liquid nitrogen[d]	618	$ / tonne	Loan term	20	years

a) Assumed cost for this scenario.

b) Costs retrieved from ChemBid.com in Mar-2022 for bulk supply (1-ton) of standard industrial grade

c) Grade of Micro-crystalline cellulose from ChemBid.com

d) Leon et al. 2020.[238]

e) Assumed industrial utilities costs for this work.

f) Ulrich et al. 2006, natural water pumped and screened, grass roots plant.[198]

g) Ulrich et al. 2006, primary and secondary treatment, grass roots plant.[198]

h) Where q is the annual effluent volume in m^3

3.2.7.3 Minimum Biopolymer Selling Price

The Minimum Biopolymer Selling Price (MBPSP, $ kg^{-1}) for each case is determined by assessing the sum of both variable and fixed cost on an annual basis, then totalling all annual spends over the lifetime of the plant to give a total cost of operating the plant for the life of the loan period. The total quantity of biopolymer product is similarly determined on an annual basis, by taking the nominal steady-state hourly production rate of the biopolymer, multiplying by the annual operating hours, and then down-rating the total quantity of product by the OEE values listed in table 3.5.

$$MBPSP = \frac{\sum_n \left(\sum_i VC_{i,n} + \sum_j FC_{j,n} \right)}{\sum_n Q_{BP,n}} \tag{3.12}$$

Where $VC_{i,n}$ and $FC_{j,n}$ are the variable and fixed costs respectively of elements i or j, during year n, and $Q_{BP,n}$ is the total quantity of biopolymer produced in year n.

3.2.7.4 Impact of Char

For the biorefinery models where pyrolysis scenarios are included, three scenarios around char valorisation are considered. In the first scenario, char is produced at cost to the biorefinery with no revenue stream generated from it as a product. The second scenario considers char as a vector for the transfer and trading of carbon credits, with the achieved price being tied to the projected traded carbon price under the EU Emission Trading Scheme according to:

$$P_{carbon,n} = \frac{P_{CO_2,n}}{C_{CO_2}} \tag{3.13}$$

$$P_{char,n} = P_{carbon,n} \times \frac{C_{char}}{100} \tag{3.14}$$

Where P refers to the unit price for CO_2, carbon, and char, and C refers to the wt. % concentration of carbon in CO_2 and char. Projected prices for the ETS price of CO_2 are taken from the UK Governments' BEIS price growth assumption publication, where prices are projected to rise from 19.11 \$ tonne^{-1} in 2020 up to 59.82 \$ tonne^{-1} in 2030 and thereafter remaining flat.[206]

The third and final scenario considers the char as a valuable product which can be sold as a soil amendment for improving soil fertility, hence commanding a higher price again. For this an initial price of 150 \$ tonne^{-1} is selected for year 0, with the unit price ratchetting up according to the annual inflation in the same fashion that utilities and raw materials costs are modelled to increase.[239]

3.3 Results

3.3.1 Aspen Plus Simulation results

Given many of the components modelled in this simulation are not conventional components found in the Aspen Plus databanks, bulk properties (e.g. heat capacity, density) are approximated based on the user defined component attributes (ULTANAL, SULFANAL, PROXANAL) and specified methods (HCJ1BOIE and DCOALIGT). Approximated values determined in Aspen Plus are listed in table 3.8, and compared to some typical experimental values previously reported in the literature.

3.3.1.1 D-301 Film Belt Dryer Optimisation

It was apparent early on that the major energy consumer of the plant would be the continuous film-belt drier, since this equipment is responsible for evaporating a significant quantity of water. Figure 3.8 shows the implementation of this drier in Aspen Plus. Drying is modelled in Flash block, where a stream of heated air is brought into close

Table 3.8: Comparison of bulk density and heat capacity, of predicted values from Aspen Plus and literature results.

	Predicted values from Aspen Plus		Experimental values from Literature		
Non-conventional component	Bulk density, ρ	Heat capacity, c_p	Bulk density, ρ	Heat capacity, c_p	Refs
	kg m^{-1}	kJ kg^{-1} K^{-1}	kg m^{-1}	kJ kg^{-1} K^{-1}	
Seaweed	1.37	1.48	0.201 (0.269)	1.441 (0.124)	[240–242]
Pyrolysis char	1.59	1.45	0.387[b,c] (0.062)	1.143[b,c] (0.413)	[83, 243–245]
Biomass Ash	2.82	0.92	0.584[a] (0.289)	2.387[a] (0.858)	[246, 247]

a) Determined from wood ash.

b) Determined from a blend of macroalgae and terrestrial crops.

c) Undefined 'biomass' pyrolyzed at high temperature.

contact with the film-forming solution in order to affect the evaporation of the water. The detail pertaining to internal drier dimension and air velocities are not considered in this work, however the total latent heat requirement to affect drying is.

A cost minimisation exercise was performed to find the optimal purge/recycle ratio of hot air from the dryer, in order to balance the heating cost for the dryer trim-heater (H-302), the electrical cost for the dryer fans (F-301 and F-302), and to respect the maximum allowable temperature for the alginate film.

Bagheri et al. (2019) reported on the impact of different drying conditions on glycerol-plasticized alginate films, and showed the differential thermal gravimetry (DTG) curves for the resulting films.[248] DTG of the different films all showed a modest change in mass around 100 °C, an inversion point at around 150 °C, followed by a sharp change in weight at just over 200 °C. A maximum allowable film temperature of 150 °C was therefore selected for the optimisation work.

The first optimisation was to determine the minimum safe operating limit for the exhaust/recycle damper position. At high-purge/low-recycle positions (e.g. exhaust damper fully open, recycle fully closed) there is minimal build up of humidity, since dying air is used in a "once through" arrangement. However, this once-through operating condition represents poor energy management since all the heated air is exhausted immediately.

Conversely a low-purge/high-recycle position (e.g. exhaust damper closed, recycle damper fully open), the majority of the hot and moist air from the dryer is recycled back through the trim-heater and back not the dryer. This represents possibly a more energetically favourable condition since the more of the heat is retained, however the decrease in the quantity of air being bled to the exhaust requires the average humidity of said air to increase in order to maintain a steady state mass balance. For practicalities sake a minimum floor of 5 % purge ratio (i.e. 5 % of the total flow entering the splitter block is diverted to the exhaust, 95 % is recycled) was selected to ensure there is always a material outlet to carry away the excess moisture.

The Sensitivity Analysis tool is used in Aspen to sweep through the dryer trim heater (H-302) set-point temperatures (100 °C to 400 °C) and purge ratios (0.05 to 1), whilst a design condition is employed to achieve a water content of ≤ 5 % by varying the total quantity of fresh inlet air being introduced via the exhaust economiser heat exchanger (H-301).

Figure 3.11 shows the result of the first optimisation exercise. When considering the imposed design condition of a maximum film temperature of 150 °C it is immediately apparent that at purge ratios below 0.20 there is risk of over-heating the polymer during the drying process depending on the operating temperature of the dryer. This is a result of the polymer being over-dried well below the 5 % wt. design specification and the loss of all water from the structure, causing rapid heating of the remaining alginate matrix.

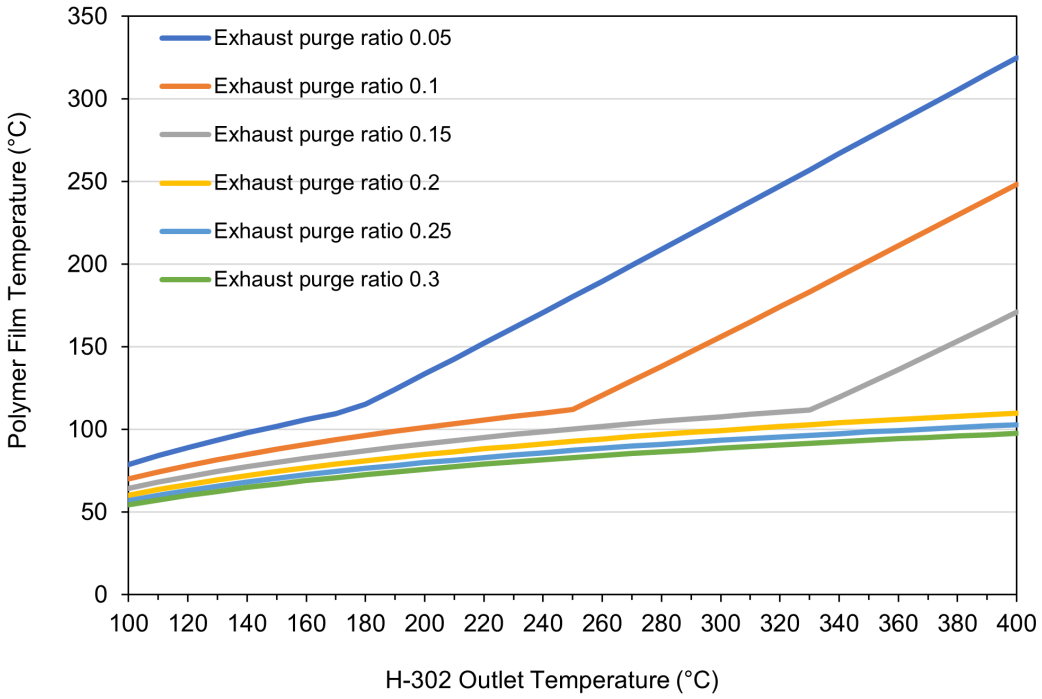

Figure 3.11: Resulting polymer film outlet temperature at different heater set-point temperatures and exhaust purge ratios, for the 10,000 ton year^{-1} biorefinery.

Figures 3.12 and 3.13 show the heat and electrical energy requirements for the main trim heater (H-302) and dryer recirc fan (F-301) respectively. The dryer recirc fan power is determined by assuming 90 % efficiency for fan blades (μ_f), drive belt (μ_B),

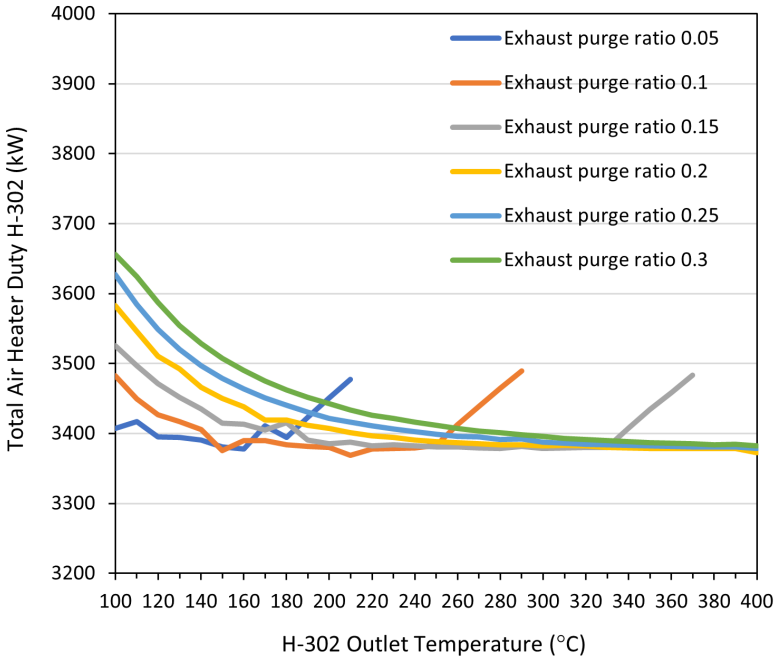

Figure 3.12: Total required duty for air trim heater (H-302) as a function of air-heater temperature set-point, for the 10,000 ton year^{-1} biorefinery, and subject to the variable fresh-air flow rate design spec to respect the maximum film moisture.

and motor (μ_m), and a differential pressure of 2 kPa (equations 3.1 and 3.2). The absorbed power is reduced to a function of the volumetric flow through the fan, thus the density of the gas stream at process conditions is also used to correct from the mass flow in Aspen.

As the trim heater (H-302) set point temperature increases, the heat requirement for the overall process decreases for almost all exhaust purge ratios (figure 3.12). This is due to the reduced total air-flow required to affect the drying at higher delivery temperature to the dryer, hence an overall lower mass of air that needs heating up.

Correspondingly, the electrical power absorbed by the recirculation fan drops dramatically at increasing trim-heater temperatures (figure 3.13), however the trend with the exhaust purge ratio inverts as the H-302 temperature set-point is increased. At low temperatures (e.g., $\leq$ 150 °C) higher exhaust purge ratio results in lower total power absorbed, compared to that at higher temperatures (e.g., $>$ 250 °C) lower purge ratios

result in overall lower power required. The inflexion point appears visually to be around an H-302 set point of 180 °C. Below this temperature there is insufficient sensible heat in the air stream to complete the drying, thus a requirement for greater and greater quantities of fresh-air to be introduced, and hence a higher total recirculation flow and higher energy cost. Conversely at temperatures greater than 180 °C there is a lower and lower requirement for fresh air to be introduced as there is increasingly more available enthalpy in the drying air stream to achieve the required drying without needing to increase the total mass-flow of air through the dryer.

This double effect is extremely noticeable on both figures 3.12 and 3.13 with sharp decreases in the heat and power required respectively at increasing temperatures up to 180 °C, followed by more modest decreases thereafter.

Hourly cost of operation is therefore simply determined by multiplying the heat and power requirement along each operating line by the unit prices quoted in table 3.7: Unit prices and financial constants for the base year, 2020 (Year 0), and summed together to give an indication of the steady state cost of operation (figure 3.14). Minimum operating price is achieved whilst running at maximum temperature set-point for H-302, and with as low purge ratio as possible without risking overheating of the polymer film. Thus, for final sizing of the equipment and costing calculations an exhaust purge ratio of 0.2 (0.8 recycle ratio) and H-302 set point of 300 °C are selected. At this condition there is a balance of relatively low operating cost, safe operation (purge ratio 0.2 never risks overheating the polymer), whilst leaving plenty of head-room above the design point of 300 °C should it be required to drive the set-point higher to maintain control authority. A higher design temperature might appear to be desirable, however the additional wall thickness to ducts and material requirements for components such as fan impellers for high temperature (operating at >350 °C) operation makes it less desirable to operate higher than this point for relatively small gains in indicated steady state running costs.

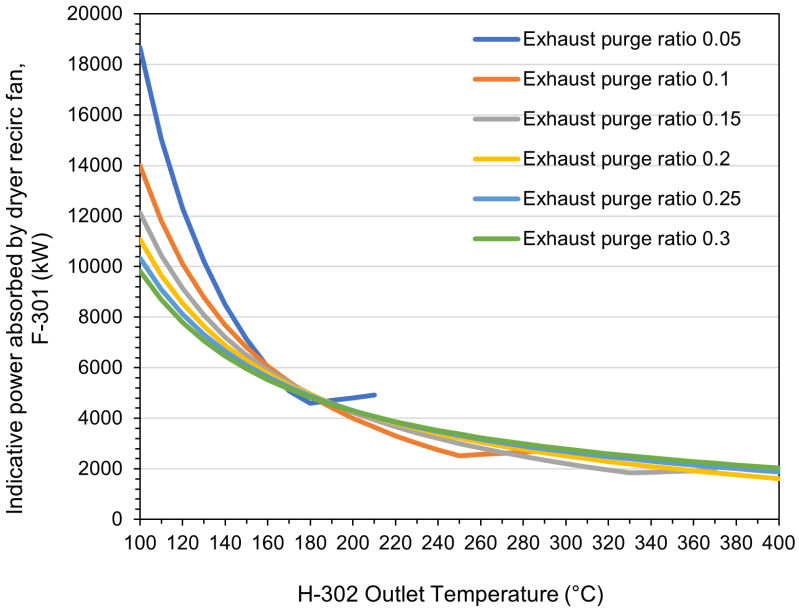

Figure 3.13: Indicative power requirement for dryer recirculation fan, F-301, as a function of H-302 outlet temperature and the exhaust purge ratio for the 10,000 ton year^{-1} biorefinery, and subject to the variable fresh-air flow rate design spec to respect the maximum film moisture. For Exhaust purge ratios of 0.05, 0.1, and 0.15 the trends are clipped for operating conditions where the maximum polymer temperature is not respected.

3.3.2 Financial results and MBPSP

3.3.2.1 Total Capital Investment

The summary of total capital investment required for different biorefinery scenarios is shown in table 3.9. Total cost of installed equipment ranges from a low of $470,840 for the 250 tonne year^{-1} scale plant without pyrolysis, to a high of $12,032,281 for the 10,000 tonne year^{-1} plant when including on-site nitrogen generation for the slow pyrolysis process.

Comparing purely the different scale plants with the same approach to pyrolysis, the impact of increasing scale from 250 tonne year^{-1} to 1,000 tonne year^{-1} (4 fold increase in scale) is associated with only an approximate 2.5 fold increase in the cost of equipment. Similarly, the 10 fold increase in scale between 1,000 tonne year^{-1} and 10,000 tonne year^{-1} is achieved with approximately 4.5 fold increase in the cost of equipment.

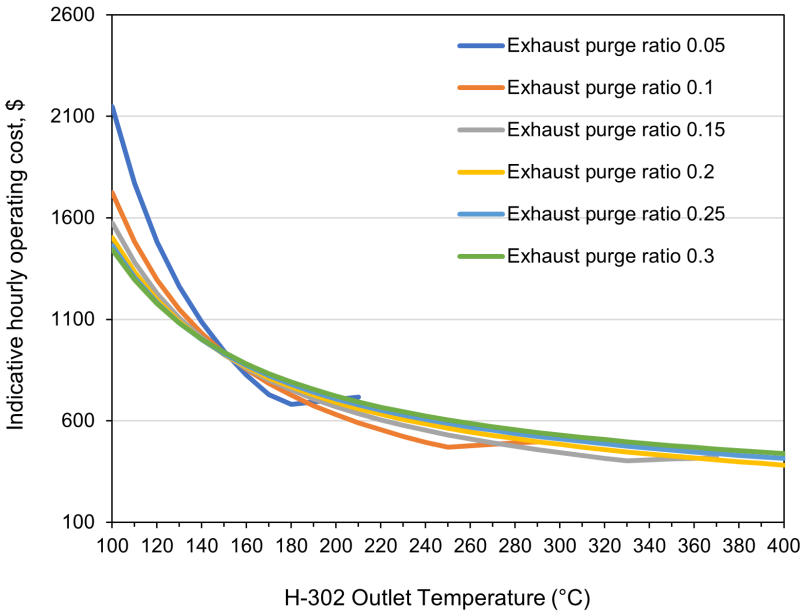

Figure 3.14: Indicative hourly operating cost for D-301 major equipment, for the 10,000 ton year-1 biorefinery and using electrical unit price of \$0.10 kWh^{-1} and thermal unit price of \$0.05 kWh^{-1}.

Figure 3.15 visually shows the difference in installed equipment costs at different scales. For all pyrolysis treatments the total installed cost scales with a power law scaling factor of 0.64 to 0.68. Figure 3.15 also shows how relatively small the capex impact of adding the slow-pyrolysis plant on only, when comparing the 'Without Pyrolysis' to the 'With Pyrolysis and buying LN_2' scenarios. Provision of nitrogen to sweep the pyrolysis reactor is considered by two options – on-site air purification to generate oxygen free nitrogen stream (high capex, low opex), and contract delivery of liquid nitrogen to site where it is vapourised to provide gaseous nitrogen on demand (low capex, high opex).

Comparing different provisions of nitrogen the same scale (table 3.9 and figure 3.15) shows that the impact of choosing to generate nitrogen on-site will demand approximately double the up-front capital investment into equipment, in order to build the air purification plant.

Table 3.9: Summary capital expenditure for 10,000 tonne year^{-1}, 1,000 tonne year^{-1}, and 250 tonne year^{-1} biopolymer biorefineries. For each scale the plant is presented in conditions: **A)** including the slow-pyrolysis section and with on-site N_2 generation, **B)** including the slow-pyrolysis section and with liquid-N_2 brought in from off-site, and **C)** without slow-pyrolysis at all.

CAPEX costs by category, 10^3 $ USD (2020)	Plant scale and pyrolysis approach: 10,000 tonne year^{-1}			1,000 tonne year^{-1}			250 tonne year^{-1}		
	A	B	C	A	B	C	A	B	C
Total Installed Equipment	12,032.3	6,189.4	5,575.7	2,762.1	1,294.4	1,186.5	1,148.9	510.1	470.8
Warehousing	481.3	247.6	223.0	110.5	51.8	47.5	46.0	20.4	18.8
Site Development	1,082.9	557.0	501.8	248.6	116.5	106.8	103.4	45.9	42.4
Ancillary piping	541.5	278.5	250.9	124.3	58.2	53.4	51.7	23.0	21.2
TOTAL DIRECT COSTS	14,137.9	7,272.5	6,551.5	3,245.4	1,520.9	1,394.1	1,349.9	599.3	553.2
Prorateable expenses	565.5	290.9	262.1	129.8	60.8	55.8	54.0	24.0	22.1
Field expenses	636.2	327.3	294.8	146.0	68.4	62.7	60.7	27.0	24.9
Home office and construction	1,456.2	749.1	674.8	334.3	156.7	143.6	139.0	61.7	57.0
Project contingency	1,413.8	727.3	655.2	324.5	152.1	139.4	135.0	59.9	55.3
Other costs	367.6	189.1	170.3	84.4	39.5	36.2	35.1	15.6	14.4
TOTAL INDIRECT COSTS	4,439.3	2,283.6	2,057.2	1,019.1	477.6	437.7	423.9	188.2	173.7
TOTAL CAPITAL INVESTMENT	**18,577.2**	**9,556.1**	**8,608.7**	**4,264.5**	**1,998.5**	**1,831.8**	**1,773.8**	**787.5**	**727.0**

3.3.2.2 Operating Expenses

Annual operating expenses for an example 10,000 tonne year^{-1} plant are shown in figure 3.16. Variable cost (utilities, raw materials) ramp up from Year-0 to Year-4 as the OEE ramp-up progresses through start-up and commissioning, with fixed costs (labour, loan repayment) remaining relatively flat over the whole operating period.

Of the variable costs the seaweed supply is by far the dominant recurrent operating expense, making up almost 74 % of the total annual operating costs for the 10,000 tonne year^{-1} plant shown in figure 3.16. Repartition of the total annual operating expenses at nominal-scale operation for different scale biorefineries is shown in figure 3.17. In all cases, with a seaweed supply cost of 2000 $ tonne^{-1} the provision of seaweed biomass is the largest single annual expense, making up 43.0 % of the recurrent operating costs for a 250 tonne year^{-1} plant operating a pyrolysis plant with on-site N_2 generation, up to a maximum of 75.6 % for the 10,000 tonne year^{-1} plant with no pyrolysis. The fraction of labour costs shrink precipitously as the scale of the plant increases however, shrinking from a maximum of 38.2 % of annual costs for the 250 tonne year^{-1} plant to

a minimum of 3.7 % of annual costs for the 10,000 tonne year^{-1} plant. This dramatic ten-fold decrease in the share of annual opex being used to cover labour costs is as a result chiefly of larger equipment with higher overall anticipated plant productivity. Whilst the total labour bill naturally increases as the scale of plant increases and the labour deployment increases (table 3.6), the specific productivity (tonnes of product produced per employee per year) of the biorefineries increase as the size of specific items of equipment increases – e.g. operating of an extraction vessel, centrifuge, or continuous dryer is much the same task for an operator independent of the size of the equipment, however clearly a larger piece of equipment is capable of producing much more product.

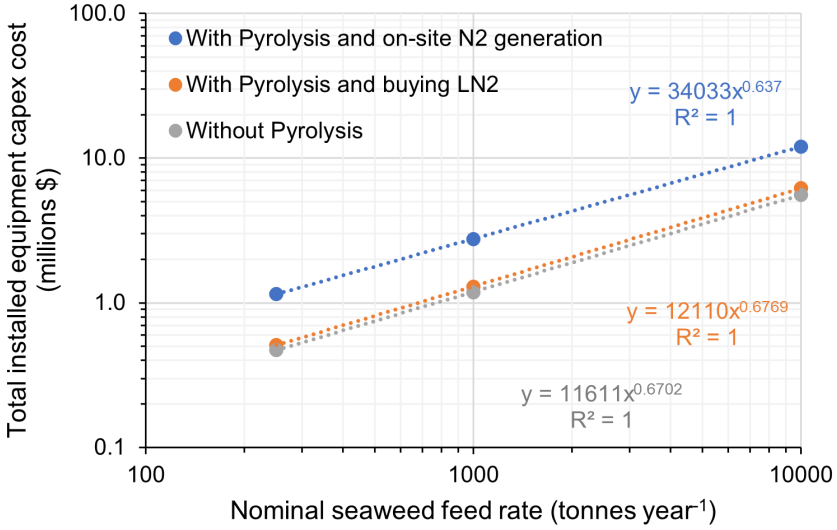

Figure 3.15: Total installed equipment cost as a function of installed plant scale, and by pyrolysis treatment option.

3.3.2.3 Minimum Biopolymer Selling Price

Total operating expenses for the proposed 20-year term are summed for each scale biorefinery, with different pyrolysis options, and at three different prices for the supply of macroalgae. This total cost of operations for the 20-year operation of the plant is then divided by the total anticipated quantity of product, to produce a base-case minimum biopolymer selling price (MBSP) (table 3.10). The minimum MBSP of 4.09 \$ kg^{-1} is achieved at the 10,000 tonne year^{-1} scale with no pyrolysis, and a macroalgae supply

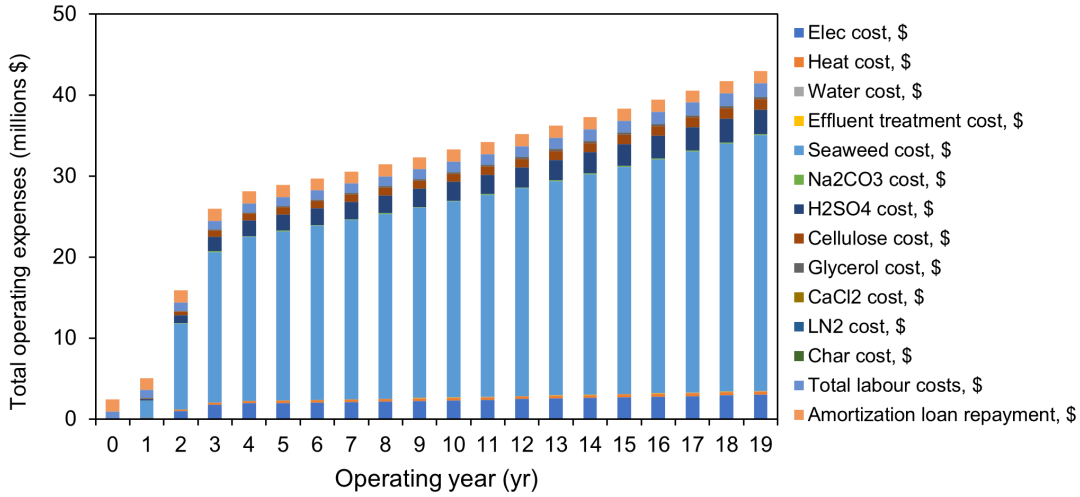

Figure 3.16: Summary of total year-on-year operating expenses incurred for a 10,000 tonne year^{-1} plant, with macroalgae supplied at 2,000 $ tonnne^{-1}, operating with a pyrolysis plant, on-site nitrogen generation, and no additional valorisation of char.

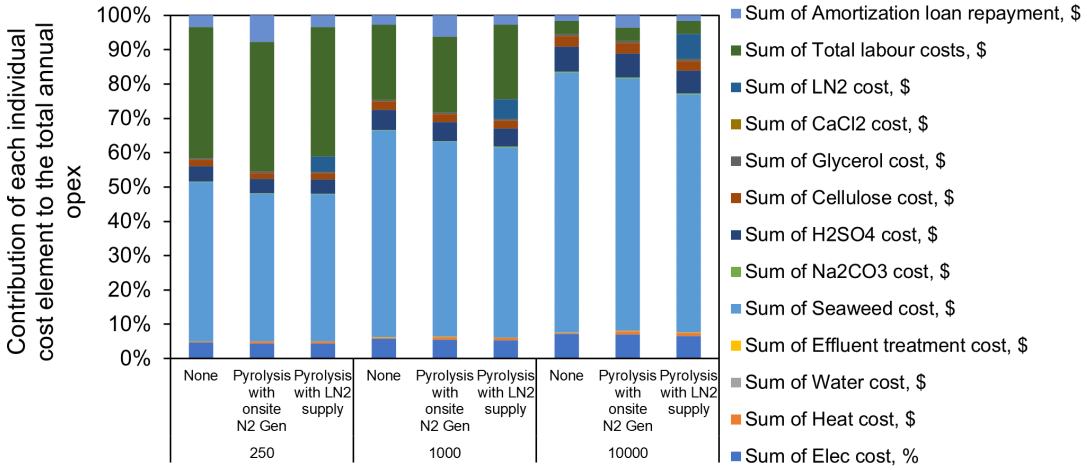

Figure 3.17: Repartition of total annual operating expenses for years in full production (year-5 onwards) for different scale plants, with different pyrolysis options, and a seaweed supply price of 2000 $ tonne^{-1}.

price of 500 $ tonne^{-1}. The maximum MBSP observed was 27.81 $ kg^{-1} for a 250 tonne year^{-1} plant operating with pyrolysis and on-site nitrogen generation.

General trends previously observed regarding the installed scale of the biorefinery are maintained, with larger plants able to produce product biopolymer for a significantly lower MBPS compared to smaller plants. Macroalgal price also has a significant impact

on the resulting MBPS, which is entirely expected from the ongoing opex repartition displayed in figure 3.17.

In all cases producing the biopolymer is cheaper without the pyrolysis step, with the lifetime cost of the pyrolysis plant adding a "pyrolysis-premium" of 0.34 \$ kg^{-1} to 1.56 \$ kg^{-1} to the MBPS. However, comparing the two scenarios for operating a pyrolysis plant (on-site nitrogen generation vs. liquid nitrogen supply) the impact on MBPS changes as a function of the plant scale. At the small scale (250 tonne $year^{-1}$), it's cheaper to operate a pyrolysis plant using liquid nitrogen to supply the required purge gas for the pyrolysis reactor. At this relatively small scale the price-premium incurred by buying in nitrogen from off-site is overall lower than the large capex impact associated with building on-site nitrogen generation (table 3.9). However, at the medium scale (1000 tonne $year^{-1}$) and above it becomes cheaper to invest up-front in on-site nitrogen generation over the 20 year financing period (table 3.9), since the higher nitrogen consumption for larger biorefineries incurs a greater total cost when buying LN_2 in from an external supplier compared to running and operating on-site air purification.

Table 3.10: Minimum biopolymer selling price for different scale biorefineries with different macroalgae cost price, with cost of finance spread evenly over 20-year amortized loan period. No additional valorisation of the char is considered.

Macroalgae Price \$ ton^{-1}	Pyrolysis, and Nitrogen provision	Seaweed Feed, tonne $year^{-1}$		
		250	1,000	10,000
		Minimum Biopolymer Selling Price \$ kg^{-1}		
500	With, on-site N_2	12.14	7.64	4.43
	With, LN_2	11.87	7.79	4.93
	Without	10.59	6.75	4.09
2,000	With, on-site N_2	17.37	12.86	9.66
	With, LN_2	17.09	13.02	10.16
	Without	15.81	11.97	9.31
5,000	With, on-site N_2	27.81	23.31	20.10
	With, LN_2	27.54	23.46	20.60
	Without	26.26	22.42	19.76

3.3.2.4 Impact of Char Valorisation

So far, the biorefineries considered are all treating the pyrolysis char product as a zero-value by-product, being produced entirely at-cost to the biopolymer process. The impact of char valorisation is considered at multiple plants scales and multiple macroalgae prices, for the biorefinery with pyrolysis and on-site nitrogen generation. The impact on MBSP of the different char valorisation scenarios as laid out in section 3.2.7.4 is shown in table 3.11. In addition to the two different options for generating revenue from the char previously laid out, a third option is included that combines the selling of the char product as a soil amendment as well as claiming the carbon credits for trading in the ETS.

The previously highlighted "pyrolysis premium" of 0.35 \$ kg^{-1} on MBPS for the large scale biorefinery can be significantly reduced by char valorisation, with the additional cost impact on the minimum biopolymer selling price reducing to 0.28 \$ kg^{-1}, 0.12 \$ kg^{-1}, and 0.05 \$ kg^{-1} when the char is valorised by emissions offsetting, as a soil

Table 3.11: Impact of different char valorisation scenarios on MBPS, for different scale biorefineries, utilising on-site nitrogen generation and slow pyrolysis, and a fixed price of 2000 \$ $tonne^{-1}$ for seaweed supply.

Biorefinery Case, Seaweed at 2,000 \$ ton^{-1}	Seaweed Feed, tonne $year^{-1}$		
	250	1,000	10,000
	Minimum Biopolymer Selling Price \$ kg^{-1}		
No Pyrolysis	15.81	11.97	9.31
Char of zero value	17.37	12.86	9.66
Char valued as $eqCO_2$ and traded under the ETS[a]	17.30	12.79	9.59
Char sold as BioChar soil-ammendment	17.14	12.64	9.43
Char sold both as BioChar, and $eqCO_2$ credits gained under ETS	17.07	12.57	9.36

a) $eqCO_2$ is determined as the equivilent mass of CO_2 based solely on the elemental carbon wt. % of the char, trading is done via Emissions Trading Scheme (ETS) carbon credits.

amendment, and both emissions offset and as soil amendment combined. However, under no scenario or at any scale is it ever economically favourable to pyrolyse the remaining seaweed biomass.

3.4 Discussion

The predicted thermodynamic properties of biomass and pyrolysis reactions products are presented in table 3.8. Comparing the predicted values to average experimental values reported in literature, it is seen that the heat-capacities are quite similar. This gives good confidence in the accuracy of the Aspen Plus model in determining the required heat-flows, and hence the utilities requirement and the size and cost of heat exchangers.

The predicted density however is significantly different, with predicted bulk densities typically 5-6 times higher than experimentally reported values. This is likely a limitation of using the inbuilt density prediction method (DCOALIGT), which was originally developed to predict the bulk density of coal fuel. Coal is a product of compressing, heating, and decaying biomass over geological timescales, hence the organic biomass residues form higher density compounds. In this case, the higher than predicted density for non-conventional solids would mainly impact the pumping and separation equipment, if Aspen was used to size this equipment. In this work, the sizing and costing of pumping and separation equipment was based on scaling laws in previously published biorefinery models, hence the large discrepancy in the predicted vsàctual density of non-conventional components is likely to have minimal impact on the overall biorefinery scale or costs.

Additionally, as presented in figure 3.17, the main factors that contribute to the lifetime cost of running the biorefinery are the seaweed supply and the labour provision, with the overall impact of utilities (e.g. heat, electric) or servicing of debt (e.g. higher/lower capex equipment) contributing a relatively minor component to the overall running costs. Thus, whilst the Aspen Plus model developed in this work certainly has some room for improvement, it is not considered that improved accuracy in the Aspen model

would yield particularly significant effects on the lifetime costs of the plant and/or MBSP.

The estimated total capital investment presented in table 3.9 and figure 3.15 covers a range of scales and difference operating scenarios. The indicated total capital expenditure compares well to established manufacturing processes for commercial biopolymer projects (figure 3.18), with good correlation between the total polymer production rate and the total capital investment across 4 orders of magnitude.

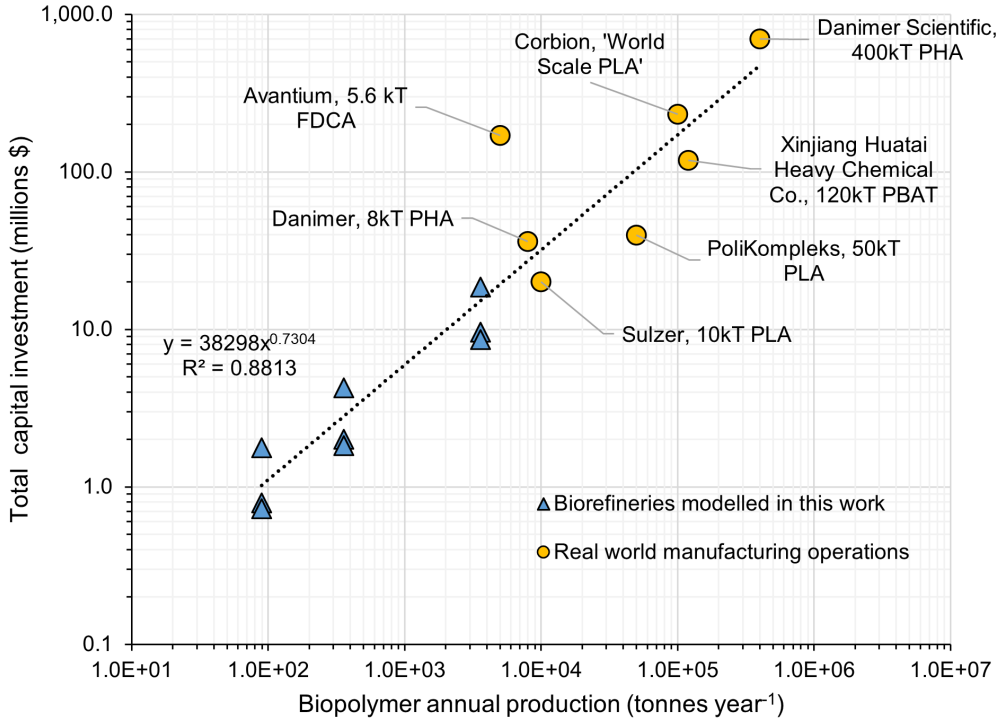

Figure 3.18: Annual biopolymer production quantity vs. total capital investment for biorefineries modelled in this work, and various commercial scale biopolymer plants including PLA, PBAT, PHA, and FDCA production facilities.[**hktAnotherProjectStarted2022**, 249–253]

The close correlation in figure 3.18 gives good confidence in the capital expenditure estimates, and thus with confidence both in the utilities and energy consumption from Aspen Plus and good confidence in the capital costing, there is good confidence in the indicative lifetime cost of polymer (MBSP) given the caveats and raw material prices as given.

A sample of bulk supply prices of various polymers, biopolymers, and recycled polymer resindsresins are plotted in figure 3.19, along with the MBSP for the 10,000 tonne year^{-1} biorefinery presented in this work at the low and medium seaweed supply price. Even at the lowest seaweed supply price, the minimum selling price of the alginate/CNC polymer presented in this work is significantly higher than the majority of traditional virgin bulk polymers (e.g. PE, PP, PET, PS).[254–263] Specialist high performance virgin polymers like PTFE remain relatively high cost in comparison to the cheap bulk products. The unit price of alginate/CNC composite presented in this work that are produced with cheap seaweed supply ends up well in-line with many established biopolymers already available (PLA, PBAT, PLA/PBAT blends). At the high seaweed price the resultant price of alginate/CNC is typically higher than most bulk biopolymers, however significantly below the price for PHA which has a complex production process.

Supply capability has an impact on unit pricing also. Figure 3.20 shows the bulk-supply price of the same selection of polymers and biopolymers, against the individual manufacturers supply capability. The resulting scatter plot shows a clear trend for decreasing bulk supply price with increasing supply capability, which completely aligns with the values presented in table 3.10. The three scales of biorefinery presented in this work sit neatly along a line of best-fit drawn through the commercially available bulk polymers, suggesting that whilst figure 3.19 suggests the price of the alginate/CNC polymer product presented in this work is somewhat higher than established products, it sits approximately where it would be expected given the scale of production considered in this work.

Up until this point all costings were considered on a per kilogram basis, however the plant was designed to produce reels of film i.e. for the food packaging industry. Assuming a product density of 1.34 g cm^{-3}, 1 kg of finished film will produce almost 15 m^2 of film at a thickness of 50 micron, and using a price of 9.66 \$ kg^{-1} (10 kT year^{-1} seaweed feed, 2 \$ kg^{-1} seaweed price, pyrolysis with on-site N_2 generation, table 3.10) this gives a specific cost of film of 0.647 \$ m^{-2}.[101] If this film were used for wrapping fruit punnets (e.g. a standard K37 top-seal fruit punnet, with dimensions 183 mm x 116

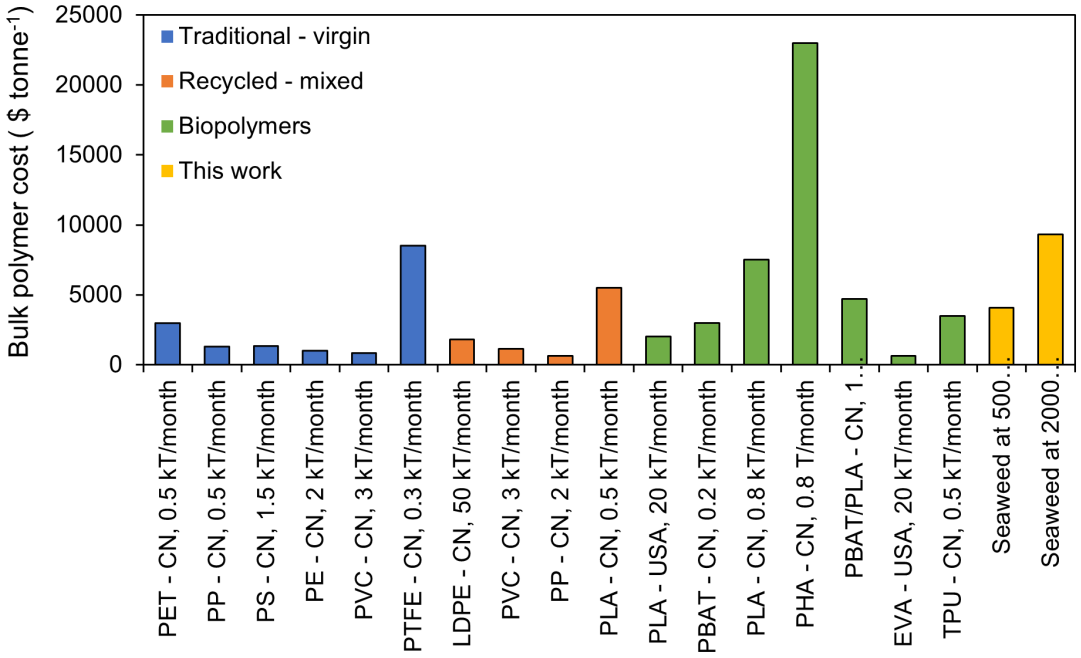

Figure 3.19: Comparison of bulk polymer prices for a range of traditional virgin polymers, recycled resins of mixed sources (traditional and biopolymers), biopolymers, and the alginate/cellulose composite polymer presented in this work at seaweed supply prices of 500 \$ tonne^{-1} and 2000 \$ tonne^{-1}.[254–263]

mm x 50 mm, double-wrapped with a 30 mm overhang at each end), each fruit punnet would require approximately 0.161 m2 of film, at a cost of \$ 0.104 per unit. Adding such as small amount to each unit cost does not represent a large 'green premium', and would be acceptable to most producers, especially of high end goods.

Finally, the impact of char valorisation was considered. For the European emissions trading scheme (ETS) valuation, the carbon content of slow pyrolysis char is used to determine an equivalent mass of CO_2 based on equal masses of carbon. From here, projections on the commodity price for traded CO_2 in carbon credits for UK businesses, as produces by the UK Government Department (BEIS) are used to assign an 'ETS ' value to the char. When considering just the ETS value of the char and the service it provides by being a high carbon content material, it brings in a revenue stream worth approximately \$ 0.07 for every kilogram of finished product (table 3.11). Utilisation of a pyrolysis char as a long-term carbon sequestration material however raises the question

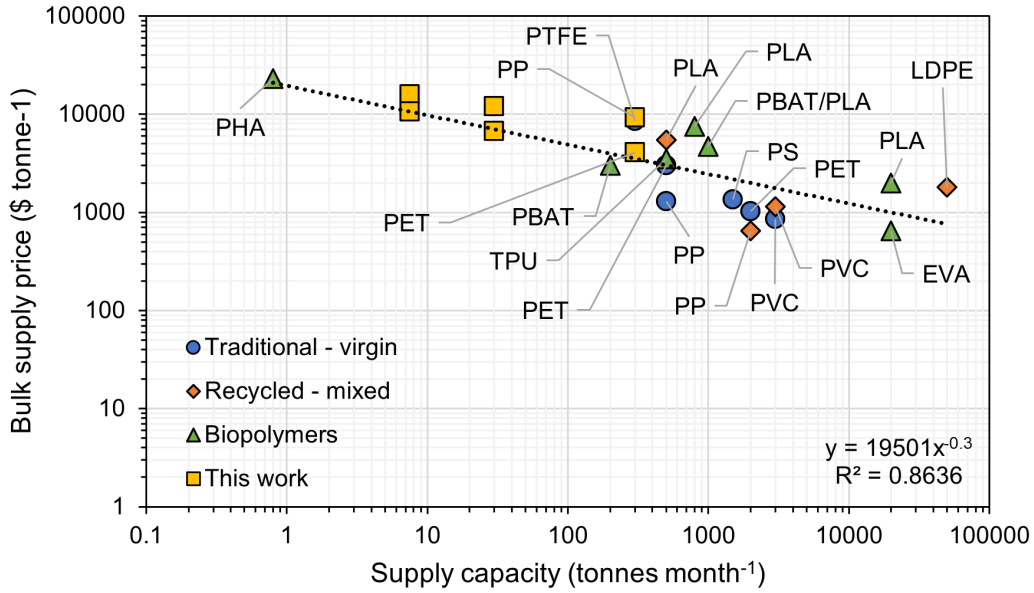

Figure 3.20: Scatter plot of various polymer bulk supply prices compared to the bulk supply capacity for various polymer, biopolymer, and recycled granules, from suppliers with available on-line pricing.[254–263]

of long-term stability of the pyrolyis char, since the benefit of burying pyrolysis char is only realised if the carbon remains stable and in the ground, rather than being oxidised and the carbon returned to the atmosphere as CO_2.

However, pyrolysis char of waste biomass residues is finding a market as Biochar where it is used as a soil amendment. Using a base cost of 150 \$ tonne^{-1}, the financial impact of selling the pyrolysis char as a soil amendment delivers a revenue stream equivalent to \$ 0.23 per kilogram of finished biopolymer. This result brings the MBSP of the pyrolysis process significantly closer to the base-case process where there is no pyrolysis added on, however still somewhat more expensive.

Combining both the ETS and Biochar values of the char results in achieving a best MBSP of 9.36 \$ kg^{-1} for the pyrolysis, compared to a base case value of 9.33 \$ kg^{-1}. This is tantalisingly close to matching the pure financial projections of the base-case where there is no pyrolysis process. In fact, modest increase in the initial price of the biochar from 150 \$ tonne^{-1} to 170 \$ tonne^{-1} brings the MBSP to parity with the

no-pyrolysis base case.

3.5 Conclusions

In this work, a simple technoeconomic analysis was performed, using the Aspen Plus chemical process software as the base process model. Aspen Plus is a useful tool for estimating simple biorefinery processes, achieving moderately accurate estimates of some key thermodynamic properties of biomass (table 3.8), and providing accurate information to allow sizing of CAPEX equipment.

The resulting predicted capital cost of the biorefineries modelled in this work are broadly in-line with established biorefinery operations, offering further confidence in the model and method employed.

Economic viability over a long plant lifetime (20 years) reveals that raw materials costs dominate the ongoing OPEX for large plants, whereas labour costs become more significant at smaller scale. The "productivity premium" gained by scale-up (larger reactors produce more materials, but require only marginally more supervision and maintenance spend) works to shrink the impact of labour costs in the final goods, resulting in a process and product that is extremely price sensitive to the raw-materials costs.

Despite this cost sensitivity, this work demonstrates that alginate/CNC composite biopolymer film can be produced at a cost comparable to other biopolymers currently available, when the seaweed supply is found at the right price. Additionally, inclusion of a pyrolysis step for the production of a potential second value-stream (macroalgal biochar) puts a relatively small price premium on-top of the cost-price of the polymer, whilst simultaneously offering the opportunity to sequester carbon from the atmosphere. In fact, the majority of the pyrolysis premium is likely able to be recovered by valorisation of the waste stream, e.g. through ETS or as Biochar for soil amendment.

Finally, at the 10 kT/year (feed) scale film can be produced that would cost in the order of \$0.10 /unit for consumer convenience food packages. Whilst this does represent a

significant increase in the cost price of a packaging material, an additional $0.10 or so on the final sales price of a premium product would likely be an acceptable "green premium" to the end user. The perceived advantage of shifting away from traditional petroleum based polymers allows companies to better differentiate their products on the shelf, whilst the use of an environmentally benign and degradable material for food packaging helps to reduce the amount of petro-polymer waste entering the ocean.

However, there are some outstanding assumptions in this work that need addressing. This system was built assuming a model “seaweed” to simplify the process model, however both the quality and quantity of actual seaweed supply is both temporally and spatially variable. Feed agnosticism is however a good target to aim for with a biorefinery, thus better exploration of the behaviour of mixed seaweeds through a biorefinery is required.

The targeted extraction of sodium alginate modelled in this work allows the production of a relatively simply and well-published on biopolymer film, however sodium alginate is far from the only valuable biomolecule found in seaweed. Agar and carrageenan are commodity materials, already extracted at scale and traded globally, with more speciality chemicals like fucoxanthins being identified as possible high-value precursor compounds. Additionally, non-carbohydrate materials such as lipids and proteins might be interesting to co-extract in this biorefinery, given they’re sent to waste via the pyrolysis in this example.

Finally, the functional performance of this type of film needs to be demonstrated. Sodium alginate itself is water soluble, and hygroscopic - thus any wrapping or packaging solution that required a water barrier would likely not be well served by a plain and un-modified sodium alginate film. Many of the published results of functional testing of sodium alginate films only consider short-term applications, or are otherwise limited in their scope. Water absorption and film swelling have been reported on throughout the literature for these types of films, thus a behavioural change in customers may be required in order to prevent spoiling of wrapped products.

Chapter 4

Experimental Biorefinery and Polysaccharide Film Development

4.1 Introduction

Work in the previous chapter (Chapter 3) has demonstrated seaweed to be a highly attractive prospect for the production of polymeric materials. However, the previous model assumes that all extracted polysaccharide is suitable for use in a simple polymer film. This indiscriminate approach of extracting the polysaccharides into a single fraction, whilst attractive for its simplicity, abandons the inherent value that may be gained from separation and concentration of different marine polysaccharides.

One possible approach might be to fractionate the seaweed biomass into multiple valuable fractions, by using increasingly harsh chemical techniques in series, and collecting the different fractions separately. This approach allows the isolation different biochemical components of the starting biomass (e.g. proteins, carbohydrates, lipids), and potentially the isolation of valuable marine polysaccharides. This approach has been demonstrated a few times through the literature, with single seaweed species at a time.[264–266] However, in each case the cascading multi-fractionating approach demonstrated has only been used on a single species of seaweed, leaving the question of what happens

when different seaweed species are received.

Additionally, both the effectiveness of performing a thermochemical process on the extracted macroalgal residues, *and* the properties of the resulting carbon rich char are unknown. Previous chapters have demonstrated the potential for significant revenue to be achieved from the production of a stable carbon material for soil amelioration and/or long term carbon sequestration. However, much of the value of this product is assigned to the carbon content under the assumption that the char material may be traded as a $CO_{2,eq}$ commodity under various emissions trading scheme frameworks.

There is extensive experimental work in the literature demonstrating the suitability of marine polysaccharides and composites of marine polysaccharides for the production of thin-films for the application of food packaging. There is also much published work considering the extraction of marine polysaccharides from macroalgaes, both in a singularly targeted approach and a limited amount of work exploring the multiple fractionating approach. There is however a gap in the literature to combine the experimental multi-fractionation approach with the production and assessment of polysaccharide based films. Additionally combining this experimental biorefinery with a thermochemical process for the production of char has not been demonstrated or evaluated.

In this chapter, five different species of seaweed were assessed for extraction of target polysaccharides in both a single targeted approach, as well as within a cascading multiple extraction scheme. On recovery of the individual fractions, alginate was processed into films and these were assessed for their barrier performance. Furthermore, the effectiveness of two different thermochemical treatments (slow-pyrolysis and hydrothermal carbonisation) for the production of a high-carbon char is considered in terms of the stable carbon sequestration potential, and the potential toxic or inhibitory effects of the char on germination and growth of plants.

Finally, following the assessment of native marine polysaccharide films, the extracted agar fraction was functionalised with fatty-acid residues to produce a material with far better water resistance properties. Whilst this functionalised-agar material has been

reported on previously, there has been no demonstrations of processing it into a useful form or any assessment of it as a barrier material. Thus, functionalised material is characterised for molten flow properties by rheometry and micro-compounding extrusion techniques.

The five different seaweed species are selected as representative examples of different broad classes of available biomass. *Saccharina latissima* (SL) is selected as a representative brown seaweed, commonly found in the Northern Atlantic and a likely candidate for future European macroalgae farming projects. *Ulva lactuca* (UL) as a representative green macroalgae, often traded as a food crop known as Sea Lettuce. *Gracillaria sp.* (GR) is included as an existing cash-crop that's currently used in Vietnam in the production of agar, and *Spinosum sp.* (SP) (a common name for one of many Eucheumoid algaes) a cash-crop used throughout Southeast Asia to produce Carrageenan products. Finally, mixed *Sargassum sp.* (SG) are included as a high-volume opportunity crop, given the relative abundance of Sargasso blooms occurring on an annual cycle in the Mid- and Southern-Atlantic.

4.2 Materials and Methods

4.2.1 Materials

Saccharina lattisima (SL), and *Ulva lactuca* (UL) were purchased ready milled and dried of extrinsic moisture, from Connemara Organic Seaweed Ltd (Co. Galway, Ireland). *Gracilaria sp.* (GR) and *Spinosum sp.* (SP) species seaweeds were sourced in Vietnam and supplied freeze-dried and milled by Nutri-San Ltd (Kent, UK). *Sargassum sp.* (SG) species were sourced in Saint Lucia and supplied sun-dried and whole by Algas Organics (La Caye, Saint Lucia).

Arcos Organics branded micro crystalline cellulose (MCC) with average particle size of 50 µm was purchased from Fisher Scientific and used without further treatment. Glycerol, technical grade and biological grade agar, sodium alginate, and κ-carrageenan were purchased from Fisher Scientific and used without further purification. Palimtoyl-

chloride, lauroyl-chloride, and stearoyl chloride were purchased from TCI Chemicals Ltd. Pyridine was purchased from Merck, and 99.8 % ethanol purchased from VWR and both used without further purification.

Radish seeds (*Raphanus sativus*) for germination testing and toxicity assessment were ordered from Moles Seeds Ltd (Colchester, UK). *Raphanus sativus* was selected as the model organism for this study due to the well-established sensitivity to phytotoxins and in petri-dish germination studies, as well as the relatively large seed size which makes handling and root measurements more practicable.[267]

4.2.2 Analytical Methods

4.2.2.1 Thermal Characterisation

Basic extrinsic moisture was assessed by overnight drying at 65 °C in a laboratory oven.

Thermogravimetric analysis (TGA) was performed on a Setaram Setsys Evolution TGA 16/18, and the Calisto program was used to collect and process data. Samples were grinded and sieved to 500 μm, and 20 mg loaded individually into a 170 μL alumina crucible. Under inert atmosphere, samples were held for 10 minutes at ambient temperature to establish a baseline mass, heated at 10 °C/min to 110 °C then held for 10 minutes to determine mass loss due to intrinsic moisture. Temperature is then ramped from 110 °C at 25 °C/min to 450 °C (still in inert atmosphere) and held for 10 minutes to establish the mass loss associated with release of volatiles, then ramped to 800 °C to reduce the biomass to ash. Finally, air is introduced to the furnace chamber to allow oxygen to combust the carbon in the char, the remaining mass after combustion is the ash. The mass of extrinsic moisture ($M\%_{65°C}$), intrinsic moisture ($M\%_{110°C}$), ash ($Ash\%$), volatile matter ($VM\%$), and fixed carbon ($FC\%$) are determined as described by equations 4.1 to 4.5.[268]

$$M\%_{65°C} = \frac{W_{tare} - W_{moist}}{W_{tare} - W_{65°C}} \times 100 \tag{4.1}$$

$$M\%_{110^{\circ}C} = \frac{W_{init} - W_{110_{\circ}C}}{W_{init}} \times 100 \tag{4.2}$$

$$Ash\% = \frac{W_{850^{\circ}C}}{W_{110^{\circ}C}} \times 100 \tag{4.3}$$

$$VM\% = \frac{W_{110_{\circ}C} - W_{450_{\circ}C}}{W_{450_{\circ}C}} \times 100 \tag{4.4}$$

$$VM\% = \frac{W_{450_{\circ}C} - W_{850_{\circ}C}}{W_{110_{\circ}C}} \times 100 \tag{4.5}$$

Where W refers to a sample mass, with subscripts tare, moist, and 65 °C refer to the crucible tare weight, initial moist sample mass, and mass at 65 °C from the lab oven. Subscripts 110 °C, 850 °C, and 450 °C refer to an average mass determined via TGA at the respective furnace temperature.

4.2.2.2 Elemental Microanalysis (C,H, N, and S)

Elemental analysis (C, H, N, and S) was performed by OEA Laboratories Ltd (Exeter, UK). Where appropriate, Oxygen content was approximated by subtracting C, H, N, and S content from 100 %. In percentage elemental analysis (EA) of CHNSO, milligram amounts of samples are combusted or pyrolyzed at high temperature in a helium carrier gas. After suitable preparation the measurable gases (CO_2, H_2O, N_2, SO_2, or CO) are separated on a chromatography column. The gases are passed in turn through a thermal conductivity detector (TCD) where the gases are quantified against know reference standards.

4.2.2.3 FT-IR Spectroscopy

FT-IR spectroscopy was performed using a PerkinElmer Frontier FT-IR Spectrometer. The spectrometer was configured using an MIR (8000 - 30) cm^{-1} source, and an MIR TGS (15000 - 370) cm^{-1} detector. Spectra were collected using the PerkinElmer Spectrum software (Application version: 10.03.09.0139), and data processed in desktop spreadsheet software.

4.2.2.4 Film permeability

Gas permeability was measured using the time-lag methodology, and a custom built membrane permeability rig.[269–271]

The diffusion time-lag methodology allows the determination of diffusion, solubility, and permeability coefficients of simple gasses through polymeric membranes. Starting from an initial set-up where there is zero penetrant gas within the polymer membrane, introducing a high concentration of penetrant gas to one side (upstream) of the membrane results in penetrant gas absorbing into the dense polymer, diffusing, and exiting from the downstream face. This mass-transport process is driven by the concentration gradient which is maintained over the membrane, however starting from initial state, studying the transient nature of penetrant gas concentration over time allows determination of the diffusion, solubility, and permeability coefficients.

Considering a polymer membrane of thickness l with an initial concentration of penetrant gas C_0 throughout at time $t = 0$, and concentrations of penetrant gas set to C_1 and C_2 for the downstream and upstream faces of the polymeric membrane respectively. The cumulative amount of penetrant per unit area exiting the downstream surface of the polymer membrane (Q_t) verses time can be obtained as a solution to Fick's second law, where the diffusion coefficient (D) is constant, and there are no chemical reactions of adsorption processes occurring within the polymer.

The Fick's second law solution reduces to an asymptotic line described by equation 4.6 under the assumptions that $C_1 = C_0 = 0$ (zero initial concentration in polymer and downstream), and that the experiment is run long enough to ensure that the dQ_t/dt plot (e.g. presented in figure 4.1) has reached steady state:

$$Q_t = \frac{(DC_2)}{l}\frac{t - l^2}{6D} \tag{4.6}$$

This steady-state line intercepts the time axis at $t = \Theta$, where Θ represents the time-lag caused by the saturation of the polymer membrane from the initial state (C_0).

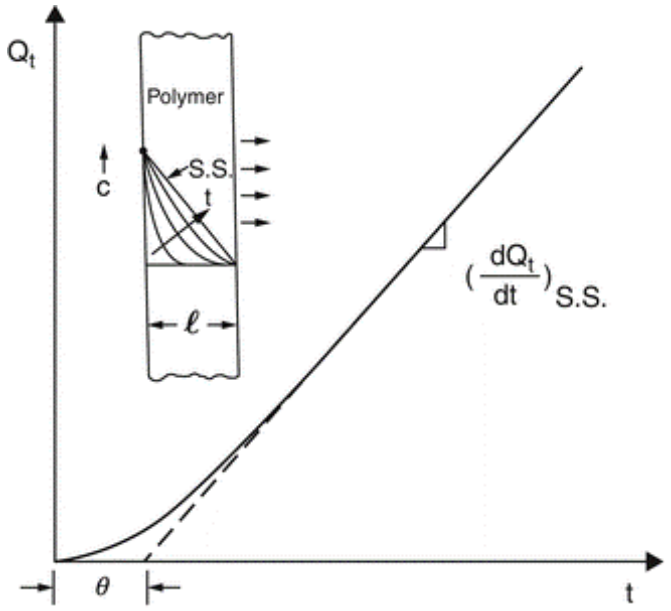

Figure 4.1: Typical lag-time plot of pressure (or Q_t) as a function of changing time (t) used to assess gas permeability of polymeric membranes. Steady-state gradient (dQT/dt) is used in calculating the permeability coefficient. Image from Paul, D.R. (2016).[269]

$$\Theta = \frac{l^2}{6D} \tag{4.7}$$

The permeability coefficient, P, can be calculated from the gradient of the steady-state portion of the graph Q_t vs. t according to equation 4.8:

$$P = \frac{1}{p_2} \times \frac{dQ_t}{ds}_{(s.s.)} \tag{4.8}$$

Finally, the gas solubility within the polymer membrane (S) may be determined by solving equation 4.9 with the values of D and P determined using equations 4.7 and 4.8.[269]

$$P = DS \tag{4.9}$$

The rig (figure 4.2) utilises a constant upstream supply pressure of penetrant gas

applied to one side of a film sample held in a test-cell, whilst the other side is held under vacuum. An exploded view of the test-cell is shown in figure 4.3. The test-cell is an adapted 47 mm stainless steel filter membrane holder (Merck Millipore XX4404700), where the test-article is supported from beneath with a fine gauge mesh, and pressure seal achieved from above with a compression o-ring.

Initially, the gas supply (V-1) is isolated and the entire rig drawn to a vacuum. Once a steady-state vacuum is achieved, the vac pump is switched off, and the supply/permeate sides of the test cell are isolated by closing valves V-2 and V-3. Data-logging of the pressure on the permeate side of the test cell is started, and the gas supply opened slowly (V-1). Upstream pressure is verified with the pressure indicator gauge on the supply side, and the system left to reach equilibrium. The change in downstream pressure over time is recorded with a data-logger, and the penetrant gas permeability coefficient is determined during a period of steady-state gas permeation according to equation 4.10:

$$P_i = \frac{d\Delta P_t}{dt} \times \frac{V_L}{R \times T} \times V_m \times \frac{l}{A_f} \times \frac{1}{P_{A_0} \times 10^{10}} \tag{4.10}$$

Where P_i is the permeability coefficient (units of Barrer, or 10^{-10} $cm_{(STP)}{}^3$ cm / cm^2 s cmHg), $\frac{d\Delta P_t}{dt}$ is the steady state pressure gradient (cmHg/s), V_L is the internal volume of the test rig (cm^3), R is the molar gas constant (in units of cm^3 cmHg mol^{-1} K^{-1}), T is the ambient temperature during the experiment (K), V_m is the ideal molar volume at standard temperature and pressure (cm^3 mol^{-1}), l is the film thickness (cm), A_f is the cross sectional area of the membrane/film that gas transports through (cm^2), and P_{A_0} is the upstream gas supply pressure (cmHg).

Water Vapour Permeability (WVP) was tested with an adapted method according to ASTM E96 / E96M Standard Test Methods for Water Vapor Transmission of Materials (2010).[272] 30 mL glass sample vials were first prepared by measuring in the internal diameter of the open end, and then by application of a bead of 50:50 molten rosin/beeswax around the open rim of the vial. Once the beeswax/rosin seal was partially set, 15 mL of DI water was placed into the vial, and a single piece of test film

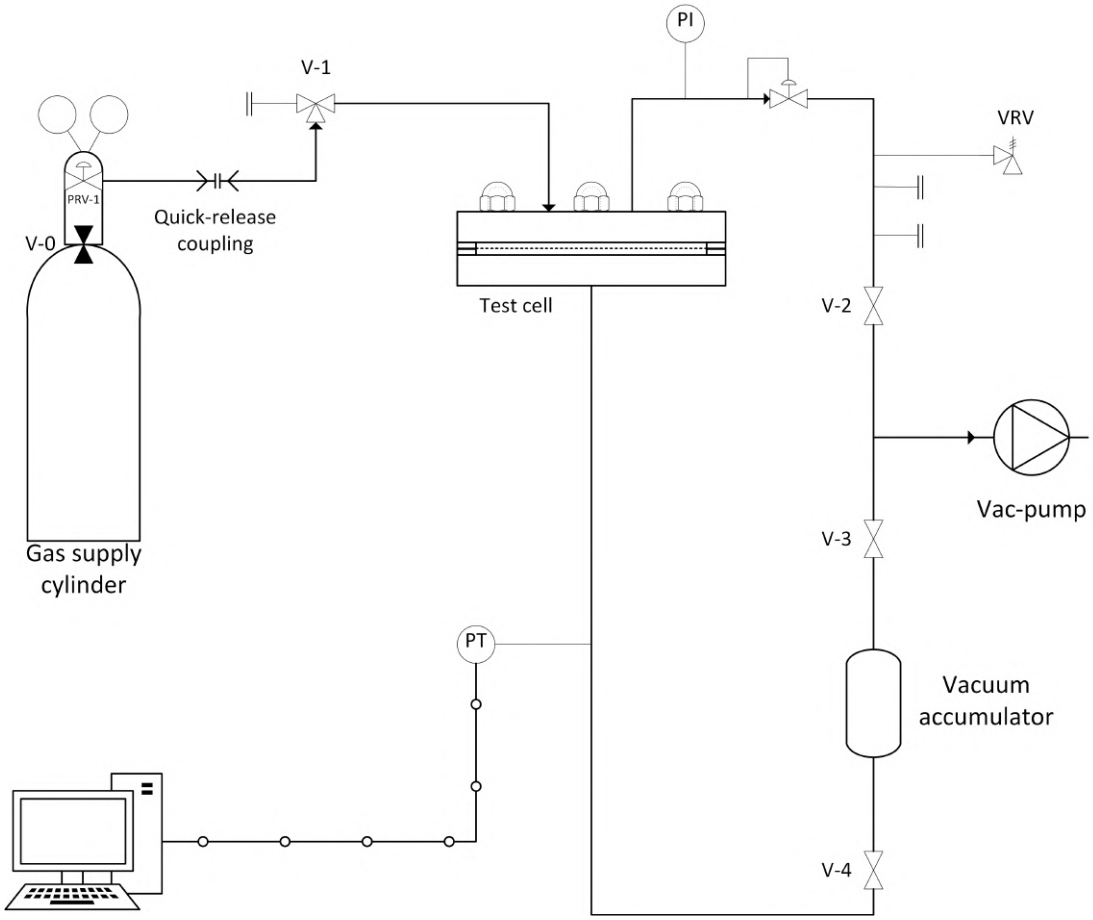

Figure 4.2: Diagram of custom gas permeation rig used to test the gas permeability of various test films, utilising the time-lag methodology.

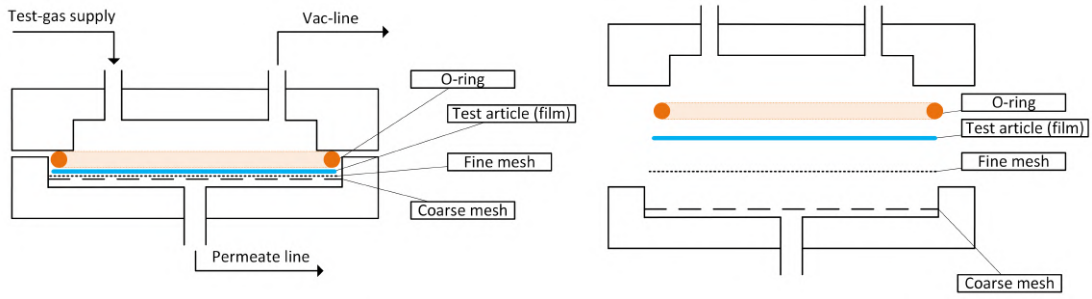

Figure 4.3: Exploded schematic view of test-cell used in gas permeation rig. Left: Assembled and in use, Right: Exploded view for further detail.

was placed over the opening. The flat-bottom of a pre-warmed glass beaker was used to press the test film flat into the seal, and to partially re-melt the seal material against the test film and thus create an air and water tight seal between the glass vial and the

test film.

The test vial/film assembly is weighed and the initial weight (m_0) recorded against the test start time (t_0). The entire vial and test-film assembly is then placed into a desiccator chamber with fresh anhydrous calcium carbonate in the adsorbent tray, and left undisturbed. The assembly is removed and re-weighed periodically over a period of 48 hours, and both time and weight are recorded ($m_1, m_2, m_3, \ldots, m_n$ and $t_1, t_2, t_3, \ldots, t_n$). For each measurement, the difference in mass (Δm_n) and difference in time (Δt_n) for sample record n are determined and plotted on an x y scatter plot. A linear line of least squares regression is drawn through the points, and the water vapour transmission rate is determined:

$$\Delta m_n = m_0 - m_n \tag{4.11}$$

$$\Delta t_n = t_0 - t_n \tag{4.12}$$

$$WVTR = 240 \times \frac{dm}{dt} \times \frac{1}{A} \tag{4.13}$$

Where $\frac{dm}{dt}$ is the gradient of the gain in mass verses time from the least-squares regression model, A is the water vapour permeation area, determined from the measurements of the previously measured internal diameter of the vial.

4.2.2.5 Water contact angle

Surface contact angle of water droplets on test articles (biopolymer and functionalised material films) was measured using a DataPhysics OCA 25 instrument, and data collected and processed with the DataPhysics SCA 20 module base software. The sessile drop technique was used, with deionised water and a 5 μL drop, to characterise the initial static contact angle, as well as the dynamic contact angle over 45 seconds. Full instrument settings are listed in table A3.

4.2.3 Experimental Methods

4.2.3.1 Washing and pre-processing of macroalgae

SG macroalgae was received sun-dried and whole, hence contained significant quantities of sand, salt, and grit. A sample of SG as received was assessed for extrinsic moisture at 65 °C, and then SG was placed into a bucket and soaked in cold tap-water to remove excess salt and sand from the biomass. Wet and tap-water washed SG was then rinsed with DI water, and spread out on a wire rack to air-dry at ambient lab conditions. The resulting water washed and air-dried SG was then re-assessed for moisture at 65 °C, and the relative difference in dry-mass before and after washing was attributed to sand, salt, and grit contaminants. Washed and dried SG was then coarsely milled with a domestic kitchen blender (Nutri Ninja, BL480UKSG) and stored in a polyethylene bag before further processing.

4.2.3.2 Polysaccharide extractions

Fractionation of whole seaweed biomass was carried out in steps described by Wahlstrom et al. (2018), with small modifications at individual steps (figure 4.4).[266] For the single-fraction (SF) extractions, whole seaweed biomass was used as a starting solids biomass. For multi-fractionation (MF), the extractions were performed stepwise as depicted in figure 4.4, with residual solids from each preceding step making up the starting solids for the next step.

In all cases, final yield of each fraction is related back to the dry and ash-free (DAF) mass of starting material, and for the MF procedure the individual stepwise yield is also determined to account for transfer losses.

Briefly, the individual extraction steps are described hereafter:

Crude protein isolate was extracted by a simplified pH inversion method. Dried and milled macroalgae was suspended in a mixture of distilled water and crushed ice chips at a 1:6 mass ratio (wet weight), and homogenised at 18,000 rpm for 5 minutes with an IKA Ultra-Turrax T25 digital disperser. The resulting homogenate was stirred for

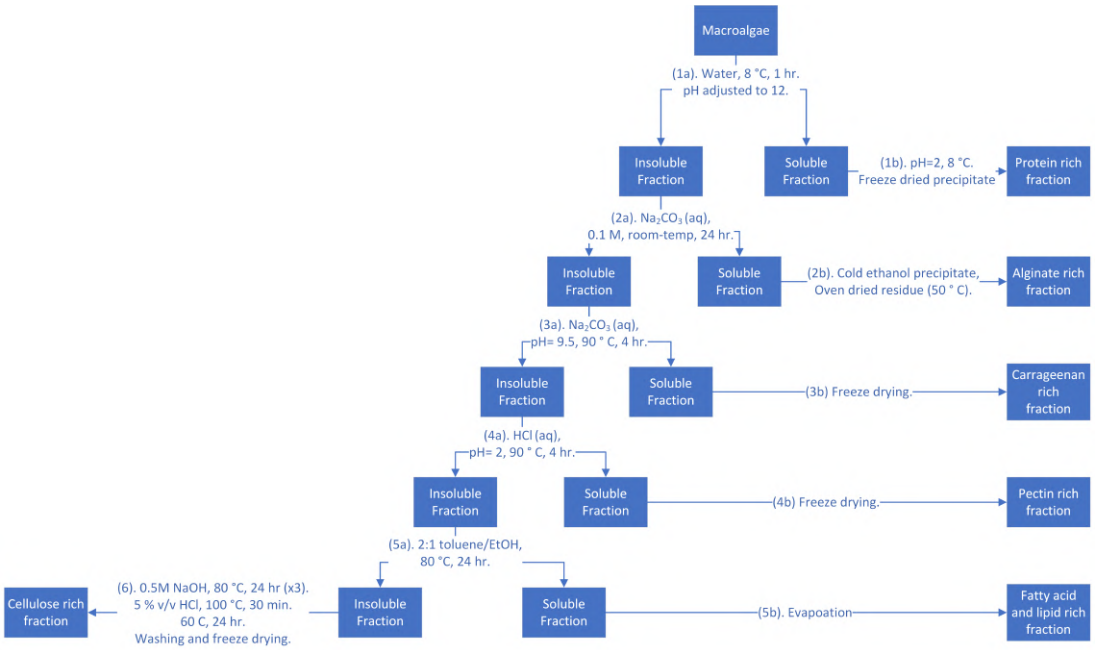

Figure 4.4: Cascading multi-step extraction procedure, modified from Wahlstrom et al. (2018).[266]

1 hr at 8 °C. Whilst keeping the homogenate on ice, pH was adjusted to 12 with 1 M NaOH, and the mixture centrifuged at 3000 RCF for 30 mins. The supernatant was decanted and kept on ice whilst the pH was adjusted to 2 with 1 M HCl, and the insoluble residue was frozen at -20 °C and set aside for further processing. Supernatant was frozen overnight at -20 °C, then thawed and centrifuged at 3000 RCF for 30 mins. The protein-rich pellet was collected and freeze-dried, and dry fraction stored for later analysis.

Alginate rich extracts were prepared from either the insoluble residue from step 1, OR whole and untreated macroalgal seaweed mass was suspended in a solution of 0.1 M trisodium citrate at 10 % w/v, and stirred at 80 °C for 2 hours. The resulting slurry was filtered at elevated temperature through a pleated Grade 1 laboratory filter to separate residual solids from the extracted species dissolved in the aqueous solution. Residual solids were dried at 50 °C and set aside for later processing. Alginate was recovered from the filtrate solution as sodium alginate by precipitation, by slow dropping of the aqueous solution to 2 volumes of chilled ethanol being gently stirred. The resulting

fibrous precipitate was removed, further washed with clean ethanol, and let to dry in a laboratory oven at 50 °C. The dried sodium alginate precipitate product was weighed and set aside for later analysis. Finally, the total extracted mass of sodium alginate was adjusted down to alginic acid equivalent mass by the following:

$$M_{\mathrm{HA}_{eq}} = M_{\mathrm{NaA}} \times \frac{m_{w_{\mathrm{NaA}}}}{m_{w_{\mathrm{HA}}}} \tag{4.14}$$

Where M refers to the extracted mass, m_w to the molecular weight a of a single monomer, and subscripts HA and NaA refer to the acid and sodium salt forms of alginate.

Agar and carrageenan rich isolate was achieved by an NaOH soak-out process. Macroalgae was soaked overnight in 1 M NaOH at room temperature, and then heated to 85 °C and stirred for 2 hours. Solids were recovered by centrifugation at 3000 RCF for 30 minutes, and then washed twice with deionised water to remove the bulk of NaOH. Solids were then washed with dilute acetic acid (1 % v/v) to neutralise any residual NaOH, and washed twice more with DI water. The resulting solids were resuspended in deionised water, and agar/carrageenan extracted whilst stirring at 85 °C for 2 hours. The extract solution was then filtered with a Grade 1 lab filter, whilst being maintained at elevated temperature to prevent gelling. Residual solids were retained and stored for later processing, and the filtrate was allowed to cool and gel overnight, and then freeze dried to remove water.

Ulvans and pectin rich extract fractions were recovered by acid digestion of the solids. 6 w/v % solids were suspended in DI water, and adjusted to pH 2 with 1 M HCl. Extraction proceeded at 80 °C and for 2 hours under stirring. Following extraction, solids were recovered by filtration with a Grade 1 lab filter. The solids residue was dried in a laborator oven overnight at 50 °, and set asside for later processing. Filtrate was frozen at -20 °C, and then water and residual HCl removed by freeze drying to recover the ulvan/pectins solids.

Lipids and fatty-acids are extracted from residue solids and seaweed by simple solvent

extraction. Solids were suspended in a 2:1 Ethanol:Toluene solvent mixture at a 7 % w/v ratio, and stirred for 24 hours at 80 °C. Residue solids and extract were separated with a Grade 1 laboratory filter, with filtrate being collected in a pre-tared round bottomed flask. Solvent was removed with a rotary evaporator under vacuum, and the residual mass of lipid/fatty-acid remaining in the RBF weighed for yield calculation. Lipid/FA was then transferred to a storage vial with a minimal quantity of 2:1 EtOH:Toluene, which was again removed with rotary evaporation

4.2.3.3 Nanocellulose production

Neutrally buoyant nano-cellulose suspensions were prepared using the acid digestion method as described by Miao *etàl* (2016), and Bondeson *etàl* (2006).[75, 273] Briefly, 100 mL of 64 wt. % H_2SO_4 was placed in a in a three neck round-bottomed flask with magnetic stirring, and heated to 44 °C in a circulating water bath. 10 g of micro-crystalline cellulose (50 μm mean diameter) was added to the flask, and stirring maintained for 2 hours, with sufficient intensity to keep the MCC in suspension. To stop the reaction, the contents of the flask were decanted into approximately 6 volumes of chilled deionised water. This solution was then centrifuged for 10 mins (4000 rpm, 3000 RCF), acid supernatant discarded, and the cellulose pellet resuspended in DI water to remove acid residue. This water washing was repeated a minimum of 5 times, and was stopped once the supernatant became turbid to prevent loss of yield of the CNC. Turbid supernatant (CNC in solution) was decanted into a separate flask, and further nano-particles were liberated from the cellulose pellet by using a high-shear rushton turbine driven at 2000 rpm by an overhead mixer (Hiedolph RZR 2051) and centrifuged a further 2 times, with turbid supernatants combined each time.

The suspended particles in the CNC solution were assessed with dynamic light scattering (DLS) using a Malvern Zetasizer, and further imaged under FeSEM to determine shape and confirm size. The particle size distribution (by volume) of the CNC solution as measured is shown in figure 4.5a. The PSD shows a clear bi-modal distribution, with peak distribution frequencies at 115.4 nm and 518.8 nm for the small and large distributions respectively. This bi-modal distribution can be explained by the shape of

the particles, with the expected shape being elongated rods as the naturally elongated cellulose fibres are digested at the amorphous regions. This was confirmed by FeSEM imaging, where the high aspect ratio rod shaped fibres are clearly visible (figure 4.5b).

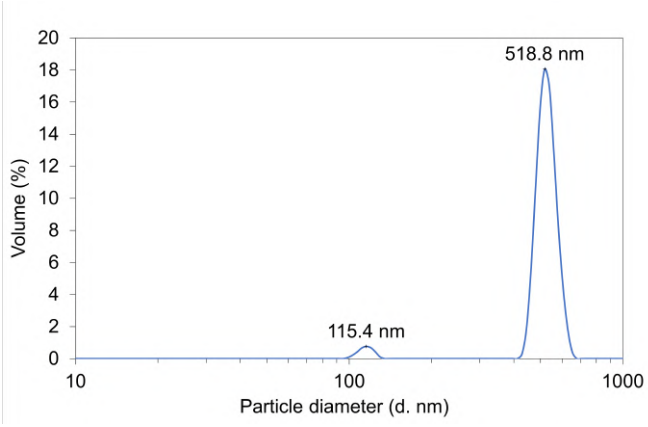

(a)

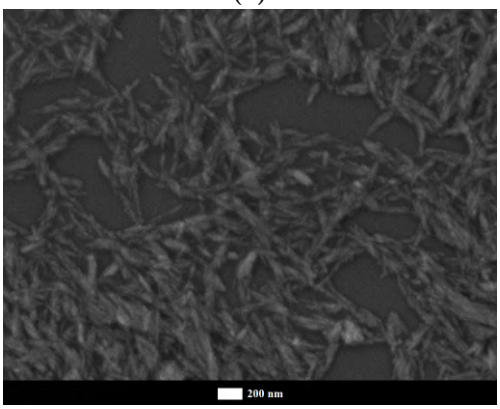

(b)

Figure 4.5: a) Particle size distribution (PSD) of the crystalline nanocellulose solution (CNC) produecd by acid digest of micro-crystalline cellulose, and measured by dynamic light scattering, and **b)** FeSEM imagery of crystalline nanocellulose solution. 30,000x magnificatiion.

4.2.3.4 Thermochemical processing

Hydrothermal carbonisation (HTC) was achieved following the methods of Massaya *etál* (2021).[274] Biomass solids (whole biomass, or extracted residues) were suspended in deionised water at 10 % w/v (dry basis) within a high-pressure bench-top stirred reactor (Parr Instruments Company, Illinois, USA), with a 300-mL Hastelloy reaction vessel. A thermocouple in the centre of the reactor head and PID temperature controller

was used to maintain isothermal reaction conditions of 260 °C. Reaction temperature was achieved and maintained after a 5.4 °C/minute temperature ramp rate, and then maintained for 4 hours for the reaction to take place. After reaction time had elapsed, the reactor was cooled by use of internal cooling coil and a glycol chiller. Reaction products were then passed through a Whatmann Grade 1 quantitative filter paper to separate the residue solids (hydro-char) and dissolved aqueous products.

Slow pyrolysis (SP) was carried out in the same bench-top reactor (Parr Instruments Company, Illinois, USA) with the overhead stirrer removed. Biomass solids were placed within a 40 mL ceramic crucible and suspended in the centre of the reactor vessel at the same height as the tip of the thermocouple. Reactor gas volume was replaced by nitrogen, by way of three repetitions of alternate pressurising and venting with 1-bar of nitrogen. After the pressure-swings, a continuous flow of N_2 at 3 L min^{-1} delivered to the bottom of the reactor and vented from the top maintained inert environment and swept any vapour or gaseous reaction products from the reactor. Reactor off-gas was passed through an ambient temperature air-condenser to recover any condensable vapours, and the tails-gas discharged to a fume extraction hood. Pyrolysis reactions were carried out at 350 °C for 60 minutes, following an initial 7.3 °C/minute temperature ramp rate from room-temperature to reaction temperature. After the reaction time had elapsed, the reactor heating mantle was removed and the reactor allowed to cool to $<$ 50 °C under continuous flowing nitrogen. Once cooled sufficiently low enough to handle, the crucible and the product pyrolysis char (pyro-char) were recovered.

4.2.3.5 Char stability and germination trials

Hydro- and pyro-char oxidative stability was assessed using the Edinburgh stability tool, as described by Cross and Sohi (2013).[275] Briefly, biochar containing 0.1 g C is ground to a fine powder and treated in a test tube with 7 ml of 5 % H_2O_2 at room temperature until effervescence was observed to have stopped, and then at 80 °C for 48 hours. During this time the test-tubes are loosely covered to prevent evaporation progressing too quickly, and lightly agitated periodically to mix the contents. Thereafter, the cover is removed and the samples allowed to dry fully. The stable carbon fraction is

expressed as the percentage of the initial 0.1 g C that remains after oxidation, assessed from gravimetric mass loss and determinations of C content by CHN analysis before and after oxidation.[275, 276]

Germination trials were set up in triplicate in 90 mm polystyrene petri dishes, with radish 'Cherry Belle' (*Raphanus sativus*) selected as the test seeds.[83, 277, 278] Biochar solids (from either HTC or Pyrolysis) was suspended in DI water (1:5 w/v ratio) and stirred at room temperature for 24 hours. Solids were removed by filtration with general purpose laboratory filter paper, and the aqueous extract was collected. To each dish, two 87 mm diameter general purpose filter papers were placed in the base, and 5 mL of test solution was added. Test solutions were either DI water (control), 100 % v/v, 10 % v/v, or 1 % v/v dilutions of the aqueous extracts from HTC and pyrolysis chars. Seeds were inspected and any damaged or misshapen seeds were discarded, and to each petri dish 24 seeds were added.

Petri dishes were incubated in the dark and maintained at 20 °C, and inspected at 24 hr and 48 hr intervals where germination rate was assessed. The operational definition of germination used in this study was a visible radicle. At 48 hours 5 mL (equal volume to test solution) of absolute ethanol was added to each dish, and dishes placed in a laboratory freezer at -20 °C to stop growth. Radicle length was then measured, and the total germination index (GI) is determined by equations 4.15 to 4.18.

$$SG = \frac{\text{Number of germinated seeds}}{\text{Total number of seeds}} \times 100\% \tag{4.15}$$

$$RSG = \frac{\text{Number of germinated seeds (sample)}}{\text{Number of germinated seeds (control)}} \times 100\% \tag{4.16}$$

$$RRG = \frac{\text{Total radicle length of germinated seeds (sample)}}{\text{Total radicle length of germinated seeds (control)}} \times 100\% \tag{4.17}$$

$$GI = RSG \times RRG \times 100\% \tag{4.18}$$

where SG, RSG, and RRG are the seed germination rate, relative germination rate, and relative radicle growth respectively.

4.2.3.6 Functionalisation of polysaccharides

Extracted polysaccharide fractions of agar and carrageenan, and pure agar/carrageenean materials were functionalised with C16 fatty-acids following the methods of Aburto et al. (1997, 1999), and Thiébaud et al. (1997).[279–281] Polysaccharides were suspended in room temperature pyridine at approximately 6 % w/v in a round-bottomed flask with magnetic stirring. 5 molar equivalents (relative to polysaccharide) of palmitoyl chloride was added dropwise to control the exotherm, then and air condenser fitted and reaction mixture raised to 105 °C, and stirring maintained for 1 hr. After reaction, the whole reaction mixture was decanted into 5 volumes of room-temperature ethanol to quench the reaction. Solids were recovered by filtration, and solids were washed with hot ethanol to remove residual palmitic acid. Solids were dried on the filter paper in a 40 °C laboratory oven overnight, then recovered and stored in a glass vial for later analysis.

4.2.3.7 Films and coatings

Polysaccharide films were prepared in a number of ways. Solution casting of films was utilised for water soluble polysaccharides (alginates, agar, carrageenan). A film-forming solution of 1 % (w/v) of polysaccharide in hot DI water (75 °C) was prepared under gentle stirring, with 0 to 80 % w/w (relative to biopolymer) of plasticiser (glycerol), and nanocellulose added and stirring maintained for 1 hour to ensure homogeneity. This solution was cast into 90 mm diameter polystyrene petri-dishes, and dried in a laboratory convection oven at 50 °C overnight, thereafter films were peeled from the dishes and stored at ambient conditions for later analysis.

Sodium-alginate films were then rendered insoluble by treatment with either 3 % w/v calcium chloride solution or 1 M HCl, to convert sodium alginate in the film to calcium alginate and alginic acid respectively. Treatment was achieved by full immersion of the film into the treatment solution for 60 seconds, following which the film was removed from the treatment solution, allowed to drip-drain into the treatment solution vessel, and then immersed into a DI water bath and gently agitated for a further 60 seconds

to remove residual treatment solution. Treated and washed films were removed from the DI water wash, patted dry with laboratory paper towels to remove surface water, and then spread out flat on the underside of their petri-dishes and air-dried at ambient laboratory conditions.

Alginate based coatings were achieved by preparing a film-forming solution as described above, which was then brush-applied to the inside surface of a bagasse pulp-based food tray. Film forming solution was continuously brushed about the inside of the tray to ensure an even coating as the excess moisture dried, leaving a thin sodium alginate layer on the inside of the tray. The tray was then dried in a lab oven at 50 °C overnight. This coating was rendered insoluble by addition of a small volume of either 1M HCl or 3 % w/v calcium chloride inside of the tray, which was then also brushed about the inside of the tray for 60 seconds to ensure even coverage of the internal surfaces as well as sufficient time to convert the sodium alginate salt to its insoluble form. Excess liquid was poured out, and the tray rinsed multiple times with DI Water to remove acid or calcium residues, and the tray dried again overnight at 50 °C.

The barrier properties of the tray coating were assessed by filling the trays with one of three fillings (tap water, 0.1 M citric acid, or pre-prepared pasta-sauce bought from a local supermarket). An impermeable top-seal of aluminium foil was applied to the trays, and the loss in mass over approximately 14 days was assessed.

4.2.3.8 Rheometery

Rheology of molten functionalised materials was assessed using a TA Instruments Discovery HR-3 Rheometer, fitted with a 40 mm diameter 1° cone plate, and Peltier plate steel. Approximately 1 g of functionalised carbohydrate was placed in the centre of the Peltier plate and pre-heated to the analysis temperature (140 °C to 180 °C). The cone plate was adjusted to allow for an 800 μm sample gap, and the powdered material worked into a homogenous molten fluid under a constant plate rotation speed of 0.5 radians s^{-1} and any excess spill-out material removed. Isothermal flow sweep measurements were made whilst recording viscosity (η, in Pa.s) and stress (σ, in MPa) as a

function of shear rate (γ, s^{-1}), at shear rates from 5.7 s^{-1} to 570 s^{-1}. A minimum of 120 seconds of zero-torque heat-soak time was allowed between measurements to allow relaxation of the polymer at temperature before any rotation torque was applied for data collection. Values for η and σ at each shear-rate (γ) were recorded as an average value over 30 seconds, and allowing 5 seconds of stabilisation time at each set-point.[282]

Flow behaviour and regime were determined by characterisation of the Flow Consistency Index (K, Pa.s) and Flow Behaviour Index (n, dimensionless), modelled as power law fluid according to equations 4.19 to 4.20.[282, 283]

$$\sigma = K\left(\frac{\partial u}{\partial \gamma}\right)^{n} \tag{4.19}$$

$$\eta_{eff} = K\left(\frac{\partial u}{\partial \gamma}\right)^{n-1} \tag{4.20}$$

Where $\frac{\partial u}{\partial \gamma}$ is the shear rate, and dimensionally equivalent to γ.

4.2.3.9 Extrusion

Approximately 5 g of biopolymer (functionalised agar and carrageenan) were intimately mixed with plasticizer (10 wt. % soybean-oil) using a Haake Minilab II micro-compounding twin-screw extruder (20-150 rpm, 40-150 °C). Prior to loading any materials, a zero-load calibration was performed at operating temperature to normalise the screw torque measurements with respect to the frictional drag, at low (20 rpm) and high (170 rpm) rotation speeds. Materials were internally recirculated within the extruder to ensure thorough mixing, after which key extruder operating parameters (extruder screw motor torque, screw rotational speed, heating block temperature, inlet and outlet pressure of the internal recirculation channel) were recorded at 0.5 second intervals by use of serial data acquisition script written in Python. Motive power (the power required to convey the material within the extruder) was calculated by the relationships in equations 4.21 and 4.22:

$$P = \tau \times \omega \tag{4.21}$$

$$\omega = \left(\frac{2\pi \times n}{60} \right) \tag{4.22}$$

Where P is the motive power (Watts), τ is the screw torque (Nm), ω is the angular velocity (radians s^{-1}), and n is the screw rotation speed (rpm).

4.3 Results

4.3.1 Macroalgae characterisation

The results of characterisation of the starting biomass is shown in table 4.1. Extrinsic moisture of the as-delivered seaweed across all species was between 9.1 % and 25.7 %, with the four pre-dried and ground species (SL, UL, GR, and SP) falling between 9.1 % and 12.3 %. SG was supplied sun-dried and whole, thus in its as-delivered form had significantly higher level of intrinsic moisture compared to the other species.

The impact of washing, drying, and rough-milling of the whole SG resulted in a loss of almost 34 % of the starting mass as sand, salt, and grit being washed out of the beach-dried seaweed. Additionally, after washing and air-drying in ambient temperature on a wire-rack, the intrinsic moisture of SG was reduced to 10.0 %, bringing it in-line with the other 4 species (9.1 % to 12.3 %, table 4.1).

Thermogravimetric analysis (TGA) was used to measure the intrinsic moisture, ash, total volatile matter, and fixed carbon in each of the macroalgae species. Despite pre-drying at 65 °C in a lab oven, there was still additional moisture liberated when drying to 110 °C. Intrinsic moisture levels when drying at 110 °C revealed an additional 4.2 % to 12.6 % of free moisture was liberated under heating. Ash content determined at 850 °C was found to be between 18.2 % (GR) and 41.3 % (UL). Interestingly, even the SG had significant ash content (30.4 %) despite being water-washed upon receipt. The combination of high ash content and high moisture content can result in excess of 50 % of the received mass being non-valuable for the biorefinery process (table 4.1).

Table 4.1: Summary results of thermal and elemental characterisation of macroalgal species. Values in parenthesis represent the 95 % confidence interval about the mean, n=3.

Value	Units	Macroalgae species				
		SL	UL	GR	SP	SG
Proximate Analysis						
Extrinsic moisture (65 °C)[a]	% wt.	9.1	12.2	10.8	12.3	25.7
Sand, salt, and grit[a,b]	% wt.	-	-	-	-	33.9
Post wash moisture (65 °C)[b]	% wt.	-	-	-	-	10.0
TGA						
Intrinsic moisture (110 °C)[c]	% wt.	8.5	11.8	4.2	6.5	12.6
Ash	% dry wt.	30.0	41.3	18.2	23.4	30.4
Volatile Matter	% dry wt.	55.0	33.7	70.5	75.8	44.4
Fixed carbon	% dry wt.	15.1	25.0	11.4	0.8	25.0
Elemental analysis						
C	% daf wt.	48.6	37.7	41.6	30.0	54.8
H	% daf wt.	8.1	6.5	6.9	5.3	8.4
N	% daf wt.	2.0	2.0	3.6	0.9	1.3
S	% daf wt.	0.5	4.7	3.7	9.3	1.6
O[d]	% daf wt.	40.8	49.1	44.2	54.4	33.9

a) Measured on macroalgae as recieved.

b) Assessed on *Sargassum sp* only.

c) Measured by thermogravimetric analysis.

d) Determined as 100% - (C% + H% + N% + S%)

Total volatile matter (VM) was between 33.7 % and 75.8 %. The two highest values VM (SP: 75.8 %, GR: 70.5 %) coincided with both the lowest level of intrinsic moisture (SP: 6.5 %, GR: 4.2 %), and the lowest quantity of ash (SP: 23.4 %, GR: 18.2 %). Finally, fixed carbon (FC) was between 0.8 % and 25.0 %. The higher quantity of FC typically correlates with higher concentrations of recalcitrant polysaccharides (e.g. cellulose). In this case, the highest FC values (UL: 25.0 %, SG: 25.0 %) occur in the macroalgae species with the lowest VM (UL: 33.7 %, SG: 44.4 %), and highest intrinsic moisture (UL: 11.8 %, SG: 12.6 %).

Carbon content determined by elemental analysis ranged between 30.0 % for SP, and 54.8 % for SG. Hydrogen content correlates with carbon, with higher hydrogen concentrations occurring in species with higher carbon concentrations. Across all species, the C/H mass ratio was between 5.7 and 6.5, which sits broadly in line with published

values for various species of macroalgae.[284, 285]

Finally, nitrogen concentration ranged from 0.9 % (SP) to 3.6 % (GR), and sulfur from a minimum of 0.5 % (SL) to a maximum of 9.3 % (SP). Whilst a seemingly small difference in absolute values, the difference in mass concentration of both nitrogen and sulfur heteroatoms in the macroalgaes spans an order of magnitude between the lowst and highest values. Nitrogen content in biomass is typically due to the protein content, thus one may predict the highest and lowest protein yields from GR and SP respectively, whereas sulfur content can be attributed to sulfated polysaccharide content (e.g. carrageenan, fucoidan), as well as sulfur containing amino acid in the protein fraction.

4.3.2 Polysaccharide extractions

Single fractionations, where whole macroalgal biomass is used as the initial material for each extraction method listed in section 4.2.3.2 were performed first to establish a 'baseline' quantity of each fraction (protein, alginate, agar/carrageenan, pectin/ulvan, and lipid/fatty-acid) in each seaweed. Thereafter, multi-fractionations were performed as shown in figure 4.4, where the residual solids from each step is cascaded to the next extraction step such that, in theory, the total mass of each seaweed species is effectively distributed into the various fractions, such that they can be utilised as the crude extract or further processed into valuable materials.

4.3.2.1 Single fractions

Results of the single extractions are displayed in figure 4.6. The mean average protein yield across all species was 3.1 %, with *SP* giving the lowest total protein yield at 1.1 %, and *SL* the highest at 8.8 %. The total protein fraction recovered from each species is low, but within the broad range that is typically reported within the literature.[286]

Total recovery of the alginate-rich fraction had the largest range across all the species, with UL providing the lowest yield (0.5 %), SL the highest (72.0 %), and an average across all species of 31.6 %. This distribution of yields falls within expectations with

the species, with a brown seaweed (SL) resulting in the largest yield, and the green seaweed (UL) returning the lowest.

Agar and carrageenan extraction methods are broadly identical (NaOH treatment with hot-water extraction), thus in this work a single method was applied that would extract agar and/or carrageenan if either or both are present in the seaweed. The highest yield was from SP seaweed (28.4 %), then GR (19.3 %), SG (16.1 %), UL (6.5 %), and SL the lowest (1.5 %). Both SP and GR are commercially important species for the production of carrageenan and agar respectively, this the production of the highest yield in this extraction is unsurprising.

The hot-acid extract (pectins, ulvans, fucoidans etc.) targets cell-wall polysaccharides that are liberated during digestion of the biomass under hot and acidic conditions. The exact composition of the extracted polysaccharides will be highly dependant on the starting biomass, with green seaweeds (UL) giving much higher proportion of ulvans, brown seaweeds (SL, SG) typically giving higher fucoidan or laminarin. Highest total yield of this extract was SP at 57.6 %, UL and GR producing similar yields (13.4 % and 15.1 % respectively), and the brown seaweeds producing the lowest yield (SL: 3.6 %, and SG: 6.3 %).

Finally, lipids and fatty acids were extracted. Similar to the protein extraction yields, the quantity of extracted material was very low. The highest yield was 3.2 % (UL), then 2.8 %, 1.9 %, 1.1 %, and 0.9 % for SL, GR, SP, and SG respectively. These yields are low, but well within the typical range for macroalgae (0.2 % to 8 %).[287]

In addition to the total mass yields, individual fractions are analysed with FT-IR to establish their crude composition. FT-IR spectra of individually isolated fractions are show in figures 4.7 to 4.11. The protein rich extracts are shown in 4.7, and include spectra of a commercially available soy protein food-product. Figure 4.7a shows the crude spectra for all five macroalgaes. A dominant and broad transmittance peak occurs between 950 cm^{-1} and 1150 cm^{-1} for all the macroalgae extracts, which can be attributed to ν OH and ν C-O moieties. Presence of large peaks in this region suggests significant

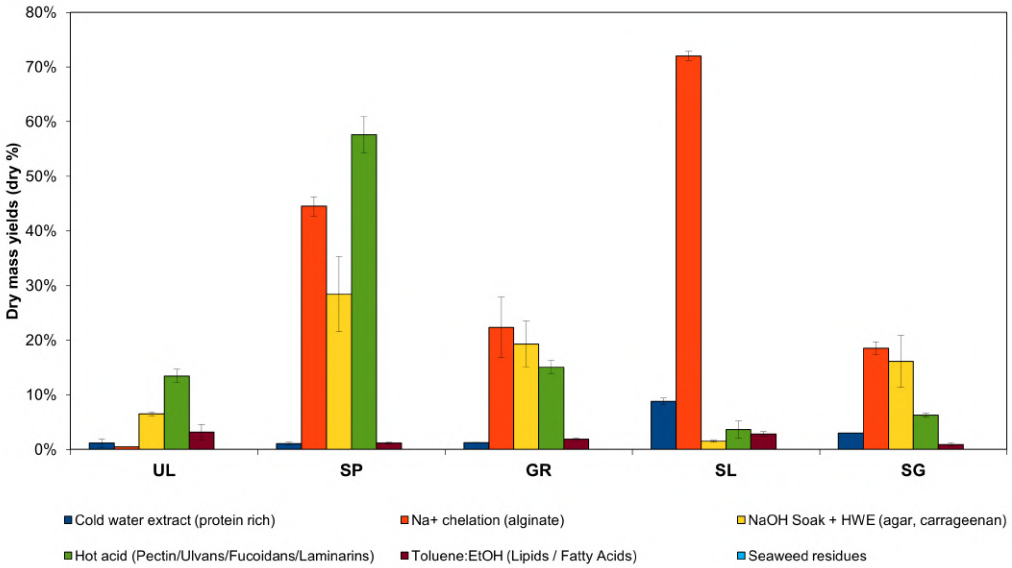

Figure 4.6: Mass yields of single-step extractions of macroalgae species using different extraction techniques to target different components. *Ulva lactuca* (UL), *Spinosum sp.* (SP), *Gracillaria sp.* (GR), *Saccharina latissima* (SL), and *Sargassum sp.* (SG). Error bars are at 95 % confidence interval in the mean, n = 3.

carbohydrate content is present in the crude protein extract, despite the mild extraction conditions.[288]

Distinct primary and secondary amide peaks are seen in the soy protein isolate at 1650 cm^{-1} (Amide I, ν C=O; ν C-N), and 1525 cm^{-1} (Amide II, δ N-H; ν C-N), as has been typically found in other food-product protein powders.[288] The crude spectra the primary and secondary amide peaks do not appear present, however the normalised spectra (figure 4.7b) show the distinct double Amide I and II peaks in GR and SL, and a single strong Amide I peak (1650 cm^{-1}) in SG, SP, and UL. The presence of these distinct peaks, albeit less well resolved in the macroalgae extracts compared to the commercial protein isolate, shows that there is likely a modest quantity of protein in the extracted powder.

The alginate rich extracts are shown in 4.8, and include spectra of a commercially available sodium alginate. Figure 4.8a shows the crude spectra for all five macroalgaes. Similarly to with the protein spectra, a dominant and broad transmittance peak occurs

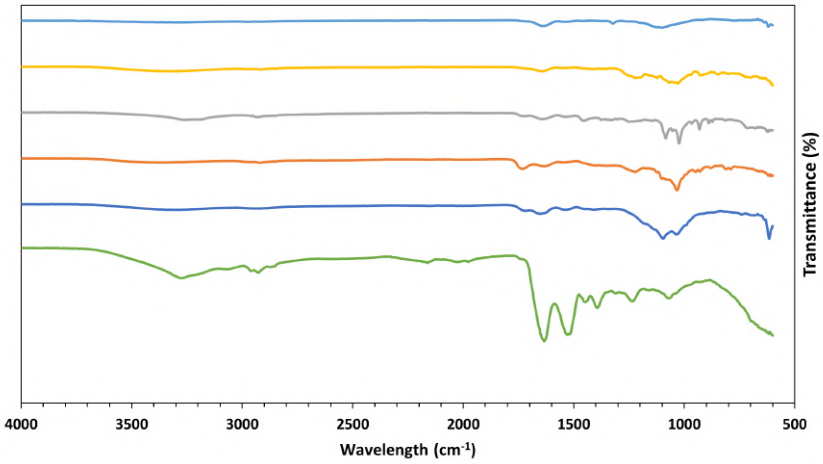

(a)

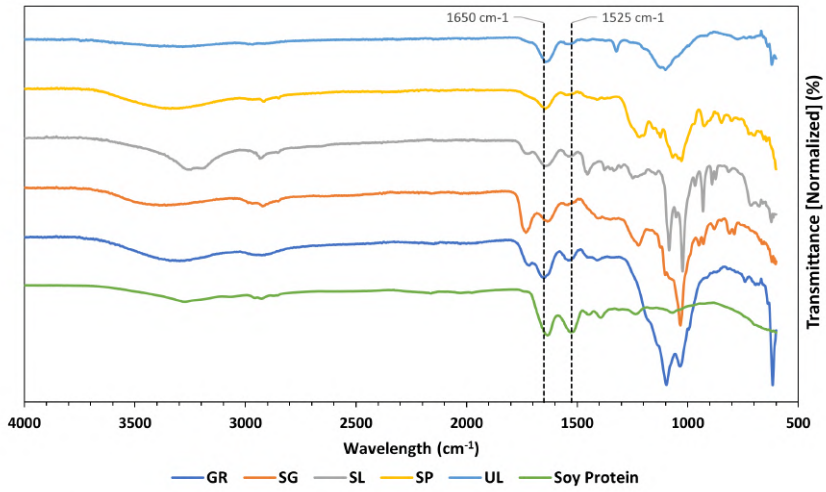

(b)

Figure 4.7: FT-IR spectra of single-fraction protein rich isolates from macroalgaes, with commercial soy protein isolate included as a reference. **(a)** shows the crude spectra, and **(b)** shows the normalized spectra. Seaweeds are *Ulva lactuca* (UL), *Spinosum sp.* (SP), *Gracillaria sp.* (GR), *Saccharina latissima* (SL), and *Sargassum sp.* (SG).

between 950 cm^{-1} and 1150 cm^{-1} for all the macroalgae extracts, but also the sodium alginate standard. Again, this can be attributed to the same ν OH and ν C-O bonds which are common through the alginate backbone.

Figure 4.8b shows the normalized spectra. A distinct pair of peaks are seen in all samples at approximately 1600 cm^{-1}, and 1390 cm^{-1} (O-C-O stretching), as has been reported previously in the literature.[289]

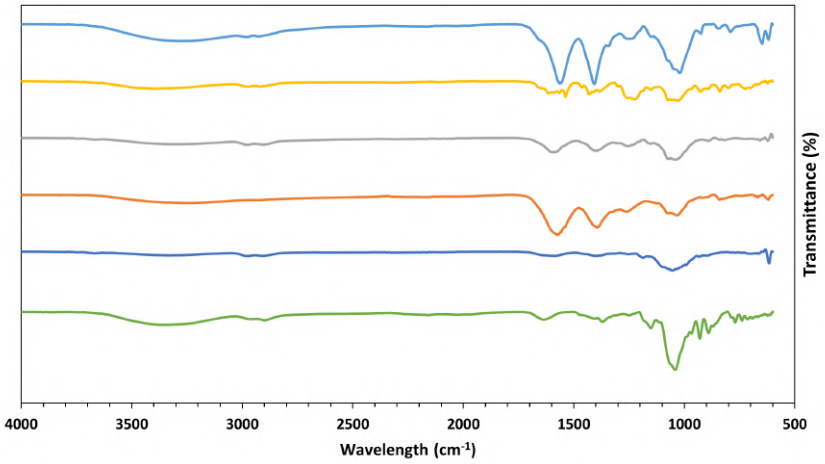

(a)

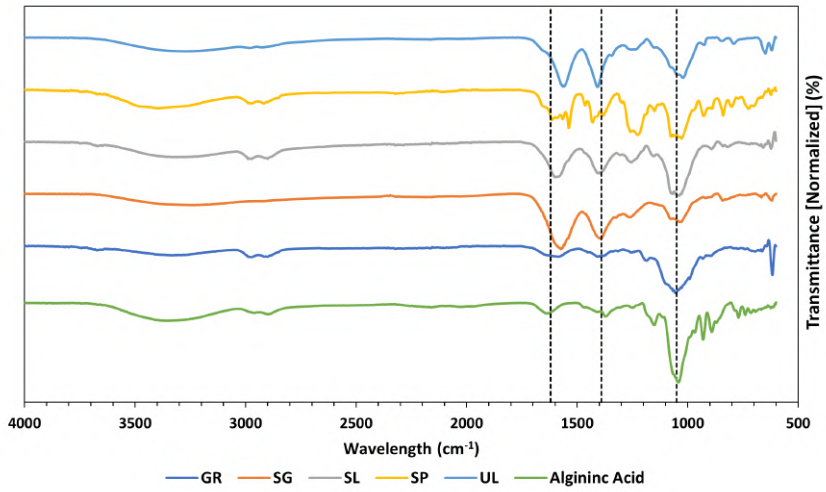

(b)

Figure 4.8: FT-IR spectra of single-fraction alginate rich isolates from macroalgaes, with commercial alginic acid included as a reference. **(a)** shows the crude spectra, and **(b)** shows the normalized spectra. Seaweeds are *Ulva lactuca* (UL), *Spinosum sp.* (SP), *Gracillaria sp.* (GR), *Saccharina latissima* (SL), and *Sargassum sp.* (SG).

Agar and carrageenan rich extracts are shown in figure 4.9, and include spectra of a commercially available agar and κ-carrageenan. Figure 4.9a shows the crude spectra for all five macroalgaes, and figure 4.9b the normalized spectra. Agar and κ-carrageenan are differentiated in FT-IR spectra by the presence of a unique peaks at 1600 cm^{-1} and 1410 cm^{-1} caused by C=O (carbonyl) and C-C/C-H in agar, and 1230 cm^{-1} in κ-carrageenan attributed to the -SO_3 stretching.[290] From the normalised spectra (figure

4.9b), GR, SG, and SL show the clear double-peaks attributable to the amide I and II (C=O and CH respectively), indicating presence of agar. SP shows the unique peak at 1230 cm^{-1} caused by the presence of the sulfate group on the molecule, as well as lack of amide II (CH) at 1410 at cm^{-1}, thus suggesting presence of carrageenan.[291] However, it is not possible to discern the form of carrageenan extracted from SP (kappa, iota, delta, gamma, etc.).

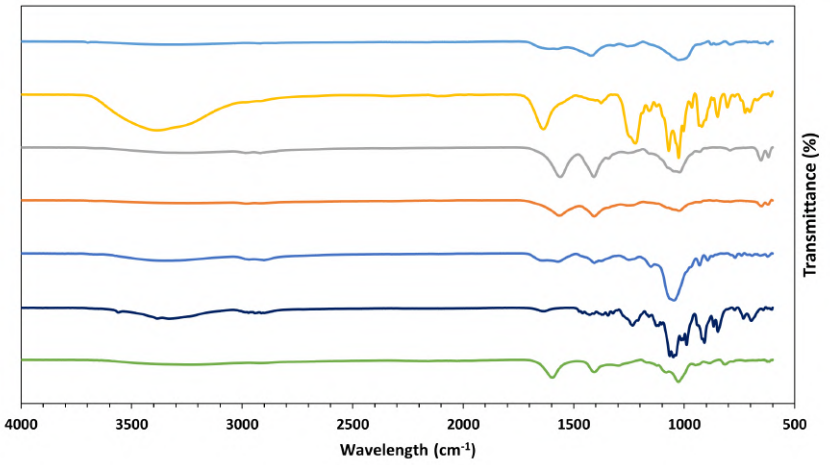

(a)

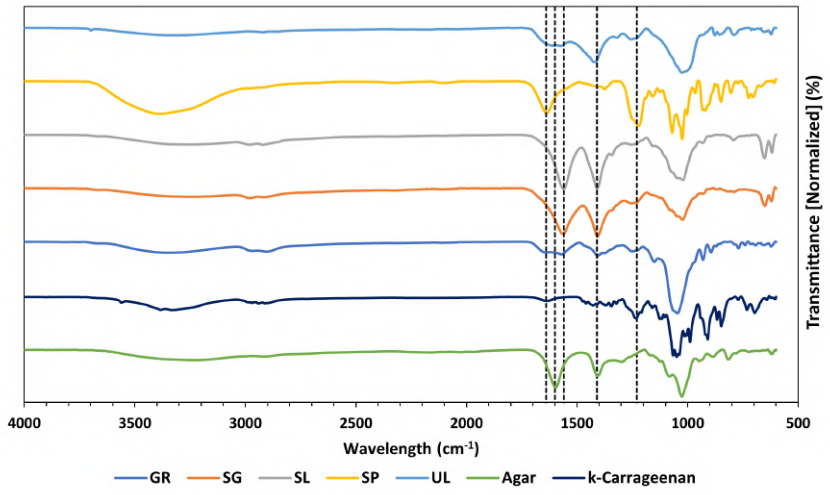

(b)

Figure 4.9: FT-IR spectra of single-fraction agar/carrageenan rich isolates from macroalgaes, with commercial agar and κ-carrageenan included as a reference. **(a)** shows the crude spectra, and **(b)** shows the normalized spectra. Seaweeds are *Ulva lactuca* (UL), *Spinosum sp.* (SP), *Gracillaria sp.* (GR), *Saccharina latissima* (SL), and *Sargassum sp.* (SG).

Similar normalised FT-IR spectra are displayed for the products of the hot-acid extraction (figure 4.10) and the toluene:ethanol extraction (figure 4.11). The hot-acid extract includes two cell-wall polysaccharides, fucoidan and laminarin for peak references. The fucoidan reference contains the same 1230 cm^{-1} peak that was found in κ-carrageenan that was previously attributed to the -SO_3 stretching. This peak is also found in the SP spectra as previously in the carrageenan/agar extract (figure 4.9), but also in this case in the SG spectra. The laminarin reference includes common peaks around 1590 cm^{-1}, 1400 cm^{-1}, and 1130 cm^{-1}. Macroalgal extracts GR, SG, SL, and UL all include peaks in the 1590-1630 cm^{-1} region as has been common in most extracts, but additionally SG has a distinct peak at 1400 cm^{-1}.

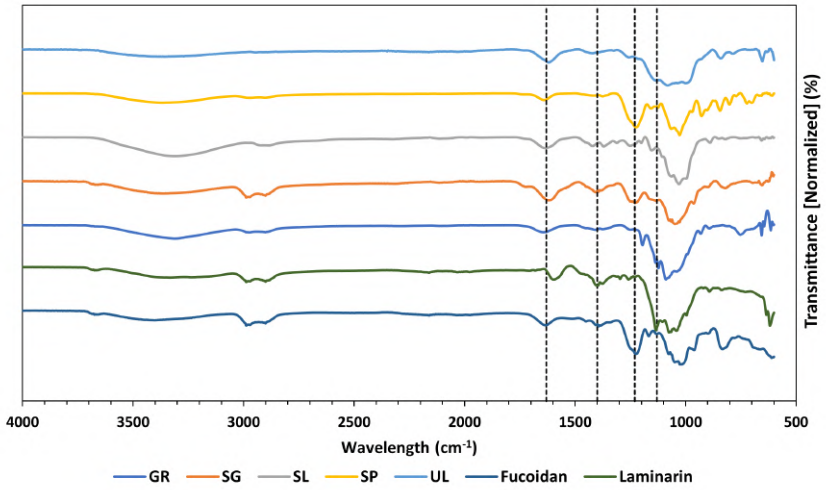

Figure 4.10: FT-IR spectra of single-fraction isolates produced with the hot-acid extraction from macroalgaes, with commercial laminarin and fucoidan included as a reference. Seaweeds are *Ulva lactuca* (UL), *Spinosum sp.* (SP), *Gracillaria sp.* (GR), *Saccharina latissima* (SL), and *Sargassum sp.* (SG).

Lipid and fatty-acid spectra (figure 4.11) include two commercial food-grade oils for comparison. All spectra include a highly distinct peak at around 1730 cm^{-1} characteristic of the η C=O ester found in lipids, and a peak around 1455 cm^{-1} caused by the δ CH_2 bonds found on the fatty-acid residue. Interestingly, UL, SP, SL, and SG all have distinct peaks at 1260 cm^{-1} suggesting the presence of PO_2^- groups of phospholipids in the crude lipid/fatty-acid extract.[292] Both example oils also show a broad set of peaks around 1160 cm^{-1} that can be attributed to O-CH_2-C asymmetric axial stretch-

ing, however this peak is absent in all macroalgal extracts.[293] Finally, all macroalgal extracts with the exception of GR had a peak at 1020 cm^{-1} indicating C-O-C bending of polysaccharide residues.[294]

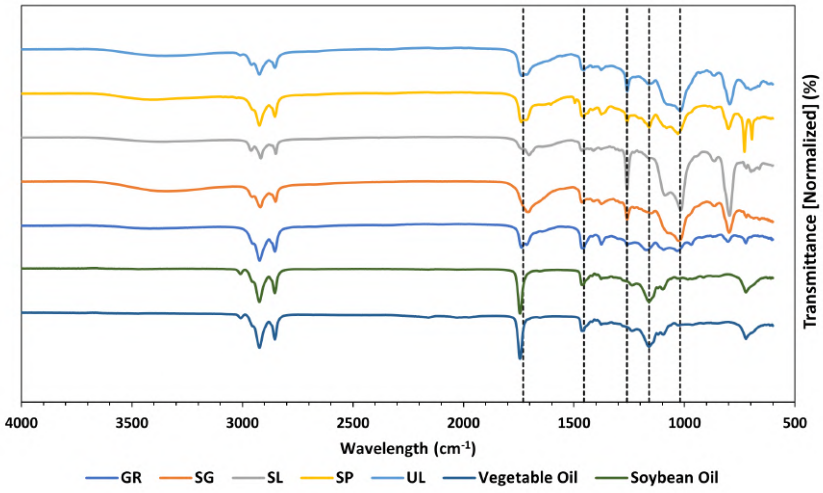

Figure 4.11: FT-IR spectra of single-fraction Lipid/Fatty-acid isolates produced with the hot-acid extraction from macroalgaes, with vegetable oil and soybean oil included as a reference. Seaweeds are *Ulva lactuca* (UL), *Spinosum sp.* (SP), *Gracillaria sp.* (GR), *Saccharina latissima* (SL), and *Sargassum sp.* (SG).

4.3.2.2 Multi-fractionation

Cascading multi-fractionations were carried out, and the overall product recovery yields for each species is shown in figure 4.12. Total protein fraction recovery is identical to that presented in figure 4.6, since the protein extraction is the first step of the cascading process presented in figure 4.4. The overall trend of fraction yields is conserved between species. For example, for UL the highest total fraction yield, for both single-fraction extraction and the cascading multi-fractionation, was from the hot acid extraction (pectin/ulvan), with the NaOH soak (agar/carrageenan) and toluene:ethanol (lipids and fatty-acids) similar but lower, followed by protein yield, and barely any mass recovered using the sodium tricitrate Na^{+} chelation (alginate) extraction.

Similarly for SP, the alginate fraction remains a large portion of the recovered mass, however the result of both the NaOH (agar/carrageenan) and hot-acid (pectin/ulvans etc.) extraction has dropped significantly. This is likely a result of the sequential

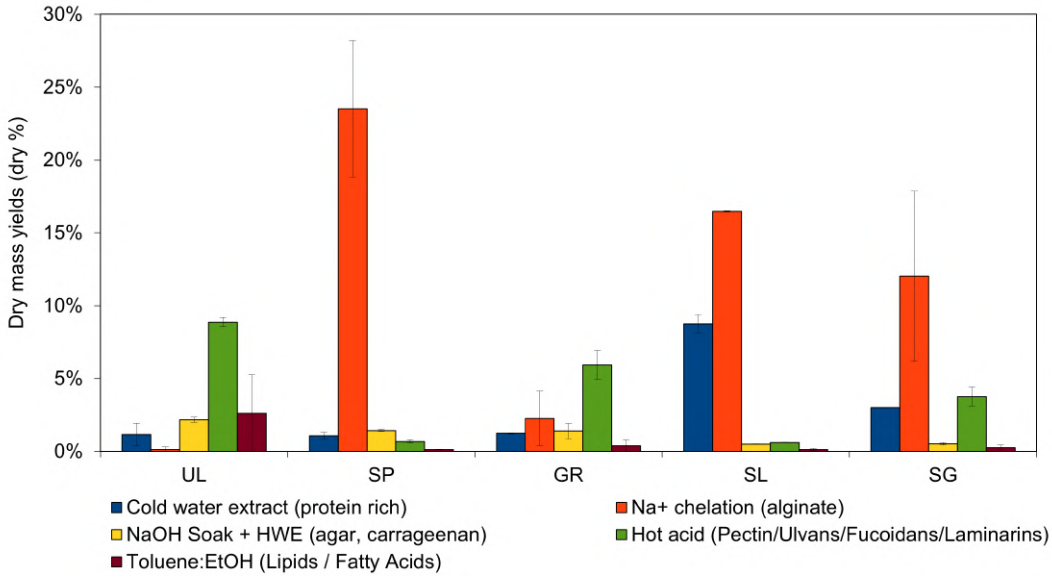

Figure 4.12: Dry and ash-free mass yields of multi-step extractions of macroalgae species, relative to the original starting mass, using stepwise application of different extraction techniques to target different components. *Ulva lactuca* (UL), *Spinosum sp.* (SP), *Gracillaria sp.* (GR), *Saccharina latissima* (SL), and *Sargassum sp.* (SG). Error bars are at 95 % confidence interval in the mean, n = 2.

nature of the extractions, with the Na^+ chelation step removing polysaccharide from the SP biomass earlier in the operation that might otherwise have been extracted by the NaOH/HWE step, or hydrolysed under the acid conditions and recovered as sugar-acid residues (e.g. mannuronate or guluronate).

Overall the largest impact appears to have been on the total yield of agar/carrageenan (NaOH/HWE), with the impact of targeting these polysaccharides at this stage in a multi-fractionation being that the total mass recovered is significantly lower than if these polysaccharides are targeted in the first case. A scatter plot comparing the total mass yield of recovered fractions under single extractions, to the mass yield of the same fraction recovered under cascading multi-fractionation is displayed in figure 4.13.

Figure 4.13 shows a reasonable correlation ($R^2 = 0.568$), i.e. higher mass recoveries in single-fraction approach correlate with higher recoveries in the cascading multi-fractionation approach, but confirms that total mass yield recovered under the cascading multi-fractionation approach is on average one quarter of that recovered under the

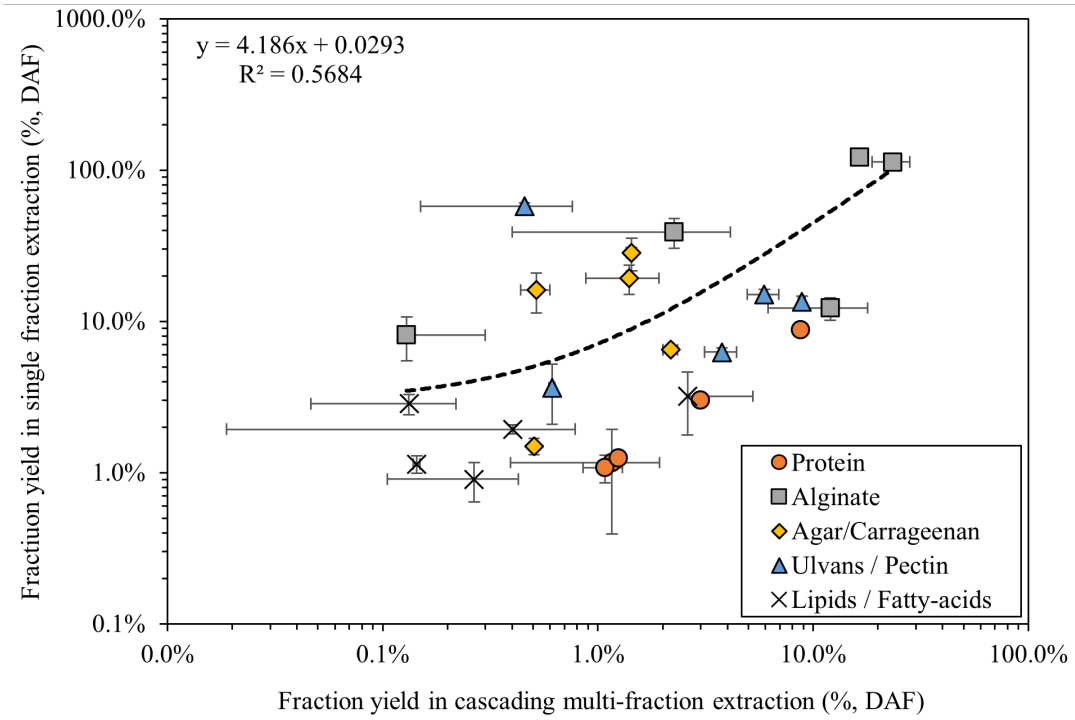

Figure 4.13: Scatter plot comparing total mass yield (dry and ash-free basis, DAF) of different fractions recovered by single-fraction approach vs. cascading mutli-fractionation approach. Error bars are 95 % confidence interval about the mean result.

single-fraction approach (gradient of linear best-fit = 4.186). In addition to the effect of sequential extractions potentially causing an impact on downstream yields, there is significant mass-lost in the recovery and work-up between each of the steps.

Figure 4.14 shows the total mass repartition of the cascading multi-fractionation approach, including accounting for the residual solids remaining at the end of the final extraction process, and the total missing mass assumed to have been lost in work-up and isolation. Determination of the missing mass is simply the balance remaining when the sum of individual fractions and residual mass are fully accounted for, and subtracted from 100 %.

Total quantity of residual solids remaining at the end of the extraction cascade range from a low of 6.1 % (SP), to a high of 25.7 % (SG). In fact, for species UL, GR, and SG, the residual solids make up the largest accountable mass even after the serial extractions. In the case of both SP and SL the highest individual accounted fraction in

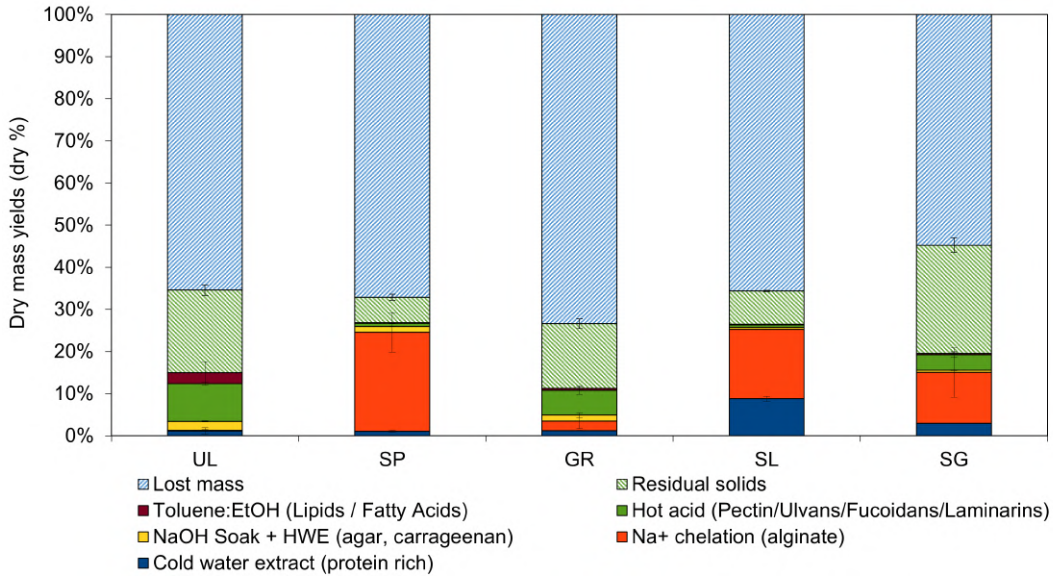

Figure 4.14: Bar plot of total mass repartition throughout the cascading multi-fractionation approach. Seaweeds are *Ulva lactuca* (UL), *Spinosum sp.* (SP), *Gracillaria sp.* (GR), *Saccharina latissima* (SL), and *Sargassum sp.* (SG).

the multi-fractionation approach is the Na^+ chelation fraction (alginate) at 23.5 % and 16.5 % for SP and SL respectively.

In all cases however, the total unaccounted "missing" mass is the largest component of the repartition (figure 4.14). Total unaccounted mass ranges from a low of 54.7 % (SG) to a high of 73.5 % (GR), representing a large loss in total starting mass when performing experimental workup steps (e.g. washing, filtering, etc.) Step-wise processing necessitates the isolation of intermediate fractions and residue, thus the repeat washing and resulting disposal of soluble components is likely responsible for a large fraction of the lost mass. Characterisation of the lost soluble mass was not done in this work, however there are numerous examples in the literature of both characterisation and valorisation of soluble seaweed hydrolysates.[95, 176]

In addition to the mass yields and total repartition, the composition of fractions is considered. Fingerprint identification of individual fractions was made with FT-IR spectroscopy in order to confirm each separate techniques successfully isolates an extract of a different chemical composition. The FT-IR spectra for all fractions generated by

GR during the cascading multi-fraction are shown in figure 4.15.

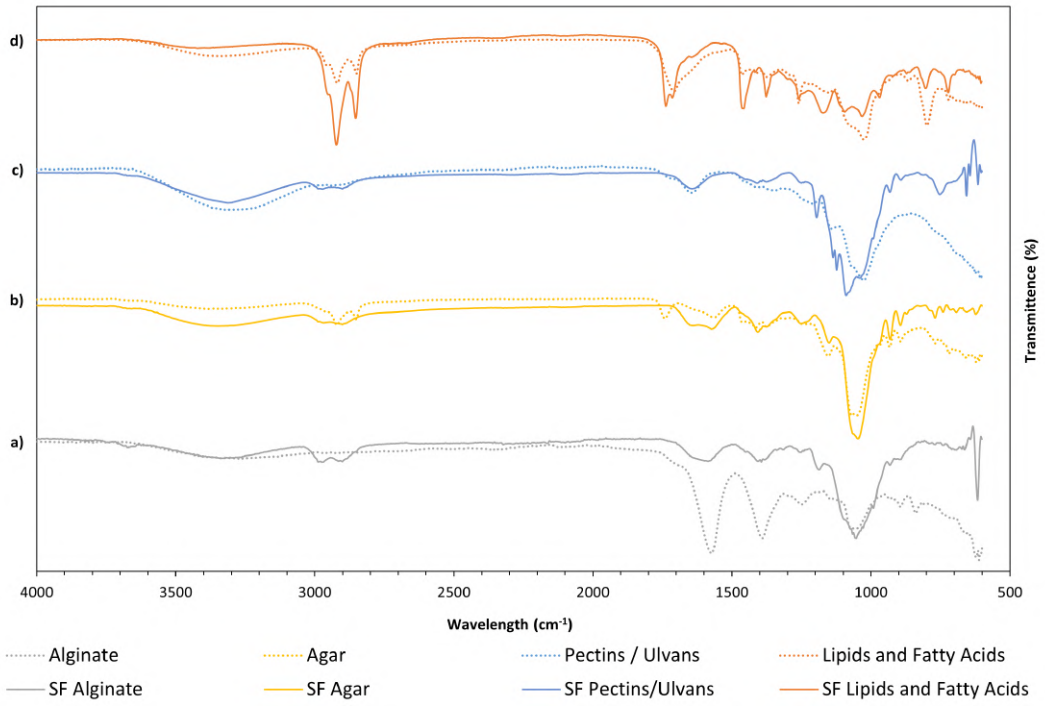

Figure 4.15: FT-IR spectra of different extract fractions of *Gracillaria sp.* (GR), extracts are **a)** alginate rich fraction produced with trisodium citrate extraction, **b)** agar / carrageenan fraction produced with the hot-water extraction, **c)** ulvan/pectin fraction produced with the mild-acid digest, and finally **d)** lipid / fatty-acid fraction produced with the toluene:ethanol extraction. Solid lines are spectra for extracts produced in the cascading multi-fractionation approach, and dotted lines are spectra for extracts produced from the single fractionation approach.

Figure 4.15 excludes the protein fractions, since in both the single-fractionation an multi-fractionation approach, the protein fraction is produced from biomass that has undergone identical treatment. The multi-fractionation spectra (solid lines) are overlayed with the singe-fractionation spectra (dotted lines). For the alginate fraction (figure 4.15**a)**) the main peaks are present, however less cleanly resolved at 1400 cm^{-1} and 1580 cm^{-1}. Similar trends are noticeable in the agar/carrageenan fractions (**b)**), the pectin/ulvan extracts (**c)**), and the lipid/fatty-acid extract (**d)**).

Similar comparisons of the spectra for UL, SP, SL, and SG are displayed in the appendix in figures A1 to A4. The comparison of the spectra confirms that, despite a lower overall mass yield when compared to single-fractionation (figures 4.12 and 4.13), the

composition of the extracted fractions appears to be maintained.

4.3.3 Thermochemical processing of seaweeds and extracted residues

Thermochemical processing of insoluble seaweed residues was performed to test the coupling of a polysaccharide extraction biorefinery process with a thermochemical char production process. Converting the low-value insoluble seaweed residues that remain after the polysaccharide extraction process offers the opportunity to further valorise the residual seaweed biomass as a carbon-rich soil ameliorant and/or $CO_{2,eq}$ vector for long term carbon sequestration. Hydrothermal carbonisation (HTC) and slow pyrolysis (SP) techniques were employed on the wet biomass and dried biomass respectively.

Saccharina latissima (SL), *Ulva lactuca* (UL) and *Sargassum sp.* (SG) species were selected to represent commercially attractive brown (SL) and green (UL) seaweeds, and as an abundant opportunity crop (SG). Additionally, a sample of SL residue solids following a simple hot-water extraction (2 hr, 80 °C) were included as a representative of how biorefinery residual solids might behave in a thermal process, labelled SW-HWE.

Table 4.2 contains the summary information for the thermal processing by hydrothermal liquefaction and slow pyrolysis of macroalgaes and extracted residues. Direct comparison of the total mass yields of char produced by each method shows that in almost all cases, the SP process yields a higher total mass of char compared to HTC. The outlier is in the SL-HWE sample which achieved almost equal mass yields with the two techniques.

Total char mass yield generated in HTC is typically lower than for SP, however, it can be seen that there is a significant yield of material into the HTC aqueous phase. In comparison, the yield of room-temperature condensate recovered from the SP gas is very low, and with no continuous aqueous phase present in the SP process, a larger proportion of the starting material appears to remain in the solid char.

Concentration of carbon in the char is higher in HTC chars than SP chars all test cases, albeit marginal in the case of SG. For SL and SL-HWE however there is a significant

Table 4.2: Summary results from the thermal and hydrothermal processing of macroalgae and macroalgal solids by hydrothermal carbonisation (HTC) and slow pyrolysis (SP). Values in parenthesis represent the 95 % confidence interval about the mean, n=3.

		Feedstock			
	Thermal Process	SL	SG	UL	SL-HWE
HTC Char	Char mass yield (%)	18.3 (0.6)	36.9	31.5	48.2
	Aq. residue mass yield (%)	48.3 (3.9)	19.5	36.4	32.5
	Char C %	61.7	49.8	26.7	59.2
	Char H %	6.0	4.4	2.9	6.0
	Char N %	3.1	1.4	1.4	2.5
	Char S %	1.7	1.8	5.1	Nd[a]
SP Char	Char mass yield (%)	51.0 (0.8)	55.8 (0.1)	72.9 (0.4)	47.5
	Condensate mass yield (%)	2.7 (2.3)	0.6 (0.1)	1.0 (0.3)	0.0
	Char C %	36.5	49.5	23.5	49.4
	Char H %	2.0	4.0	1.7	4.2
	Char N %	2.0	1.3	1.3	2.7
	Char S %	1.0	1.8	4.9	0.2

a) Value below LoD.

gap between the concentration of carbon in the HTC char compared to the SP char, suggesting that under the aqueous HTC conditions a higher proportion of relatively low-carbon components are partitioned into the aqueous phase. This is supported by the observations made in figure 4.6, that SL was found to have the highest recovery of protein rich fraction (relatively high N), thus removal of the high N species in the aqueous processing leaving relatively carbon rich residues in the solids and char fraction.

4.3.4 Char stability and germination

Production of char by either HTC or SP in this case is considered for the purpose of carbon sequestration and soil amendment. Thus, a lower char mass yield combined with a higher carbon fraction (e.g. HTC-SL compared to SP-SL) may still result in an overall higher mass of captured carbon.

Furthermore, the form of the captured carbon is important. It is not simply enough to return a carbon rich material to the soil, the carbon must be stable and the material non-toxic. Oxidative stability of the char is assessed by the Edinburgh stability tool as

previously described, with summary results displayed in table 4.3. Despite the typically higher content of carbon partitioned into the HTC chars compared to SP chars (table 4.2), the overall sequestration potential of the chars is universally higher for SP char.

This is a product of both the higher char production yield (average of 566 g_{char}/kg_{init} for SP char compared to 267 g_{char}/kg_{init} for HTC char), but also the total stable fraction of carbon (79.8 % for SP char, compared to 67.5 % for HTC char). The combination of higher char yield and higher carbon stability results in an significantly higher overall sequestration potential when considering the SP route to produce char, with SP achieving a P_{seq} of between 95.2 and 188.7 g_C/kg_{init}, compared to 58.6 to 116.1 g_C/kg_{init} for and HTC process.

Table 4.3: Summary of char oxidative stability and biomass carbon sequestration potential for a selection of macroalgae chars produced under hydrothermal carbonisation (HTC) and slow pyrolysis (SP). P_{seq} refers to the total carbon sequestration poteintial.

Biomass	HTC Char			SP Char		
	Char production yield g_{Char}/kg_{Init}	Stable fraction of carbon content %	P_{seq} g_C/kg_{Init}	Char production yield g_{Char}/kg_{Init}	Stable fraction of carbon content %	P_{seq} g_C/kg_{Init}
SG	368.9	63.2 (0.9)	116.1 (1.6)	558.0	68.3 (9.7)	188.7 (26.9)
SL	184.5	29.2 (1.1)	67.5 (7.2)	500.5	96.8 (2.7)	176.9 (5.0)
UL	320.7	72.3 (1.5)	62 (1.3)	729.0	55.6 (0.8)	95.2 (1.4)
SL-HWE	193.7	75.4 (0.004)	58.6 (0.003)	475.4	98.6 (1.3)	156.8 (20.4)
Average of all biomass	266.9 (45.1)	67.5 (3.7)	76.1 (13.2)	565.7 (56)	79.8 (10.4)	154.4 (20.4)

Potential toxicity of chars is assessed by germination testing as described in section 4.2.3.5. Germinated radish seeds after 48 hours of incubation are shown in figure 4.17a. When measuring the radicle length, care was taken to measure only the length of juvenile root up to the hypocotyl, and not any length of the juvenile stem or leaf (e.g. as per figure 4.16). Total radicle length (root length), of radish seeds exposed to different concentrations of char extract, after 48 hours of incubation is shown in figure 4.17b. The control group (DI water only) had an average radicle length of 19.2 mm (± 0.5

mm 95 % CI). Seeds germinated in SP char extracts had average lengths of 1.0 mm (± ND - only one germinated), 10.9 mm (± 2.8 mm), and 19.9 mm (± 4.7 mm) for the 100 % v/v, 10 % v/v, and 1 % v/v solutions respectively of aqueous SP char extract. Seeds germinated in HTC char extracts had average lengths of 6.7 mm (± 2.1 mm), 16.9 mm (± 1.6 mm), and 16.9 mm (± 9.0 mm) for the 100 % v/v, 10 % v/v, and 1 % v/v solutions respectively of aqueous HTC char extract.

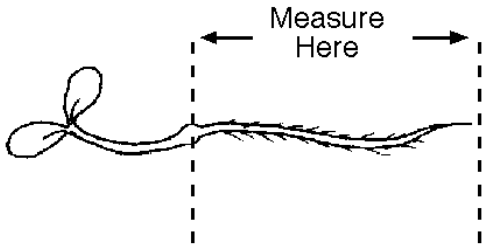

Figure 4.16: Sketch of the appropriate position to take the radicle length measurement from. Image from Cornell (2009).[295]

Germination rates at 24 hr and 48 hr (SG_{24}, SG_{48}), relative germination frequency (RSG), relativel radicle growth (RRG), and total germination index (GI) for both HTC and SP extracts at different concentrations is shown in table 4.4. For all measures (SG, RSG, RRG, and GI), anything below 100 % indicates *worse* performance compared to the DI water control.

For both types of char (SP and HTC), germniation of radish seeds is signicantly impacted on exposure to high strength extract concentrations, with an overall GI % of 0.0 % and 30.1 % for the SP and HTC char extracts respectively when used at full strength (100 % v/v dilution strength). In the case of SP char, this is a result of both an extremely low RSG (1.4 %) and a low RRG (0.2 %), so both the initial germination *and* the early stages of growth were negatively impacted. For the HTC char however, the RSG was reasonable (92.8 %) showing that the initial swelling and germination of the seed was only minorly affected, however the post-germination root growth was severely impacted, with and RRG of 32.4 % when compared to the control.

At 10 % dilution strength, there is significant improvement compared to 100 %. RSG raises up to 102.9 % and 98.6 % for SP and HTC chars respectively, indicating that

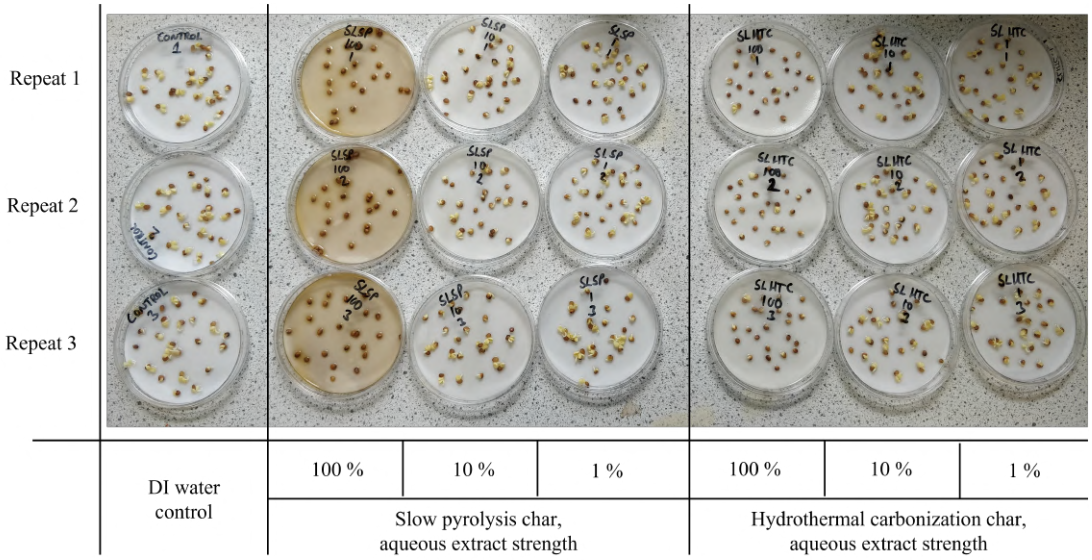

(a)

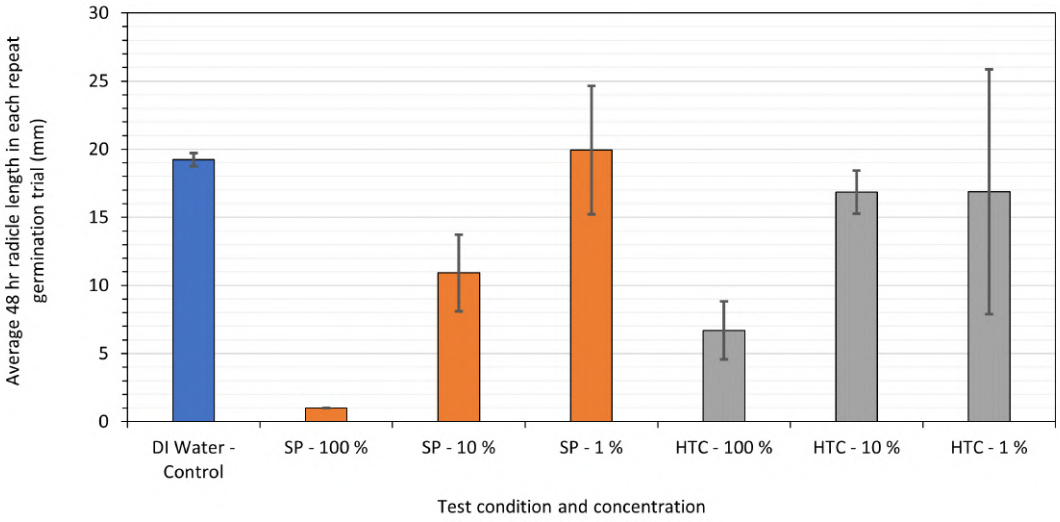

(b)

Figure 4.17: a) Germinated radish seeds after 48 hours of incubation in various test conditions, and **b)** average radicle length for each test condition. n=3 replicates for each condition, each replicate contains 24 seeds. Error bars are at 95 % confidence interval in the mean.

at solutions of 10 % and below the total germination rate will be largely unaffected by the choice of char production process. RRG however once again shows a clear difference between the two techniques, with SP char extract resulting in an RRG of 59.5 % compared to the 86.6 % of HTC char extract. This, again, suggests that both

Table 4.4: Summary results of the germination rates, relative radicle growth, and germination index for radish seeds germinated in different strength aqueous extractions of slow pyrolysis char (**SP**) and hydrothermal carbonisation hydrochar (**HTC**). **SG** refers to seed germination rate at 24 and 48 hours, **RSG** is the relative germination frequency (vs. the control group), **RRG** is the relative radicle growth (total root length vs. control group), and **GI** is the germination index (equations 4.15 to 4.18).

Char Type	Dilution Strength %	$\mathbf{SG_{24}}$ %		$\mathbf{SG_{48}}$ %		**RSG** %	**RRG** %	**GI** %
		ave	stdev	ave	stdev			
Control	0	95.8	4.2	97.2	2.4	100.0	100.0	100.0
SP	100	0.0	0.0	1.4	2.4	1.4	0.2	0.0
SP	10	97.2	2.4	100.0	0.0	102.9	59.5	61.2
SP	1	94.4	2.4	97.2	2.4	100.0	103.7	103.7
HTC	100	56.9	12.7	90.3	13.4	92.9	32.4	30.1
HTC	10	94.4	2.4	95.8	4.2	98.6	86.6	85.3
HTC	1	95.8	7.2	97.2	4.8	100.0	89.2	89.2

char extracts are having an impact on the post-germination root-growth, causing slower growth, with SP char having a more severe impact than HTC char.

At 1 % dilution strength however, the picture changes. For both HTC and SP chars the germination frequency (RSG) is now identical to the control group, achieving 100 % for both char types. Radicle growth (RRG) however now shows some significant differences. SP char extract results in seeds with an average radicle length of 103.7 % of the length of the control group, compared to 89.2 % for HTC char extracts. This significant jump for the SP char extract (when comparing use between 10 % and 1 %) now suggests that there may now be a benefit to the nascent seedling when using SP char to ameliorate the germination media. However, the lower RRG seen with the HTC char at 1 % dilution has not significantly changed from the RRG observed with HTC char extract was used at 10 % concentration. The continued stunting of root growth now starts to suggest that there may be a specific herbicidal compound formed in the process to produce HTC chars, that's *not* produced during slow-pyrolysis of the same biomass.

The end result is an overall germination index (GI) impact of 89.2 % and 103.7 % for HTC char and SP char respectively when used adequately diluted (1 % v/v solution

of aqueous extract). This demonstrates that slow pyrolysis is an excellent technique to recover carbon in this process, since the slow pyrolysis process both produces char with higher sequestration potential (table 4.3), *and* when used in an appropriately dilute concentration results in a germination index slightly higher than 100 %.

4.3.5 Films and coatings

To assess the suitability of macroalgal extracts as a packaging material, a selection of extracted alginate *and* commercially supplied alginate were used to form self-standing flexible films, as well as brush-coated onto a bagasse tray substrate. Production of films and application of the film solution (FS) to a substrate allows assessment of the barrier properties of the native polysaccharide, as well as the differential impact of using different techniques to render the native alginate insoluble, namely conversion to calcium alginate or to alginic acid using calcium chloride and hydrochloric acid solutions respectively.

4.3.5.1 Thin films

Alginate films were produced as described in section 4.2.3.7, and functionally tested by a number of measures that are critical to their performance in the context of food packaging. Namely, gas (oxygen) and water vapour barrier properties are determined by measurement of the oxygen permeability and water vapour transmission rate (WVTR) respectively, since control of moisture and oxygen are critical to the rate of food spoilage Additionally, the water-contact angle is briefly assessed to indicate the relative hydrophobicity/-philicity of the film surface, as well as the film behaviour in prolonged contact with liquid water.

Gas permeability of various alginate based films was tested, with oxygen supplied at 1 bar(g) as the penetrant gas as described in section 4.2.2.4. Alginate based films were produced as described in section 4.2.3.7, with sodium alginate (Na-Alg), alginic acid (H-Alg) where the acid conversion has been performed with 1M hydrochloric acid (HCl) or 1M citric acid (CA), and calcium alginate (Ca-Alg). In all cases, 25 % (w/w) of glycerol was included as a plasticizer. Commercially available food-safe kitchen clingwrap

(Polyethylene – PE, polyvinylchloride – PVC, and a PLA/PBAT blend) are included as a point of comparison, as well as aluminium kitchen foil. Figure 4.18 shows the results of the oxygen permeability testing.

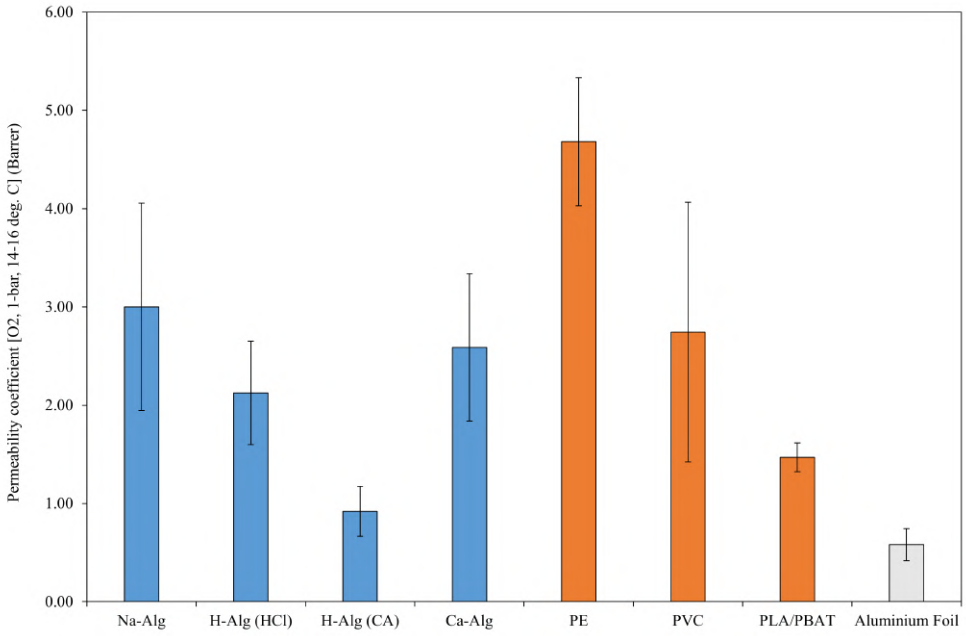

Figure 4.18: Oxygen permeability coefficients for alginate based films of sodium alginate (Na-Alg), calcium alginate (Ca-Alg), and alginic acid (H-Alg) produced by immersing alginate films in 1M hydrochloric acid (HCl) or 1M citric acid (CA). Also included are traditional food-wrap films, polyethylene (PE), polyvinylchloride (PVC), poly-lactic acid/ Polybutylene adipate terephthalate blend (PLA/PBAT), and aluminium kitchen foil. Error bars show 95 % confidence interval about the mean.

In all cases, the alginate based films have an oxygen permeability coefficient lower than or equal to the ubiquitous food-wrap films. This demonstrates that the base alginate matrix has inherently good oxygen barrier properties, and that simple treatments (e.g. a salt-swap to calcium alginate, or conversion to alginic acid) does not hamper the performance. In fact, the film where citric acid was used to regenerate alginic acid resulted in the lowest permeability coefficient of all polymer films, only being beaten by the aluminium foil.

Water vapour permeability of various alginate based films was also tested, as described in section 4.2.2.4. Again, commercial PE and PLA/PBAT films are included for comparison, as well as aluminium foil. Figure 4.19 shows the results of the water

vapour permeability tests.

In all cases, the water vapour transmission rate (WVTR) of alginate based films is significantly higher than both PE, and PLA/PBAT films. Comparing just to PE the average result for the alginate films is two orders of magnitude higher than the PE film, showing that alginate films present a significantly worse barrier to the passage of water vapour compared to traditional PE food wrap. Similarly, the PE/PBAT film is approximately one order of magnitude lower in WVTR compared to the alginate films, but itself presents a worse water vapour barrier than the PE film. Comparison amongst the alginate films a quite similar trend to that seen in the O_2 permeability chart (figure 4.18), where both metal-salt forms of alginate (Na- and Ca-Alg) perform almost identically, however the acid form (H-Alg) appears to perform slightly better. However, since repeat measurements of these values were not performed it is harder to have confidence in the apparent difference presented here within the family of alginate films. The comparison between the family of alginate films, and PE and PLA/PBAT however is significant, since figure 4.19 is presented with a logarithmic y-axis the initially modest difference in visual heights actually represents an order of magnitude difference, and similarly the comparison with aluminium foil represents multiple orders of magnitude difference to both alginate and PE/PLA/PBAT films.

Water Contact Angle (WCA) is measured as described in section 4.2.2.5. Water contact angle is a quick indication of the water-shedding properties of the polymer film, with higher contact angles (i.e. at angles ≥ 90 °) the result of a more hydrophobic film surface that's more likely to shed water as it beads up and rolls from the film surface. Low contact angles (i.e. at angles < 90 °) indicate a more hydrophilic surface, with water tending to flatten and wet against the surface of the film rather than bead up and run off. The water contact angle (WCA) at 2 seconds for a native alginate film, an alginate film with 10 wt. % nano-cellulose incorporate, a polyethylene film, polyvinylchloride, and PLA/PBAT blend are summarised in table 4.5.

Standard sodium-alginate film had a low contact angle at 46.58 °, indicating a hydrophilic surface that the water droplet readily wetted against (figure 4.20a). PE had

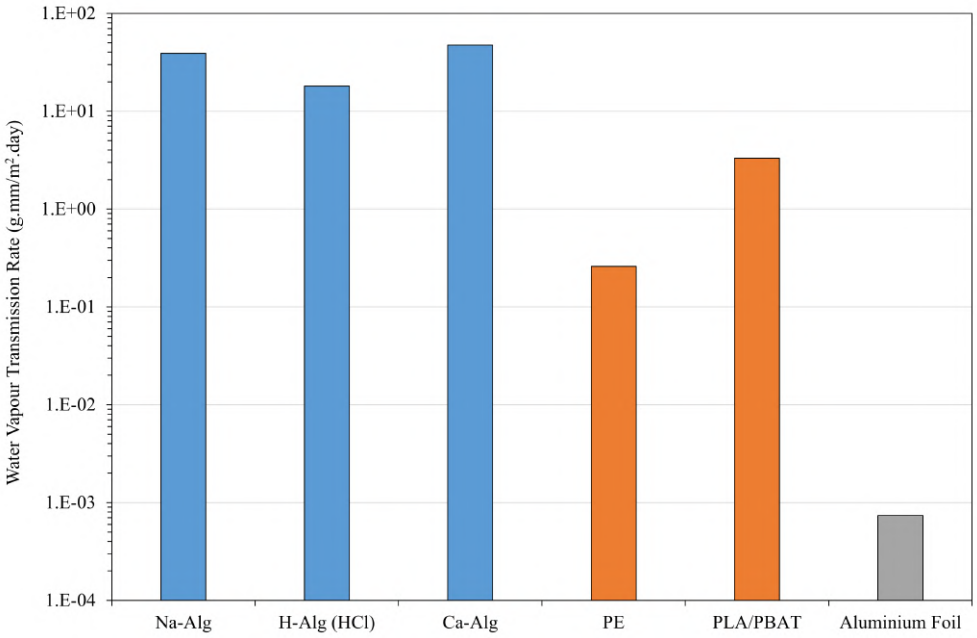

Figure 4.19: Water vapour transmission rate (WVTR) for alginate based films of sodium alginate (Na-Alg), calcium alginate (Ca-Alg), and alginic acid (H-Alg) produced by immersing alginate films in 1M hydrochloric acid (HCl). Also included are traditional food-wrap films, polyethylene (PE), poly-lactic acid/ Polybutylene adipate terephthalate blend (PLA/PBAT), and aluminium kitchen foil.

Table 4.5: Summary of 2s water contact angle measurements for alginate based films, PE, PVC, and PLA/PBAT films.

Film	2s Contact Angle (°)
Na-Alg	46.58 ± 0.4
Na-Alg + CNC	84.03 ± 1.7
PE	83.60 ± 2.6
PVC	72.50 ± 2.1
PLA/PBAT	79.50 ± 8.5

the highest contact angle of the commercially available films, however all of these films had a WCA of > 70 ° resulting in a moderate amount of beading (e.g. figure 4.20b). Interestingly, the addition of 10 wt. % crystalline nano-cellulose to the alginate film dramatically increased the contact angle to the point that it matched the performance of the PE film (table 4.5).

However, the evolution of the WCA over 60 seconds reveals more than has typically been reported on in the literature to date. Despite an initial resistance to water, at extended

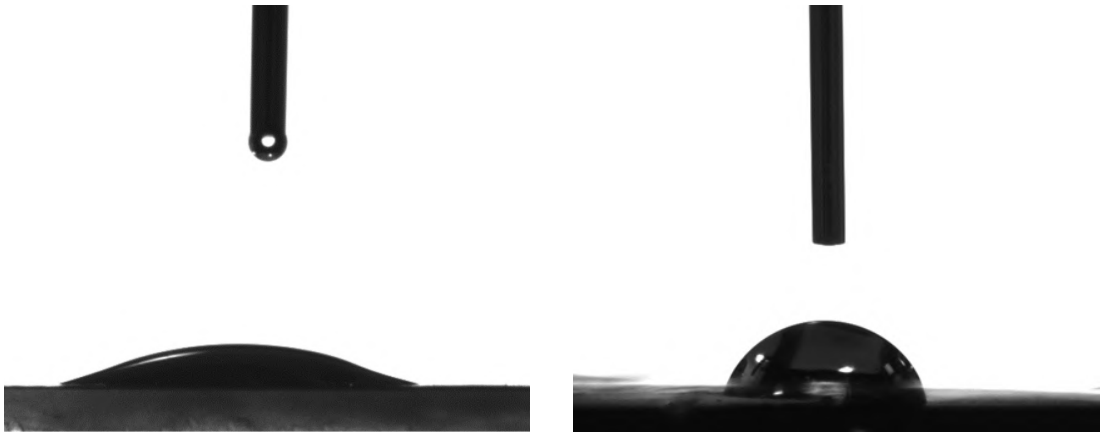

(a) **(b)**

Figure 4.20: 2-second Water Contact Angle silhouettes for **a)** standard sodium alginate, and **b)** polyvinylchloride.

contact times the water droplets are clearly absorbing into the surface of the film and causing local swelling of the polymer (figure 4.21a). This is most apparent with the plain sodium alginate film, where the WCA can been seen to drop significantly over time as the droplet first wets against the surface and is then absorbed. It is also noticeable with the CNC modified alginate however, despite a relatively steady evolution of WCA over time (figure 4.21b). Whilst the WCA appears to remain reasonably high, when the droplet profile is actually inspected it is clear that the film is swelling and warping as the droplet is absorbed. So, despite the first appearance that the WCA is maintained over time, it is clear that extended contact with liquid water causes significant swelling of the film (figure 4.22).

4.3.5.2 Coatings

Bagasse food trays were used to assess the effectiveness of alginate based film coatings as a barrier against water transmission through the tray. Tap water, 0.1 M citric acid, and shop bought pasta sauce were used as test materials. For the tap-water test a plain un-coated tray was included (figure 4.23). Trays were approximately cuboid in shape with dimensions 175 mm x 125 mm x 50 mm, and internal volume approximately 650 mL. Trays were prepared in triplicate, and the average mass of applied coating were 2.85 g m^{-2} ($\pm$ 1.55) for the calcium alginate coatings, and 0.68 g m^{-2} ($\pm$ 0.13) for the

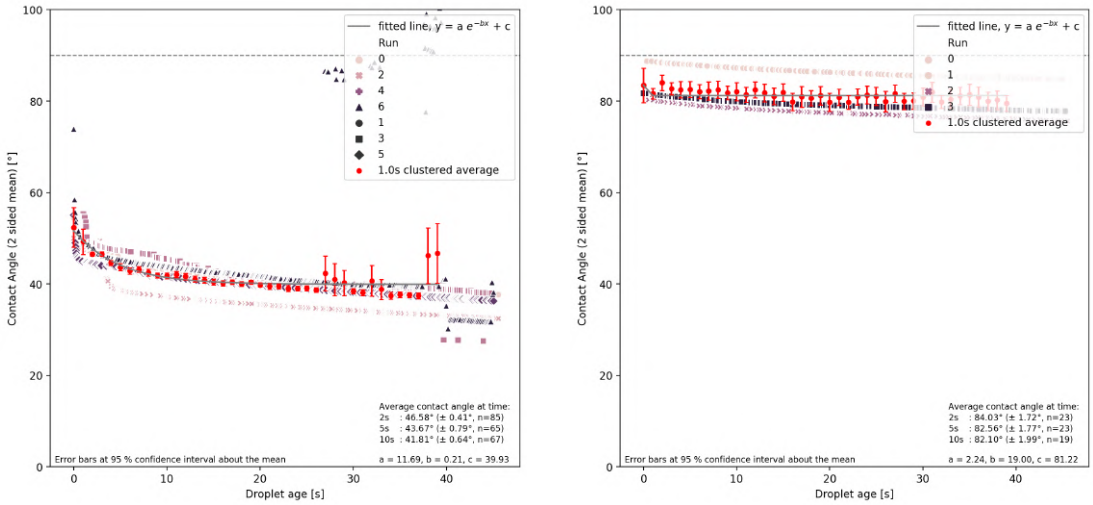

(a) **(b)**

Figure 4.21: Water contact angle (WCA) evolution over time for a) standard sodium alginate film, and b) sodium alginate film with 10 % wt. crystalline nano-cellulose included.

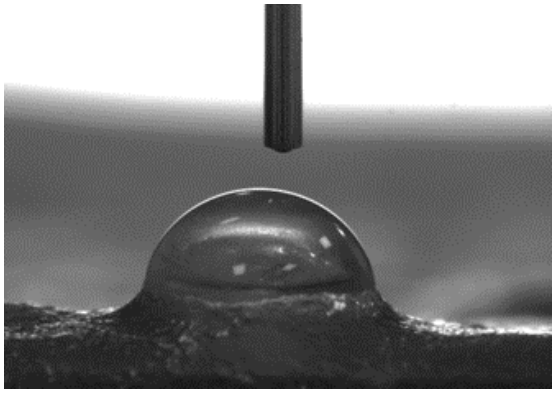

Figure 4.22: Example of the type of swelling observed with all alginate based films during extended water contact (60s).

alginic acid coating.

Figure 4.23 shows the loss-in-mass from the bagasse food trays for calcium alginate and alginic acid coated trays, exposed to three different fillings of tap water (figure 4.23a), 0.1 M citric acid (figure 4.23b), and shop bought pasta-sauce (figure 4.23c). In the tap-water condition (figure 4.23a) a plain and un-coated tray was included as a point of comparison. After 2 weeks, both calcium alginate and alginic acid coatings result in significantly less loss in mass in the tap-water condition (figure 4.23a). After an initial

period (approximately 48 hours) where the mass loss from all trays is relatively limited, a significant gap is opened up between the unlined and lined trays. By day 5 (120 hr) a consistent gap also starts to open up between calcium alginate and alginic acid coatings, with the alginic acid coated tray achieving a lower total mass loss by the end of the test.

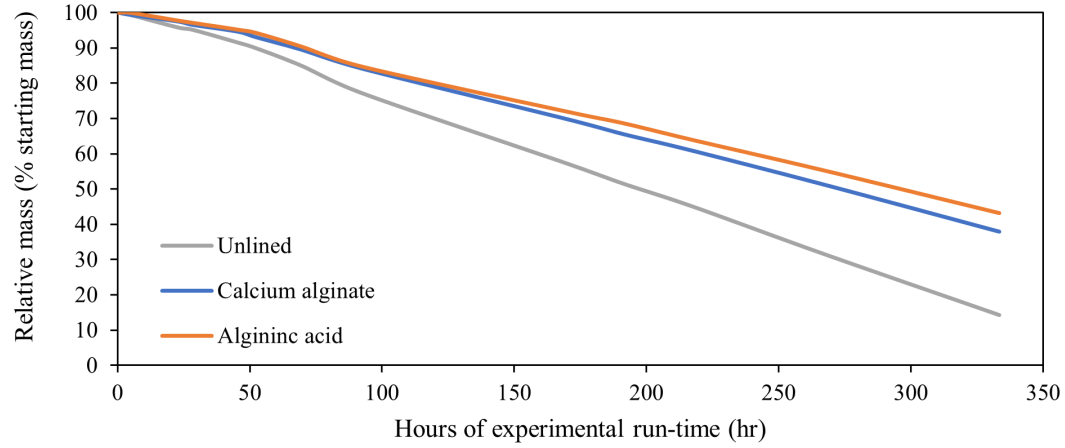

(a)

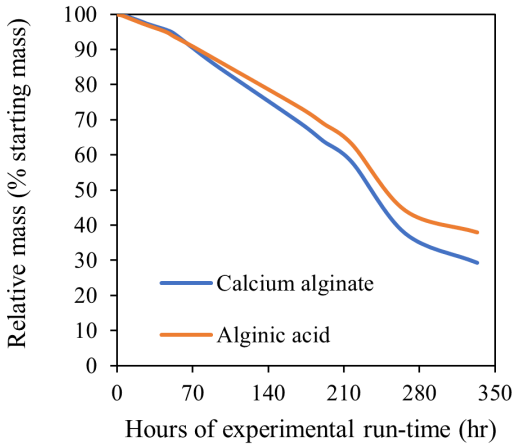

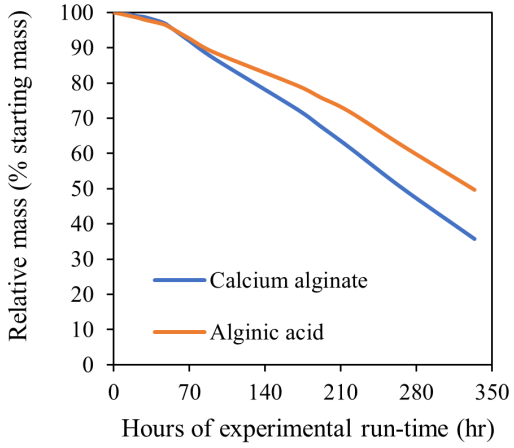

(b) **(c)**

Figure 4.23: Loss in mass vs time for different applied coatings when bagasse trays are used to contain **a)**, tap water; **b)** 0.1 M citric acid; and **c)** shop-bought pasta sauce.

Similarly, in the citric-acid condition (figure 4.23b) and the pasta-sauce condition

(figure 4.23c) the alginic acid coated food tray outperformed the calcium alginate coated tray after an initial period (approx. 70 hours) where both coatings perform more-or-less identically. In the citric-acid condition there is a rapid drop in mass in both coated trays with the onset around 210 to 240 hours.

However, despite increased performance the alginate based systems do not offer a complete water barrier over a few minutes in direct contact with water or typical food stuffs. To deliver a superior film, then alternative fractions of the seaweed need to be explored.

4.3.6 Functionalisation of extracted agar fractions

Agar is another fraction that has been isolated from the seaweed, and has been demonstrated as a free standing film as well as the base polysaccharide in a composite matrix.[59, 105, 219, 296] Excitingly a number of reports demonstrate that the agar/polysaccharides can be functionalised with fatty acids to produce a more water resistant product. Though no processing data exists on functionalised agar. To assess whether this functionalised agar material could be a suitable material for a longer term water barrier, it was first synthesised with using agar extracted from the *Gracilaria sp.* seaweed. Thereafter the material was assessed for melt-flow processing via rhemoetry and extrusion.

FTIR spectra of commercially available agar, the extracted agar fraction from Gracilaria seaweed, palmitic acid, and the C16-functionalised agar are shown in figure 4.24. Figures 4.24a and 4.24b both show broadly the same chemical profile, with main peaks at 1041 cm^{-1} and 1067 cm^{-1} respectively, aligning with the enhanced glycosidic peak found through the literature.[297]

The peaks at 2848 cm^{-1} and 2915 cm^{-1} found in both palmitic acid and functionalised agar (figures 4.24c and 4.24d) can be assigned to stretching of the $-CH_3$ and $-CH_2-$ groups respectively.[298] This demonstrates the presence of the long hydrophobic fatty acid tail from the palmitic acid after the functionalisation reaction. Furthermore, the shifting of the 1698 cm^{-1} peak found in palmitic acid (figure 4.24c) to a 1745 cm^{-1} peak in the functionalised agar (figure 4.24d) represents the reaction of a carboxylic acid (-COOH) to an ester (-COO-) linkage.[281]

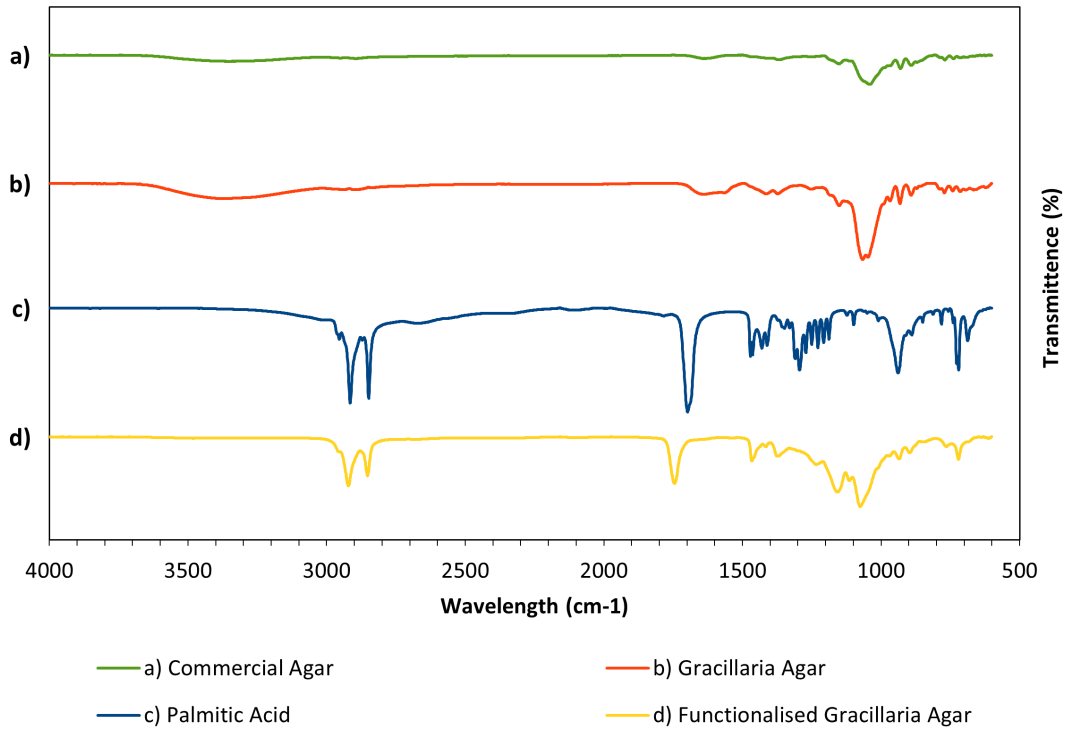

Figure 4.24: FTIR transmittance spectra of **a)** commercial agar, **b)** agar extracted from Gracilaria seaweed, **c)** palmitic acid, and **d)** Gracilaria agar that has been functionalised with palmityl-chloride.

4.3.7 Rheometry

Establishment that the ester bond has been formed and the fatty-acid residue was confirmed with FT-IR analysis (figure 4.24). Additionally, the resulting powder from the synthesis reaction appears insoluble in both water (cold and hot), and common laboratory solvents (ethanol, acetone, chloroform). No processing data is known on these materials in the literature. Therefore data that follows represents the first characterisation of the molten flow properties of C16 functionalised agar, a vital first step in characterising this material to allow prototyping of products and process development.

Rheograms of viscosity (η, Pa.s) and shear-stress (σ, MPa) plotted against shear rate (γ, s-1) for the C16 functionalised biological grade agar at temperatures 140 °C to 180 °C under heating conditions are displayed in figures A5 to A12, and rheograms of

same under cooling conditions from 180 °C to 140 °C in figures A13 to A17.

Rheograms generated at 140 °C and 150 °C (figures A5 and A6 respectively) were impacted by the maximum torque limit on the rheometer, hence are not plotted over the full range of desired shear-rate. At temperatures 155 °C to 180 °C under heating conditions, the general trend is equal for all. A linear drop in viscosity and linear rise in shear-stress against shear rate whilst plotted on a log-log plot, indicates a degree of non-Newtonian flow behaviour at the tested shear rates and these temperatures. The trend of increasing temperature appears to be that of decreasing viscosity at all shear-rates, similarly the material stress decreases as a function of increasing temperature.

For each plot, the power-law lines of least-squares regression for each data set is fitted such that $y = cx^m$. The intercept coefficient c is equivalent to the flow consistency index (K), and the exponent m is equivalent to flow behaviour index (n and n^{-1} for the stress vs. shear-rate and viscosity vs. shear-rate plots respectively). Correlation coefficient for the fitted power-law regression lines indicates strong correlation, with R^2 values from 0.84 to 0.99. For the purpose of evaluating K and n the plots at T = 140 °C and T = 150 °C (figures A5 and A6 respectively) are excluded due to the aforementioned operation at torque-limit on the rheometer equipment.

Table 4.6 shows the determined values of K and n under heating conditions from T = 155 °C to T = 180 °C, and cooling from T = 180 °C to T = 140 °C. The same data are plotted in figures 4.25a and 4.25b, but with the addition of arrows as a visual aid in indicating the progression of K and n during heating and cooling.

4.3.8 Extrusion processing

The comparison of required specific motive power, P (W/kg), for two different grades of agar (technical and biological grade, AGT and AGB respectively) is shown in figure 4.26. The comparison is made with two different length fatty acid substitutions (C12 laurate, and C16 palmitate) at the same screw speed (150 rpm), and at two different screw speeds (150 rpm and 20 rpm) with the same fatty acid fragment (C16 palmitate). In all cases, the required motive power was higher for the technical grade agar

Table 4.6: Flow consistency index (K) and flow behaviour index (n) as a function of melt temperature (T) and direction of temperature change.

T $°C$	dT approach	K Pa.s	n [dimensionless]
155	Heating	4798.8	0.211
160	Heating	1300.6	0.361
165	Heating	392.1	0.472
170	Heating	246.4	0.490
175	Heating	70.1	0.586
180	Heating	23.1	0.570
175	Cooling	6.3	0.765
170	Cooling	4.0	0.816
165	Cooling	3.2	0.853
160	Cooling	3.2	0.875
140	Cooling	8.3	0.864

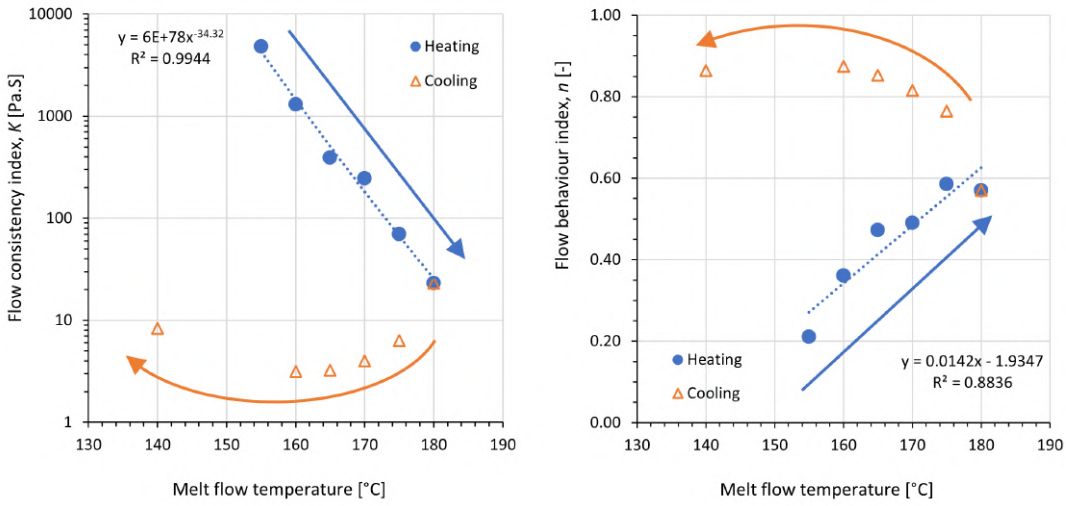

(a) **(b)**

Figure 4.25: **a)** Flow consistency index (K), and **b)** Flow behaviour index (n), of C16 functionalised biological grade agar between melt flow temperatures of 140 °C to 180 °C, under heating and cooling conditions (arrows show trajectory).

(AGT) compared to biological grade agar (AGB). The magnitude of the difference is the smallest for the C12 laurate substituted functional agar, with the effect of increasing fatty-acid fragment length working to increase the size of the difference between the required motive power at 150 rpm for AGT and AGB. The bulk of this difference

is accounted for by a relatively large decrease of the required power for AGB when comparing the C12 laurate and C16 palmitate functionalised materials.

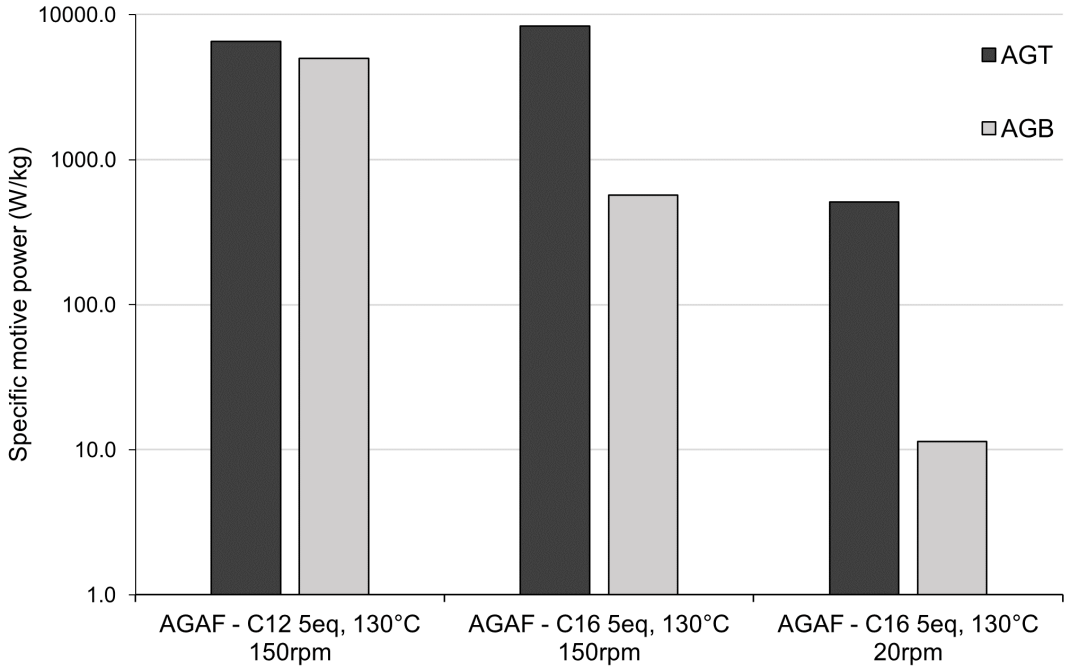

Figure 4.26: Specific motive power required to produce viscous flow of functionalised materials within the Haake Minilab II micro-compounding twin-screw extruder, for agar functionalised with 5 molar equivalents of C12-laurate and C16-palmitate, at screw speeds 150 rpm and 20 rpm.

Comparing the effect of different screw speed of the C16 palmitate substituted material, the main effect observed is that reduced screw speed requires reduced motive power. This is to be expected since the extruder internal geometry is fixed. The internal conveying screws can be thought to act together exactly as a positive displacement pump, hence any decrease in screw speed results in a corresponding linearly correlated decrease in the pumped volume. The 7.5 fold decrease in pumping speed is associated with a 16 fold reduction in required pumping power for the AGT material, but a 50 fold decrease for the AGB material. In both cases this is a departure from the normally understood pump affinity laws, where for a positive displacement pump the required power is directly proportional to the discharge rate of the pumped fluid. This suggests that both AGT and AGB functionalised materials exhibit non-Newtonian flow behaviour when

molten.

The temperature dependence of the specific motive power for C16-palmitate functionalised agar and κ-carrageenan are shown in figures 4.27a and 4.27b respectively. The overall trend is that of decreasing motive power at increasing temperature for both the functionalised agar (figure 4.27a) and functionalised κ-carrageenan (figure 4.27b).

For the functionalised agar (figure 4.27a), there appears to be a plateau at all screw speeds between temperatures of 110 °C to 130 °C, with motive power required for each screw speed level falling within the same order of magnitude. However, there is a distinct drop in required motive power at temperature above 140 °C for all screw speeds, with required power at 20 rpm, 50 rpm, and 150 rpm dropping by 1, 2, and 2 orders of magnitude respectively between temperatures of 140 °C and 150 °C .

For the functionalised carrageenan (Figure 4.27b), a similar plateau is apparent between 50 °C and 70 °C. There is again a distinct drop as temperature increases to 90 °C, however further increasing the temperature to 130 °C does not seem to significantly decrease the required motive power.

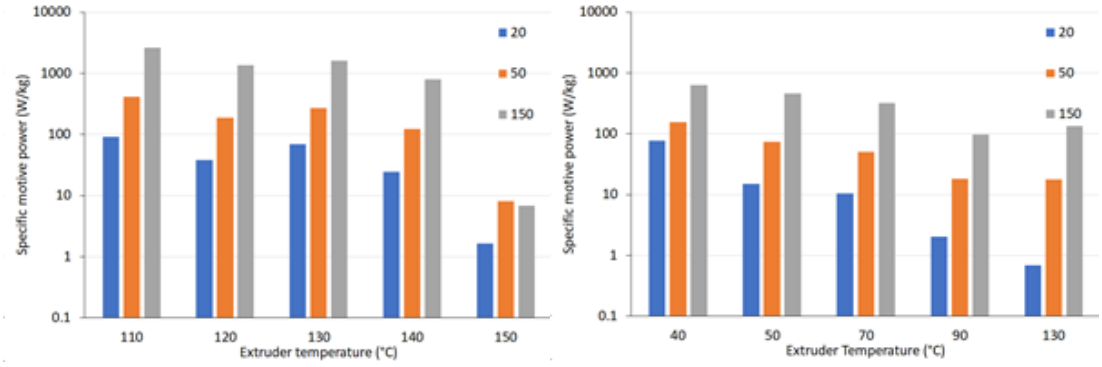

(a) **(b)**

Figure 4.27: Specific motive power required to convey: **a)** C16-palmitate functionalised agar at temperatures 110 °C to 150 °C and 20 rpm, 50 rpm, and 150 rpm; and **b)** C16-palmitate functionalised kappa-carrageenan at temperatures 40 °C to 130 °C and 20 rpm, 50 rpm, and 150 rpm.

Scatterplots of the screw torque against the extruder screw speed (figure 4.27) specifically reveals the impact of the material itself on the absorbed screw power at different

temperatures. For the functionalised agar (figure 4.28a), at each temperature the screw torque increases linearly with the screw speed. This suggests the viscous properties of the material are exhibiting a linear response to the increased shear, suggestive of Newtonian flow behaviour under those conditions. The gradient of each linear trend indicates how much the viscous properties of the material contributes to the overall rotational torque required compared to the frictional drag that can be associated with the motor and transmission of the extruder.

At low temperatures the gradient is highest, with the gradient tending to decrease with increasing temperature (figure 4.28a). Similar to the trend demonstrated in figure 4.27a, the gradients at temperature 120 °C and 130 °C are parallel, indicating no significant change in viscous properties between these temperatures. The flat gradient at 150 °C shows that at this temperature there is minimal viscous drag being contributed by the molten material.

The κ-carrageenan material (figure 4.28b) displays overall similar properties, albeit at lower temperatures. The general trend of requiring higher torque at lower temperatures is maintained, however at high temperatures there is no point where the gradient turns flat. In fact, there is no apparent change in the gradient between 90 °C and 130 °C.

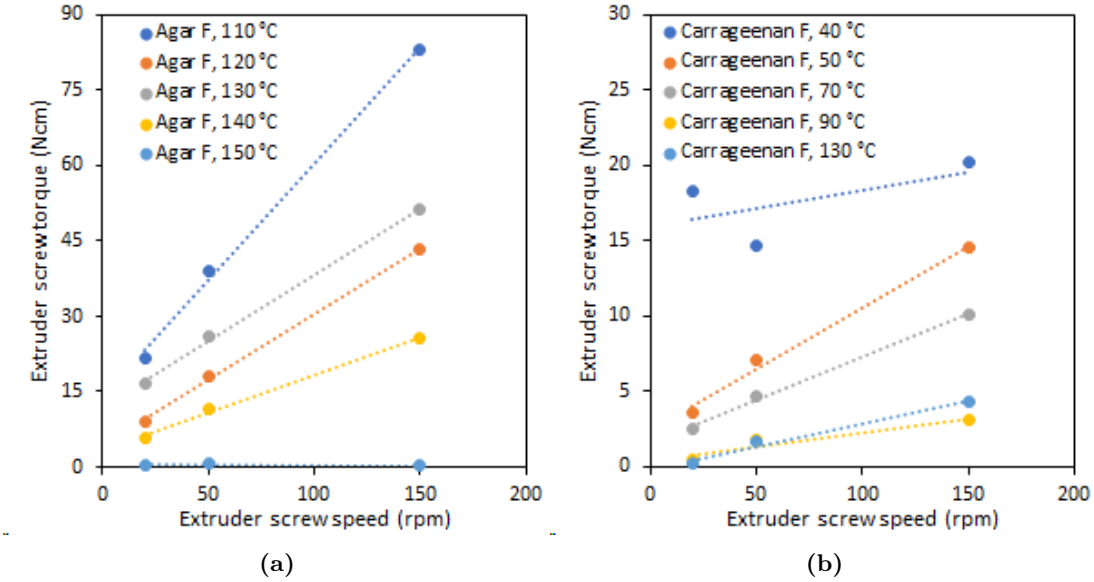

Figure 4.28: Scatter plots of extruder screw torque as a function of screw speed for **a)** C16-palmitate functionalised agar at temperatures 110 °C to 150 °C, and **b**) C16-palmitate functionalised κ-carrageenan at temperatures 40 °C to 130 °C.

Figure 4.29 shows the relationship between screw speed and screw power for both the functionalised agar and κ-carrageenan. With points averaged over the full temperature ranges measured (110 °C to 150 °C for agar, and 40 °C to 130 °C for κ-carrageenan), and across the full range of fatty-acid lengths and molar substitutions considered (C12, C16, and C18, and 3, 4, and 5 molar equivalents of acyl-chloride in the original synthesis). For both materials, there is a good fit for a least-squares line of best fit (R2 = 0.996 for both the functionalised agar and carrageenan). When increasing extruder screw speed and thus material delivery rate, the corresponding power requirement scales faster than a simple linear relationship (exponents > 1). In this case, when considering plant design extrusion equipment should be sized at the larger end of any acceptable range in order to allow comfortable operation at relatively low speeds, since the energy penalty when increasing speed is large.

Figure 6 shows the impact of changing both the length of the substituted fatty acid fragments, and also the quantity of substitution by changing the molar equivalent quantity used in the functionalisation reaction. Increasing fatty acid length from C12-laurate to

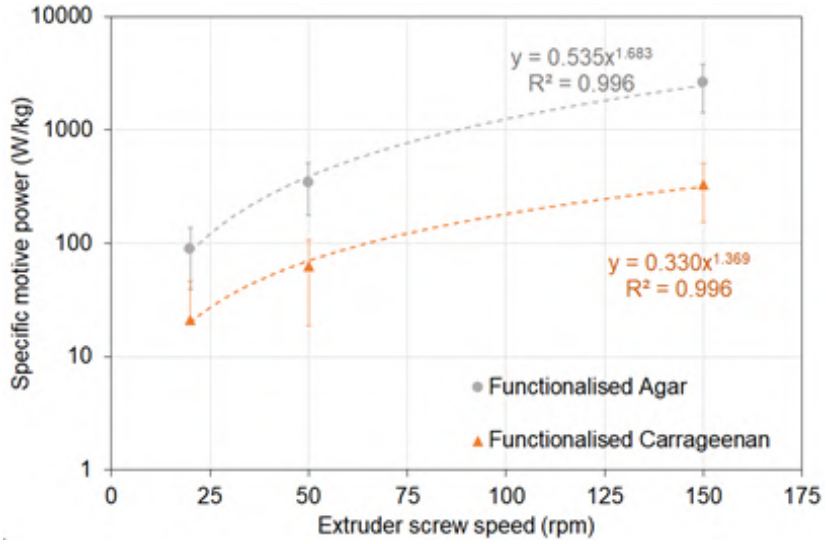

Figure 4.29: Scatter plots of extruder screw power as a function of screw speed for C16-palmitate functionalised agar at temperatures 110 °C to 150 °C, and C16-palmitate functionalised κ-carrageenan at temperatures 40 °C to 130 °C. Points are mean averages of all temperatures, and error bars are plotted as a 95 % CI, n = 5.

C18-stearate has the overall impact of decreasing the specific motive power required. Correspondingly the pressure in the internal recirculation channel decreases both at the inlet (P_{D1}) and outlet (P_{D3}) when increasing the length of the fatty-acid substitution. Considering just the C16-palmitate material, there is no clear effect observed when changing the molar quantity of acyl-chloride used in the functionalisation reaction.

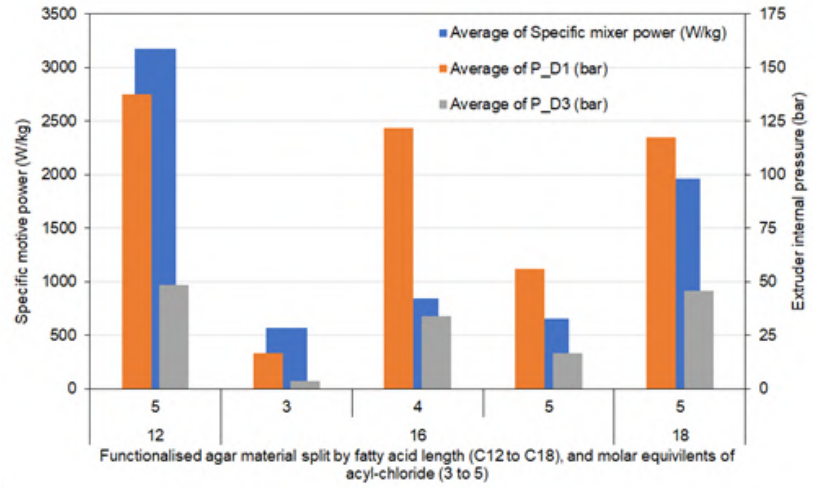

Figure 4.30: Bar plots of specific motive power (left-axis), and the internal pressure at the inlet (P_{D1}) and outlet (P_{D3}) of the extruder recirculation channel (right-axis), whilst recirculating functionalised agar at screw speeds 20 rpm to 150 rpm, and temperature of 130 °C. Materials assessed include functionalised agars substituted with C12-laurate, C16-palmitate, and C18-stearate, at 5 molar equivalents, and also 3 and 4 molar equivalents for the C16-palmitate.

4.4 Discussion

Comparison of the total quantity of extracted fractions under both the single-extraction approach (figure 4.6) and multi-extraction approach (figure 4.12), are compared in figure 4.13. There is a clear loss in individual fraction yields when serially passing the retained biomass between extraction steps. This is expected, since each processing step inevitably results in a loss of material into a waste phase. However, there doesn't appear to be a gradual decrease in the effective recovered yield as stepwise extractions are performed. Following the first extraction step (targeting protein), the average quantity of the recovered fraction was 27.9 % for the alginate step (multi-fraction yield as a % of the single-fraction yield), and 16.6 % for agar/carrageenan, 36.7 % for the hot-acid (ulvans, pectins etc.), and 29.8 % for the lipids/fatty-acids.

The total repartition of starting mass of the macroalgae during the multi-fractionation process (figure 4.14), which confirmed a significant loss in mass through the experimental biorefiniery steps. This loss in mass could be attributed to the isolation and

work-up steps, alternatively the effect of prior isolations may result in a higher purity but lower quantity yield of each fraction.

Chemical composition of the fractions is assessed with FT-IR. The single-extraction fractions are compared against either commercial isolates of the target fraction (e.g. alginate, agar, carrageenan), or with an analogue that contains the same moieties as the target fraction (e.g. soy protein isolate, soybean oil). The FT-IR spectra of the single-fractions (figures 4.7 to 4.11) show that the products of the different extraction techniques are different, although in almost all extracts there remains a broad carbohydrate peak around the 1000 cm^{-1} to 1050 cm^{-1} suggesting a not insignificant content of soluble carbohydrate in most of the crude extracts.

The individual fractions generated in the multi-fractionation approach are also characterised with FT-IR (figures 4.15 and A1 to A4). The overlayed spectra of individual fractions (excluding protein) from both the single-fractionation (SF) and multi-fractionation (MF) for each species show that although the overall yield is lower, the composition of the fractions is not significantly changed by the MF process compared to SF. The biggest outlier was the alginate fraction extracted from the *Sargassum sp.* seaweed, which has some distinctly different peaks for both the SF and MF processes, despite a reasonable fraction mass yield in both the SF (figure 4.6) and MF (figure 4.12) processes.

In general these findings are in-line with those found by Wahlström in their investigation into sequential recovery of biomacromolecules from a single red algae species.[266] In this work a single regime of sequential applications of different extraction techniques has been applied to multiple different seaweed species, and the individual fractions are demonstrated to be highly similar to those gained by single fractionation. This suggests that a multifractionation set up, with multiple seaweed sources is possible and could be used to increase the value products from a seaweed biorefinery.

Thermochemical processing (hydrothermal carbonization and slow pyrolysis) were investigated as possible options for the conversion of extracted macroalgal residues to

produce stable carbon-rich chars. Both HTC and SP processes were successful in producing char (table 4.2), however the total mass yield of char produced was significantly higher in all cases for the SP process. Conversely, the HTC process did a better job of concentrating carbon in the char phase, with HTC chars having universally higher C content compared to their counterpart SP chars.

Whilst there is more effective carbon concentration in the HTC process, the significantly lower yield of char in total when compared to the SP process results in a total lower absolute quantity of carbon ending up in the char phase. This is due to a significant partitioning of the biomass into dissolved aqueous species during the HTC process. Yield improvements may be made through the HTC process however. Heidari et al. (2018) showed that recycling the aqueous phase resulted in a 12 % increase in mass yield of solid product when performing HTC On sawdust.[299]

The effect of atmospheric oxidation was also considered by use of the Edinburgh stability assessment (table 4.3). Carbon sequestration potential (P_{seq}) combines the mass yield, carbon content, *and* crucially the chemical stability of the char when exposed to harsh oxidising conditions (hot peroxide). Comparing the P_{seq} of HTC and SP for all species shows that SP produces a significantly more stable carbon char, and in the case of performing thermochemical conversion the partially extracted material (SL-HWE), the P_{seq} for the SP process was almost 3 times higher than that for HTC.

Similarly, the impact of the different char production techniques was considered in terms of the soil toxicity/seed-germination impacts also. At high concentrations, SP chars had a bigger impact on germinating radish seeds compared to HTC. However, at dilute concentrations, the SP char matched performance of the control set and outperformed HTC char. This is likely an effect of the HTC process naturally washing out salts into the aqueous phase, when mineral content in the starting biomass will remain in the product char for the SP process. The impact of recycling aqueous phase during the HTC process would be interesting to consider at this point, since recycling the process water in order to retain solids mass yield would inevitably result in a larger partition of mineral content back into the HTC-char compared to the single-shot HTC process

utilised in this work. Similarly, the effect of more thorough fraction extraction from the starting seaweed (e.g. the previously discussed MF process) may well significantly temper the impact of high concentration SP char by initially removing many of the salts prior to the SP process entirely.

The combination of both the higher sequestration potential (P_{seq}) and the overall lower impact on seed germination index (GI, table 4.4) make slow pyrolysis an extremely attractive option for the production of a stable carbon char product when coupled to a cascading biorefinery. This is not only technically advantageousin terms of the yield, P_{seq}, and GI, but also from a materials and reactor construction standpoint. Slow pyrolysis is an establish process that has been used to produce charcoal amongst other products for millennia at atmospheric pressure, whereas HTC requires containment in a corrosion resistant pressure vessel, since water is being maintained well above its normal bubble point at atmospheric pressure.

The functional testing of the seaweed extract films and coatings was limited to the barrier properties and water-contact behaviour. There have been numerous descriptions in the literature of alginate based films, both in terms of their mechanical properties, but also extolling their virtues as a food packaging material.[102, 103, 227, 300–308]

This work confirms that alginate based films make an excellent oxygen barrier, with an oxygen permeability coefficient lower than traditional polyethylene and equal in most cases to PVC films (figure 4.18). Water vapour transport rates (WVTR) however are significantly worse for all alginate films tested in this work compared to traditional packaging films. This may be seen as desirable in some applications however, where a partially permeable and transparent membrane is desired to block the passage of oxygen but to permit the transport of water vapour.

Water contact angles were also investigated, which showed that a plain alginate film has very poor liquid water contact properties. Also that the initial contact angle may be modified by the addition of insoluble filler (nano-cellulose in this work), however the long-term performance of a water-wetted alginate film does not appear to match that

of traditional PE/PVC films, with significant swelling and distorting noticed within 60 seconds of water contact.

In many cases, the long-term impacts of water-contact are either not reported on in the literature, or the results are not discussed in the context of the films application. For example, Singh et al. (2020) did investigate the long term (7-day) effects of immersion of their citric-acid and tartaric-acid crosslinked alginate films in a number of solvents. They found that all alginate based films were fully soluble in both 1M NaOH and 1M H_2SO_4, and showed swelling when in contact with water. Yet the conclusions were that the alginate films are still suitable for food packaging.

Despite the fact that this phenomenon of alginate films either completely dissolving (i.e. sodium alginate) or swelling (calcium alginate, alginic acid, acid crosslinked) when in contact with water has been reported on, the application of alginate as a food packaging film is still recommended by many authors. [60, 103, 227] Clearly, a food packaging film that dissolves when in contact with moisture or acid (e.g. many fruits) is not desirable, so the application of the previously reported alginate films would be severely limited, e.g. to dry foods only. In addition, even if limited to dry-foods only, the risk of product wastage as the film swells and degrades in contact with moisture during transport/storage (e.g. rain during loading/offloading) would necessitate the use of a secondary packaging to protect the alginate film from external moisture.

Functionalisation of seaweed extracted agar, as well as commercial grade agar, was undertaken using a C16 fatty acid residue. By substituting a long chain fatty acid a new ester bond is formed, with the highly-hydrophobic alkane region of the fatty acid resisting the ingress and transit of water through the functionalised material. Figure 4.24 demonstrated that the functionalisation reaction proceeds with both a commercial grade agar *and* the extracted agar fraction produced by the multi-fractionation experimental work. Further investigations into the material properties of functionalised agar and carrageenan material was undertaken using commercially available grades of agar (technical and biological) and carrageenan.

Initial investigations into the properties of the functionalised materials revealed a general insolubility in a selection of common lab solvents (water, acetone, ethanol, chloroform), thus new methods of material processing for these functionalised materials are considered. Initially, extrusion processing was investigated to glean information on the melt-flow properties of functionalised materials under heat and shear. The presentation of power required with different grades of agar (figure 4.26) showed a clear difference between technical (AGT) and biological (AGB) grade. The magnitude of this difference in flow behaviours widens as the shear applied to the material decreases, suggesting that the underlying properties of the starting agar are more apparent at low flow and low shear conditions, whereas at high flow (high speed) and high shear the molten material acts more uniformly when comparing AGB and AGT.

The most common differentiator when purchasing grades of agar relate to the gel strength, which is chiefly a factor of both the average molecular weight, but also the concentration of oxygen bridges in the 3,6-anhydro-L-galactopyranose. However, there are no universal specifications for applications of bacteriological grade, food grade, and technical grade agar, though it can be expected that there are differences in physiochemical composition and bacteriological controls.[309]

Pre-extraction alkaline hydrolysis techniques are used to bring a certain degree of uniformity to the agar by cleaving methoxy and sulfate groups from the L-galactose residue, furthermore agarose and agaropectin fractionation may be used to allow manufacturers of agar products to adjust the physico-chemical composition and technical performance of their agar product by blending different ratios of agarose and agaropectin.1,3[309, 310]

Despite the observed differences in AGT and AGB materials through when being processed through the extruder, both grades were successfully processed in the extruder, with adjustments in temperature giving a strong influence on absorbed screw power (figure 4.27). The resulting material that is collected from the extruder is a consolidated amorphous self-supporting solid, which appears would be suitable for traditional melt extrusion polymer processing, e.g. sheet/film extrusion, injection moulding, extrusion

coating etc.

Rheometry assessment shows that the molten material exhibits good flow behaviour, with both viscosity and internal shear-stress decreasing as melt temperature increases (table 4.6, figures 4.25a and 4.25b). Observations from the extruder work seemed to indicate both Newtonian and non-Newtonian flow behaviours under different conditions. The flow behaviour index (n) is typically used as a classifier of flow regime, with $n = 1$ indicating Newtonian flow, $n > 1$ indication dilatant (shear-thickening) behaviour, and $0 < n < 1$ indicating pseudoplastic (shear-thinning) behaviour. Figure 4.25b shows a clear trend of increasing n as melt-flow temperature increases, but at all times the value is below 1 indicating the molten functionalised agar exhibits non-Newtonian pseudoplasticity.

The Power-Law Fluid model allows for regions of Newtonian-like flow behaviour at low shear and high shear, characterised by a flat viscosity response at low and high shear rates (η_0 and η_∞ respectively) (figure 4.31). Thus, observations made on the data from the extruder work that the fluid was behaving both as a Newtonian and non-Newtonian fluid may be explained by the typical behaviour of a shear-thinning fluid under the Power-Law Fluid model (figure 4.31), and by the large impact temperature has on the flow behaviour index (n) (Figure 4.25b).

The hysteresis is also notable in figures 4.25a and 4.25b, with flow consistency (K) and flow behaviours (n) measured during heating, not being returned to upon cooling. This practically manifests itself as a polymer that requires a relatively high energy input (temperature and/or shear) to initiate viscous flow, however once flowing, the energy required to maintain this flow appears lower than if you were to attempt to initiate flow at that lower temperature. The clear evidence for this is that when first starting flow measurements at T = 140 °C, the instrument torque limit was met (figure A5), however once heated to T = 180 °C and cooled back to T = 140 °C the shear stress and viscosity recorded were relatively low compared to the whole experimental dataset (figure A17). It is unclear from this work whether this property is entirely temperature dependant (true pseudoplastic behaviour) or if there is a time-dependant

component to it (thixotropy). Additionally the mechanism of this flow hysteresis is not quantified in this work, however qualitatively it was observed that prolonged operation under high temperature and shear conditions would result in significant darkening of the molten fluid and a distinct sweet smell, indicating a potential pyrolytic breakdown of the polysaccharide backbone in the functionalised material.

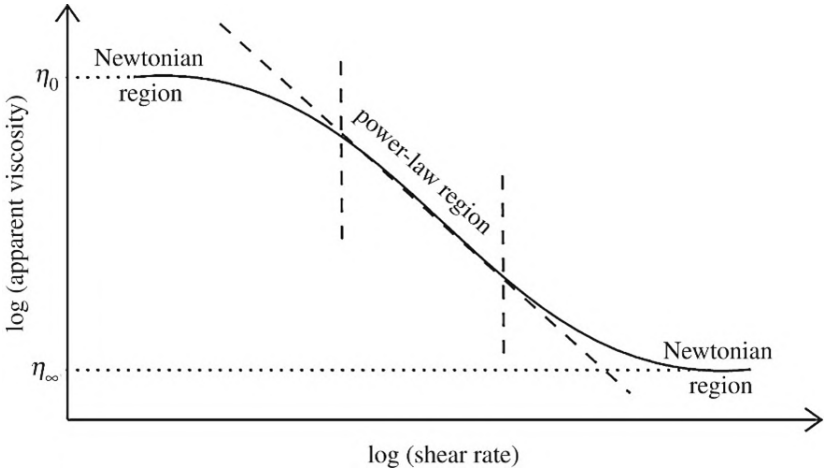

Figure 4.31: Qualitative representation of the apparent viscosity behaviour for a shear-thinning fluid, taken from Ionescue et al. (2020).[311]

K values presented in table 4.6 present the viscosity at a unit rate of shear, and thus are a useful point of comparison with traditional polymers.[312] Some typical K and n values of petro-plastic polymers and formulated products are presented in figure 4.32. In this work, the functionalised agar had a K value ranging from 4 to approximately 4,800 (table 4.6), with values below 100 at melt temperatures above 170 °C. Data from the literature reveals K values of some typical polymers and polymer formulations from 1.7 to 143, providing yet more evidence that the functionalised seaweed polysaccharide materials would be directly compatible with highly common industrial polymer processing equipment with minimal modification.

Additionally, the general trend of decreasing K and increasing n for a shear-thinning pseudoplastic molten polymer when increasing the melt temperature is upheld in all the examples of petro-polymers shown in figure 4.32. Thus, both the melt-flow viscosity behaviour and shear thinning behaviour are entirely commonplace in industrially

processed polymer resins. Additionally, it is seen that by adjusting the formulation by addition of copolymers, fillers, and plasticizers, the melt-flow behaviour of the molten resin can be manipulated. The use therefore of a functionalised polysaccharide as a direct replacement for petro-based polymer resins, or as a bio-derived and environmentally benign component in a formulated composite is a highly attractive prospect.

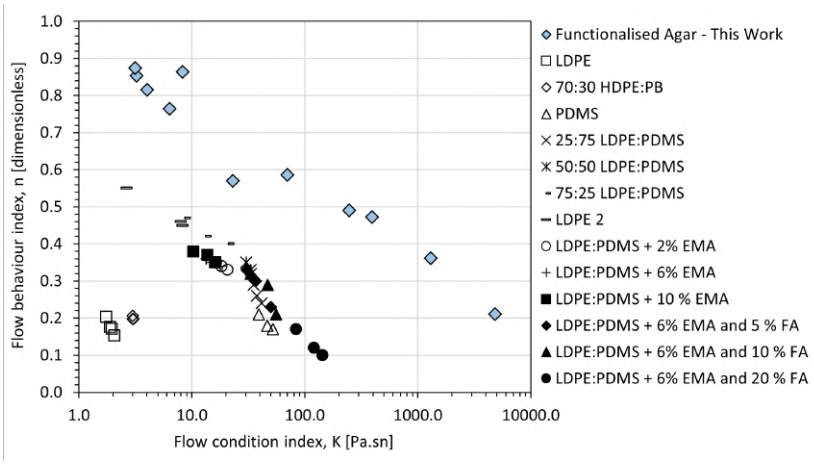

Figure 4.32: Fluid behaviour index (n) and fluid consistency index (K) for various polymers, blends of polymers, and resin formulations, tested at flow temperatures from 140 °C to 230 °C. LDPE = Low-density polyethylene, HDPE = High-density polyethylene, PB = Polybutadiene, PDMS = Polydimethylsiloxane Rubber, EMA = Ethylene methacrylate copolymer, FA = Aerosill-300 silica filler agent. Data from Jana and Nando (2005), Khalaf et al. (2014), and Saki et al. (2015).[312–314]

4.5 Conclusions

A cascading multi-fraction approach to the macroalgal biorefinery has been demonstrated as an effective way to produce distinct fractions enriched with different biomacromolecules such as proteins, alginate, and agar. Coupling a thermochemical process with a marine biorefinery is an attractive concept for processing of residual biomass into a stable char product. Slow Pyrolysis processing of macroalgal residues was demonstrated to be a preferable process for both the production of a carbon sequestration material, but also preferable when considering the potential impact of the char on the germination and early-stage growth of radish seeds.

Applications of two extracted fractions, namely alginate and agar were both demon-

strated as suitable for the production of polymeric materials. Alginate based polymeric materials were demonstrated as effective oxygen barriers, but susceptible to direct moisture contact. Despite this, alginate based coatings were demonstrated to have a net slowing down the rate of moisture loss from bagasse food trays, even when the internal coated surface is in direct contact with water, citric acid, or even a pre-prepared tomato based cooking sauce.

An attempt was made to improve the water barrier and contact properties of agar by functionalisation with fatty acid residues. Functionalised seaweed polysaccharides were produced with varying fatty-acid substitutions (C12, C16, and C18), using different polysaccharide backbones (biological grade agar, technical grade agar, and carrageenan), with different molar quantities of functionalisation (3, 4, and 5 molar equivalents).

These functionalised materials were successfully processed in a micro-compounding twin-screw extruder, and the difference in melt-flow behaviour by way of extruder torque and absorbed power was primarily attributed to different melt temperatures. Viscous flow properties of the molten materials appeared to show both Newtonian and non-Newtonian flow properties depending on the precise flow condition and extruder settings, hence the materials were further investigated with rheometry. Rheograms were produced for the C16 5eq functionalised biological grade agar, at melt temperatures 140 °C to 180 °C and shear rate 5.7 s^{-1} to 570 s^{-1}, and in doing so a power-law fluid model (Ostwald–de Waele relationship) was fit to the observations. The power-law model shows a molten pseudoplastic can display both Newtonian and non-Newtonian properties depending on shear rate, and this work additionally showed that the flow behaviour index (n) of this material tends to become less non-Newtonian as melt temperature increases.

The key melt-flow indices (K and n values) when compared to typical petro-plastics (LDPE, HDPE, PDMS, PB) at different ratios and with different copolymers and additives showed that, depending on temperature, the properties of the molten functionalised agar material fall precisely within the normal range of these extremely commonly

processed materials. The combination of successful extruder processing in addition to the insight gained by rheometry, demonstrates that these novel functionalised seaweed polysaccharides are highly applicable to current industrial processing methods, and likely would function well as a drop-in replacement for traditional petro-plastics in many applications.

Chapter 5

End-of-life Processing

5.1 Introduction

Development of novel polymers has been a goal of researchers for decades, with relatively new polymers such as PLA, PHA, and PEF becoming rapidly commercialised over the past few years. However, the rapid adoption of bio-derived polymers into the consumer packaging sector creates a new problem for waste processors. Mixed polymer waste requires sorting and separation to allow efficient recycling and reprocessing, in cases where the waste stream is particularly contaminated (e.g. with food waste) or otherwise difficult to separate, the whole waste stream is more likely to be 'recycled' in an waste-to-energy process, or worse, exported for 'recycling' in least developed and developing countries.[315]

Additionally, claims about composability or biodegradability of many polymers are often justified by an extremely limited scope of operating conditions, and in reality, most people find that supposedly compostable and biodegradable polymers (e.g. TPS, PLA, PBAT) don't appear to meaningfully degrade in typical home composting or anaerobic digestion (AD) processes.[316–318] In fact, in many case "compostable" TPS food caddy lining bags are mechanically sieved out from shredded food waste by local authority waste processing sites, and disposed as non-recyclable since they don't degrade

in any reasonable timeframe in the typical conditions of the AD plant and thus cause issues with blockages and accumulation in the solid digestate product.[319–321]

Development of yet another bio-derived polymer, whilst potentially attractive because of the source of biomass, risks simply adding another variable to the existing mixed polymer processing problem. Thus, the fate of the materials at the end of their useful life for any new polymers must be considered right at the earliest stage of their development to ensure that any newly developed materials don't cause issues downstream.

Since these materials are primarily envisaged to be used in food packaging applications, the end-of-life disposal route must be compatible with food-waste contamination. Whilst practically, any polymer product (film, coated substrate) may be washed before recycling or processing, for the sake of simplicity and in the interest in avoiding an unnecessary washing and processing step only composting and anaerobic digestion (AD) disposal is considered in this work. Both composting and AD are extremely common techniques used for the disposal of food-waste, landscaping residues, and agricultural wastes.

Composting is an aerobic biological process that relies on both thermophilic (> 45 °C) and mesophilic (< 45 °C) microbes to degrade susceptible organic matter into a stable humus-like material. It can be performed at multiple scales, from a small back-yard composting bin dealing with household waste, to large industrial windrows or air-blown static piles for the processing of large quantities of organic waste (e.g. local authority food and green-waste collections). In addition to the final compost, decomposition products of carbon dioxide and water as well as biogenic heat are produced by the compost pile as the organic material is broken down. As a process, it is used primarily to achieve one or many of the major following aims:[322]

- Decomposition of organic material for production of a soil improver.
- Disposal of an organic and putrescible waste stream to avoid more costly or impactful disposal options.
- Disinfection of pathogenically infected organic wastes into a safe, benign, and

beneficial material.

Anaerobic digestion (AD) is a process by which organic waste can be biologically transformed into another form, in the absence of oxygen. Diverse microbial populations degrade organic waste, which results in the production of biogas (predominantly CH_4, CO_2, and N_2) and other energy-rich organic compounds as end products.[323] It is considered a viable technology in the competent treatment of organic waste and the simultaneous production of a renewable energy. It is facilitated by a series of metabolic reactions such as hydrolysis, acidogenesis, acetogenesis and methanogenesis, and as a process has some advantages over aerobic processing (e.g. composting) due to a low energy requirement for operation and a low biomass production.[324]

The aim of this chapter is to experimentally assess the fate of the alginic-acid based polymers and the functionalised carbohydrates presented previously, when exposed to two common end-of-life options for traditional biodegradable materials: composting, and anaerobic digestion (AD).

5.2 Materials and Methods

5.2.1 Materials

Food grade agar (both technical and biological grade), sodium alginate, κ-carrageenan, glycerol, and soybean oil were purchase from Fisher Scientific and used as received. Unrefined sodium alginate was also extracted from *Saccharina latissima* using the previously described trisodium citrate method (section 4.2.3.2), with macroalgae supplied by Connemara Organic Seaweed Company Ltd (Co. Galway, Ireland). Pyridine was purchased from Merck, and 99.8 % ethanol purchased from VWR and both used without further purification. Palmitoyl chloride used in the functionalisation reaction was purchased from TCI.

A microbial consortia was collected directly from the GENeco anaerobic digestion facility (Bristol Sewage Treatment Works, Avonmouth), along with a sample of mixed "food waste" from their pre-processing facility.

5.2.2 Methods

5.2.2.1 Film preparation

Alginic acid films were prepared as described in the previous chapter (section 4.2.3.7). Functionalised agar (AgaF) and functionalised κ-carrageenan (CarraF) were prepared using the pyridine and acyl-chloride route described in the previous chapter (section 4.2.3.6).

AgaF and CarraF films were prepared by hot-pressing. First, the powder of functionalised material was sieved onto a silicone baking sheet to fill a circle of approximately 12 cm diameter. A second silicone baking sheet was placed over the top, and the two sheets placed between a pair of 3 mm brushed steel platen plates. The platen plates with the baking sheets and functionalised material sandwiched between were then loaded into a pre-heated sublimation press (Free-Sub ST-4050A Heat Press), at 150 °C, and pressed at maximum force (7.8 kN) for 2 minutes. After the press time elapsed the platens were removed, top platen lifted away, and the baking sheets/functionalised-material sandwich left to cool to ambient temperature. Once cool, the silicone baking sheets were peeled apart, and a transparent film of functionalised polysaccharide was peeled from the bottom sheet.

5.2.2.2 Compostability

Compostability of the biopolymer and functionalises materials is assessed in an established aerobic green-waste compost pile. Test articles are prepared by cutting films into approximate 7.5 cm x 7.5 cm squares, weighed, thickness measured with a digital micrometre, and then placed into a 15 cm x 15 cm envelope fabricated from 13 mm mesh galvanised steel wire netting (see figure 5.1). The mesh netting was used to ensure that physical breakage of the films when burying/uncovering the test articles did not occur, whilst allowing sufficient open space that the soil biota could access the test articles unimpeded.

The University of Bath landscaping and estates department composting facilities were

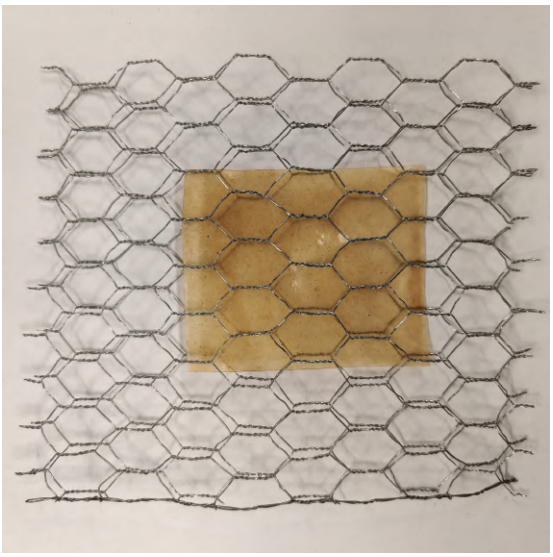

Figure 5.1: Arrangement of test-film enclosed in 13 mm mesh envelope for mechanical support during compostability testing.

utilised, where a mature (18-month) pile of mixed leaf-mould and grass clippings was selected as a test site (location 51°22'29.4"N 2°19'05.3"W). The pile was approximately a triangular prism, 3 m tall and 5 m wide front to back at the base. Before starting the composting test, a testbed was prepared on the top of the pile by scraping back the top 15-20 cm of compost and incorporating 30 L of fresh mixed kitchen waste (fruit cores/peels, coffee waste, veg peelings etc.) into the 20 cm of compost below the removed capping material. Thereafter, the test articles were placed flat in the testbed such that they made maximal contact with the compost through the 13 mm openings in the mesh (see figure 5.2a). A digital temperature data logger (RS PRO PRO-USB-1, -35 to +80 °C) was also placed into the centre of the test bed and configured to log the temperature of the composting pile at 30-minute intervals for the duration of the degradation test. Ambient temperature and meteorological conditions data were collected by a local weather station (location: 51°23'12.0"N, 2°22'59.0"W, approximately 4.70 km from the compost site), using a Davis Vantage Pro2 weather station, and data accessed through a freely accessible on-line web portal.[325] The test articles were then covered in a single layer of freshly cut stinging nettles (*Urtica dioica*), and the initial 15-20 cm of capping compost was replaced to ensure retention of heat. The location

of the testbed was demarked by use of fence stakes at the corners of the test-area (see figures 5.2a to 5.2c).

This was left to compost over a period of 8 weeks to decompose, with regular inspections made to assess the level of degradation. For both sets of films tested (Alginic acid and AgaF), 5 sets of identical samples were prepared and loaded to the compost pile at the same time. After an initial period of 4 weeks, a new pair of samples (one each of AgaF and Alginic acid) were uncovered and inspected in the lab for degradation, such that the total test time ran for 8 weeks. Degradation was observed visually, by change in mass, change in thickness, and by FT-IR of the film surface where appropriate.

(a) **(b)** **(c)**

Figure 5.2: Pictures of the final composting set up, showing **(a)** the arrangement of test articles placed into the testbed prior to capping over with fresh nettles and part-finished compost, **(b)** wide-view of the testbed on the top of the pile, and **(c)** closer view of the capped over testbed marked with four corner posts.

5.2.2.3 AD substrate characterisation

Substrates that are subject to AD are characterised for total solids (TS%, dry matter), fixed solids (FS%, ashes), and volatile solids (VS%). Substrates are first dried overnight at 105 °C in a tared crucible to determine TS%, weighed, and then reduced to ashes at 550 °C to determine FS% and VS% (see equations 5.1 to 5.3).

$$\mathrm{TS\%} = \frac{W_{550^{\circ}C} - W_{tare}}{W_{sample} - W_{tare}} \times 100\% \tag{5.1}$$

$$\mathrm{FS\%} = \frac{W_{550^{\circ}C} - W_{tare}}{W_{105^{\circ}C} - W_{tare}} \times 100\% \tag{5.2}$$

$$\text{VS\%} = \frac{W_{105^{\circ}C} - W_{550^{\circ}C}}{W_{105^{\circ}C} - W_{tare}} \times 100\% \tag{5.3}$$

Where W refers to a mass measurement, and subscripts 550 °C, 105 °C, *tare*, and *sample* refer to the total mass of sample and crucible after drying at 550 °C, total mass of sample and crucible after drying at 105 °C, the tare weight of the empty crucible, and the total initial mass of sample and crucible before any drying respectively.

5.2.2.4 Anaerobic digestion

Anaerobic Digestion (AD) is used to assess the degradation and biomethane potential (BMP) of a variety of test films. A microbial consortium inoculum was collected as sludge from the anaerobic digesters of a local authority food-waste processor (GENeco, Bristol Bioresources and Renewable Energy Park, Kings Weston Lane, Avonmouth, Bristol BS11 0YS), and stored in a laboratory bottle with the lid partially unscrewed at 4 °C before use. The protocols of Angelidaki et al., Holliger et al., and Shrestha et al., are followed in preparing and managing the AD assay.[326–328] Briefly, substrate (test polymer material or control material) is assessed for volatile solids content (VS%). 1 litre bottles are used as reactor vessels and filled to maximum of 400 mL where a ratio of $>$ 4:1 in terms of VS in the inoculum and substrate is respected to avoid problems of media acidification from the decomposition of organic matter. Comparison across different substrates is made by respecting the same total initial VS% in each vessel, which is determined to be between 20 – 60 $g_{VS\%}$ $L_{mixture}^{-1}$.

The required volume of microbial consortia is revitalised overnight in an agitated water bath set to 35 °C. Reactor vessels are primed with the required quantity of consortia, positive control, or test material as required, and then air is purged with flowing nitrogen to ensure anaerobic conditions. AD reactor vessels are incubated in an oscillating water bath at 70 rpm and 35 °C, and off gas from each reactor is collected in an up-turned volumetric cylinder filled with water. Gas volumes are recorded periodically.

5.3 Results

5.3.1 Compostability

Temperature logs from the centre of the compost pile (for day 7 onwards), as well as ambient air temperature collected by a local weather station are displayed in figure 5.3.

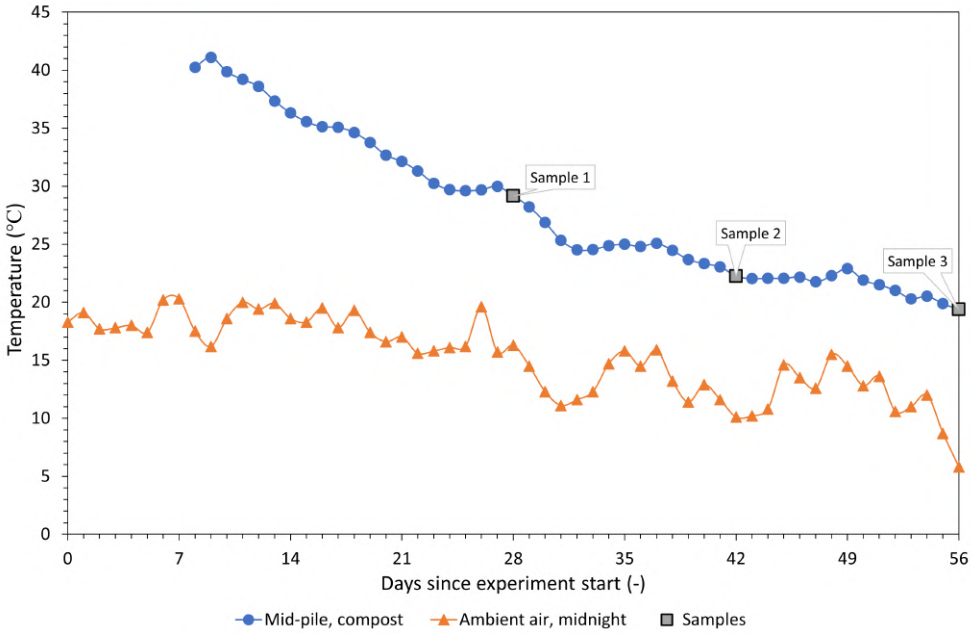

Figure 5.3: Temperature trend log from the centre of the compost testbed, as well as the ambient air temperature recorded at midnight (00:00) by a local weather station.

The centre pile temperature clearly shows that the testbed was in the mesophilic phase ($<$ 45 °C) for the duration of the logging period (day 7 to day 56), with the pile temperature ranging from 19.4 °C to 41.1 °C and an average of 27.9 °C. A typical temperature trend for the centre of a freshly assembled pile would see a brief (few days) initial mesophilic phase after initial assembly of the pile, then a thermophilic phase (sustained temperatures $>$ 45 °C) for 1 to 2 weeks, before a temperature drop indicating the commencement of the second mesophilic phase, and finally a cooling/maturation phase as the pile equilibrates with ambient temperature.[329] For the duration of the test, the centre of the compost pile was significantly above the ambient air temperature, ranging from 6.8 °C to 24.9 °C above ambient with an average of 13.2 °C above ambient

air temperature.

After an initial 4-week period, the first alginic acid and AgaF films were uncovered and inspected, and assessed for change in mass and thickness. Thereafter, a new set of samples was uncovered every two weeks. Summary visual assessment, change in mass, and change in thickness of the film samples at each sampling frequency are listed in table 5.1.

Table 5.1: Visual observations and change in mass and thickness during composting trials. ΔM (%) and ΔT (%) refer to the change in mass of each test article, relative to the starting mass at day = 0.

Sampling Week	Alginic Acid			Functionalised Agar		
	ΔM (%)	ΔT (%)	Observations	ΔM (%)	ΔT (%)	Observations
4	-97.0	N/A	Advanced degradation.	-0.87	+2.89	Cloudy appearance, some stiffness.
6	-97.8	N/A	Totally degraded.	-0.89	+3.44	Advanced clouded appearance. Free white solid at surface.
8	-99.6	N/A	Totally degraded.	-2.24	+2.86	Clouded appearance, darkened substrate. Free white solid at surface, and persistent hexagonal markings.

Upon uncovering and inspection of the first set of samples (week 4), the alginic acid film was found to have almost completely degraded (figures 5.4a and 5.4b). The first observation of the AgaF film shows a significant clouding compared to the initial visual appearance of the film, with some apparent local swelling and rippling compared to the original smooth and flat aspect (figure 5.4c).

The second set of samples uncovered (week 6, figures 5.5) reveals a complete degradation of the alginic-acid films (figures 5.5a and 5.5b), and more advanced clouding appearing on the film surface. The cloudiness is caused by an off-white waxy-solid accumulating at the surface of the AgaF, which can be rubbed and scraped off the surface of the film or washed off by common laboratory solvent such as acetone or dichloromethane.

Samples removed at week 8 (figure 5.6) are visually similar to those recovered at week

6, however the alginic acid film is now completely degraded with the only scraps of recognisable material being recovered from the inner folds of the galvanised steel wire mesh 'envelope' film holder. Additionally, a persistent hexagonal pattern remains on the week 8 film (figure 5.6b) that aligns exactly with the galvanised metal 'envelope' that was used to hold the material. This hexagonal pattern does not rub off like the general cloudiness, suggesting a different mechanism might be causing it.

The recovered alginic acid (AA) film samples were separated from the bulk compost and leaf-litter by suspension of the total sample in DI water and decanting of buoyant and soluble components of compost. Acid film fragments sank and were picked out from the bulk compost fragments with tweezers, rinsed in clean DI water, and dried overnight in a lab oven. Total recovered mass of the fragments of identifiable alginic acid film shows almost total degradation after as little as 4 weeks, with -97.0 %, -97.8 %, and -99.6 % loss of starting mass for the week 4, week 6, and week 8 samples respectively. Since the degradation of AA films was so advanced, it was not possible to assess any change in thickness of the film relative to the starting film, nor to assess any changes to the chemistry of the film by FT-IR.

Functionalised agar (AgaF) films recovered from the compost heap were significantly less degraded when compared to the AA films. AgaF film recovered at week 4 showed a very small change in mass compared to the starting mass (-0.87 %), with a similar loss in mass for the week 6 sample (-0.89 %), however a step-change at week 8 with a loss of -2.24 %. Film thickness however was seen to increase over the observed period, with film thickness increasing by +2.89 %, +3.44 %, and +2.86 % for week 4, week 6, and week 8 samples respectively. The swelling of the film samples was associated with a noticeable wave/ripple forming in the film, presumably as the film swelled unevenly and uneven tension through the film surface caused bending and buckling.

FT-IR transmission spectra of the films recovered at 4 weeks, 6 weeks, and 8 weeks are displayed in figure 5.7. Figure 5.7a shows the whole transmission spectra over the wavelength range 4500 cm^{-1} to 600 cm^{-1}. Overall, the bulk of the spectra remains identical between the day-0 control sample and the films collected and 4, 6, and 8 weeks

from the compost pile. There is however a distinct new peak in the week 4 and week 6 spectra at around 1700 cm^{-1}. There is an additional unique new peak in the week 0 8 spectra at 1538 cm^{-1} which has not been previously observed. Figure 5.7b shows an enlarged view of the same spectra over the wavelength range 2000 cm^{-1} to 1500 cm^{-1}. At this scale, the new doublet of peaks at 1698 cm^{-1} and 1705 cm^{-1} is apparent for both spectra of films collected at week 4 and week 6, as well as a slight shoulder in the week 8 spectra in this region.

5.3.2 Anaerobic digestion

Results of the characterisation of total solids (TS%), fixed solids (FS%), and volatile solids (VS%) for a variety of substrates is listed in table 5.2. TS% for the AD Sludge and Food Waste is very low indicating a high quantity of moisture in these materials. Of the test polymers, the majority have a very high TS% which indicates a low moisture, the outlies are the non-functionalised films that utilise alginate (either as calcium alginate or alginic acid). These alginate films are significantly more humid at ambient conditions, confirming the nature of the native seaweed alginate as a hygroscopic material, an observation that is paralleled in films that utilise glycerol as a plasticiser.

FS% indicates the quantity of residual mass after calcination, high FS% would suggest high ash levels or inclusion of heteroatoms that cause polymerisation when the material is heated. FS% levels are typically very low, with outliers in the control group, CarraF, the calcium alginate films, and finally the thermoplastic starch material. The AD Sludge and food-waste are expected to have high ash levels, as the material streams themselves contain notable levels of inorganic/mineral materials (e.g. grit, egg-shells, etc.). The high FS% in the calcium films will be residual calcium salts remaining both from the salt inversion process, and the resulting calcium salts material following the pyrolytic breakdown of the alginate structure at high temperature. CarraF material likely results in a small quantity of sulfureous ash/salt from the destruction of sulfate groups on the carrageenan backbone. The precise composition of the TPS test material used in this study is not known , however it is conceivable that a co-polymer could contain a stable salt forming moiety (e.g. metallocenes), or that residual catalyst from

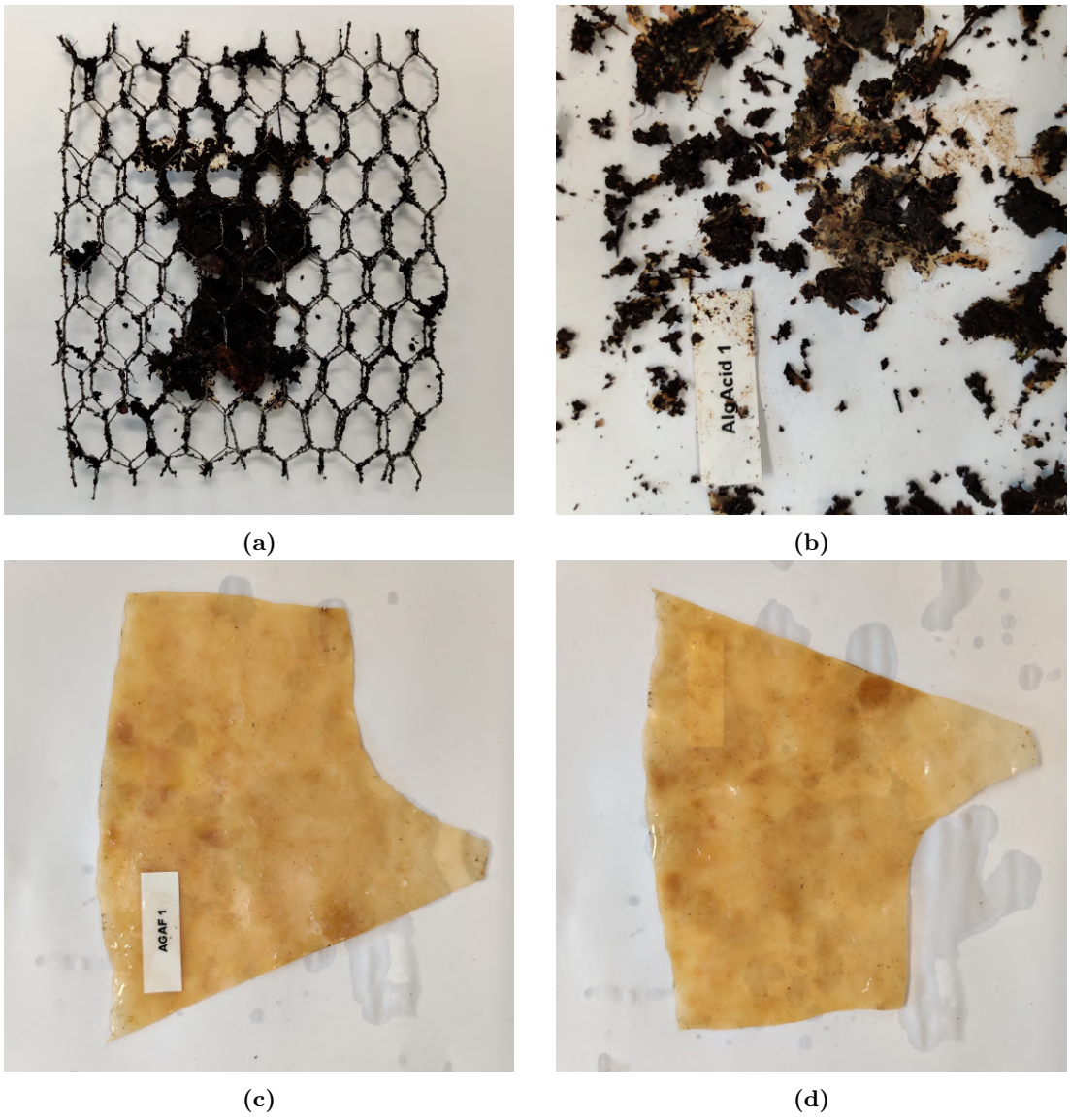

(a) **(b)**

(c) **(d)**

Figure 5.4: State of Alginic Acid and Functionalised Agar films uncovered after 4 weeks of composting. **a)** shows Alginic Acid as recovered in the support frame, **b)** a focused view on the remaining film residues, **c)** shows the front-side of functionalised agar after washing off dirt and compost, and **d)** shows the back-side of the same functionalised agar film.

the TPS production process also forms ashes/salts at high temperature.

Figure 5.8 shows the normalised excess gas volumes produced by AD of each test substrate as a function of total digestion time in anaerobic conditions. Assessment of substrate performance as a food source and susceptibility to degradation under AD conditions is made by comparison to the negative and positive controls. A trend that

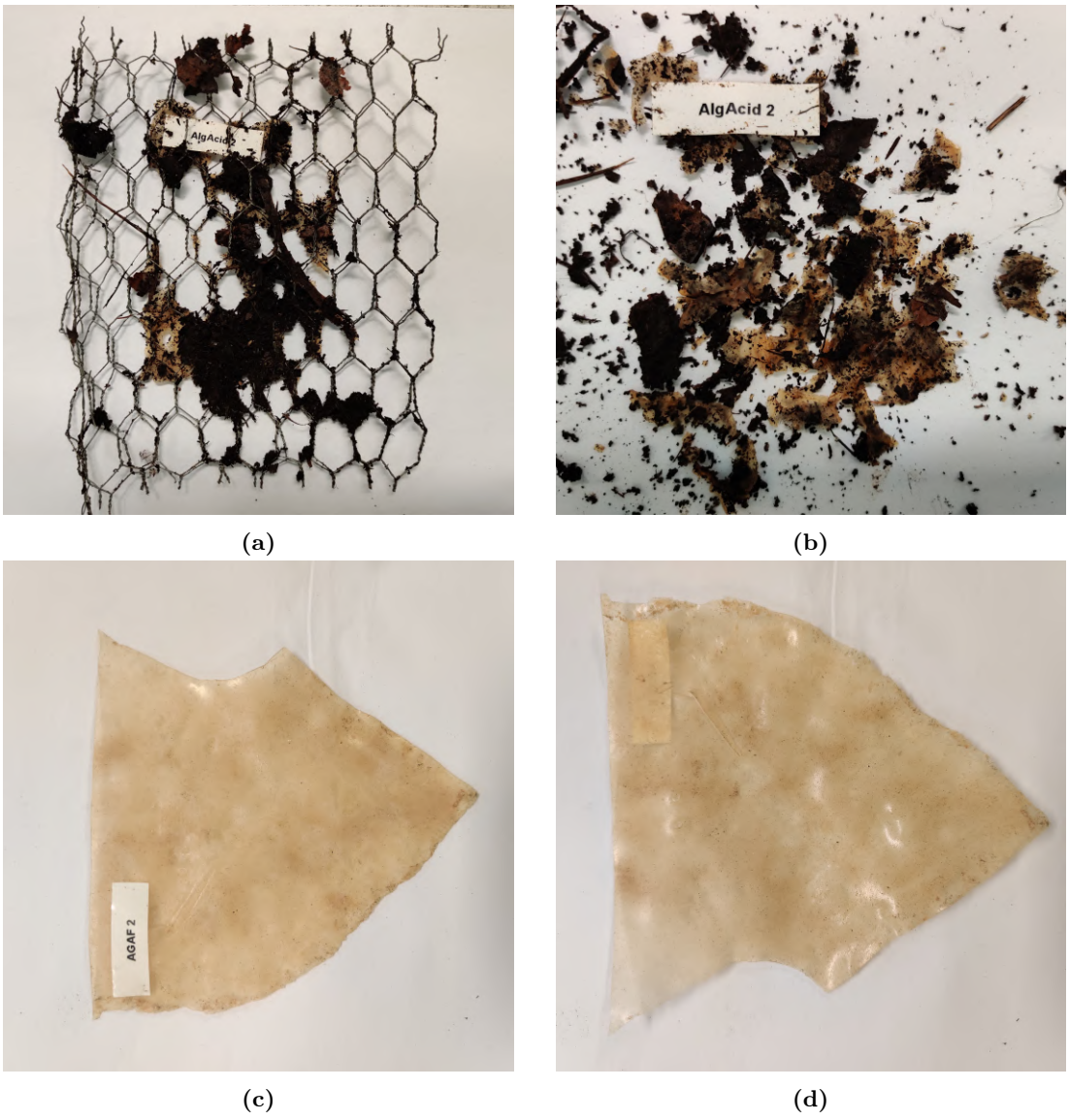

(a) **(b)**

(c) **(d)**

Figure 5.5: State of Alginic Acid and Functionalised Agar films uncovered after 6 weeks of composting. **a)** shows Alginic Acid as recovered in the support frame, **b)** a focused view on the remaining film residues, **c)** shows the front-side of functionalised agar after washing off dirt and compost, and **d)** shows the back-side of the same functionalised agar film.

goes above the positive control would indicate that at that time into the degradation process the test substrate is more susceptible to biodegradation under AD conditions compared to the food waste that the consortia is normally adjusted to. A trend that goes below the negative control would indicate the very presence of the substrate is having an inhibitory effect on the AD consortia such that the gas generation is now worse than

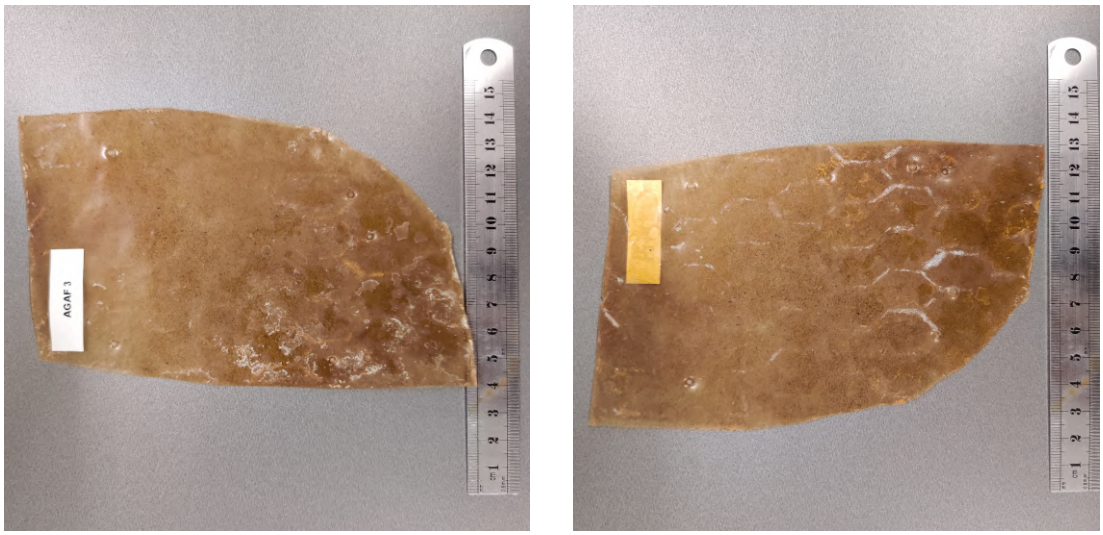

(a) **(b)**

Figure 5.6: State of Functionalised Agar film uncovered after 8 weeks of composting. **a)** shows the front-side of functionalised agar after washing off dirt and compost, and **b)** and shows the back-side of the same functionalised agar film.

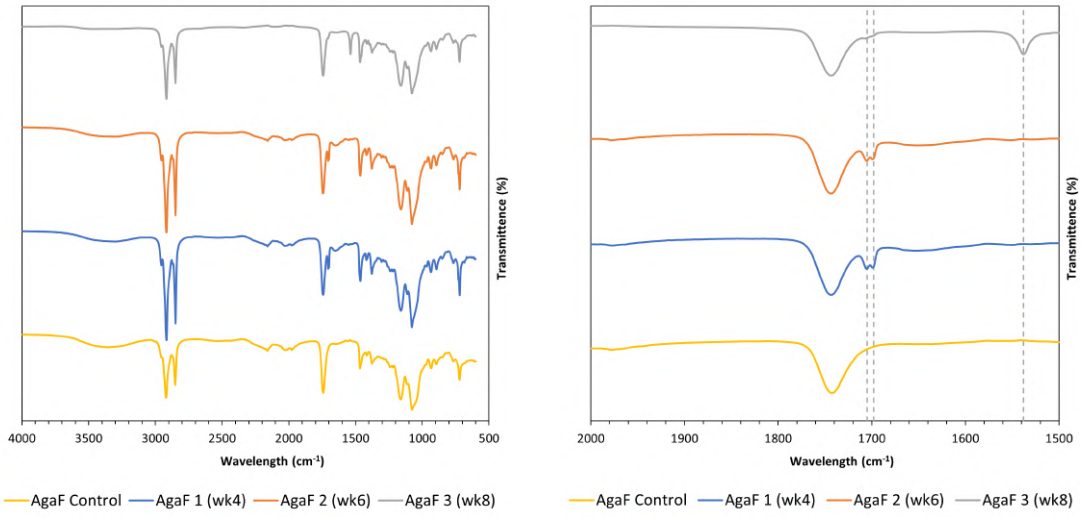

(a) **(b)**

Figure 5.7: FT-IR spectra of functionalised agar (AgaF) films recovered from the compost pile at day 0 (control), day 28 (week 4), day 42 (week 6), and day 56 (wk8). **a)** shows the full transmission spectra from wavelength 4500 cm^{-1} to 600 cm^{-1}, and **b)** shows the just the transmission spectra at wavelength 2000 cm^{-1} to 1500 cm^{-1}.

if the test material was never in the AD reactor to start with. Trends that fall between positive and negative controls are indicative of a material that is breaking down under

Table 5.2: Result of initial substrate characterisation for anaerobic digestion (AD) assay.

Material	Type	Total solids, TS%	Fixed solids, FS%	Volatile solids, VS%
AD Sludge	Control	3.5	27.6	72.4
Food Waste		8.4	8.0	92.0
AgaF	Functionalised seaweed carbs	99.7	0.1	99.9
AgaF + SO20		98.2	0.1	99.9
CarraF		97.2	7.2	92.8
$AlgCa_{Ext}$ + Gly	Non-functionalised seaweed carbs	74.1	28.7	71.3
$AlgCa_{SL}$ + Gly		73.1	33.0	67.0
Alginic Acid		85.2	0.8	99.2
Alginic Acid + Gly		79.1	0.7	99.3
TPS	"Compostable" polymers	99.6	20.8	79.3
PLA		99.9	0.2	99.8
PE	Traditional polymers	99.8	0.1	99.9
PVC		98.7	0.3	99.7

AD conditions, however at a slower rate than the food-waste positive control.

All films that incorporate glycerol as a plasticiser (AlgCa + Glycerol, and Alginic Acid + Glycerol) show a rapid gas production rate from day 1, far exceeding the early production from the positive control. This is likely due to the ease in which glycerol leaches out from the films, after which it is rapidly consumed by the AD consortia. By day 10 however, gas production in all glycerol containing films is essentially finished, with total gas production trend mostly flat for the remaining assessment period. By approximately day 15 the food-waste control reactor has caught and passed the total gas production from the glycerol containing films, thus eliminating the early advantage that the glycerol films had in the first week or so of degradation.

For the functionalised materials (square markers - AgaF, AgaF+SO20, and CarraF), the general trend appears to be flat and not particularly distinguishable from the negative control baseline, until approximately day 38. After day 38, all reactors containing functionalised carbohydrate films begin to move together in increasing gas production, indicating a definite shift away from the negative control baseline. This indicates that

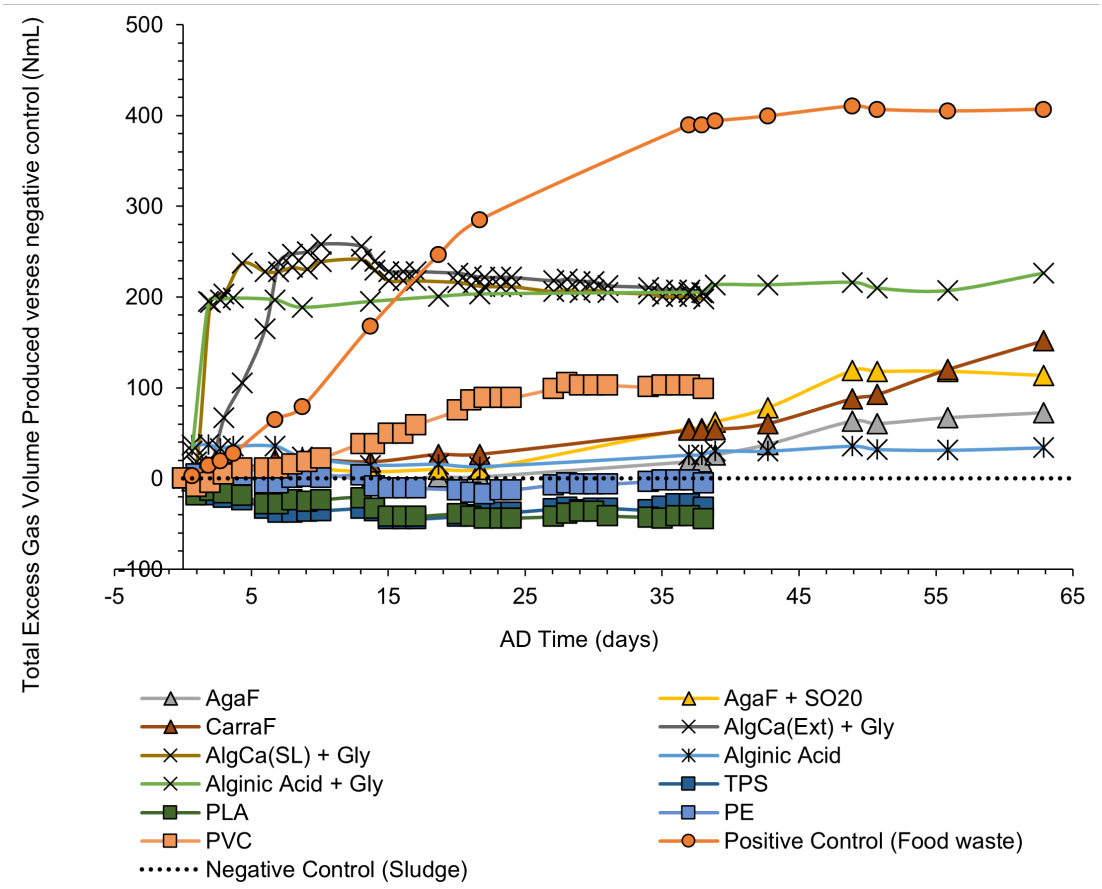

Figure 5.8: Excess biogas normal volume produced in each bioreactor in comparison to the negative control (AD sludge only). Total production is limited by ensuring that the starting VS% is the same for all reactor runs. Triangular markers indicate functionalised carbohydrate-based materials; cross markers indicate native seaweed carbohydrates in their acid or calcium salt forms; square markers indicate commercially available 'compostable' and 'traditional' polymers. The positive control (circle markers) is provided by addition of the appropriate quantity for food-waste sludge, and the negative control is the gas produced as a result incubating the AD sludge.

the functionalised material is susceptible to degradation under AD conditions. However, the fact that the excess gas production is only noticeable from day 40 onwards indicates that the functionalised materials are either more difficult to degrade, less preferable than the carbon source already in the AD sludge inoculum, and/or requiring a shift in the distribution of microbes in the consortia to boost the population of microbes capable of producing enzymes that can cleave the fatty-acid/carbohydrate ester bond.

Of the traditional and commercially available polymer samples (square markers), only

the PVC showed any excess degradation when compared to the negative control baseline. PVC showed a slow by steady accumulation of additional gas from approximately day 7 to day 28, with a flat curve from day 30 onwards. PE showed no difference compared to the negative control, suggesting that it is completely inert in these AD conditions over this time period. Curiously, both 'compostable' polymers (TPS and PLA) show worse performance compared to the negative control, with noticeable drops in gas production around days 3 to 6, and again during days 13 to 15.

5.4 Discussion

Susceptibility of the films (AA and AgaF) to biodegrade under aerobic conditions was assessed in a large and active compost heap. Compost temperature was maintained within the mesophilic phase for the duration of the logged period, indicating significant biogenic heat was being generated by active microbial activity within the composting testbed. The peak logged temperature was 41.1 °C, which is below the threshold typically applied for differentiating mesophilic and thermophilic composting phases. The lack of apparent thermophilic phase as is typical can be explained by one, or a combination of factors. Firstly, having set up the testbed in an already mature pile, the majority of thermal mass of decomposing material has already gone through a thermophilic phase and thus there isn't enough fresh material to sustain a second thermophilic phase. Secondly, since the temperature logging was only started on day 7, it is entirely that a brief thermophilic phase was achieved during the un-logged period as the freshly added material (food waste, nettles) degraded.

The lack of observed thermophilic phase is not necessarily a reason for concern, since the excess heat is a result of the rapid consumption of labile compounds (sugars, proteins) by heat-tolerant microbes. The more recalcitrant biomacromolecules (e.g. cellulose, starches) typically do not get meaningfully degraded until the slower second mesophilic phase, and the most stable compounds (lignin-humus complexes) are not formed until the final maturation/cooling phase when the proportion of fungi increases and bacterial numbers decline.[329] Therefore, biodegradation of the functionalised

fatty-acid/carbohydrate material would likely proceed in later phases of composting, as more complex materials are degraded at a slower rate.

Degradation of the films was observed visually, by change in mass, by change in thickness, and in the case of AgaF by FT-IR spectroscopy also. Visually observation revealed quickly that the alginic acid films are *highly* susceptible to biodegradation under aerobic conditions, with over 95 % of the mass degrading to unrecognisable fragments in 4 weeks (figure 5.4b). As such thickness measurements were not completed, as there was nothing left to measure.

The observation that alginic acid film is highly susceptible to biodegradation is entirely expected, since the native alginate molecule is found readily in nature and is biodegraded worldwide anywhere that seaweed rots. In fact, seaweed is often intentionally collected an added to compost heaps to boost the fertility of the resulting compost, and composting of just seaweed biomass has been suggested as a strategy for managing seaweed blooms when they wash up onto recreational beaches.[330]

Biodegradation of the AgaF material was observed to proceed significantly more slowly than the AA films. Overall visual appearance of the AgaF material showed a clear trend of decreasing clarity (increasing cloudiness) over time, however the films were not observed to have degraded to the point of mechanical weakness or disintegration as was observed in the AA films. Mass measurements showed a very slight loss in mass of each of the films over time, however the bulk of the film sample remained intact at the time of sampling.

Thickness measurements of the AgaF films revealed a slight swelling over time. This is counter-intuitive given the slight loss in mass observed over time, suggesting that whatever mechanism is causing the loss of mass and/or clouding of the surface is also resulting in an overall reduction of material density. Alternatively, if the accumulation of the white waxy substance on the film surface is a result of material degradation and exudation, the overall thickness dimension would understandably have increased as material builds up on the outside of the film.

FT-IR spectroscopy was used to investigate the change of surface chemistry at the film surface over time (figure 5.7). The general observation was that the chemical fingerprint was broadly unchanged, apart from new peaks or transmission observed at around 1700 cm^{-1}. The generation of new peaks at 1698 cm^{-1} and 1705 cm^{-1} likely represents the reverse of the original functionalisation reaction that was observed in figure 4.24 in the previous chapter. Therefore, the waxy white substance accumulating on the surface of the film is highly likely to be a crystalised free fatty acid, resulting from the degradation of the original ester linkage in the functionalised agar (-COO-), being hydrolysed to a carboxylic acid (-COOH).

The new and unique peak at 1538 cm^{-1} that was observed in the week-8 spectra (figure 5.7) has previously been attributed to carbonate and formate moieties.[331] This peak was observed uniquely on the week-8 material, and whilst sampling a section of film that had a strong white marking from the hexagonal patterning observed (figure 5.6b). It is possible that there may be an interaction between the galvanised steel wire mesh and the film in this location, or simply corrosion of the wire mesh leaving metallic salts embedded in the film surface.

Cleavage of the ester linkage results in a highly hydrophobic fatty acid accumulating atop an underlying agar, however both fatty acids and agar would be expected to fully degrade in in aerobic composting. Free fatty acids have been observed to relatively rapidly degrade in the natural soil environment (4 weeks), whereas degradation of pure agar would be expected to follow a similar velocity to that of the native alginic acid film, since agar is a natural and native polysaccharide found in whole seaweed.[332]

Susceptibility to biodegradation under anaerobic digestion conditions was assessed for a larger range of films also (figure 5.8). In most cases, the degradation under AD proceeded as would be expected. Food waste, and unmodified algal polysaccharide films rapidly degraded, producing significant gas volumes within 2 weeks (14 days). Additionally, and film that used glycerol as a plasticizer in the formulation showed *rapid* as evolution within 5 days, as the microbial consortia consumed the glycerol.

Functionalised polysaccharides (AgaF and CarraF) were initially slow to degrade but showed a significant acceleration in their breakdown around week 5-6 (day 40). This is likely a result of the lag-time as individual microbial populations express the proteins and enzymes required to properly adapt to using the functionalised materials as a substrate.

Comparisons were also made with traditional petro-polymers and commercially available compostable biopolymers. PE was essentially inert in the bioreactor, whilst PVC showed a progressive degradation between day 10 and day 18, thereafter reaching a plateau.

Neither of the commercially available compostable biopolymers was observed to degrade in the AD reactor. It might have been expected that the PLA polymer does not degrade under AD, since the AD conditions used in this study (anaerobic, 35 °C) are significantly different to the industrial hot composting conditions normally required to degrade PLA (aerobic, 50-60 °C). However, it is surprising that it appears to actively hinder the AD process when compared to the negative control. Even more surprising is the negative impact observed when including the TPS polymer, since this polymer product was bought in the form of a degradable and compostable food-waste kitchen caddy liner, sold specifically for the collection and disposal of food waste into municipal food waste treatment systems such as the GENeco AD site where the active sludge was originally collected. This active hindering of performance may perhaps be a result of residual polymerisation catalyst leaching out from the polymer films and inhibiting one or multiple species of the consortia.

5.5 Conclusions

In this final package of work, macroalgal polysaccharide film materials were studied whilst exposed to two commonly used end-of-life processing options (aerobic composting and anaerobic digestion). These waste processing options are commonly employed for processing of organic materials (e.g. municipal green waste, agricultural residues), food-waste, and similar putrescible materials.

Anaerobic digestion (AD) was performed on test-articles of films using an active microbial consortia collected from a local food-waste processing site. All bioreactors charged with macroalgal films (alginate, functionalised carrageenan, and functionalised agar) showed excess gas production over and above the negative control, suggesting that macroalgal polysaccharide-based biopolymer films are highly susceptible to biodegradation under AD conditions. This results is a marked improvement over the common biodegradable polymers tested in this work (TPS and PLA) which showed a slight negative impact on the total gas volume produced.

Aerobic composting was assessed with functionalised agar (AgaF) and alginic acid (AA) films, in a mature compost pile of mixed landscaping wastes. Alginic acid films completely degraded within 4 weeks, leaving unrecognisable residues indistinguishable from the bulk compost material. AgaF films were slower to degrade, however by week 4 the films were demonstrated to be undergoing hydrolysis and resulting in a waxy fatty-acid accumulation on the surface of the initial test films. Despite the apparently slower onset of degradation of the AgaF films compared to the AA, the accumulation of fatty-acid on the surface of the AgaF film is highly promising evidence of the early stages of biodegradation.

In both AD and the composting processes, the AA material was far more susceptible to quick biodegradation compared to the functionalised material (AgaF). This could be a result of the relative unfamiliarity of the precise fatty-acid/carbohydrate ester bond formed in the functionalisation reactions presented in this work, hence the cleavage of this ester bond would likely be the rate limiting step when considering the overall rate of biodegradation, given that both fatty acids and algal polysaccharides are rapidly biodegraded in nature.

The broad conclusions from this work however are that macroalgal polysaccharides appear to be highly susceptible to biodegradation when observed under two relatively simple assessment methods. Other end-of life processing options (e.g. recycling) have not been considered in this work. Additionally, the compostability assessment method employed in this work does not comply with various ASTM/BSI/TUV methods that

exist to standardise the reporting of compostability of polymers. However, given the relatively poor degradation performance of existing biodegradable polymers presented in this work, there can be a reasonable level of confidence that when exposed to the more rigorous compostability testing methodologies, the algal biopolymers presented in this work would biodegrade similarly quickly as was indicated in this chapter.

Chapter 6

Conclusions and Further Work

6.1 Conclusions

The overarching aim of this thesis was to investigate valorisation strategies for the use and application of macroalgal biomass in the context of the marine biorefinery.

An initial review of the existing marine biorefinery feedstocks, cultivation methods, processing methods, primary and secondary products, and downstream processing revealed the extent of the current state of development of the macroalgal biorefinery. Established industry exist already for processing single species of cash-crop macroalgae into single products (e.g. alginates, agar, carrageenan), and there are reports of secondary conversion of macroalgae crops via thermochemical and biological processes into higher value products. However, there are no examples at industrial scale of fully integrating established primary extraction techniques with secondary conversion techniques and further downstream processing for the production of multiple valuable product streams. Furthermore, the state of reported process models of different technology biorefineries was established, and a research gap identified focusing on the development of a process model for a simple macroalgal hydrothermal liquefaction (HTL) process.

A short initial experimental HTL study was undertaken to guide and inform the development of a generalised HTL reaction model, to product distribution yields from

simple characterisation of the biomass by CHNS analysis. Additionally, boil-up behaviour and bulk properties of the experimental product biocrude was investigated. At its inception, only relatively small-scale experimental studies into macroalgae HTL and the properties of the resulting biocrude had been reported on, this therefore provided an opportunity to explore the macroalgal-HTL process from an economic standpoint and to consider the effect of plant-scale in the nascent industry of thermochemical conversion of macroalgae into a bulk biocrude product for direct replacement of fossil-crude in existing petrochemical refineries.

Fundamentally, the main barrier to commercialising a macroalgal-HTL process for the production of a bulk bio-crude product is feedstock price sensitivity. At reasonable biomass prices and with legislative assistance and valorisation of the secondary products, the macroalgal-HTL process has extremely long pay-back periods, even when assuming that a considerable price-premium is achieved for the bio-BBL product over and above existing crude-oil prices. Additionally, Dept. of Energy researchers working with microalgae feedstocks which are fundamentally better suited to HTL conversion to bio-crude (simpler pre-processing, higher bio-crude yields) are encountering significant engineering challenges with manufacturing and operating medium-to-large scale pilot HTL plants.

Thus, it is apparent that pursuing the algal-HTL process primarily for the production of a bio-crude product is disadvantageous, especially so when considering locating the process in Europe where access to low-cost and high-lipid feedstocks (e.g. large-scale aquacultured microalgae) is not feasible. Therefore a more advantageous route is the elimination of the HTL process from the conceptual macroalgal biorefinery and shifting focus to the isolation of higher value bio-macromolecules (e.g. alginate, agar, or carrageenan) that are naturally found in seaweeds. This can then be coupled with an appropriate thermal or hydrothermal process for the conversion of non-valuable biomass residues into secondary value streams.

The technoeconomic feasibility of a coupled fractionation and thermal-conversion process for the production of a composite biopolymer film as a primary product, and

carbon-rich biochar as a secondary value stream was therefore studied using combined process and economic models. Shifting focus from producing a bulk low-value bio-crude product to an intermediate value biopolymer product reveals that a macroalgal film product would be produced at a minimum biopolymer selling price (MBSP) on the order of 5 to 10 k$ tonne^{-1}, which is comparable to existing commercially available biopolymers. Additionally, coupling of an appropriate thermal conversion process allows the potential to enhance both the economic viability of the process by producing a secondary value stream, but also to reduce the carbon-footprint by producing a stable carbon-rich product that would be suitable for carbon sequestration.

At this stage the conceptual macroalgae-to-biopolymer biorefinery appears an attractive prospect from a purely economical basis, however the real-world performance of both the theorised biorefinery process and the technical performance of the biorefinery products was yet to be adequately demonstrated. Lab-scale fractionation was performed on a broad selection of macroalgae species in both a targeted single-fraction approach and a cascading multi-fractionation approach. Choosing to pursue a multi-fractionation process allows a degree of feedstock agnosticism, where the biorefinery process is adapted to accept multiple mixed macroalgae streams and effectively separate a variable quality feedstock into crude fractions that are rich in different bio-macromolecules (e.g. protein, alginate, agar/carrageenan, pectin/ulvans, and mixed fatty-acids and lipids). This is an important development for the macroalgae biorefinery, since year-round supply of a single species or even a consistent quality of feedstock is unlikely and being able to pivot the main production of the biorefinery to a more suitable product fraction allows year-round operation of the process as different feedstock species and sources are cropped through the year.

Multi-fractionation does come at a price however, with lower fractional mass yields compared to a more targeted single-step fraction approach. It may therefore be more advantageous to design the mixed species macroalgal biorefinery to be agile and operate in a semi-continuous fashion, with certain fractionation steps being prioritised, de-prioritised, or eliminated entirely based on the prevailing market conditions and/or the

quality and quantity of available feedstock.

To demonstrate the suitability of this biopolymer approach, barrier performance and water-contact behaviours of alginate-based films from both extracted alginate fractions and refined commercial sodium alginate were investigated. This demonstrated that whilst the gas barrier properties of alginate films were excellent, the long-term water and water-vapour barrier properties are insufficient for many applications, despite alginate films being routinely identified as suitable for food-contact applications. Agar, an alternative algal polysaccharide, was selected as a platform for improved water barrier and water-contact performance, achieved by functionalisation with fatty-acid residues by esterification of the primary -OH sites on the agar molecule. The resulting functionalised material (AgaF) was found to be highly hydrophobic and insoluble in water, hence required alternative downstream processing to convert the reaction product (washed AgaF powder) into an industrially relevant intermediate material.

Rheometry investigations of the AgaF material revealed the melt-flow properties follow the well-established Power-Law Fluid model, with the molten biopolymer exhibiting Newtonian flow behaviour at low- and high-shear rates, but non-Newtonian flow behaviour at comparatively moderate shear rates. AgaF material was further investigated by processing with a micro-compounding extruder, where the mixed Newtonian and non-Newtonian flow behaviour was again observed. Demonstration of the ability to process the AgaF material in industrially relevant equipment is an important step to ensure that there will be a reasonably predictable process development road-map to convert the product of the downstream chemistry (Agar + Fatty-acid -> AgaF) into commercially interesting intermediates or products (e.g. extruded nurdles or sheets, blown-film extrusion, injection moulded parts etc.).

The secondary thermochemical conversion of extracted residues was also investigated, with two high-yielding char production processes being considered. Hydrothermal carbonisation (HTC) and slow-pyrolysis (SP) were applied to both fresh macroalgae and an extracted residue. The resulting char products were then assessed with for long-term stability under oxidising conditions, revealing that SP is the preferred process for

producing a high yield of stable carbon-rich char for the purposed of carbon sequestration. Furthermore, the effect on seed germination of each of the different chars was considered and showed that at an appropriate dilution the SP chars may even act as a bio-stimulant since the germination index for dilute application of the SP char exceeded that of the DI water control (103.7 % compared to 100 % respectively).

Finally, the end-of-life degradability of the algal polysaccharide films was considered when exposed to both anaerobic digestion (AD) and aerobic composting. Biopolymers based on the unmodified algal polysaccharides (e.g. alginate) degraded extremely quickly under aerobic composting (completely degraded within 6 weeks), but typically much slower under anaerobic digestion unless the biopolymer film was formed using glycerol as a plasticizer. Functionalised materials also showed significant degradation under AD after 40 days and were showing signs of progressing degradation under composting at the time of writing (8 weeks).

The process flow shown in figure 6.1 represents the final form of the macroalgal biorefinery presented in this work, where fractionation, thermochemical treatment of residues, downstream chemical conversion, and conversion to consumer goods are integrated, with the end-of-life process considered for each major product stream.

6.2 Future Work

The schematic biorefinery presented in figure 6.1 focuses entirely on the valorisation of only 2 fractions of a macroalgae feed; alginate and agar. However, the fractionation work presented in chapter 4 demonstrated the technical ability to target multiple different value fractions of the whole macroalgal biomass, thus there is the opportunity to further valorise the algal biomass. Further work to better target and refine the protein fraction with alternative extraction techniques such as alkaline hydrolysis, ammonium sulfate precipitation, or accelerated solvent extractions offer the opportunity to produce a refined protein product and/or an amino-acid hydrolysate that might be suitable for use as a food source, or as natural plant bio-stimulants.[286, 333, 334]

Incorporating similar targeting of specific high value target biomolecules (e.g. fucoidan, fucoxanthin) for specific species may also turn out to be advantageous when considering the optimal valorisation of specific species. This may be achieved through the bulk-biorefinery techniques already presented, or alternatively by introducing a small modular and reconfigurable standalone pre-extraction process that can be configured to match the precise requirements of the changing biomass throughout the season.

Furthermore, the various fractionation techniques utilised in this work (Chapter 4) ended up losing significant quantities of starting mass in work-up and washings. Inevitably a certain quantity of mass yield is bound to be lost through work-up and separation, however there is scope to significantly improve product yields by techniques such as recycling of washings to re-use as the extraction liquor, or alternatively by employing further downstream processes to gain additional value from the lost carbon such as fermentation, anaerobic digestion coupled with power generation, or recycling as aqueous nutrients back to the mariculture beds where the biomass was originally grown.

Screening of the biorefinery techniques in this work was done using a single species of macroalgae at a time, however it might be advantageous to group species together in accordance with their expected crop availability and trial co-processing of multiple species to investigate any potential inter-species interactions through the biorefinery processes. Furthermore, supplementation of the macroalgal biomass with alternative marine biomass (e.g. chitinous shellfish waste) and/or non-biomass feedstock (e.g. petro-plastic waste such as lost fishing gear) may be interesting. Previous studies have reported a potential benefit from hydrothermal co-processing of macroalgae and petro-plastic wastes, thus introducing petro-plastic waste collected from the marine environment into ahead of the slow-pyrolysis step may provide an attractive route to both treat a troublesome ecosystem pollutant and enhance the value of products produced in the thermochemical processing.

The chemical synthesis method reported in this work for the production of functionalised carbohydrates, whilst effective, does not align well with green chemistry principles.

It requires high temperature, and significant quantities of pyridine. In this reaction pyridine functions both as a solvent, and a base catalyst to initiate the reaction. There is therefore an opportunity to work towards a cleaner green synthesis using a more benign solvent or solvent system, and potentially with a different catalyst.

In parallel to working towards a green synthesis route for the functionalised algal polysaccharides, full characterisation of this material is required. Basic polymer processing information such as the melting point, melt-flow index, and tensile modulus will be essential to allow rapid progress towards appropriate industrial processing technologies, in addition to technical performance characteristic (e.g. water and gas diffusivity constants). Furthermore, a thorough chemical characterisation of the functionalised material and its degradation products will be required to demonstrate that it is safe for use in food contact applications. Additionally, a more in-depth understanding of the chemistry of the functionalised polysaccharide material will enable fine-tuning of the material properties, e.g. by using fatty-acid residues of different chain lengths or degree of saturation, or by introducing a covalent cross-linking species into the reaction.

Finally, a thorough end-to-end life-cycle assessment (LCA) should be developed ahead of any serious investment into scale-up or pilot development of the materials. Considering the total system impacts of using macroalgae through the proposed biorefinery including the optional downstream processes for efficient valorisation of the biomass will give good confidence in the total system sustainability and give a basis from which to make informed comparisons against the incumbent polymeric materials that the products of this macroalgae biorefinery would aim to replace. Furthermore, development of an LCA will highlight any particular 'hot-spots' of the process that are more responsible for the total system impact, thus helping focus the efforts of future researchers and engineers towards working on improvements that will have the greatest impact first.

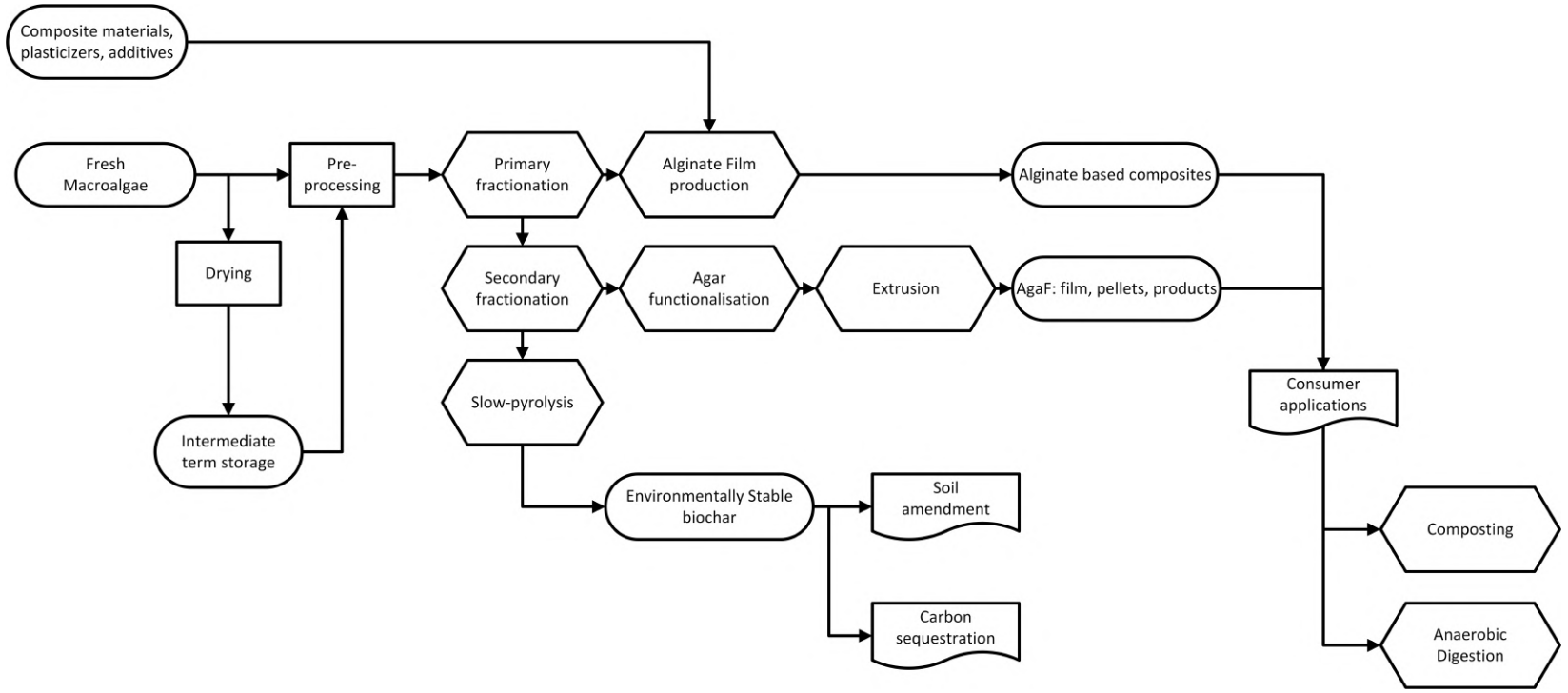

Figure 6.1: Macroalgae biorefinery process flow where pre-treatment, multi-step fractionation, thermochemical treatment of residues, and secondary chemical conversion are integrated for the production of multiple product streams, and end-of-life disposal options are included.

Bibliography

(1) UNFCCC, COP26 The Glasgow Climate Pact: COP26 Outcomes, 26th Session of the Conference of the Parties, United Nations Framework Convention on Climate Change, Glasgow, 2021.

(2) P. Sorknæs, R. M. Johannsen, A. D. Korberg, T. B. Nielsen, U. R. Petersen and B. V. Mathiesen, *Energy*, 2022, **254**, 124339.

(3) Z. Zhu and Z. Xu, *Renewable and Sustainable Energy Reviews*, 2020, **134**, 110308.

(4) M. V. de Oliveira Magalhães, in *Computer Aided Chemical Engineering*, ed. R. M. de Brito Alves, C. A. O. do Nascimento and E. C. Biscaia, Elsevier, 2009, vol. 27, pp. 107–112.

(5) W. A. Rutala and D. J. Weber, *Infection Control & Hospital Epidemiology*, 2001, **22**, 248–257.

(6) F. McGain, D. Story, T. Lim and S. McAlister, *BJA: British Journal of Anaesthesia*, 2017, **118**, 862–869.

(7) K. Marsh and B. Bugusu, *Journal of Food Science*, 2007, **72**, R39–R55.

(8) T. Ghosh, H. C. Kim, R. De Kleine, T. J. Wallington and B. R. Bakshi, *Sustainable Materials and Technologies*, 2021, **28**, e00263.

(9) G. Bailey and N. Milner, *Before Farming [online version]*, 2002, **3_4**, 1–15.

(10) D. B. Stengel and S. Connan, in *Natural Products From Marine Algae: Methods and Protocols*, ed. D. B. Stengel and S. Connan, Springer, New York, NY, 2015, pp. 1–37.

(11) M. Shahbandeh, *Commercial Seaweed: Global Market Value 2020-2028*, Statista, 2021, https://www.statista.com/statistics/603851/value-commercial-seaweed-market-worldwide/ (visited on 09/15/2022).

(12) P. Schiener, S. Zhao, K. Theodoridou, M. Carey, K. Mooney-McAuley and C. Greenwell, *Biomass Conversion and Biorefinery*, 2017, **7**, 221–235.

(13) S. Raikova, C. Le, T. Beacham, R. Jenkins, M. Allen and C. Chuck, *Biomass and Bioenergy*, 2017, **107**, 244–253.

(14) S. He, M. Zhao, J. Wang, Z. Cheng, B. Yan and G. Chen, *Science of The Total Environment*, 2020, **712**, 135677.

(15) M. G. Borines, R. L. de Leon and J. L. Cuello, *Bioresource Technology*, 2013, **138**, 22–29.

(16) D. López Barreiro, M. Beck, U. Hornung, F. Ronsse, A. Kruse and W. Prins, *Algal Research*, 2015, **11**, 234–241.

(17) K. Sudhakar, R. Mamat, M. Samykano, W. H. Azmi, W. F. Ishak and T. Yusaf, *Renewable and Sustainable Energy Reviews*, 2018, **91**, 165–179.

(18) K. A. Jung, S. R. Lim, Y. Kim and J. M. Park, *Bioresource Technology*, 2013, **135**, 182–190.

(19) L. Hasselström, W. Visch, F. Gröndahl, G. M. Nylund and H. Pavia, *Marine Pollution Bulletin*, 2018, **133**, 53–64.

(20) M. R. Tredici, L. Rodolfi, N. Biondi, N. Bassi and G. Sampietro, *Algal Research*, 2016, **19**, 253–263.

(21) D. F. Lozano-Garcia, S. P. Cuellar-Bermudez, E. del Rio-Hinojosa, F. Betancourt, G. S. Aleman-Nava and R. Parra-Saldivar, *Algal Research*, 2019, **39**, 101459.

(22) FAO, in *Fishery and Aquaculture Statistics. Global Aquaculture Production 1950-2018 (FishstatJ)*, Food and Agriculture Organization of the United Nations, Rome, 2020.

(23) DOS SANTOS FERNANDES DE ARAUJO Rita, LUSSER Maria, SANCHEZ LOPEZ Javier and AVRAAMIDES Marios, *Brief on Algae Biomass Production*, Publications Office of the European Union, Luxembourg, 2019.

(24) F. Ferdouse, S. L. Holdt, R. Smith, P. Murúa and Z. Yang, *FAO Globefish Research Programme*, 2018, **124**, 120.

(25) S. W. K. van den Burg, H. Dagevos and R. J. K. Helmes, *ICES Journal of Marine Science*, 2019, ed. F. Pernet, DOI: 10.1093/icesjms/fsz183.

(26) S. W. K. van den Burg, A. P. van Duijn, H. Bartelings, M. M. van Krimpen and M. Poelman, *Aquaculture Economics & Management*, 2016, **20**, 235–252.

(27) U. G. Bak, A. Mols-Mortensen and O. Gregersen, *Algal Research*, 2018, **33**, 36–47.

(28) R. E. Rodríguez-Martínez, P. D. Roy, N. Torrescano-Valle, N. Cabanillas-Terán, S. Carrillo-Domínguez, L. Collado-Vides, M. García-Sánchez and B. I. van Tussenbroek, *PeerJ*, 2020, **8**, e8667.

(29) C. Hu, L. Feng, R. F. Hardy and E. J. Hochberg, *Remote Sensing of Environment*, 2015, **167**, 229–246.

(30) M. Wang and C. Hu, *Remote Sensing of Environment*, 2016, **183**, 350–367.

(31) M. Wang, C. Hu, B. B. Barnes, G. Mitchum, B. Lapointe and J. P. Montoya, *Science*, 2019, **365**, 83–87.

(32) M. Wang, C. Hu, B. B. Barnes, G. Mitchum, B. Lapointe and J. P. Montoya, *Science*, 2019, **365**, 83–87.

(33) S. K. Praetorius, *Nature*, 2018, **556**, 180–181.

(34) R. E. Rodríguez-Martínez, A. E. Medina-Valmaseda, P. Blanchon, L. V. Monroy-Velázquez, A. Almazán-Becerril, B. Delgado-Pech, L. Vásquez-Yeomans, V. Francisco and M. C. García-Rivas, *Marine Pollution Bulletin*, 2019, **146**, 201–205.

(35) P. Fogarty, *BBC News, Latin America & Caribbean*, 2018.

(36) P. Brown, *NACLA*, 2020.

(37) D. Resiere, R. Valentino, R. Nevière, R. Banydeen, P. Gueye, J. Florentin, A. Cabié, T. Lebrun, B. Mégarbane, G. Guerrier and H. Mehdaoui, *The Lancet*, 2018, **392**, 2691.

(38) J. A. Sembera, E. J. Meier and T. M. Waliczek, *HortTechnology*, 2018, **28**, 80–84.

(39) H. H. Gojon-Báez, D. A. Siqueiros-Beltrones and H. Hernández-Contreras, *Ciencias Marinas*, 1998, **24**, 463–481.

(40) J. J. Milledge and P. J. Harvey, *Journal of Marine Science and Engineering*, 2016, **4**, 60.

(41) S. R. Yende, U. N. Harle and B. B. Chaugule, *Pharmacognosy Reviews*, 2014, **8**, 1–7.

(42) *Commission Regulation (EU) No 1275/2013 of 6 December 2013 Amending Annex I to Directive 2002/32/EC of the European Parliament and of the Council as Regards Maximum Levels for Arsenic, Cadmium, Lead, Nitrites, Volatile Mustard Oil and Harmful Botanical Impurities Text with EEA Relevance*, 2013.

(43) F. A. for Environmental Protection, *NORMA OFICIAL MEXICANA NOM-147-SEMARNAT/SSA1-2004*, 2007.

(44) A. Vincent, A. Stanley and J. Ring, *Hidden Champion of the Ocean: Seaweed as a Growth Engine for a Sustainable European Future*, Seaweed for Europe, 2020.

(45) *BBC News, Business*, 2022.

(46) *Ocean Rainforest Raises $1.5 Million to Scale Farming Operations*, Agrigate Global, 2020, https://agrigateglobal.com/europe/ocean-rainforest-raises-1-5-million-to-scale-farming-operations/ (visited on 09/13/2022).

(47) T. F. Site, *Ocean Rainforest Leads Successful €9 Million Seaweed Grant Bid*, 2022, https://thefishsite.com/articles/ocean-rainforest-leads-successful-9-million-seaweed-grant-bid (visited on 09/13/2022).

(48) M. von Keitz, *Macroalgae Research Inspiring Novel Energy Resources*, MARINER | arpa-e.energy.gov, 2017, https://arpa-e.energy.gov/technologies/programs/mariner (visited on 12/10/2020).

(49) M. E. Capron, J. R. Stewart, A. de Ramon N'Yeurt, M. D. Chambers, J. K. Kim, C. Yarish, A. T. Jones, R. B. Blaylock, S. C. James, R. Fuhrman, M. T. Sherman, D. Piper, G. Harris and M. A. Hasan, *Energies*, 2020, **13**, 4972.

(50) M. T. Sherman, R. Blaylock, K. Lucas, M. E. Capron, J. R. Stewart, S. F. DiMarco, K. Thyng, R. Hetland, M. Kim, C. Sullivan, Z. Moscicki, I. Tsukrov, M. R. Swift, M. D. Chambers, S. C. James, M. Brooks, B. von Herzen, A.

Jones and D. Piper, OCEANS 2018 MTS/IEEE Charleston, OCEANS 2018 MTS/IEEE Charleston, 2018, pp. 1–6.

(51) NSF, *Mission - North Sea Farmers*, `https://www.northseafarmers.org/about-us/mission` (visited on 09/13/2022).

(52) D. J. McHugh, *A Guide to the Seaweed Industry*, in collab. with FAO, Food and Agriculture Organization of the United Nations, Rome, 2003, 105 pp.

(53) H. P. S. Abdul Khalil, Y. Y. Tye, C. K. Saurabh, C. P. Leh, T. K. Lai, E. W. N. Chong, M. R. Nurul Fazita, J. Mohd Hafiidz, A. Banerjee and M. I. Syakir, *Express Polymer Letters*, 2017, **11**, 244–265.

(54) I. P. S. Fernando, D. Kim, J.-W. Nah and Y.-J. Jeon, *Chemical Engineering Journal*, 2019, **355**, 33–48.

(55) H. P. S. Abdul Khalil, T. K. Lai, Y. Y. Tye, S. Rizal, E. W. N. Chong, S. W. Yap, A. A. Hamzah, M. R. Nurul Fazita and M. T. Paridah, *Express Polymer Letters*, 2018, **12**, 296–317.

(56) A. I. Usov, in *Advances in Carbohydrate Chemistry and Biochemistry*, ed. D. Horton, Academic Press, 2011, vol. 65, pp. 115–217.

(57) I. J. Joye and D. J. McClements, *Current Opinion in Colloid & Interface Science*, 2014, **19**, 417–427.

(58) R. Jumaidin, S. M. Sapuan, M. Jawaid, M. R. Ishak and J. Sahari, *Current Analytical Chemistry*, 2018, **14**, 249–267.

(59) J. W. Rhim, L. F. Wang and S. I. Hong, *Food Hydrocolloids*, 2013, **33**, 327–335.

(60) J.-W. Rhim, *LWT - Food Science and Technology*, 2004, **37**, 323–330.

(61) M. Gomaa, A. F. Hifney, M. A. Fawzy and K. M. Abdel-Gawad, *Food Hydrocolloids*, 2018, **82**, 239–247.

(62) C. Zhang, P.-L. Show and S.-H. Ho, *Bioresource Technology*, 2019, **289**, 121700.

(63) S. Saji, A. Hebden, P. Goswami and C. Du, *Sustainability*, 2022, **14**, 5181.

(64) M. D'Este, M. Alvarado-Morales, A. Ciofalo and I. Angelidaki, *Energy & Fuels*, 2017, **31**, 7166–7175.

(65) J. Necas and L. Bartosikova, *Veterinární Medicína*, 2013, **58**, 187–205.

(66) J. Venkatesan, S. Anil, S.-K. Kim and M. S. Shim, *Polymers*, 2016, **8**, 30.

(67) V. D. Alves, N. Costa and I. M. Coelhoso, *Carbohydrate Polymers*, 2010, **79**, 269–276.

(68) H. Kylin, *Journal Biological Chemistry*, 1913, **83**, 171–197.

(69) B. Kloareg, *Physiologie vegetale*, 1984, **22**, 47–56.

(70) X. Liu, B. Liu, X. Wei, Y. Shi, A. Jia and C. Wang, *Journal of Applied Phycology*, 2021, **33**, 523–531.

(71) J. J. Milledge and P. J. Harvey, *Journal of Applied Phycology*, 2016, **28**, 3021–3030.

(72) R. Zhang, X. Zhang, Y. Tang and J. Mao, *Carbohydrate Polymers*, 2020, **228**, 115381.

(73) D. Klemm, B. Heublein, H.-P. Fink and A. Bohn, *Angewandte Chemie International Edition*, 2005, **44**, 3358–3393.

(74) T. Huq, S. Salmieri, A. Khan, R. A. Khan, C. Le Tien, B. Riedl, C. Fraschini, J. Bouchard, J. Uribe-Calderon, M. R. Kamal and M. Lacroix, *Carbohydrate Polymers*, 2012, **90**, 1757–1763.

(75) D. Bondeson, A. Mathew and K. Oksman, *Cellulose*, 2006, **13**, 171.

(76) X. Feng, X. Meng, J. Zhao, M. Miao, L. Shi, S. Zhang and J. Fang, *Cellulose*, 2015, **22**, 1763–1772.

(77) N. Wahlström, U. Edlund, H. Pavia, G. Toth, A. Jaworski, A. J. Pell, F. X. Choong, H. Shirani, K. P. R. Nilsson and A. Richter-Dahlfors, *Cellulose*, 2020, **27**, 3707–3725.

(78) Y. Habibi, L. A. Lucia and O. J. Rojas, *Chemical Reviews*, 2010, **110**, 3479–3500.

(79) A. F. Abdel-Fattah, M. M.-D. Hussein and H. M. Salem, *Carbohydrate Research*, 1974, **33**, 9–17.

(80) Y. S. Ovodov, V. A. Khomenko and T. F. Guseva, *Chemistry of Natural Compounds*, 1970, **6**, 285–288.

(81) M. T. Ale, J. D. Mikkelsen and A. S. Meyer, *Marine Drugs*, 2011, **9**, 2106–2130.

(82) J. T. Kidgell, M. Magnusson, R. de Nys and C. R. K. Glasson, *Algal Research*, 2019, **39**, 101422.

(83) J. M. M. Adams, L. B. Turner, T. A. Toop, M. E. Kirby, C. Rolin, E. Judd, R. Inkster, L. McEvoy, W. M. Mirza, M. K. Theodorou and J. Gallagher, *GCB Bioenergy*, 2020, **12**, 706–727.

(84) J. A. Gallagher, L. B. Turner, J. M. Adams, S. Barrento, P. W. Dyer and M. K. Theodorou, *Journal of Applied Phycology*, 2018, **30**, 2305–2316.

(85) M. Suutari, E. Leskinen, K. Fagerstedt, J. Kuparinen, P. Kuuppo and J. Blomster, *Phycological Research*, 2015, **63**, 1–18.

(86) A. Silva, H. Abreu, A. Silva and S. Cardoso, *Marine Drugs*, 2019, **17**, 90.

(87) G. Skjåk-Bræk, E. Murano and S. Paoletti, *Biotechnology and Bioengineering*, 1989, **33**, 90–94.

(88) G. Hernández-carmona, D. J. McHugh, D. L. Arvizu-Higuera and Y. E. Rodríguez-montesinos, *Journal of Applied Phycology*, 1998, **10**, 507–513.

(89) S. J. Lim and W. M. Wan Aida, in *Seaweed Polysaccharides*, ed. J. Venkatesan, S. Anil and S.-K. Kim, Elsevier, 2017, pp. 27–46.

(90) N. Flórez-Fernández, H. Domínguez and M. D. Torres, *International Journal of Biological Macromolecules*, 2019, **124**, 451–459.

(91) L. Allahgholi, R. R. R. Sardari, S. Hakvåg, K. Z. G. Ara, T. Kristjansdottir, I. M. Aasen, O. H. Fridjonsson, T. Brautaset, G. O. Hreggvidsson and E. N. Karlsson, *Journal of Applied Phycology*, 2020, **32**, 1933–1947.

(92) M. Cregut and E. Rondags, *Process Biochemistry*, 2013, **48**, 1861–1871.

(93) H. Porse and B. Rudolph, *Journal of Applied Phycology*, 2017, **29**, 2187–2200.

(94) C. Deepika, G. A. Ravishankar and A. R. Rao, in *Sustainable Global Resources Of Seaweeds Volume 1: Bioresources , Cultivation, Trade and Multifarious Applications*, ed. A. Ranga Rao and G. A. Ravishankar, Springer International Publishing, Cham, 2022, pp. 17–44.

(95) F. Abeln, J. Fan, V. L. Budarin, H. Briers, S. Parsons, M. J. Allen, D. A. Henk, J. Clark and C. J. Chuck, *Algal Research*, 2019, **38**, 101411.

(96) E. T. Kostas, D. A. White and D. J. Cook, *BioEnergy Research*, 2019, DOI: 10.1007/s12155-019-10054-1.

(97) A. S. Zaky, D. Greetham, G. A. Tucker and C. Du, *Scientific Reports*, 2018, **8**, 12127.

(98) K. K. Kadimpati, S. Thadikamala, K. Devarapalli, L. Banoth and K. B. Uppuluri, *Biomass Conversion and Biorefinery*, 2021, DOI: 10.1007/s13399-020-01270-3.

(99) Y. Jiang, J. Li, Y. Ni, Y. Tang, M. Wu, W. Zhang, F. Xin and M. Jiang, *Fuel*, 2022, **307**, 121867.

(100) A. Schultze-Jena, R. C. Vroon, A. K. A. Macleod, G. Ó. Hreggviðsson, B. T. Adalsteinsson, N. P. E. Engelen-Smit, T. de Vrije, M. A. W. Budde, H. van der Wal, A. M. López-Contreras and M. A. Boon, *Algal Research*, 2022, **62**, 102618.

(101) G. Lavrič, A. Oberlintner, I. Filipova, U. Novak, B. Likozar and U. Vrabič-Brodnjak, *Polymers*, 2021, **13**, 2523.

(102) R. Gheorghita (Puscaselu), G. Gutt and S. Amariei, *Coatings*, 2020, **10**, 166.

(103) B. Deepa, E. Abraham, L. A. Pothan, N. Cordeiro, M. Faria and S. Thomas, *Materials*, 2016, **9**, 50.

(104) A. M. M. Sousa and M. P. Gonçalves, *Carbohydrate Polymers*, 2015, **132**, 196–204.

(105) J.-W. Rhim, *Journal of Food Science*, 2012, **77**, N66–N73.

(106) N. Canabarro, J. F. Soares, C. G. Anchieta, C. S. Kelling and M. A. Mazutti, *Sustainable Chemical Processes*, 2013, **1**, 22.

(107) M. Möller, P. Nilges, F. Harnisch and U. Schröder, *ChemSusChem*, 2011, **4**, 566–579.

(108) A. R. Gollakota, N. Kishore and S. Gu, *Renewable and Sustainable Energy Reviews*, 2018, **81**, 1378–1392.

(109) P. Biller and A. Roth, in *Biokerosene: Status and Prospects*, ed. M. Kaltschmitt and U. Neuling, Springer, Berlin, Heidelberg, 2018, pp. 607–635.

(110) A. Matayeva, D. Bianchi, S. Chiaberge, F. Cavani and F. Basile, *Fuel*, 2019, **240**, 169–178.

(111) L. Sheng, X. Wang and X. Yang, *Bioresource Technology*, 2018, **247**, 14–20.

(112) S. Changi, M. Zhu and P. E. Savage, *ChemSusChem*, 2012, **5**, 1743–1757.

(113) T. Minowa, S. Inoue, T. Hanaoka and Y. Matsumura, *Journal of the Japan Institute of Energy*, 2004, **83**, 794–798.

(114) E. M. Lozano, T. H. Pedersen and L. A. Rosendahl, *Applied Energy*, 2019, **254**, 113654.

(115) Y. Li, S. Leow, A. C. Fedders, B. K. Sharma, J. S. Guest and T. J. Strathmann, *Green Chemistry*, 2017, **19**, 1163–1174.

(116) Y. Jiang, S. B. Jones, Y. Zhu, L. Snowden-Swan, A. J. Schmidt, J. M. Billing and D. Anderson, *Algal Research*, 2019, **39**, 101450.

(117) P. Biller and A. B. Ross, *Bioresource Technology*, 2011, **102**, 215–225.

(118) A. Dutta, A. Sahir and E. Tan, *Process Design and Economics for the Conversion of Lignocellulosic Biomass to Hydrocarbon Fuels: Thermochemical Research Pathways with In Situ and Ex Situ Upgrading of Fast Pyrolysis Vapors*, NREL/TP-5100-62455, PNNL-23823, National Renewable Energy Lab. (NREL), Golden, CO (United States), 2015, p. 275.

(119) P. Spath, A. Aden, T. Eggeman, M. Ringer, B. Wallace and J. Jechura, *Biomass to Hydrogen Production Detailed Design and Economics Utilizing the Battelle Columbus Laboratory Indirectly-Heated Gasifier*, NREL/TP-510-37408, 15016221, National Renewable Energy Lab. (NREL), Golden, CO (United States), 2005, NREL/TP-510–37408, 15016221.

(120) D. Humbird, R. Davis, L. Tao, C. Kinchin, D. Hsu, A. Aden, P. Schoen, J. Lukas, B. Olthof, M. Worley, D. Sexton and D. Dudgeon, *Process Design and Economics for Biochemical Conversion of Lignocellulosic Biomass to Ethanol: Dilute-Acid Pretreatment and Enzymatic Hydrolysis of Corn Stover*, NREL/TP-5100-47764, 1013269, National Renewable Energy Lab. (NREL), Golden, CO (United States), 2011, NREL/TP-5100–47764, 1013269.

(121) R. Davis, J. Markham, C. Kinchin, N. Grundl, E. C. Tan and D. Humbird, *Process Design and Economics for the Production of Algal Biomass: Algal Biomass Production in Open Pond Systems and Processing Through Dewatering for Downstream Conversion NREL/TP-5100-64772*, National Renewable Energy Laboratory (NREL), Golden, CO (United States), 2016.

(122) T. H. Pedersen, N. H. Hansen, O. M. Pérez, D. E. V. Cabezas and L. A. Rosendahl, *Biofuels, Bioproducts and Biorefining*, 2018, **12**, 213–223.

(123) S. B. Jones, Y. Zhu, D. B. Anderson, R. T. Hallen, D. C. Elliott, A. J. Schmidt, K. O. Albrecht, T. R. Hart, M. G. Butcher, C. Drennan, L. J. Snowden-Swan, R. Davis and C. Kinchin, *Process Design and Economics for the Conversion of Algal Biomass to Hydrocarbons: Whole Algae Hydrothermal Liquefaction and Upgrading*, PNNL-23227, Pacific Northwest National Lab. (PNNL), Richland, WA (United States), 2014.

(124) J. Hoffmann, S. Rudra, S. S. Toor, J. B. Holm-Nielsen and L. A. Rosendahl, *Bioresource Technology*, 2013, **129**, 402–410.

(125) IEA, *World Energy Model – Analysis*, IEA, 2020, `https://www.iea.org/reports/world-energy-model` (visited on 12/17/2020).

(126) United Nations, *Summary of the Paris Agreement - EN*, United Nations Framework Convention on Climate Change, Paris, 2015.

(127) IEA, *Sustainable Development Scenario – World Energy Model – Analysis*, IEA, 2020, `https://www.iea.org/reports/world-energy-model/sustainable-development-scenario` (visited on 12/17/2020).

(128) O. f. L. E. V. Department for Transport and E. bibinitperiod I. S. Department for Business, *Government Takes Historic Step towards Net-Zero with End of Sale of New Petrol and Diesel Cars by 2030*, GOV.UK, 2020, `https://www.gov.uk/government/news/government-takes-historic-step-towards-net-zero-with-end-of-sale-of-new-petrol-and-diesel-cars-by-2030` (visited on 12/17/2020).

(129) M. Unglert, D. Bockey, C. Bofinger, B. Buchholz, G. Fisch, R. Luther, M. Müller, K. Schaper, J. Schmitt, O. Schröder, U. Schümann, H. Tschöke, E. Remmele, R. Wicht, M. Winkler and J. Krahl, *Fuel*, 2020, **268**, 117227.

(130) BP Global, *BP Statistical Review of World Energy - All Data, 1965-2018 (XLSX 2.4MB)*, BP Statistical Review of World Energy, 2019, `https://www.bp.com/en/global/corporate/energy-economics/statistical-review-of-world-energy/downloads.html` (visited on 11/13/2018).

(131) J. Teter, J. Tattini and A. Petropoulos, *Tracking Transport 2020 – Analysis*, IEA, May-2020, https://www.iea.org/reports/tracking-transport-2020 (visited on 12/17/2020).

(132) J. Rogelj, D. Shindell, K. Jiang, S. Fifita, P. Forster, V. Ginzburg, C. Handa, S. Kobayashi, E. Kriegler, L. Mundaca, R. Séférian, M. V. Vilariño, K. Calvin, J. Emmerling, S. Fuss, N. Gillett, C. He, E. Hertwich, L. Höglund-Isaksson, D. Huppmann, G. Luderer, D. L. McCollum, M. Meinshausen, R. Millar, A. Popp, P. Purohit, K. Riahi, A. Ribes, H. Saunders, C. Schädel, P. Smith, E. Trutnevyte, Y. Xiu, W. Zhou, K. Zickfeld, G. Flato, J. Fuglestvedt, R. Mrabet and R. Schaeffer, in *Global Warming of 1.5°C. An IPCC Special Report on the Impacts of Global Warming of 1.5°C above Pre-Industrial Levels and Related Global Greenhouse Gas Emission Pathways, in the Context of Strengthening the Global Response to the Threat of Climate Change, Sustainable Development, and Efforts to Eradicate Poverty*, IPCC, 2018, p. 82.

(133) S. N. Naik, V. V. Goud, P. K. Rout and A. K. Dalai, *Renewable and Sustainable Energy Reviews*, 2010, **14**, 578–597.

(134) D. Bockey, *OCL*, 2019, **26**, 40.

(135) L. Panichelli, A. Dauriat and E. Gnansounou, *The International Journal of Life Cycle Assessment*, 2009, **14**, 144–159.

(136) Iogen, *Cellulosic Ethanol: Technology Scale-up and Validation*, 2015, http://www.iogen.ca/cellulosic_ethanol/scale-up.html (visited on 11/16/2018).

(137) R. S. Gajraj, G. P. Singh and A. Kumar, in *Biofuels: Greenhouse Gas Mitigation and Global Warming: Next Generation Biofuels and Role of Biotechnology*, Springer India, New Delhi, 2018, pp. 307–325.

(138) E. Sadatshojaei, D. A. Wood and D. Mowla, in *Sustainable Green Chemical Processes and Their Allied Applications*, ed. Inamuddin and A. Asiri, Springer International Publishing, Cham, 2020, pp. 575–588.

(139) D. (D. of Energy)., *National Algal Biofuels Technology Review*, U.S. Department of Energy, Office of Energy Efficiency and Renewable Energy, Bioenergy Technologies Office, 2016, p. 212.

(140) D. Castello, T. Pedersen and L. Rosendahl, *Energies*, 2018, **11**, 3165.

(141) D. C. Elliott, P. Biller, A. B. Ross, A. J. Schmidt and S. B. Jones, *Bioresource Technology*, 2015, **178**, 147–156.

(142) M. S. Vlaskin, A. V. Grigorenko, N. I. Chernova and S. V. Kiseleva, *Energy Exploration & Exploitation*, 2018, **36**, 1546–1555.

(143) M. S. Seshasayee and P. E. Savage, *Applied Energy*, 2020, **278**, 115673.

(144) K. Anastasakis and A. B. Ross, *Bioresource Technology*, 2011, **102**, 4876–4883.

(145) J. L. Wagner, C. D. Le, V. P. Ting and C. J. Chuck, *Fuel Processing Technology*, 2017, **165**, 102–111.

(146) S. Raikova, H. Smith-Baedorf, R. Bransgrove, O. Barlow, F. Santomauro, J. L. Wagner, M. J. Allen, C. G. Bryan, D. Sapsford and C. J. Chuck, *Fuel Processing Technology*, 2016, **142**, 219–227.

(147) C. Jazrawi, P. Biller, A. B. Ross, A. Montoya, T. Maschmeyer and B. S. Haynes, *Algal Research*, 2013, **2**, 268–277.

(148) A. J. Mørup, J. Becker, P. S. Christensen, K. Houlberg, E. Lappa, M. Klemmer, R. B. Madsen, M. Glasius and B. B. Iversen, *Industrial & Engineering Chemistry Research*, 2015, **54**, 5935–5947.

(149) N. Nwaokocha, *The Chemical Engineer*, 2019.

(150) T. Voisin, A. Erriguible, D. Ballenghien, D. Mateos, A. Kunegel, F. Cansell and C. Aymonier, *The Journal of Supercritical Fluids*, 2017, **120**, 18–31.

(151) M. Piccini, S. Raikova, M. J. Allen and C. J. Chuck, *Sustainable Energy & Fuels*, 2019, **3**, 292–301.

(152) I. Johannsen, B. Kilsgaard, V. Milkevych and D. Moore, *Processes*, 2021, **9**, 234.

(153) K. Anastasakis, P. Biller, R. B. Madsen, M. Glasius and I. Johannsen, *Energies*, 2018, **11**, 2695.

(154) R. L. Holliday, B. Y.M. Jong and J. W. Kolis, *The Journal of Supercritical Fluids*, 1998, **12**, 255–260.

(155) *Handbook of Petroleum Refining Processes*, ed. R. A. Meyers, McGraw-Hill, New York, 3rd ed, 2004, 1 p.

(156) A. Palacios, M. E. Navarro, Z. Jiang, A. Avila, G. Qiao, E. Mura and Y. Ding, *Solar Energy*, 2020, **201**, 437–452.

(157) I. A. Choudhury and M. A. El-Baradie, *Journal of Materials Processing Technology*, 1998, **77**, 278–284.

(158) B. Gaweł, M. Eftekhardadkhah and G. Øye, *Energy & Fuels*, 2014, **28**, 997–1003.

(159) D. Xu, G. Lin, S. Guo, S. Wang, Y. Guo and Z. Jing, *Renewable and Sustainable Energy Reviews*, 2018, **97**, 103–118.

(160) D. Zhou, L. Zhang, S. Zhang, H. Fu and J. Chen, *Energy & Fuels*, 2010, **24**, 4054–4061.

(161) S. Bjelić, J. Yu, B. B. Iversen, M. Glasius and P. Biller, *Energy & Fuels*, 2018, **32**, 3579–3587.

(162) J. Hoffmann, C. U. Jensen and L. A. Rosendahl, *Fuel*, 2016, **165**, 526–535.

(163) B. O. I. Ltd, *Crudes Assays | Features and Updates*, Global energy trading, 2017, `https://www.bp.com/en/global/bp-global-energy-trading/features-and-updates/technical-downloads/crudes-assays.html` (visited on 02/26/2021).

(164) G. Caeiro, A. F. Costa, H. S. Cerqueira, P. Magnoux, J. M. Lopes, P. Matias and F. R. Ribeiro, *Applied Catalysis A: General*, 2007, **320**, 8–15.

(165) D. Dong, S. Jeong and F. Massoth, *Catalysis Today*, 1997, **37**, 267–275.

(166) G. F. Stolz, E. R. Nesbitt and J. J. Gersic, *Organic Commodity Chemicals*, Industry & Trade Summary USITC Publication 3590, Office of Industires, U.S. International Trade Comission, 2003, p. 48.

(167) Y. Bai and Q. Bai, in *Subsea Engineering Handbook (Second Edition)*, ed. Y. Bai and Q. Bai, Gulf Professional Publishing, Boston, 2019, pp. 435–453.

(168) M. M. Ramirez-Corredores, in *The Science and Technology of Unconventional Oils*, ed. M. M. Ramirez-Corredores, Academic Press, Amsterdam, 2017, pp. 295–385.

(169) M. K. Khan, W. Kwek and J. Kim, *Fuel*, 2018, **218**, 78–88.

(170) C. A. Mullen and A. A. Boateng, *Fuel*, 2019, **245**, 360–367.

(171) S. Cheng, L. Wei, M. Alsowij, F. Corbin, E. Boakye, Z. Gu and D. Raynie, *AIMS Environmental Science*, 2017, **4**, 417–430.

(172) D. C. Elliott, T. R. Hart, A. J. Schmidt, G. G. Neuenschwander, L. J. Rotness, M. V. Olarte, A. H. Zacher, K. O. Albrecht, R. T. Hallen and J. E. Holladay, *Algal Research*, 2013, **2**, 445–454.

(173) J. A. Ramirez, R. J. Brown and T. J. Rainey, *Energies*, 2015, **8**, 6765–6794.

(174) J. A. Ramirez, R. J. Brown and T. J. Rainey, *Fuel Processing Technology*, 2017, **167**, 674–683.

(175) M. S. Vlaskin, N. I. Chernova, S. V. Kiseleva and L. A. Dombrovsky, International Heat Transfer Conference 16, Begel House Inc., 2018.

(176) E. S. Jones, S. Raikova, S. Ebrahim, S. Parsons, M. J. Allen and C. J. Chuck, *Journal of Chemical Technology and Biotechnology*, 2020, DOI: 10.1002/jctb.6443.

(177) S. Raikova, T. D. J. Knowles, M. J. Allen and C. J. Chuck, *ACS Sustainable Chemistry & Engineering*, 2019, **7**, 6769–6781.

(178) B. Biswas, A. Arun Kumar, Y. Bisht, R. Singh, J. Kumar and T. Bhaskar, *Bioresource Technology*, 2017, **242**, 344–350.

(179) A. B. Ross, J. M. Jones, M. L. Kubacki and T. Bridgeman, *Bioresource Technology*, 2008, **99**, 6494–6504.

(180) P. Virtanen, R. Gommers, T. E. Oliphant, M. Haberland, T. Reddy, D. Cournapeau, E. Burovski, P. Peterson, W. Weckesser, J. Bright, S. J. van der Walt, M. Brett, J. Wilson, K. J. Millman, N. Mayorov, A. R. J. Nelson, E. Jones, R. Kern, E. Larson, C. J. Carey, İ. Polat, Y. Feng, E. W. Moore, J. VanderPlas, D. Laxalde, J. Perktold, R. Cimrman, I. Henriksen, E. A. Quintero, C. R. Harris, A. M. Archibald, A. H. Ribeiro, F. Pedregosa and P. van Mulbregt, *Nature Methods*, 2020, **17**, 261–272.

(181) C. R. Harris, K. J. Millman, S. J. van der Walt, R. Gommers, P. Virtanen, D. Cournapeau, E. Wieser, J. Taylor, S. Berg, N. J. Smith, R. Kern, M. Picus, S. Hoyer, M. H. van Kerkwijk, M. Brett, A. Haldane, J. F. del Río, M. Wiebe,

P. Peterson, P. Gérard-Marchant, K. Sheppard, T. Reddy, W. Weckesser, H. Abbasi, C. Gohlke and T. E. Oliphant, *Nature*, 2020, **585**, 357–362.

(182) S. Leow, J. R. Witter, D. R. Vardon, B. K. Sharma, J. S. Guest and T. J. Strathmann, *Green Chemistry*, 2015, **17**, 3584–3599.

(183) J. Wagner, R. Bransgrove, T. A. Beacham, M. J. Allen, K. Meixner, B. Drosg, V. P. Ting and C. J. Chuck, *Bioresource Technology*, 2016, **207**, 166–174.

(184) Y. Li, S. Leow, A. C. Fedders, B. K. Sharma, J. S. Guest and T. J. Strathmann, *Green Chemistry*, 2017, **19**, 1163–1174.

(185) R. Shakya, S. Adhikari, R. Mahadevan, S. R. Shanmugam, H. Nam, E. B. Hassan and T. A. Dempster, *Bioresource Technology*, 2017, **243**, 1112–1120.

(186) G. Teri, L. Luo and P. E. Savage, *Energy & Fuels*, 2014, **28**, 7501–7509.

(187) J. Lu, Z. Liu, Y. Zhang and P. E. Savage, *ACS Sustainable Chemistry & Engineering*, 2018, **6**, 14501–14509.

(188) L. Sheng, X. Wang and X. Yang, *Bioresource Technology*, 2018, **247**, 14–20.

(189) P. J. Valdez, V. J. Tocco and P. E. Savage, *Bioresource Technology*, 2014, **163**, 123–127.

(190) J. D. Sheehan and P. E. Savage, *Bioresource Technology*, 2017, **239**, 144–150.

(191) M. Jatzwauck and A. Schumpe, *Biomass and Bioenergy*, 2015, **75**, 94–100.

(192) D. Jung, M. Zimmermann and A. Kruse, *ACS Sustainable Chemistry & Engineering*, 2018, **6**, 13877–13887.

(193) D. Knorr, J. Lukas and P. Schoen, *Production of Advanced Biofuels via Liquefaction - Hydrothermal Liquefaction Reactor Design: April 5, 2013*, NREL/SR-5100-60462, National Renewable Energy Lab. (NREL), Golden, CO (United States), 2013.

(194) S. B. Jones, Y. Zhu, D. B. Anderson, R. T. Hallen, D. C. Elliott, A. J. Schmidt, K. O. Albrecht, T. R. Hart, M. G. Butcher, C. Drennan, L. J. Snowden-Swan, R. Davis and C. Kinchin, *Process Design and Economics for the Conversion of Algal Biomass to Hydrocarbons: Whole Algae Hydrothermal Liquefaction and Upgrading*, PNNL–23227, 1126336, 2014, PNNL–23227, 1126336.

(195) O. J. Broch and D. Slagstad, *Journal of Applied Phycology*, 2012, **24**, 759–776.

(196) D. C. Elliott, T. R. Hart, G. G. Neuenschwander, L. J. Rotness, G. Roesijadi, A. H. Zacher and J. K. Magnuson, *ACS Sustainable Chemistry & Engineering*, 2014, **2**, 207–215.

(197) BSI, *BS 1600: 1991 Specification for Dimensions of Steel Pipe for the Petroleum Industry*, BS 1600, BSI, 1992.

(198) G. D. Ulrich and P. T. Vasudevan, *Chemical Engineering*, 2006, 4.

(199) B. Zhang, H. Feng, Z. He, S. Wang and H. Chen, *Energy Conversion and Management*, 2018, **159**, 204–212.

(200) E. M. Lozano, T. H. Pedersen and L. Rosendahl, 'Generic Approach for the Modeling of Liquefied Thermochemical Products and Biomass Heat of Formation. Case Study: HTL Biocrude, Pyrolysis Oil and Assessment of Energy Requirements', 2019.

(201) J. Yang, Q. (He, K. Corscadden, H. Niu, J. Lin and T. Astatkie, *Applied Energy*, 2019, **233–234**, 906–915.

(202) A. Palomino, L. C. Montenegro-Ruíz and R. D. Godoy-Silva, *Algal Research*, 2019, **44**, 101669.

(203) Y.-P. Xu, P.-G. Duan and F. Wang, *Fuel Processing Technology*, 2015, **130**, 268–274.

(204) D. Li, L. Chen, D. Xu, X. Zhang, N. Ye, F. Chen and S. Chen, *Bioresource Technology*, 2012, **104**, 737–742.

(205) N. Sönnichsen, *UK: Wholesale Price Projection of Crude Oil 2020-2040*, Statista, 2021, `https://www.statista.com/statistics/496324/crude-oil-prices-projection-uk/` (visited on 03/29/2021).

(206) Department for Business, Energy & Industrial Strategy, *Annex M: Growth Assumptions and Prices*, Updated energy and emissions projections: 2018, 2019, `https://www.gov.uk/government/publications/updated-energy-and-emissions-projections-2018` (visited on 03/29/2021).

(207) Agriculture and Rural Delivery Directorate, *Scottish Agriculture Tables - Economic Report: 2020 Edition*, 2020, `https://www.gov.scot/publications/`

economic-report-on-scottish-agriculture-tables-2020-edition/ (visited on 03/29/2021).

(208) Y. Zhu, A. Schmidt, P. Valdez, L. Snowden-Swan and S. Edmundson, *Hydrothermal Liquefaction and Upgrading of Wastewater-Grown Microalgae: 2021 State of Technology*, PNNL-32695, 1855835, 2022, PNNL–32695, 1855835.

(209) K. Kallupalayam Ramasamy, M. Thorson, J. Billing, J. Holladay, C. Drennan, B. Hoffman and Z. Haq, *Hydrothermal Liquefaction: Path to Sustainable Aviation Fuel*, PNNL-31930, 1821809, 2021, PNNL–31930, 1821809.

(210) M. Asgher, S. A. Qamar, M. Bilal and H. M. N. Iqbal, *Food Research International (Ottawa, Ont.)*, 2020, **137**, 109625.

(211) a. M.
bibinitperiod C. World Economic Forum, Ellen Macarthur Foundation, *The New Plastics Economy - Rethinking the Future of Plastics*, Ellen Macarthur Foundation, 2016.

(212) M. Haward, *Nature Communications*, 2018, **9**, 667.

(213) J.-W. Rhim, *Journal of Food Science*, 2011, **76**, N68–N72.

(214) J. P. Reddy and J.-W. Rhim, *Carbohydrate Polymers*, 2014, **110**, 480–488.

(215) M. Atef, M. Rezaei and R. Behrooz, *International Journal of Biological Macromolecules*, 2014, **70**, 537–544.

(216) D. Phan The, F. Debeaufort, A. Voilley and D. Luu, *Journal of Food Engineering*, 2009, **90**, 548–558.

(217) M. G. A. Vieira, M. A. da Silva, L. O. dos Santos and M. M. Beppu, *European Polymer Journal*, 2011, **47**, 254–263.

(218) A. M. Sousa, H. K. Souza, L. Liu and M. P. Gonçalves, *International Journal of Biological Macromolecules*, 2015, **76**, 138–145.

(219) K. Liu, X. Lin, L. Chen, L. Huang and S. Cao, *Cellulose*, 2014, **21**, 519–528.

(220) N. V. S. N. M. Konda, S. Singh, B. A. Simmons and D. Klein-Marcuschamer, *BioEnergy Research*, 2015, **8**, 1046–1056.

(221) M. Soleymani and K. A. Rosentrater, *Bioengineering*, 2017, **4**, 92.

(222) B. Brigljević, P. Fasahati and J. Jay Liu, in *Computer Aided Chemical Engineering*, ed. M. R. Eden, M. G. Ierapetritou and G. P. Towler, Elsevier, 2018, vol. 44, pp. 337–342.

(223) T. Y. Chong, S. A. Cheah, C. T. Ong, L. Y. Wong, C. R. Goh, I. S. Tan, H. C. Y. Foo, M. K. Lam and S. Lim, *Energy*, 2020, **210**, 118491.

(224) B. Brigljevic and J. Liu, 2017 6th International Symposium on Advanced Control of Industrial Processes (AdCONIP), 2017 6th International Symposium on Advanced Control of Industrial Processes (AdCONIP), 2017, pp. 493–498.

(225) K. H. Wong, I. S. Tan, H. C. Y. Foo, L. M. Chin, J. R. N. Cheah, J. K. Sia, K. T. X. Tong and M. K. Lam, *Energy Conversion and Management*, 2022, **253**, 115155.

(226) *Production and Utilization of Products from Commercial Seaweeds*, ed. D. J. McHugh, Food and Agriculture Organization of the United Nations, Rome, 1987, 189 pp.

(227) M. A. da Silva, A. C. K. Bierhalz and T. G. Kieckbusch, *Carbohydrate Polymers*, 2009, **77**, 736–742.

(228) U. Siemann, in *Scattering Methods and the Properties of Polymer Materials*, Springer Berlin Heidelberg, Berlin, Heidelberg, 2005, pp. 1–14.

(229) J. I. Morán, V. A. Alvarez, V. P. Cyras and A. Vázquez, *Cellulose*, 2008, **15**, 149–159.

(230) Q. Chen, Y. Shi, G. Chen and M. Cai, *International Journal of Biological Macromolecules*, 2020, **142**, 846–854.

(231) T. Abitbol, D. Kam, Y. Levi-Kalisman, D. G. Gray and O. Shoseyov, *Langmuir*, 2018, **34**, 3925–3933.

(232) M. R. Tabassum, A. Xia and J. D. Murphy, *Energy*, 2017, **140**, 546–551.

(233) A. J. O'Neil, R. D. Jee and A. C. Moffat, *Analyst*, 1999, **124**, 33–36.

(234) M. J. Kabir, A. A. Chowdhury and M. G. Rasul, *Energies*, 2015, **8**, 7522–7541.

(235) X. Xianjun, S. Zongkang, M. Peiyong, Y. jin and W. zhaobin, *Energy Procedia*, 2015, **66**, 293–296.

(236) D. E. Daugaard and R. C. Brown, *Energy & Fuels*, 2003, **17**, 934–939.

(237) J. C.-C. Chan, P. C.-K. Cheung and P. O. Ang, *Journal of Agricultural and Food Chemistry*, 1997, **45**, 3056–3059.

(238) M. León, J. Silva, S. Carrasco and N. Barrientos, *Processes*, 2020, **8**, 945.

(239) L. Zhongchuang Xingyuan Chemical Technology Co., *Bamboo Biochar Fertilizer, Organic Fertilizer, Bio Fertilizer*, Alibaba, 2022, `https://www.alibaba.com/product-detail/Bamboo-Biochar-Fertilizer-Organic-fertilizer-Bio_60767471467.html` (visited on 08/15/2022).

(240) U. D. of Agriculture, *FoodData Central: Seaweed, Kelp, Raw (FDC ID: 168457)*, FoodData Central, 2019, `https://fdc.nal.usda.gov/fdc-app.html#/food-details/168457/measures` (visited on 08/15/2022).

(241) U. D. of Agriculture, *FoodData Central: Seaweed, Dried (FDC ID: 1103574)*, FoodData Central, 2020, `https://fdc.nal.usda.gov/fdc-app.html#/food-details/1103574/portions` (visited on 08/15/2022).

(242) S. Wang, X. M. Jiang, Q. Wang, H. S. Ji, L. F. Wu, J. F. Wang and S. N. Xu, *Journal of Thermal Analysis and Calorimetry*, 2014, **115**, 2071–2077.

(243) J. H. Choi, S.-S. Kim, D. J. Suh, E.-J. Jang, K.-I. Min and H. C. Woo, *Korean J. Chem. Eng.*, 2016, **33**, 8.

(244) M. Gupta, J. Yang and C. Roy, *Fuel*, 2003, **82**, 919–927.

(245) C. Dupont, R. Chiriac, G. Gauthier and F. Toche, *Fuel*, 2014, **115**, 644–651.

(246) A. K. James, R. W. Thring, S. Helle and H. S. Ghuman, *Energies*, 2012, **5**, 3856–3873.

(247) M.-M. Alhadj-Mallah, Q. Huang, X. Cai, Y. Chi and J. Yan, *Environmental Technology*, 2015, **36**, 654–660.

(248) F. Bagheri, M. Radi and S. Amiri, *Food Hydrocolloids*, 2019, **90**, 162–171.

(249) C. Goldsbury, *Corbion and Total to Build First World-Scale PLA Plant in Europe*, plasticstoday.com, 2020, `https://www.plasticstoday.com/biopolymers/corbion-and-total-build-first-world-scale-pla-plant-europe` (visited on 08/18/2022).

(250) A. Scott, *C&EN Global Enterprise*, 2019, **97**, 15–15.

(251) A. Tullo, *PHA: A Biopolymer Whose Time Has Finally Come*, Chemical & Engineering News, 2019, https://cen.acs.org/business/biobased-chemicals/PHA-biopolymer-whose-time-finally/97/i35 (visited on 08/18/2022).

(252) ECHEMI, *120,000 Tons Per Year of PBAT Project in Xinjiang Will Be Built Soon - ECHEMI.Com*, ECHEMI, 2022, https://www.echemi.com/cms/531059.html (visited on 08/18/2022).

(253) D. D. Guzman, *Sulzer to Build 10KTY PLA Plant in Asia*, Green Chemicals Blog, 2013, https://greenchemicalsblog.com/2013/04/30/sulzer-to-build-10kty-pla-plant-in-asia/ (visited on 08/18/2022).

(254) L. Hebei Yaoluo Trade Co., *Factory Direct Pvc Recycle Material Recycled Pvc Granule Scrap Regind Material - Buy Rubber/Plastic Raw Materials,Polyvinyl Chloride Pvc,Pvc Resin White Granules Product on Alibaba.Com*, 2022, https://www.alibaba.com/product-detail/Factory-Direct-PVC-Recycle-Material-Recycled_1600256939662.html (visited on 08/18/2022).

(255) L. Hebei Xiongye Machine Trade Co., *Recycle Pp /Virgin Polypropylene Homopolymer For Injection Grade,Polypropylene/ Recycled Plastic Pp - Buy Recycle Pp /Virgin Polypropylene Homopolymer For Injection Grade Polypropylene/ Recycled Plastic Pp,Recycle Pp /Virgin Polypropylene Homopolymer For Injection Grade Polypropylene/ Recycled Plastic Pp,Recycle Pp /Virgin Polypropylene Homopolymer For Injection Grade Polypropylene/ Recycled Plastic Pp Product on Alibaba.Com*, 2022, https://www.alibaba.com/product-detail/Recycle-PP-virgin-polypropylene-homopolymer-for_60254178176.html (visited on 08/18/2022).

(256) L. Shanghai Hengsi New Material Science&technology Co., *Recycled Natureworks Ingeo Plastic Pla Resin Pellets Supplier From China - Buy Natureworks Ingeo Plastic Pla Resin Pellets,Pps Recycled Plastic Pellets Price,Plastic Price Recycled Abs Plastic Granules Product on Alibaba.Com*, 2022, https://www.alibaba.com/product-detail/Recycled-Natureworks-Ingeo-Plastic-Pla-Resin_60832177777.html (visited on 08/18/2022).

(257) T. A. LLC, *Export Supply Price Plastic Biopolymer Polylactic Acid Resin Price - Buy Raw Material In Plastic Industry,Polylactic Acid Resin,Bulk Plastic Resin Product on Alibaba.Com*, 2022, https://www.alibaba.com/product-detail/Export-Supply-price-plastic-biopolymer-polylactic_1700006540439.html (visited on 08/18/2022).

(258) L. Shanghai Huiang Industrial Co., *Wholesale Compostable Pbat Biodegradable Pellets - Buy Biodegradable Plastic Bag Raw Material,Pbat Biodegradable Pellets,Compostable Pbat Biodegradable Pellets Product on Alibaba.Com*, 2022, https://www.alibaba.com/product-detail/Wholesale-Compostable-PBAT-Biodegradable-Pellets_60730471730.html (visited on 08/18/2022).

(259) L. Julier (xiamen) Technology Co., *High Quality Polylactic Acid Biodegradable Best Seller Pla Pellets - Buy Pla Compostable Plastic Granules,Plastic Raw Material Pla,Pla For 3d Filament Extrusion Product on Alibaba.Com*, 2022, https://www.alibaba.com/product-detail/High-Quality-Polylactic-acid-biodegradable-Best_1600202156907.html (visited on 08/18/2022).

(260) L. Hebei Luoxing Tech Co., *100% Biodegradable Modified Resin Pha Polyhydroxyalkanoate Pha Resin Price - Buy Polyhydroxyalkanoate Pha Resin Price,Resin Pha,100% Biodegradable Modified Resin Pha Product on Alibaba.Com*, 2022, https://www.alibaba.com/product-detail/100-biodegradable-modified-resin-pha-polyhydroxyalkanoate_1600433580977.html (visited on 08/18/2022).

(261) L. Handan Feisite Technology Co., *Pbat/Pla/Pbs/Pva Raw Material Cornstarch Biodegradable Compound - Buy Degradable Plastics,Hotselling Chinese Factory,Fully Degradable Plastics Industry Product on Alibaba.Com*, 2022, https://www.alibaba.com/product-detail/PBAT-PLA-PBS-PVA-raw-material_1600566543507.html (visited on 08/18/2022).

(262) T. A. LLC, *Usa Supplier Ethylene-vinyl Acetate Copolymer Eva Resin - Buy Abs Plastic Raw Material,Eva Resin,Ethylene-vinyl Acetate Supply Usa Product on Alibaba.Com*, 2022, https://www.alibaba.com/product-detail/USA-SUPPLIER-Ethylene-vinyl-acetate-copolymer_1600332707575.html (visited on 08/18/2022).

(263) L. Xiamen Keyuan Plastic Co., *Thermoplastic Polyurethane !Tpu Recycling Granules For Converse All Star Shoes - Buy Thermoplastic Polyurethane,Tpu Recycling Granules,Tpu Granules For Converse All Star Shoes Product on Alibaba.Com*, 2022, https://www.alibaba.com/product-detail/thermoplastic-polyurethane-tpu-recycling-granules-for_60642337401.html (visited on 08/18/2022).

(264) M. Sterner, M. S. Ribeiro, F. Gröndahl and U. Edlund, *Journal of Applied Phycology*, 2017, **29**, 3175–3189.

(265) M. Sterner, *J Appl Phycol*, 2016, 14.

(266) N. Wahlström, H. Harrysson, I. Undeland and U. Edlund, *Industrial & Engineering Chemistry Research*, 2018, **57**, 42–53.

(267) X. Gui, M. Rui, Y. Song, Y. Ma, Y. Rui, P. Zhang, X. He, Y. Li, Z. Zhang and L. Liu, *Environmental Science and Pollution Research*, 2017, **24**, 13775–13781.

(268) S. Munir, S. S. Daood, W. Nimmo, A. M. Cunliffe and B. M. Gibbs, *Bioresource Technology*, 2009, **100**, 1413–1418.

(269) D. R. Paul, in *Encyclopedia of Membranes*, ed. E. Drioli and L. Giorno, Springer, Berlin, Heidelberg, 2016, pp. 1902–1904.

(270) S. W. Rutherford and D. D. Do, *Adsorption*, 1997, **3**, 283–312.

(271) Y. Yampolskii, in *Advanced Membrane Science and Technology for Sustainable Energy and Environmental Applications*, ed. A. Basile and S. P. Nunes, Woodhead Publishing, 2011, pp. 22–55.

(272) A. E96/E96M-10, *Standard Test Methods for Water Vapor Transmission of Materials*, ASTM International, West Conshohocken, PA, 2010.

(273) J. Miao, Y. Yu, Z. Jiang and L. Zhang, *Cellulose*, 2016, **23**, 1209–1219.

(274) J. Massaya, K. H. Chan, B. Mills-Lamptey and C. J. Chuck, *Biomass Conversion and Biorefinery*, 2021, DOI: 10.1007/s13399-020-01231-w.

(275) A. Cross and S. P. Sohi, *GCB Bioenergy*, 2013, **5**, 215–220.

(276) K. Crombie, O. Mašek, S. P. Sohi, P. Brownsort and A. Cross, *GCB Bioenergy*, 2013, **5**, 122–131.

(277) D. A. Roberts and R. de Nys, *Journal of Environmental Management*, 2016, **169**, 253–260.

(278) Y. Luo, J. Liang, G. Zeng, M. Chen, D. Mo, G. Li and D. Zhang, *Waste Management*, 2018, **71**, 109–114.

(279) J. Aburto, S. Thiébaud, I. Alric, E. Borredon, D. Bikiaris, J. Prinos and C. Panayiotou, 1997, DOI: 10.1016/S0144-8617(97)00053-2.

(280) J. Aburto, H. Hamaili, G. Mouysset-Baziard, F. Senocq, I. Alric and E. Borredon, *Starch - Stärke*, 1999, **51**, 302–307.

(281) S. Thiébaud, J. Aburto, I. Alric, E. Borredon, D. Bikiaris, J. Prinos and C. Panayiotou, 1997, DOI: 10.1002/(SICI)1097-4628(19970725)65:4<705::AID-APP9>3.0.CO;2-O.

(282) M. I. Ltd, *A Basic Introduction to Rheology*, Whitepaper, Malvern Instruments Ltd, Worcestershire, 2016.

(283) J. Vlachopoulos and D. Strutt, in *Multilayer Flexible Packaging*, ed. J. R. Wagner, William Andrew Publishing, Boston, 2010, pp. 57–72.

(284) Y. Yang, M. Zhang, A. I. Alalawy, F. M. Almutairi, M. A. Al-Duais, J. Wang and E.-S. Salama, *Environmental Technology & Innovation*, 2021, **24**, 101848.

(285) C. Zhang, L. Zhang, J. Gao, S. Zhang, Q. Liu, P. Duan and X. Hu, *Algal Research*, 2020, **48**, 101900.

(286) P. Thiviya, A. Gamage, N. S. Gama-Arachchige, O. Merah and T. Madhujith, *Phycology*, 2022, **2**, 216–243.

(287) D. Lopes, T. Melo, F. Rey, J. Meneses, F. L. Monteiro, L. A. Helguero, M. H. Abreu, A. I. Lillebø, R. Calado and M. R. Domingues, *Molecules*, 2020, **25**, 3883.

(288) J. Andrade, C. G. Pereira, J. C. de Almeida Junior, C. C. R. Viana, L. N. d. O. Neves, P. H. F. da Silva, M. J. V. Bell and V. d. C. dos Anjos, *LWT*, 2019, **99**, 166–172.

(289) Helmiyati and M. Aprilliza, *IOP Conference Series: Materials Science and Engineering*, 2017, **188**, 012019.

(290) R. Qari and S. Haider, *Biological Sciences - PJSIR*, 2021, **64**, 263–273.

(291) E. A. El-Hefian, M. M. Nasef, A. H. Yahaya and R. A. Khan, *Journal of the Chilean Chemical Society*, 2010, **55**, 130–136.

(292) L. M. L. Laurens and E. J. Wolfrum, *BioEnergy Research*, 2011, **4**, 22–35.

(293) N. N. Mahamuni and Y. G. Adewuyi, *Energy & Fuels*, 2009, **23**, 3773–3782.

(294) N. Nunes, G. P. Rosa, S. Ferraz, M. C. Barreto and M. A. A. P. de Carvalho, *Journal of Applied Phycology*, 2020, **32**, 759–771.

(295) *Environmental Inquiry - Lettuce Seed Bioassays*, Cornell University and Penn State University, 2009, `http://ei.cornell.edu/toxicology/bioassays/lettuce/data.html` (visited on 09/16/2022).

(296) T. D. Phan, F. Debeaufort, D. Luu and A. Voilley, *Journal of Agricultural and Food Chemistry*, 2005, **53**, 973–981.

(297) S. Bhat, A. Tripathi and A. Kumar, *Journal of The Royal Society Interface*, 2011, **8**, 540–554.

(298) Z. K. Genc, C. A. Canbay, S. S. Acar, M. Sekerci and M. Genc, *Journal of Thermal Analysis and Calorimetry*, 2015, **120**, 1679–1688.

(299) M. Heidari, S. Salaudeen, A. Dutta and B. Acharya, *Energy & Fuels*, 2018, **32**, 11576–11586.

(300) H. Doh and W. S. Whiteside, *POLYMER CRYSTALLIZATION*, 2020, **3**, e10133.

(301) C. Gao, E. Pollet and L. Avérous, *Food Hydrocolloids*, 2017, **63**, 414–420.

(302) P. Singh, P. Baisthakur and O. S. Yemul, *Heliyon*, 2020, **6**, e03026.

(303) X. Hou, Z. Xue, Y. Xia, Y. Qin, G. Zhang, H. Liu and K. Li, *International Journal of Biological Macromolecules*, 2019, **125**, 1289–1298.

(304) L. C. Paixão, I. A. Lopes, A. K. D. Barros Filho and A. A. Santana, *Journal of Applied Polymer Science*, 2019, **136**, 48263.

(305) G. Tedeschi, J. J. Benitez, L. Ceseracciu, K. Dastmalchi, B. Itin, R. E. Stark, A. Heredia, A. Athanassiou and J. A. Heredia-Guerrero, *ACS Sustainable Chemistry & Engineering*, 2018, **6**, 14955–14966.

(306) B. Samakar, Z. Gholami, Z. sadat Tabatabaei, A. Abrishami and A. Akhgari, *International Pharmacy Acta*, 2018, **1**, 14–15.

(307) C. Gutiérrez-Jara, C. Bilbao-Sainz, T. McHugh, B.-s. Chiou, T. Williams and R. Villalobos-Carvajal, *Food Hydrocolloids*, 2020, **109**, 106133.

(308) Y. Zhang, Q. Ma, F. Critzer, P. M. Davidson and Q. Zhong, *LWT - Food Science and Technology*, 2015, **64**, 423–430.

(309) R. Armisen and F. Galatas, in *Production and Utilization of Products from Commercial Seaweeds*, FOOD AND AGRICULTURE ORGANIZATION OF THE UNITED NATIONS, Rome, 1987.

(310) K. Matyjaszewski and M. Möller, *Polymers in Biology and Medicine*, Elsevier, Amsterdam, 2012, vol. 9 Polymers in Biology and Medicine.

(311) C. M. Ionescu, I. R. Birs, D. Copot, C. I. Muresan and R. Caponetto, *Philosophical Transactions of the Royal Society A: Mathematical, Physical and Engineering Sciences*, 2020, **378**, 20190284.

(312) R. N. Jana and G. B. Nando, *Journal of Elastomers & Plastics*, 2005, **37**, 149–168.

(313) M. N. Khalaf, *Journal of King Saud University - Science*, 2014, **26**, 190–199.

(314) T. A. Saki, *Arabian Journal of Chemistry*, 2015, **8**, 191–199.

(315) S. Salhofer, A. Jandric, S. Soudachanh, T. Le Xuan and T. D. Tran, *International Journal of Environmental Research and Public Health*, 2021, **18**, 4203.

(316) D. Meeks, T. Hottle, M. M. Bilec and A. E. Landis, *Resources, Conservation and Recycling*, 2015, **105**, 134–142.

(317) M. Rujnić Havstad, L. Juroš, Z. Katančić and A. Pilipović, *Polymers*, 2021, **13**, 2785.

(318) C. Aversa and M. Barletta, *Chinese Journal of Polymer Science*, 2022, DOI: 10.1007/s10118-022-2734-0.

(319) S. Kakadellis, J. Woods and Z. M. Harris, *Resources, Conservation and Recycling*, 2021, **169**, 105529.

(320) M. C. Council, *Food Waste FAQs*, Monmouthshire, 2020, https://www.monmouthshire.gov.uk/recycling-and-waste/food-waste-faqs/ (visited on 09/28/2022).

(321) T. Aspray and D. Tompkins, *Plastic in Food Waste at Compost Sites*, Scottish Environmental Protection Agency, 2019, p. 62.

(322) E. Epstein, *The Science of Composting*, CRC Press, 2017, 504 pp.

(323) Y. Li, C. P. Alaimo, M. Kim, N. Y. Kado, J. Peppers, J. Xue, C. Wan, P. G. Green, R. Zhang, B. M. Jenkins, C. F. A. Vogel, S. Wuertz, T. M. Young and M. J. Kleeman, *Environmental science & technology*, 2019, **53**, 11569–11579.

(324) A. Khalid, M. Arshad, M. Anjum, T. Mahmood and L. Dawson, *Waste Management*, 2011, **31**, 1737–1744.

(325) P. Wilman, *Bath Weather: Historic Data*, Bath Weather, 2022, `https://www.paulwilman.com/weather_data1.php` (visited on 09/22/2022).

(326) I. Angelidaki, M. Alves, D. Bolzonella, L. Borzacconi, J. L. Campos, A. J. Guwy, S. Kalyuzhnyi, P. Jenicek and J. B. van Lier, *Water Science and Technology*, 2009, **59**, 927–934.

(327) C. Holliger, M. Alves, D. Andrade, I. Angelidaki, S. Astals, U. Baier, C. Bougrier, P. Buffière, M. Carballa, V. de Wilde, F. Ebertseder, B. Fernández, E. Ficara, I. Fotidis, J.-C. Frigon, H. F. de Laclos, D. S. M. Ghasimi, G. Hack, M. Hartel, J. Heerenklage, I. S. Horvath, P. Jenicek, K. Koch, J. Krautwald, J. Lizasoain, J. Liu, L. Mosberger, M. Nistor, H. Oechsner, J. V. Oliveira, M. Paterson, A. Pauss, S. Pommier, I. Porqueddu, F. Raposo, T. Ribeiro, F. Rüsch Pfund, S. Strömberg, M. Torrijos, M. van Eekert, J. van Lier, H. Wedwitschka and I. Wierinck, *Water Science and Technology*, 2016, **74**, 2515–2522.

(328) A. Shrestha, M. C. A. A. van-Eerten Jansen and B. Acharya, *Sustainability*, 2020, **12**, 4231.

(329) T. Sokač, D. Valinger, M. Benković, T. Jurina, J. Gajdoš Kljusurić, I. Radojčić Redovniković and A. Jurinjak Tušek, *Processes*, 2022, **10**, 229.

(330) E. Madejón, M. Panettieri, P. Madejón and A. Pérez-de-Mora, *Waste and Biomass Valorization*, 2022, **13**, 863–875.

(331) Y. Lyu, R. Xu, O. Williams, Z. Wang and C. Sievers, *Journal of Catalysis*, 2021, **404**, 334–347.

(332) C. Hita, E. Parlanti, P. Jambu, J. Joffre and A. Amblès, *Organic Geochemistry*, 1996, **25**, 19–28.

(333) J. Massaya, Alternative Format Thesis, University of Bath, Bath, 2022, 234 pp.

(334) H. Harrysson, M. Hayes, F. Eimer, N.-G. Carlsson, G. B. Toth and I. Undeland, *Journal of Applied Phycology*, 2018, **30**, 3565–3580.

Supporting Information

Example code and input files

A publicly accessible git repository containing python models, analysis scripts, and example input files is available in the public git repository linked by the following URL:

`https://github.bath.ac.uk/ej220/Thesis_2022`

Figure SI1: QR code of URL directing to public git repository of on-line supplementary information

Ethics

Research will be approached within agreement with the universities Concordat to Support Research Integrity. All work will be recorded primarily in written lab-books, and digitised for archival on the research group directory on the university X: drive, in accordance with the data management plan. Wherever possible we will endeavour to make all research data freely available with any publication, however this must be done with consideration for, and in consultation with, our external partners who assist with materials and funding in completing the research. To that end, all research data collected primarily, or re-used from previous work by either myself or by other researchers, will be clearly identified as such, cited as required, and where data is primary source full methods will be issued with any publication as a minimum in the supporting information.

In accordance with the primary funding body (Engineering and Physical Sciences Research Council - EPSRC), the "RCUK Policy and Guidelines on Governance of Good Research Conduct" (April 2017) guide as provided by UK Research and Innovation (UKRI) will be used as a framework to assess and manage any ethical issues that arise during research. At this time it is not thought that full ethical approval will be required. However, at any stage, any further clarification will be sought via the Chemical Engineering Dept. Research Ethics Officer, Dr Benedek Plosz.

References consulted in consideration of project research ethics (accessed 16-Oct-2019):

`https://epsrc.ukri.org/funding/applicationprocess/basics/goodpractice/`

`https://www.ukri.org/about-us/policies-and-standards/research-integrity/`

Appendix

A0.1 Supplementary Figures

A0.1.1 IR Spectra

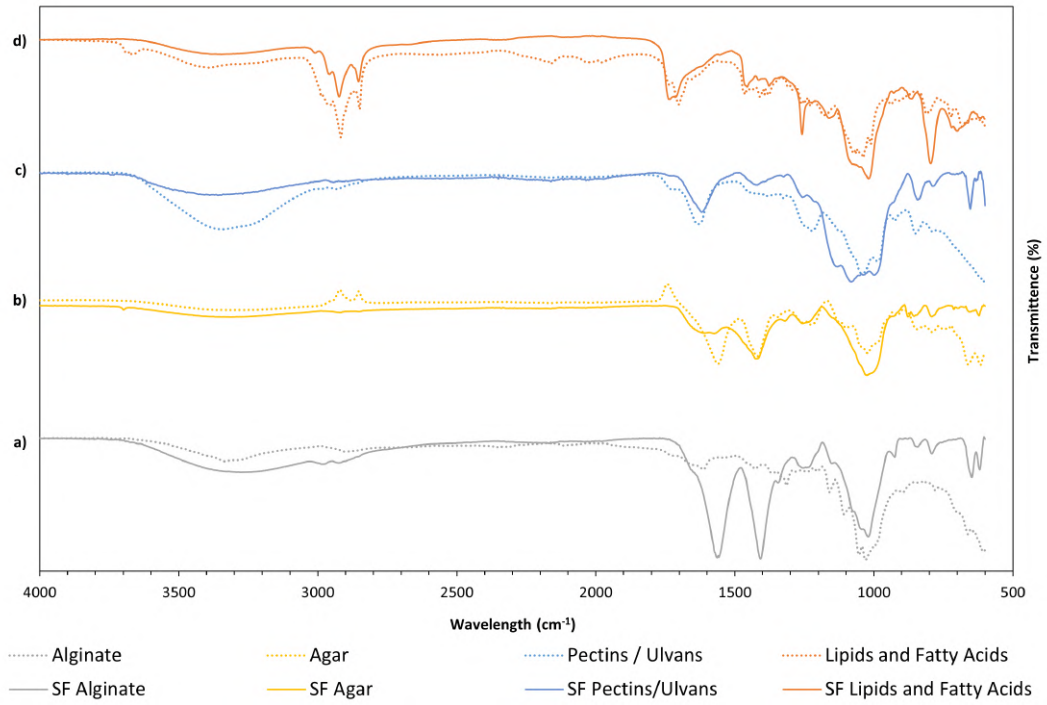

Figure A1: FT-IR spectra of different extract fractions of *Ulva lactuca* (UL), extracts are **a)** alginate rich fraction producued with trisodium citrate extraction, **b)** agar / carrageenan fraction produced with the hot-water extraction, **c)** ulvan/pectin fraction produced with the mild-acid digest, and finally **d)** lipid / fatty-acid fraction produced with the toluene:ethanol extraction. Solid lines are spectra for extracts produced in the cascading multi-fractionation approach, and dotted lines are spectra for extracts produced from the single fractionation approach.

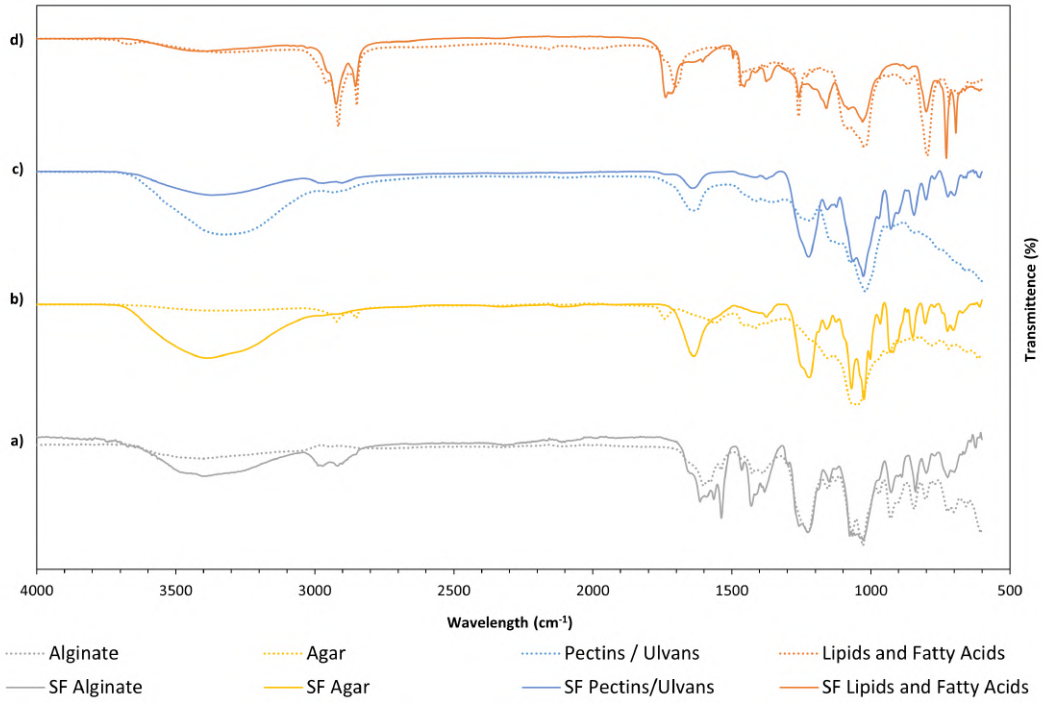

Figure A2: FT-IR spectra of different extract fractions of *Spinosum sp.* (SP), extracts are **a)** alginate rich fraction producued with trisodium citrate extraction, **b)** agar / carrageenan fraction produced with the hot-water extraction, **c)** ulvan/pectin fraction produced with the mild-acid digest, and finally **d)** lipid / fatty-acid fraction produced with the toluene:ethanol extraction. Solid lines are spectra for extracts produced in the cascading multi-fractionation approach, and dotted lines are spectra for extracts produced from the single fractionation approach.

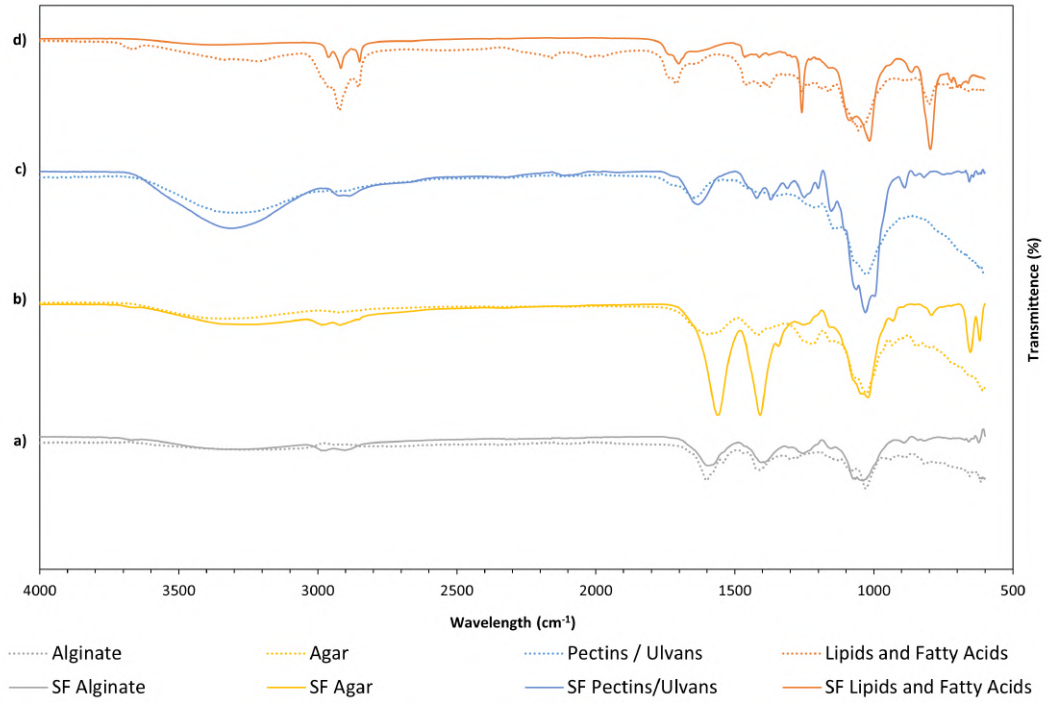

Figure A3: FT-IR spectra of different extract fractions of *Saccharina latissima* (SL), extracts are **a)** alginate rich fraction producued with trisodium citrate extraction, **b)** agar / carrageenan fraction produced with the hot-water extraction, **c)** ulvan/pectin fraction produced with the mild-acid digest, and finally **d)** lipid / fatty-acid fraction produced with the toluene:ethanol extraction. Solid lines are spectra for extracts produced in the cascading multi-fractionation approach, and dotted lines are spectra for extracts produced from the single fractionation approach.

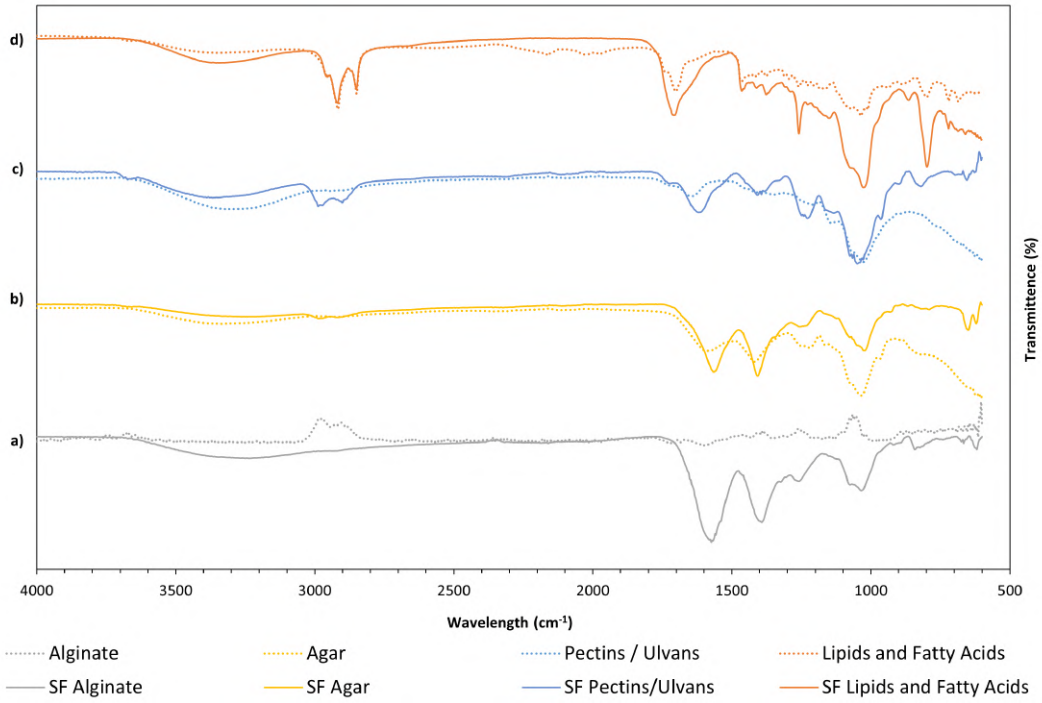

Figure A4: FT-IR spectra of different extract fractions of *Sargassum sp.* (SG), extracts are **a)** alginate rich fraction producued with trisodium citrate extraction, **b)** agar / carrageenan fraction produced with the hot-water extraction, **c)** ulvan/pectin fraction produced with the mild-acid digest, and finally **d)** lipid / fatty-acid fraction produced with the toluene:ethanol extraction. Solid lines are spectra for extracts produced in the cascading multi-fractionation approach, and dotted lines are spectra for extracts produced from the single fractionation approach.

A0.1.2 Rheograms

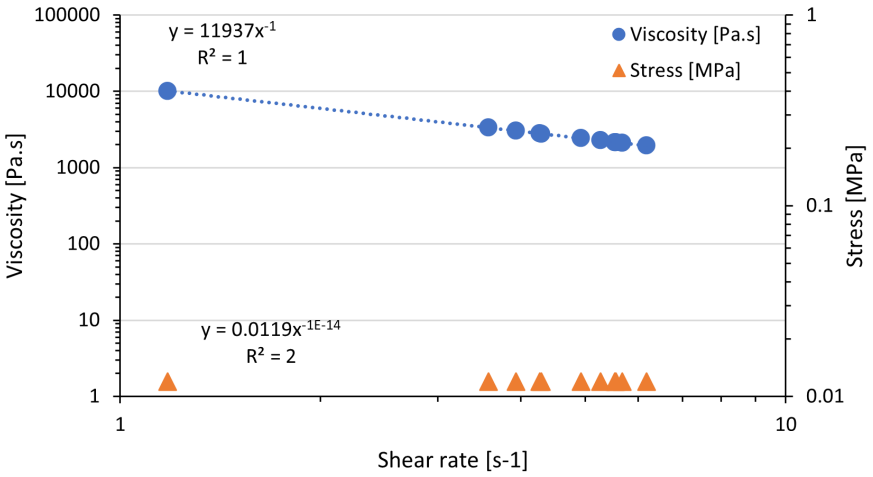

Figure A5: Flow-sweep rheogram of viscosity (η, Pa.s) and shear-stress (σ, MPa) plotted against shear rate (γ, s^{-1}) for the C16 functionalised biological grade agar 140 °C.

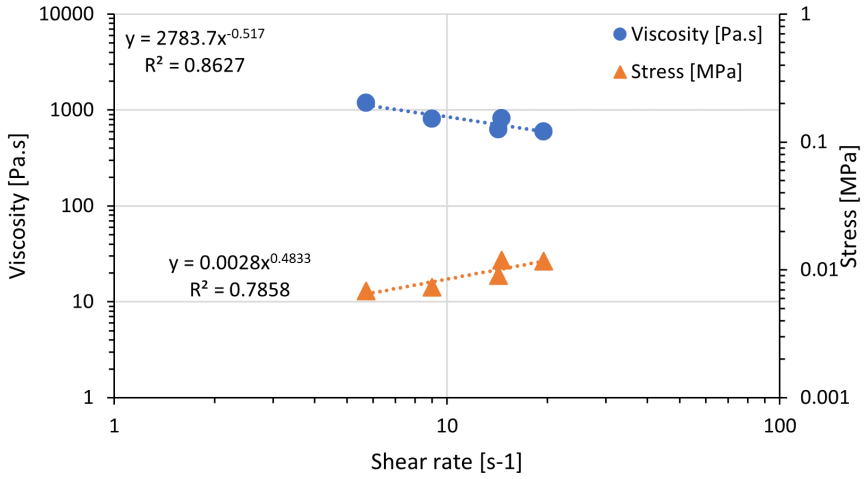

Figure A6: Flow-sweep rheogram of viscosity (η, Pa.s) and shear-stress (σ, MPa) plotted against shear rate (γ, s^{-1}) for the C16 functionalised biological grade agar 150 °C.

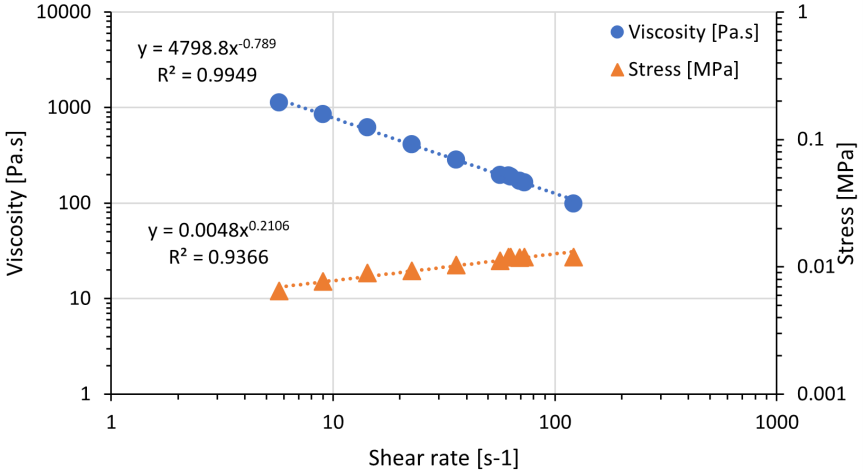

Figure A7: Flow-sweep rheogram of viscosity (η, Pa.s) and shear-stress (σ, MPa) plotted against shear rate (γ, s^{-1}) for the C16 functionalised biological grade agar 155 °C.

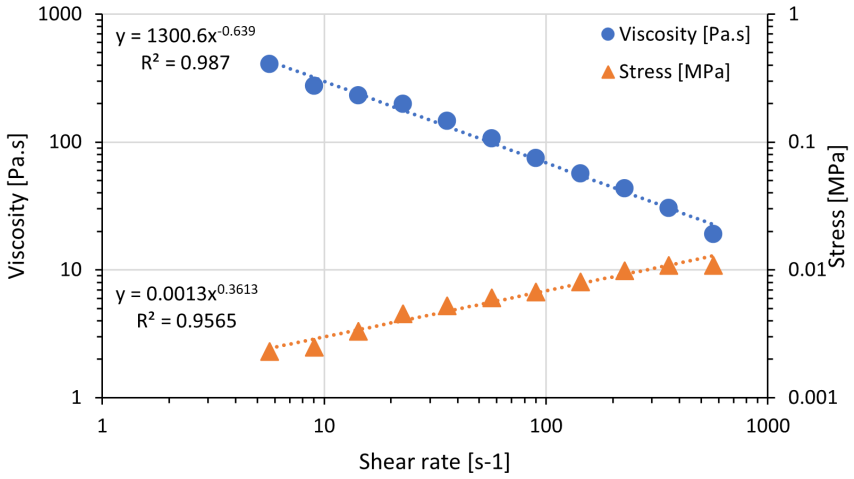

Figure A8: Flow-sweep rheogram of viscosity (η, Pa.s) and shear-stress (σ, MPa) plotted against shear rate (γ, s^{-1}) for the C16 functionalised biological grade agar 160 °C.

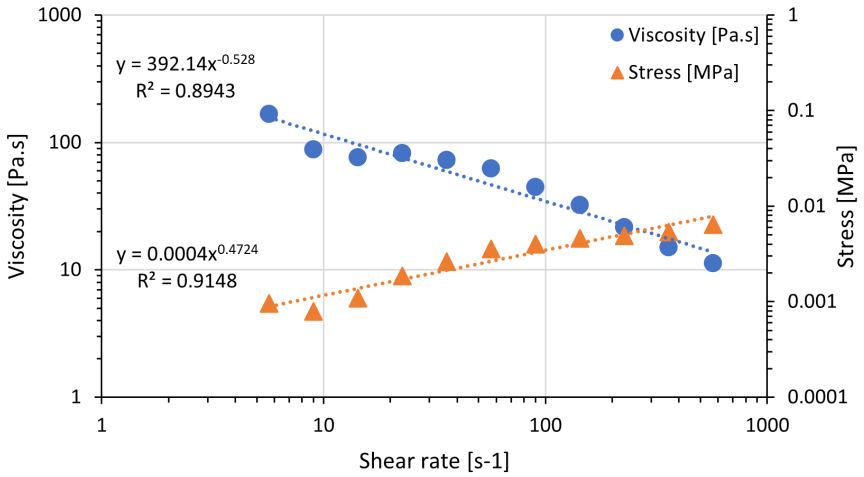

Figure A9: Flow-sweep rheogram of viscosity (η, Pa.s) and shear-stress (σ, MPa) plotted against shear rate (γ, s^{-1}) for the C16 functionalised biological grade agar 165 °C.

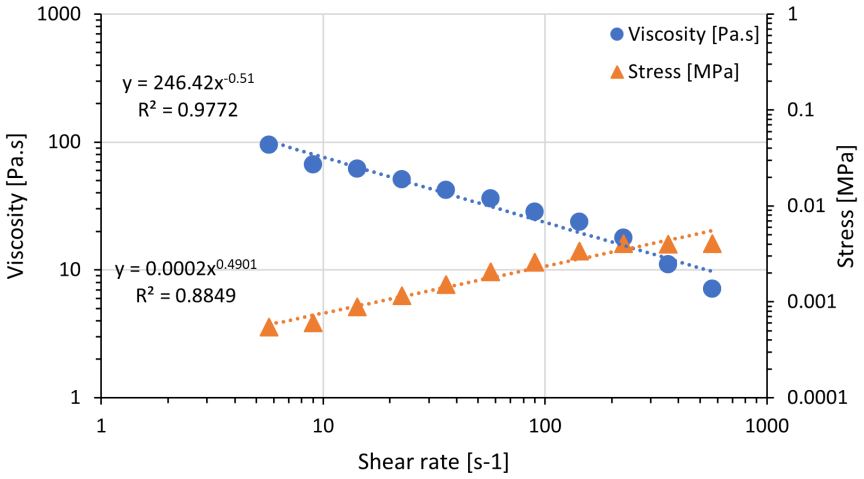

Figure A10: Flow-sweep rheogram of viscosity (η, Pa.s) and shear-stress (σ, MPa) plotted against shear rate (γ, s^{-1}) for the C16 functionalised biological grade agar 170 °C.

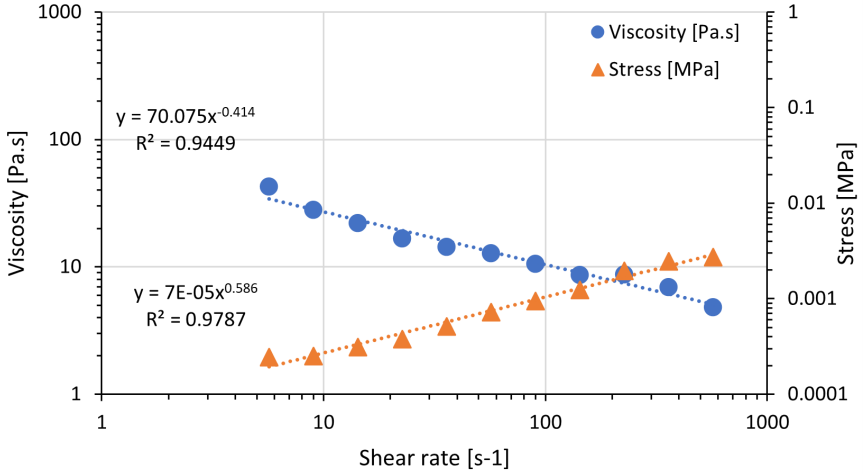

Figure A11: Flow-sweep rheogram of viscosity (η, Pa.s) and shear-stress (σ, MPa) plotted against shear rate (γ, s^{-1}) for the C16 functionalised biological grade agar 175 °C.

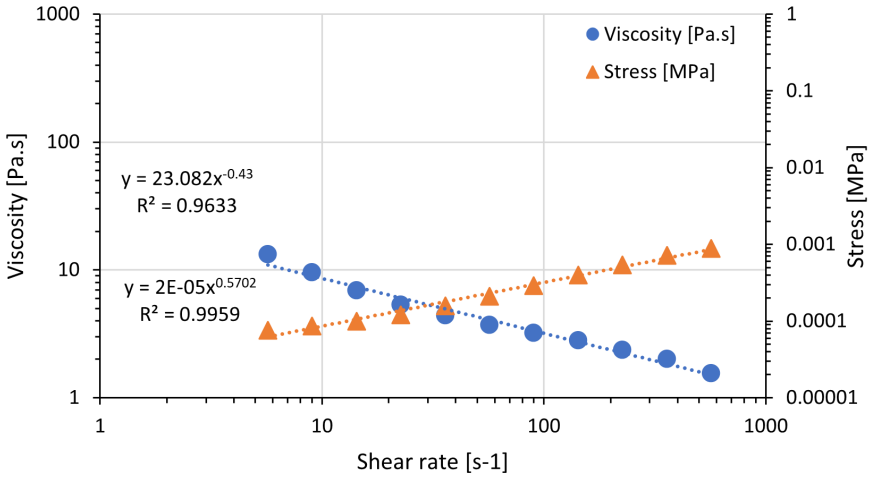

Figure A12: Flow-sweep rheogram of viscosity (η, Pa.s) and shear-stress (σ, MPa) plotted against shear rate (γ, s^{-1}) for the C16 functionalised biological grade agar 180 °C.

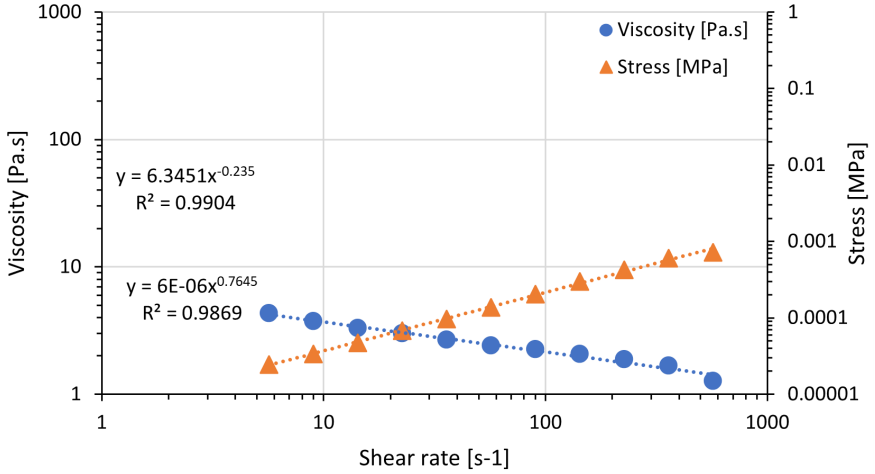

Figure A13: Flow-sweep rheogram of viscosity (η, Pa.s) and shear-stress (σ, MPa) plotted against shear rate (γ, s^{-1}) for the C16 functionalised biological grade agar 175 °C after descending in temperature from having been worked at 180 °C.

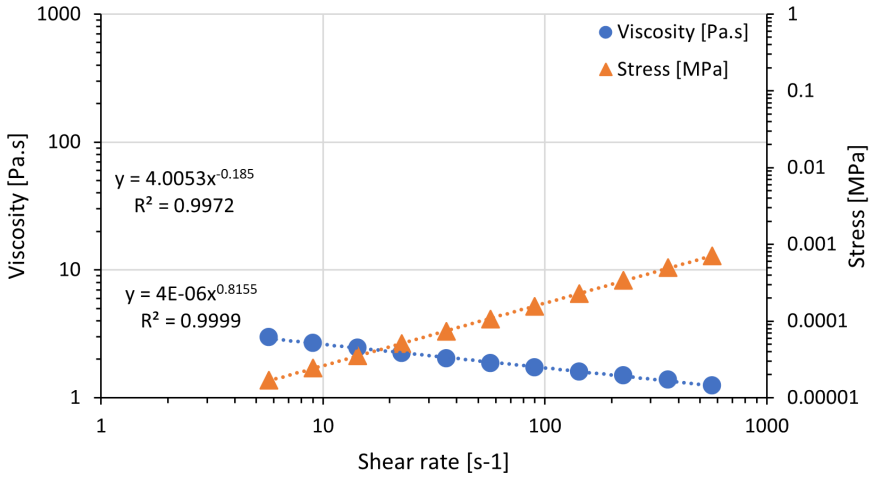

Figure A14: Flow-sweep rheogram of viscosity (η, Pa.s) and shear-stress (σ, MPa) plotted against shear rate (γ, s^{-1}) for the C16 functionalised biological grade agar 170 °C after descending in temperature from having been worked at 180 °C.

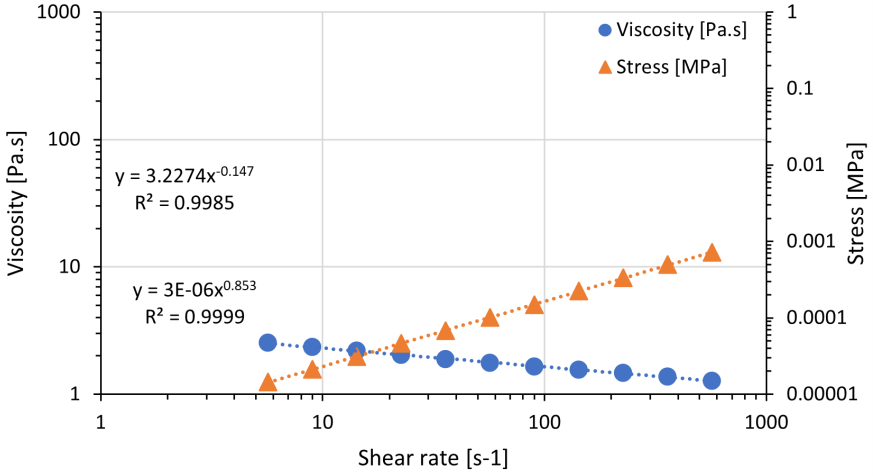

Figure A15: Flow-sweep rheogram of viscosity (η, Pa.s) and shear-stress (σ, MPa) plotted against shear rate (γ, s^{-1}) for the C16 functionalised biological grade agar 165 °C after descending in temperature from having been worked at 180 °C.

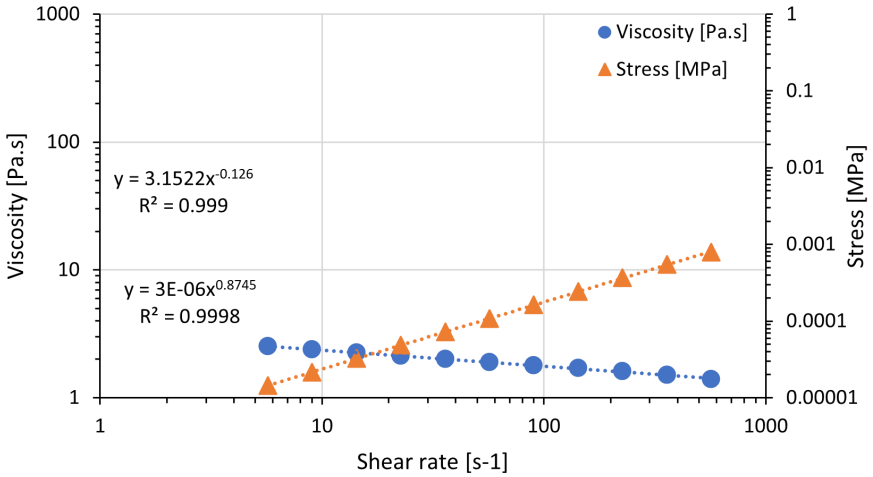

Figure A16: Flow-sweep rheogram of viscosity (η, Pa.s) and shear-stress (σ, MPa) plotted against shear rate (γ, s^{-1}) for the C16 functionalised biological grade agar 160 °C after descending in temperature from having been worked at 180 °C.

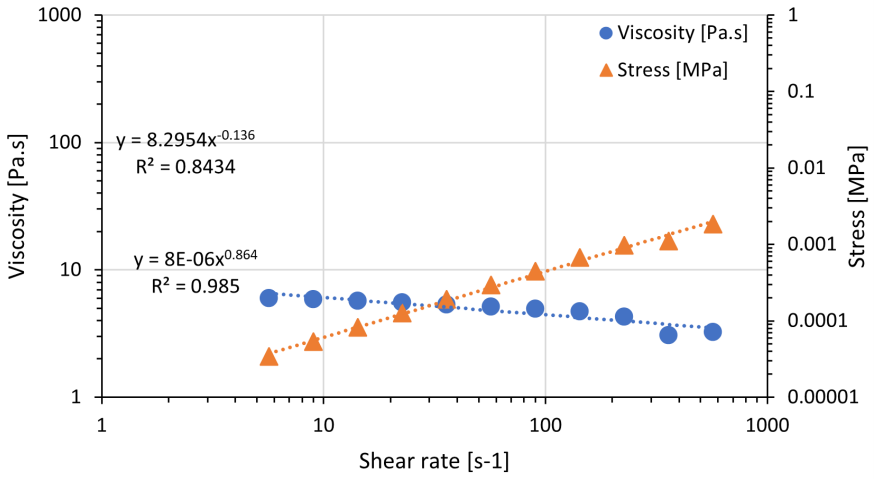

Figure A17: Flow-sweep rheogram of viscosity (η, Pa.s) and shear-stress (σ, MPa) plotted against shear rate (γ, s^{-1}) for the C16 functionalised biological grade agar 140 °C after descending in temperature from having been worked at 180 °C.

A0.2 Supplementary Tables

Table A1: P-values for significance of contriobution of calculated $a_{i,j}$ parameters to the models described by equations 2.15 to 2.18.

P-value	M_C	M_H	M_N	M_O
x_{Carb}	1.01E-25	3.23E-18	7.43E-01	7.55E-55
x_{Lipd}	1.11E-02	1.87E-09	8.48E-01	7.04E-01
x_{Prot}	6.02E-14	3.43E-07	2.86E-31	2.92E-01
b_i	1.37E-09	4.59E-79	1.00E+00	8.13E-01

Table A2: P-values for significance of contribution of calculated $a'_{i,j}$ parameters for use in estimation of biochemical proximate analysis (carbohydrate, lipid, protein) from elemental ultimate analysis (C, H, O, N wt. %), using equation 2.22.

P-values	x_{Carb}	x_{Prot}	x_{Lipd}
M_C	2.13E-14	8.22E-01	7.59E-17
M_H	1.00E+00	1.00E+00	1.00E+00
M_N	1.00E+00	9.07E-30	6.41E-23
M_O	4.74E-66	1.00E+00	1.00E+00
b_j	1.00E+00	4.29E-01	1.00E+00

Table A3: Full instruement setting details for the DataPhysics OCA 20 contact angle measurement.

Parameter	**Value**	**Units**
Drop phase	Water	
Drop density	0.9982	g cm^{-3}
Ambient phase	Air	
Ambient density	0.00129	g cm^{-3}
Dosing vol.	5.00	μL
Ambient temp.	20.0	°C
Rel. humidity	0.0	% RH
Dosing rate	0.50	μL s^{-1}
Ref. size	2.00	mm
Magnification	20.227	pixel mm^{-1}
Method	Elipse Filtering	
Aspect	1.000	
Acceleration, g	9.810	m s^{-2}